An Experimental and Modelling Study of
Natural-Circulation Boiling Water Reactor Dynamics

AN EXPERIMENTAL AND MODELLING STUDY OF NATURAL-CIRCULATION BOILING WATER REACTOR DYNAMICS

PROEFSCHRIFT

ter verkrijging van de graad van doctor
aan de Technische Universiteit Delft,
op gezag van de Rector Magnificus prof.dr.ir. J. T. Fokkema,
voorzitter van het College voor Promoties,
in het openbaar te verdedigen op dinsdag 24 september 2002 om 10:30 uur

door

Róbert ZBORAY

mérnök-fizikus TU Budapest
geboren te Sátoraljaújhely, Hongarije

Dit proefschrift is goedgekeurd door de promotoren:
Prof. dr. ir. H. van Dam
Prof. dr. ir. T.H.J.J. van der Hagen

Samenstelling promotiecommissie:

Rector Magnificus, voorzitter
Prof. dr. ir. H. van Dam,   Technische Universiteit Delft, promotor
Prof. dr. ir. T.H.J.J. van der Hagen, Technische Universiteit Delft, promotor
Prof. dr. ir. M-O. Coppens,   Technische Universiteit Delft
Prof. dr. J. L. Muñoz-Cobo,   Universidad Politecnica de Valencia, Spanje
Prof. dr. M. Z. Podowski,   Rensselaer Polytechnic Institute, V.S.
Prof. dr. ir. R. F. Mudde,   Technische Universiteit Delft
Dr. ir. F. J. M. Schrauwen,   Shell Global Solutions International BV

Printed in the Netherlands

To Nóra

Contents

Chapter 1

Introduction

The application of natural circulation of the coolant in a boiling water nuclear reactor (BWR) is a promising concept, since the natural-circulation design can be more economical and safer than present-day, forced-circulation BWRs. In a natural-circulation BWR, the coolant flow is driven by the density difference between the boiling two-phase mixture in the core + the riser and the single-phase fluid in the downcomer (figure 1.1). This gravity-driven, passive process ensures the coolant circulation as long as heat is being produced in the core. It also largely simplifies the system by eliminating the need for recirculation pumps, which are present in forced-circulation BWRs. This is in line with the trend towards simplicity and passive safety in modern reactor design philosophy in the last two decades (Taylor, 1989; McCandless and Redding, 1989; Murley, 1990).
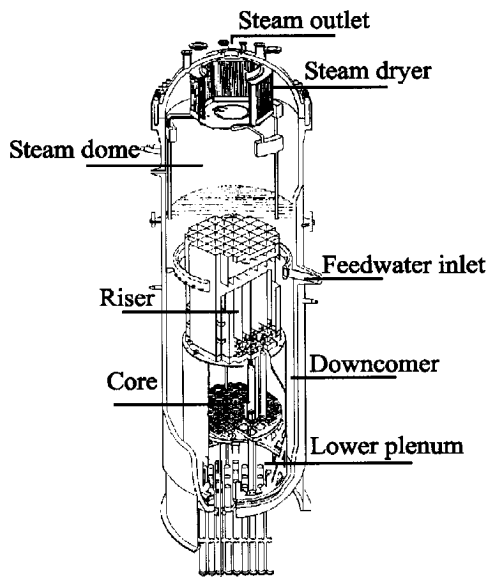
Figure 1.1: A cut-away scheme of the vessel of the Dodewaard natural-circulation BWR. No recirculation pumps are present in this design. A relatively long riser is placed on the top of the core to increase the natural-circulation flow rate.

However, the concept of natural-circulation BWRs is not new. A commercial natural-

circulation BWR plant was put into operation in the Netherlands between 1968-1997, called the Dodewaard reactor. The reactor was a design of the General Electric Company (GE) with a relatively low power of 57 MWe. A cut-away view of the vessel of the Dodewaard reactor is shown in figure 1.1. To enhance the natural-circulation flow rate a relatively long unheated section, a so-called riser (chimney), is placed on top of the core, as is shown on the figure. This reactor can be considered as a prototype of the natural-circulation BWRs.

As response to the renewed interest in natural circulation and passive processes, GE started with the design of a natural-circulation BWR again, in 1982. This 670 MWe Simplified Boiling Water Reactor (SBWR) design has, apart from the natural circulation of the coolant, several additional safety systems that rely predominantly on passive processes, such as the isolation condensers and the gravity driven emergency core cooling system (McCandless and Redding, 1989). In 1996, the SBWR concept was followed by the more economical, 1190 MWe, ESBWR (Challberg *et al.*, 1998; Cheung *et al.*, 1998), where E stands for European. The significant power uprate from the SBWR to the ES-BWR design requires certain changes to assure sufficient coolant flow rate. The magnitude of the natural-circulation flow rate depends on the driving head and the losses through the circulation path. The chimney height was increased to enhance the core flow rate. The ESBWR has an unrestricted downcomer flow area, which was optimized to minimize losses. The effective fuel height remained the same, which means relatively less pressure loss over the core. A very important aspect for both the natural-circulation flow and the stability of the reactor is the design of the steam separator on the top of the chimney. An improved, reduced pressure drop steam separator is incorporated in the ESBWR. These changes must be thoroughly evaluated with respect to reactor safety and stability.

The stability of BWRs has always been a very important issue since the first BWR designs were proposed. The research on BWR dynamics, started at that time, has resulted in significant progress in understanding the physics and modelling of the stability of this type of reactors. Although experiments on the stability of BWRs have been performed in the past, the experimental database is still poor. Especially, experimental results on natural-circulation systems should be gathered for code validation. There is no confidence that the state-of-the-art thermal-hydraulic codes available are able to reproduce within acceptable margins the behavior of natural-circulation BWRs at all practically interesting operating conditions. It is particularly true for the prediction of nonlinear, unstable behavior. Furthermore, all relevant physics involved in the dynamics of natural-circulation BWRs should be well understood.

Driven by these needs, this thesis focuses on investigating several problems associated with the dynamics and stability of natural-circulation BWRs. Part of the work contributes to a coordinated research project, Natural Circulation and Stability Performance of BWRs (NACUSP), which was started in 2000 within the European-Union Fifth Framework Programme. The main aims of the project are to increase the understanding of the physics of the phenomena involved in natural-circulation BWRs, to provide with a large experimental database, to validate state-of-the-art thermal-hydraulic codes and to give guidelines on how to prevent instabilities in operating and future BWRs (like the ESBWR).

In the next section, after a brief historical review on BWR stability analysis, the different BWR instability types and the tools used for studying BWR stability are introduced. Finally, the objectives of the work are listed and an outline of the thesis is given.

1.1 Boiling Water Reactor Stability

1.1.1 A short historical review on BWR stability investigation

The concept of a BWR was examined first by the Argonne National Laboratory (ANL). There was a series of BWR experiments, BORAX (Kramer, 1958), starting in 1953, designed to study aspects of BWR behavior. The lessons of the BORAX experiments led to the design of the Experimental Boiling Water Reactor (EBWR) (Kramer, 1958) and commercialization starting at the Dresden unit. The EBWR was operated at ANL-Illinois from 1957 until 1967 at power levels up to 100 MWt with an electrical output of 5 MW. Its missions included demonstrating the BWR concept for electricity generation with various fuel enrichments. The first large-scale, utility-owned BWR was the 200 MWe plant at Dresden. It started operation in 1960 and ran until 1978.

It has already been recognized in the framework of the Dresden project that a BWR is analogous to a feedback amplifier that might become unstable if the feedback signal acquires 180 degree phase shift at a gain of unity. This was the starting point of the analysis of dynamics and stability. The experimental tests on the EBWR and the Dresden reactor were in reasonable agreement with the result of the first BWR dynamic models and showed that these BWRs are very stable (Thie, 1957; DeShong and Lipinski, 1958; Beckjord, 1957). It was then clear that a large BWR for commercial power generation can be designed without concern about stability. At sufficiently high operating pressure, due to the relatively weak feedback from void production to power, no stability problems were expected. Using oxide pellet fuel was also very important for the stability of these designs: due to its long thermal time constant it attenuates oscillations in the void-reactivity feedback and prevents instability (D'Auria et al., 1997). However, several fuel modifications have been carried out in the course of development of BWRs and the core power density of later designs has been increased. These changes resulted in stability problems in operating BWRs in the 1970s and 1980s. The unexpected instability events in the Caorso power plant in 1984 (GE, 1983) and in the LaSalle power plant in 1988 (IRS, 1988) have reinforced the research in BWR stability. In the early 1990s several operating BWRs have also experienced stability incidents. A comprehensive review of BWR stability is given in the OECD-NEA report: State of the Art Report on Boiling Water Reactor Stability (SOAR) (D'Auria et al., 1997). In the next section, a short introduction is given on the different types of instabilities occurring in BWRs.

1.1.2 Review of BWR instability types

The instabilities occurring in BWRs are classified in the literature in different ways. Several authors distinguish, in the first place, between *thermal-hydraulic* instability and *coupled neutronic-thermalhydraulic* instability (Bouré et al., 1973; Lahey and Moody, 1993). The former one is basically represented by the so-called density-wave oscillations. The mechanism of density-wave oscillations in boiling channels, such as a BWR fuel assembly, can be explained in a number of equivalent ways (Bouré et al., 1973; Yadigaroglu, 1981; Lahey and Moody, 1993). The most commonly accepted explanation is as follows. Flow perturbations at the channel inlet create enthalpy fluctuations in the single-phase region. At the boiling boundary (the elevation at which the bulk of the liquid reaches the saturation temperature and starts to boil) the enthalpy perturbations are transformed into void-fraction variations that travel with the flow through the system. Obviously, the position of the boiling boundary fluctuates as well. The combined effect of flow, void-fraction

and boiling-boundary perturbations causes fluctuations in the pressure drop across the channel. Since the total pressure drop across the channel is imposed externally by the characteristics of the system feeding the channel, variations in the pressure drop produce a feedback perturbation in the inlet flow. Under specific conditions, the pressure-drop perturbations can acquire appropriate phases and the inlet flow-oscillations become self-sustained. Thus, transportation delay and pressure-drop characteristics are of paramount importance for the stability of the system (Bouré *et al.*, 1973; Yadigaroglu, 1981; Lahey and Moody, 1993). The well-accepted terminology "density-wave oscillations" originates from Stenning and Veziroglu (1965) and illustrates that packages of alternatively lower- and higher-density mixture travel with the flow through the system. Density-wave oscillations represent *dynamic* instabilities of the boiling, two-phase flow system in contrast to the *static*, excursive type (Ledinegg) instabilities (Bouré *et al.*, 1973; Lahey and Moody, 1993).

Thermal-hydraulic instabilities can also be divided into *high-pressure* versus *low-pressure* instabilities. Under normal operating pressure in a BWR ($\simeq 75$ *bar*), the so-called *Type-I* and *Type-II* oscillations can occur (Fukuda and Kobori, 1979). At low-power and low-pressure start-up conditions *flashing-induced instabilities* might occur. This instability is pronounced in natural-circulation systems with long risers. The void flashing phenomenon is the sudden boiling of the coolant in the riser caused by the considerable decrease of the saturation temperature along the riser due to the decreasing hydrostatic pressure. Void flashing in the riser results in oscillations of the driving force of the natural-circulation flow.

Density-wave oscillations form the basis for coupled neutronic-thermalhydraulic instabilities (Lahey and Moody, 1993). Due to the strong influence of the coolant on the neutron population in the reactor - as it also serves as moderator - oscillations in the coolant flow rate and void fraction result in power oscillations in BWRs. The strength of the coupling between the thermalhydraulics and the neutronics, the void-reactivity feedback, has an important effect on the stability of an BWR.

Typical example of the interplay between neutronics and thermalhydraulics, the so-called *out-of-phase* (regional) power oscillations, have been observed in several operating BWR plants. During out-of-phase oscillations, the power in one half of the reactor core oscillates opposite to the power in the other half, as does the coolant flow through the core. This instability is in contrast with *in-phase* (core wide) oscillations where the power (and the flow) in the whole core oscillates simultaneously. It was pointed out that the out-of-phase oscillations are less stable from thermal-hydraulic point of view (March-Leuba and Rey, 1993), but they are damped by the subcritical neutronic mode (first azimuthal mode). While the in-phase oscillations are thermalhydraulically more stable, they are destabilized by the strong feedback from the fundamental (critical) neutronic mode.

The core of a BWR consists of hundreds of fuel bundles, which are practically parallel-coupled two-phase flow channels. With respect to this, distinction is usually made between *single-channel* and *parallel-channel* instability (D'Auria *et al.*, 1997). The former one refers to the case when one of the several parallel channels is oscillating in a stable system. A single oscillating channel may trigger more complex instabilities, regional instability or core-wide reactor instability. The latter one is related to the stability of different fuel bundles up to including the entire core and to the way they are coupled to each other through the external boundary conditions. Parallel channel oscillations may be either core wide or regional.

1.1.3 Tools for BWR stability investigation

Three tools are used in this thesis to study the stability of natural-circulation BWRs: an experimental facility, a reduced-order model and a thermal-hydraulic system code. These tools are introduced briefly below:

The experimental facility

The most obvious way to investigate the stability of a natural-circulation BWR is to carry out measurements on it. Recently, an extensive series of stability measurements was carried out at the Dodewaard reactor (Van der Hagen *et al.*, 1997), where the reactor conditions varied from very stable to unstable. Although these measurement results are extremely valuable for stability analysis, the experimental possibilities are quite restricted in an actual reactor. The number and types of sensors that are present in a reactor are also limited. Therefore, it was decided at the Department of Reactor Physics of the Interfaculty Reactor Institute to build a natural-circulation experimental facility that can provide with experimental data that it would not be possible to measure otherwise. Obviously, such a facility has also its own limitations and the actual BWR cannot be imitated perfectly with it. However, concentrating on the relevant phenomena and parameters, a model facility can be designed that simulates the real system fairly well with respect to these phenomena.

One commonly used technique to achieve this in case of two-phase flows is scaling. A facility, consisting of a scaled copy of a fuel bundle of the natural-circulation Dodewaard reactor, has been designed (Van de Graaf *et al.*, 1994a). The flexible design of the facility allows the study of new natural-circulation reactor designs as well. The Delft Simulated Reactor (DESIRE) facility - a natural-circulation, boiling two-phase flow loop - became operational in 1994. Using the facility, valuable information on natural-circulation two-phase flows can be obtained like the void fraction, the void-fraction distribution and the natural-circulation flow rate. Later on the loop was equipped with an artificial void-reactivity feedback simulation (Kok and Van der Hagen, 1999). The void-reactivity feedback simulation must be optimized to enable realistic simulation and investigation of coupled neutronic-thermalhydraulic oscillations encountered in actual BWRs. A detailed description of the facility is given in Chapter 3.

The reduced-order model

To model BWR dynamics and stability, two main approaches can be distinguished. One approach develops and uses advanced system-transient codes, which are based on a detailed description of the underlying physical phenomena. These codes incorporate state-of-the-art models for the three-dimensional neutron kinetics, the fuel-to-coolant heat transfer and the coolant thermalhydraulics. The other approach focuses on the utilization of so-called low-dimensional or reduced-order models (March-Leuba *et al.*, 1986a; Rao *et al.*, 1995; Karve *et al.*, 1997). Reduced-order models capture only the most significant physical processes determining the dynamics of a BWR and usually consist of a limited number of ordinary differential equations. This simplification obviously occurs at the expense of accuracy. Nevertheless, it leads to the development of fast-running models that generate qualitatively correct predictions of stability trends for a wide range of operating and design parameters. This makes reduced-order models very suitable for fast parametric studies on BWR stability, in contrast to the time-consuming advanced codes. Another very important advantage of simplified models is that they allow increasing insight into

the physics of BWR dynamics and enable the identification of the relevant dynamical processes responsible for instabilities. This possibility is quite limited, or not feasible at all, with advanced state-of-the-art BWR system codes due to their inherent complexity. Van Bragt and Van der Hagen (1998a) have developed a reduced-order model of natural-circulation BWR dynamics. They evaluated the stability measurements carried out on the Dodewaard reactor. They showed that the model predicts the measured trends in BWRs reasonably well. The model is described in detail in Chapter 2.

The thermal-hydraulic system code

The state-of-the-art thermal-hydraulic code, MONA 1.9, is used as a complementary numerical tool for reference calculations and for quantitative comparison with experimental results. MONA 1.9 is a commercial thermal-hydraulic code for steam-water/inert gas systems developed by Scandpower (Hoyer, 1994a). The code has been developed with the aim of improving the thermal-hydraulic models used in the reactor dynamic code RAMONA 5. Possible applications of the code range from pressurization, flow and temperature transients to the analysis of density-wave oscillations.

1.2   Objectives

Using the tools introduced above, the thesis examines the following aspects of natural-circulation BWR dynamics and stability:

- increasing the insight into the role of different physical phenomena involved in thermal-hydraulic and coupled neutronic-thermalhydraulic instabilities of natural-circulation BWRs applying the reduced-order model, improving the model and the understanding of the physics of instabilities;

- investigating several practical linear stability and nonlinear dynamical problems of natural-circulation BWRs numerically;

- investigating the thermal-hydraulic stability of natural-circulation two-phase flows experimentally for as wide range of stability situations as possible: from very stable (linear behavior) to strongly unstable (nonlinear behavior);

- improving the artificial void-reactivity feedback simulation in the DESIRE facility to enable realistic simulation of coupled neutronic-thermalhydraulic oscillations encountered in actual BWRs, investigating the coupled neutronic-thermalhydraulic stability of natural-circulation BWRs experimentally;

1.3   The outline of the thesis

This thesis is organized as follows:

In Chapter 2, a linear stability analysis of natural-circulation BWRs and the underlying thermalhydraulics is presented using the aforementioned reduced-order model. The root loci (poles) of the system are examined as a function of the operating conditions, riser length, and void-reactivity coefficient. The origin of the poles and their importance for the stability of the system are investigated. Furthermore, the relevant physical phenomena driving the instabilities are studied to gain more insight into their influence on

the dynamics. The study includes the stability analysis of forced-circulation systems as well.

Experimental investigations on the linear stability of natural-circulation two-phase flows are presented in Chapter 3. First, it is described how the DESIRE facility is destabilized on purpose to enable the study of unstable situations. Stability maps are obtained under different experimental conditions such as changing the friction distribution along the loop, or changing the axial heating profile. Assessment of the measurements using the reduced-order model and the MONA code is also given.

In Chapter 4, two distinct applications of the reduced-order model are discussed. The first problem is related to the stability monitoring of BWRs. It is examined how the decay ratio, which is almost exclusively used for stability monitoring, is related to safety (stability) margins expressed in operational parameters. The second problem addressed is the influence of core-inlet temperature variations on the thermal-hydraulic stability of BWRs. For this purpose, the model is extended to account for the dynamics of the core inlet subcooling. The problem is examined using the MONA code as well.

In Chapter 5, numerical bifurcation analysis of the nonlinear dynamics of BWRs is performed examining the influence of asymmetrical axial power profiles. Thermal-hydraulic and coupled neutronic-thermalhydraulic systems are treated separately.

Experiments on the nonlinear dynamics of natural-circulation, boiling two-phase flows are discussed in Chapter 6. The character of density-wave oscillations measured close to the stable operating region is examined first. The strongly nonlinear density-wave oscillations measured deep in the unstable operating region are analyzed using nonlinear time series analysis methods. An overview of these methods is given as well.

Chapter 7 is devoted to the investigation of coupled neutronic-thermalhydraulic stability of BWRs. The study concentrates on improving the artificial void-reactivity feedback simulation in the DESIRE facility. Experiments on the coupled neutronic-thermalhydraulic stability of the system are carried out using the improved void-reactivity feedback simulation.

Conclusion and recommendations are given in Chapter 8.

Chapter 2

Understanding the linear stability characteristics of BWRs

2.1 Introduction

The first simplified BWR dynamic models were already developed in the 1950's by, among others, DeShong and Lipinski (1958) and Thie (1958) These models have been used to study the reactivity-to-power transfer function and the root loci of the natural-circulation Experimental BWR (EBWR) reactor (Thie, 1958). A simple point-kinetics (zero-power transfer function) description of the neutronics was used. It became clear already from these early models that a higher-order modelling of the void production process - several poles and zeros in the transfer function describing the power to void-reactivity feedback mechanism - is needed to represent the transfer function of the reactor correctly and to be able to predict instabilities. In the 1960's, Miida and Suda (1963) built a detailed model considering steam load and recirculation flow dynamics for a natural-circulation BWR. After that, the concept of natural circulation was abandoned and attention was focused on forced-circulation BWRs.

In the 1960's and 1970's, as research on the stability of boiling two-phase flow systems was intensified, some authors tried to couple the sophisticated thermal-hydraulic models developed in that field with a simple neutronic (mostly point-kinetic) model to study BWRs (Lahey and Moody, 1993; Yadigaroglu, 1981). However, this effort was in most cases the starting point for the development of large-scale transient codes rather than of reduced-order models.

In the 1980's, a pioneering work was accomplished by March-Leuba *et al.* (1986a,b), in the sense that they developed a simplified, phenomenological model to study linear and nonlinear dynamical behavior of BWRs. They used a strongly simplified description for the thermalhydraulics, a second-order model that is not able to predict two-phase flow instabilities. However, coupled with the neutronics, it can describe instabilities of BWRs. They found that at least three zeros and four poles are needed to properly represent the reactivity-to-power transfer function of a BWR. Moreover, these poles and zeros have been associated with physical processes that occur in the reactor.

In order not to underestimate the important role of the thermalhydraulics even in reduced-order BWR stability models, the trend in the last decade was to develop simplified models that do capture the most significant physical processes involved in the thermalhydraulics and to couple it with a usually simple description of the neutron kinetics. The reader is referred to the models of, e.g., Rao *et al.* (1995) and Karve *et al.* (1997).

This last tendency was accompanied by a renewed research interest in reduced-order natural-circulation BWR models. Progress herein was supported by the development of more elaborate, but still reasonably simple, models concerning the thermal-hydraulic stability of natural-circulation two-phase flow systems, for instance, by Clausse and Lahey (1991); Lee and Lee (1991); Wang *et al.* (1994); Pinheiro Rosa and Podowski (1994); Garea *et al.* (1994); Chang and Lahey (1997). Chang and Lahey (1997) analyzed the stability of the Simplified Boiling Water Reactor (SBWR) using a more sophisticated model for the dynamics of the natural-circulation two-phase flow in the reactor. They concluded that under typical low-pressure startup conditions, the SBWR is quite stable. However, large-amplitude limit-cycle oscillations may occur under abnormal operating conditions.

This chapter elaborates on the linear stability of natural-circulation BWRs and the underlying (two-phase) thermal-hydraulic system via the root-locus method. The reduced-order model of Van Bragt and Van der Hagen (1998a) is used, which is just sophisticated enough to predict the thermal-hydraulic instability phenomena. Because of its simplicity, it has the potential to increase the insight into the relation between the main physical processes determining BWR stability. The root loci (the poles) of the system are examined as a function of the operating conditions, riser length, and void-reactivity coefficient. The origin of the poles and their importance for the stability of the system are investigated. Furthermore, the paper studies the relevant physical phenomena driving the instabilities and attempts to gain more insight into their influence on the dynamics. It is examined whether these physical phenomena can be related to the poles of the system.

The model is briefly described in Section 2.2. To make the analysis more transparent, the thermal-hydraulic subsystem (both forced and natural circulation) of a BWR is investigated separately in Section 2.3. In Section 2.4, a natural-circulation BWR is analyzed.

2.2   The reduced-order model

Figure 2.1 gives an schematic overview of the flow path in a natural-circulation BWR loop showing all the components that are accounted for in the reduced-order model of Van Bragt and Van der Hagen (1998a). Although the steam dome above the riser is not modelled explicitly (compare with figure 1.1), a constant water level in the system is assured by adjusting the feedwater flow to the steady-state steam flow. The system components outside of the reactor vessel are not modelled therefore the steam line pressure and feedwater temperature are imposed as boundary conditions. Local pressure losses are modelled using friction factors at the core inlet, core exit, riser exit and downcomer inlet. Distributed pressure losses (tube friction) is modelled in the core and in the riser.

The most important assumptions and approximations applied in the reduced-order model can be summarized as follows:

1. The neutron kinetics is modelled by the point-kinetic equations with one effective delayed neutron group.

2. The heat transfer from fuel to coolant is modelled as a first-order process using one effective time constant.

3. The two-phase flow in the multiple parallel coolant channels of a BWR is analyzed on the basis of the one-dimensional homogeneous-equilibrium-mixture (HEM) model using one effective (average) coolant channel.
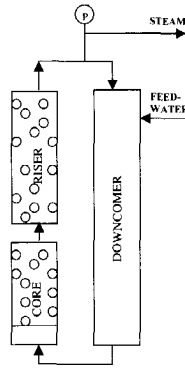
Figure 2.1: Schematic of a natural-circulation BWR as it is represented in the reduced-order model. The arrows indicate flow directions.

4. The core section is divided into a single-phase and a two-phase axial node. The differential balance equations are integrated over each node by assuming a time-dependent and spatially linear profile of the one-phase enthalpy and the two-phase flow quality in the axial direction. Whereas, the axially varying mass-flux density in the two-phase region is assumed to be constant and equal to the core-exit mass-flux density in the integration process.

5. Subcooled boiling and void flashing phenomena are ignored.

6. To analyze a system with a riser, the riser is divided into several axial nodes, and the aforementioned linear spatial approximation is used for the flow quality and mass flux within each node.

7. The liquid in the downcomer is assumed to be one-phase (no carry under) and incompressible with a fluid temperature uniform in space and time.

The governing differential balance equations for the thermalhydraulics are transformed into ordinary differential equations (ODEs) using the above assumptions. The influence of these assumptions on the accuracy of prediction will be discussed in Section 3.3.2 comparing measurement results with model calculations. A comprehensive list of the model equations is given in Appendix A.

Van Bragt *et al.* (1999) have shown that using four axial nodes in the riser is a reasonably good approximation for the case of the Dodewaard natural-circulation reactor. The data set and geometry of this reactor (see Appendix B), dividing the riser into four axial nodes, is used as a model reactor in this study.

Using four nodes in the riser the model consists of ten nonlinear ODEs, which are linearized and Laplace- transformed to facilitate a frequency-domain analysis. The underlying relations between the system variables can be represented in the block diagram shown in figure 2.2. For the thermal-hydraulic subsystem, shown within the dashed rectangle, $G_{x,y}$ denotes the normalized transfer function from variable y to x. The explicit expressions of the transfer functions are listed in Appendix A. The transfer functions in the block diagram are all functions of the Laplace variable $s = \sigma + i\omega$, where σ is the real part and ω is the imaginary part. The model represents the inherent feedback mechanisms in a BWR (void- and Doppler-reactivity feedback), as depicted in figure 2.2. The transfer
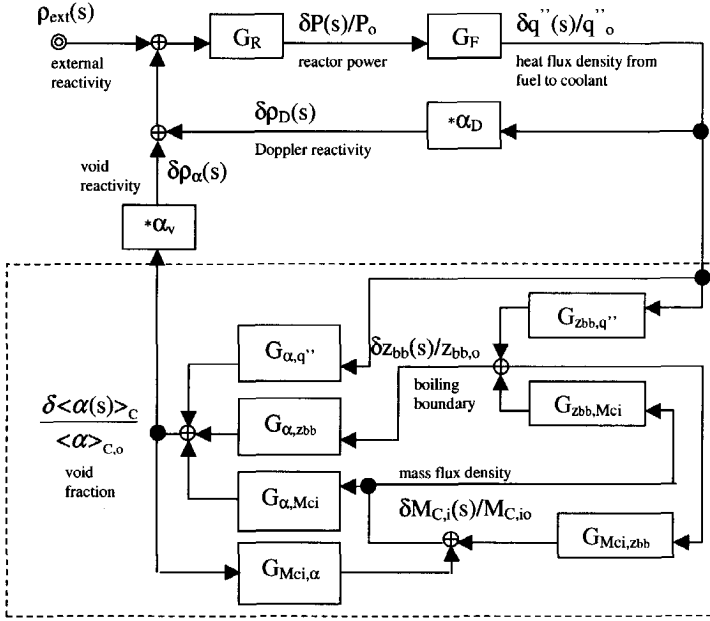
Figure 2.2: Block diagram representing the closed-loop, 'external reactivity' to 'reactor power', transfer function of a BWR for the linearized, frequency-domain model. The thermal-hydraulic transfer functions are clustered in the dashed rectangle. The Doppler and void reactivity is obtained by multiplying the fuel-temperature and void-fraction oscillations with the corresponding reactivity coefficients, α_D and α_V.

function of the thermal-hydraulic subsystem from heat flux to core-average void fraction is given by

$$G_A \equiv \frac{\frac{\delta <\alpha(s)>_C}{<\alpha>_{C,o}}}{\frac{\delta q''(s)}{q''_o}} = \frac{G_1}{1 + G_{M_{C,i},\alpha}G_1 + G_{M_{C,i},z_{bb}}G_{z_{bb},q''}} \qquad (2.1)$$

where

$$G_1 = G_{\alpha,q''} + G_{\alpha,z_{bb}}G_{z_{bb},q''}$$

The closed-loop reactor transfer function from external reactivity to reactor power is then

$$G_T = \frac{\frac{\delta P}{P_o}}{\rho_{ext}} = \frac{G_R}{1 - G_R G_F[\alpha_V + \alpha_D G_A]}. \qquad (2.2)$$

The poles of the closed-loop transfer function are obtained by considering the roots of the characteristic equation:

$$1 - G_R G_F[\alpha_D + \alpha_V G_A] = 0. \qquad (2.3)$$

The closed-loop transfer function of a higher-order system, as with a BWR, has several poles, which are real and/or form complex conjugate pole pairs. The dynamic stability of a pole is usually quantified by its decay ratio (DR), which is defined as $DR = \exp 2\pi\sigma/|\omega|$ for a pole at $s = \sigma + i\omega$. The least stable pole, with the largest $\sigma/|\omega|$ ratio, determines

the stability of the system. The poles of the system at a specific operating point are determined by a numerical search algorithm, a quasi-Newton method. Or specifying the least stable pole (the stability of the system), the corresponding operating conditions can be determined the same way.

To make the analysis more transparent, the thermal-hydraulic subsystem is examined separately. The characteristic equation of the thermal-hydraulic subsystem, using Eq. 2.1, is

$$1 + G_{M_{C,i},\alpha}(G_{\alpha,q''} + G_{\alpha,z_{bb}}G_{z_{bb},q''}) + G_{M_{C,i},z_{bb}}G_{z_{bb},q''} = 0. \qquad (2.4)$$

Considering that

$$G_{M_{C,i},\alpha} = -\frac{\frac{\delta\Delta P_{total}}{\delta<\alpha>_C}}{\frac{\partial\Delta P_{total}}{\partial M_{C,i}}}\frac{<\alpha>_{C,o}}{M_{C,i,o}}, G_{M_{C,i},z_{bb}} = -\frac{\frac{\delta\Delta P_{total}}{\delta z_{bb}}}{\frac{\partial\Delta P_{total}}{\partial M_{C,i}}}\frac{z_{bb,o}}{M_{C,i,o}} \qquad (2.5)$$

and

$$G_{z_{bb},M_{C,i}} = -G_{z_{bb},q''}, G_{\alpha,q''} = -G_{\alpha,M_{C,i}} \qquad (2.6)$$

the characteristic equation of the thermal-hydraulic subsystem can be written in a form that is frequently used in literature (Yadigaroglu, 1981; Rao *et al.*, 1995)

$$\frac{\delta\Delta P_{total}}{\delta M_{C,i}}(s) = 0, \qquad (2.7)$$

where $\frac{\delta\Delta P_{total}}{\delta M_{C,i}}(s)$ is the total transfer function from the inlet mass flux to the total pressure drop over the circulation loop. The left side of this characteristic equation (the characteristic polynomial) can be split into a sum of transfer functions from inlet mass flux to the different types of physical pressure drops:

$$\frac{\delta\Delta P_{total}}{\delta M_{C,i}}(s) = \sum_{j=1-\phi,2-\phi}\frac{\delta\Delta P_{in}}{\delta M_{C,i}}(s)_j + \frac{\delta\Delta P_{fr}}{\delta M_{C,i}}(s)_j + \frac{\delta\Delta P_{gr}}{\delta M_{C,i}}(s)_j + \frac{\delta\Delta P_{acc}}{\delta M_{C,i}}(s)_j = 0. \quad (2.8)$$

The following physical pressure drop terms are distinguished in both the one- and the two-phase region: inertial, frictional, gravitational, and accelerational pressure drop. We will refer to the foregoing transfer functions from inlet mass flux to the different types of pressure drop shortly as pressure drop transfer functions throughout the text. By fixing all the system parameters except one, the threshold of *dynamic* instability for that parameter and the corresponding oscillation frequency can be obtained numerically from Eq. 2.8 if one sets $s = i\omega$ (the latter corresponds to DR = 1). Incrementally varying another system parameter an entire stability map can be drawn in a two-dimensional parameter space. Equation 2.8 also provides the threshold of the *static* instability as the $\omega \to 0$ limit is taken (Lahey and Yadigaroglu, 1982). We note here that if a system without riser is modelled, then all the transfer functions in the characteristic equation, Eq. 2.4, are (ratios of) second- or first-degree polynomials in s in such combination that the left side of the equation is equivalent to a third-degree polynomial (third-order system). If a system with four riser nodes is modelled, then the order of the system increases to seven. Obviously, the same holds for Eq. 2.7.

2.3 Analysis of the thermal-hydraulic stability

In Section 2.3.1 and 2.3.2, the root loci of the thermal-hydraulic system of a BWR (the roots of Eq. 2.8) are studied. The contributions of the individual pressure drop transfer functions in Eq. 2.8 are examined as well.

2.3.1   Forced-circulation system

First, a forced-circulation boiling channel is investigated, with the dimensions of one average fuel assembly in the Dodewaard reactor under nominal Dodewaard operating pressure (75.5 bar). Figure 2.3 shows the linear stability map with the static and dynamic stability boundary (SB) of the system in the so-called Zuber (or phase-change) number (N_{Zu}) and subcooling number (N_{sub}) plane (Saha *et al.*, 1976); N_{Zu} and N_{sub} are both dimensionless numbers and are defined as follows:

$$N_{Zu} = \frac{P}{\Phi(h_g - h_f)} \frac{\rho_f - \rho_g}{\rho_g} \text{ and } N_{sub} = \frac{h_f - h_{in}}{h_g - h_f} \frac{\rho_f - \rho_g}{\rho_g}.$$
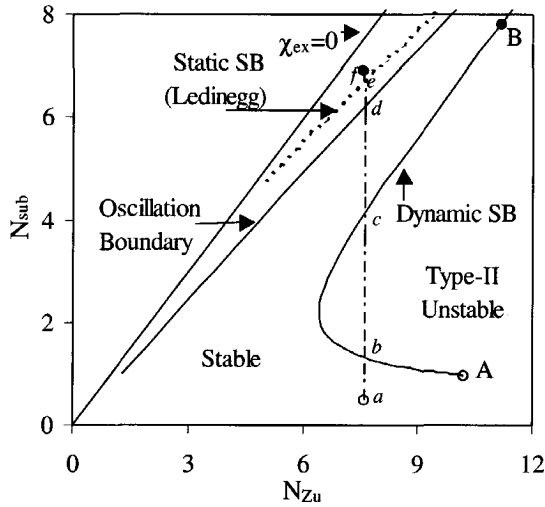
Figure 2.3: Stability map of a forced-circulation two-phase boiling channel obtained for a constant pressure drop boundary condition. The term $\chi_{ex} = 0$ denotes the zero exit thermodynamic equilibrium quality line (Lahey and Moody, 1993).

These two numbers are commonly used in stability analysis of boiling two-phase flow systems. The stability of the channel depends on the amount of inlet flow feedback, which is determined by the characteristics of the recirculation loop. In the case of forced circulation, the recirculation loop and the pump dynamics impose the boundary condition for the inlet flow feedback. The stability map in figure 2.3 is obtained with a constant pressure drop over the channel as boundary condition, which corresponds practically to a constant pumping head in the system (set to 195 mbar). This is the most unstable type of boundary condition for a forced-circulation system since it provides no damping of the inlet-flow oscillations by inertial and frictional effects (pressure drop variations) in the downcomer. For the natural-circulation system examined in Section 2.3.2, the pressure drops in the downcomer influence the stability. The dynamic SB separates the stable and the so-called Type-II unstable operating region. The Type-II instability is mainly driven by the interplay between the one- and the two-phase frictional pressure drops (Fukuda and Kobori, 1979).

Figure 2.4 shows the poles of the system along the vertical trajectory of operating points (from point a to f) in figure 2.3. Moving along a vertical trajectory in the operating plane, in practice, corresponds to increasing the inlet subcooling in the channel

while keeping the power/flow-rate ratio constant. Since a boiling channel without a riser is modelled as a third-order system (the simplest model that can predict the dynamic instability of the two-phase flow), it has three poles. Two of them form a complex conjugate pole pair in each operating point below the oscillation boundary.
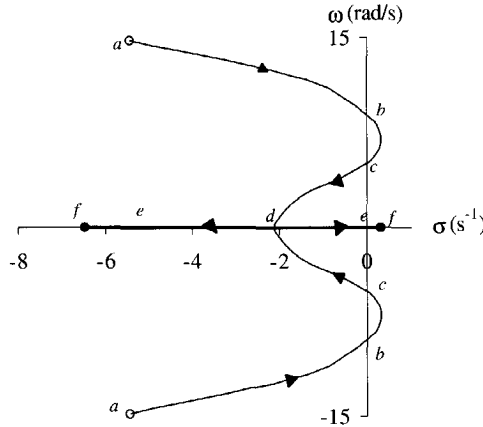
Figure 2.4: The root locus of the complex conjugate pole pair of the forced-circulation system along the vertical trajectory of operating points (from a to f) in figure 2.3. The third pole of the system is not depicted because it is irrelevant for the stability.

This complex conjugate pole pair is responsible for the Type-II instability as they shift into the right half-plane of the complex domain when the operating conditions change from point a through point b to the Type-II unstable region. At point c, the system becomes again stable. Passing through point d, the oscillation boundary is reached; the complex pole pair becomes real, and the two real poles move in opposite directions. In operating points above the oscillation boundary (but below the static SB), all of the poles are real, and the system does not give an oscillatory but an exponentially changing (decaying) response to perturbations. As the static (Ledinegg) SB is reached (point e), the pole moving in the positive direction crosses the origin. In point f, the system is statically unstable; i.e., it exhibits excursive (exponentially diverging) behavior when disturbed. In general, the Ledinegg instability in forced-circulation systems occurs when for the derivative of the total static pressure drop versus inlet flow curve (Lahey and Moody, 1993).

$$\frac{\partial \Delta P_{total,channel}}{\partial M_{C,i}} - \frac{\partial \Delta P_{drivinghead}}{\partial M_{C,i}} \leq 0, \tag{2.9}$$

which reduces in the case of our simple constant pressure drop boundary condition to

$$\frac{\partial \Delta P_{total,channel}}{\partial M_{C,i}} \leq 0. \tag{2.10}$$

Note that since $\omega = 0$, the total pressure drop transfer function is just the derivative of the total static pressure drop with respect to the inlet flow. Accordingly, Eq. 2.8 is equivalent to the equality in Eq. 2.10, marking the threshold of the Ledinegg instability.
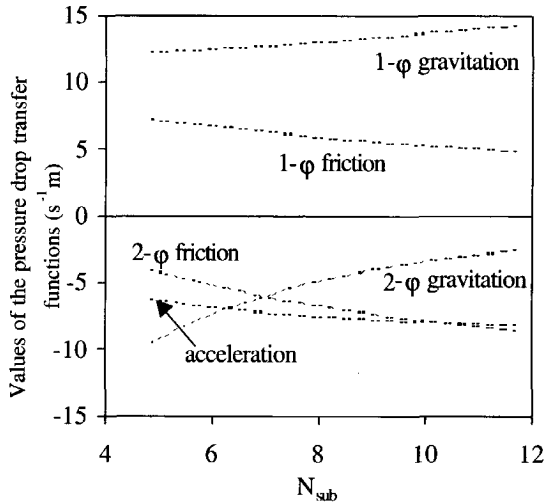
Figure 2.5: The values of the different types of static pressure drop derivatives along the Ledinegg SB as a function of N_{sub}. The inertial pressure drop derivatives are zero on the static SB.

Figure 2.5 shows how the contributions of the different types of static pressure drop derivatives to the characteristic equation, Eq. 2.8, change along the Ledinegg SB. In view of Eq. 2.10, the negative contribution of the frictional, the accelerational, and the gravitational pressure drop terms in the two-phase region are responsible for the Ledinegg instability. On the other hand, the positive contributions from the one-phase frictional and gravitational pressure drop have a stabilizing influence. (There is no accelerational pressure drop in the one-phase region since the channel cross section is uniform.) The static instability occurs at high subcoolings (low exit flow qualities) because then the negative (destabilizing) pressure drop derivatives become too large to be compensated for by the positive, stabilizing terms. This is due to the sudden change in the void fraction induced by fluctuations in the flow quality at low exit qualities.

Figure 2.6 shows the contributions of the individual pressure drop transfer functions to Eq. 2.8 in operating points along the dynamic (Type-II) SB. Note that the accelerational, two-phase frictional and two-phase gravitational pressure drop transfer function all have a large phase lag (close to $-180°$) with respect to the inlet flow perturbations. On the contrary, the frictional and gravitational pressure drop in the one-phase region have no or a small phase lag, respectively. This explains the physical mechanism of the instability: because of the large delay (phase lag) in the two-phase pressure drops with respect to the inlet flow perturbations, fluctuations in the total pressure drop over the channel can become out of phase with the inlet flow fluctuations. This results, via the constant pressure drop boundary condition, in a positive feedback and self-sustained oscillations in the inlet flow. In case of single-phase flow, i.e. in absence of the two-phase pressure drop terms with large phase lags, the characteristic equation (Eq. 2.7) could not be fulfilled for any $s = i\omega$ (the resultant of the complex vectors in figure 2.6 could never be zero). This means that the system is always stable, which is known from experimental experience as well. In this sense, one can say that the accelerational, two-phase frictional and two-phase gravitational pressure drops are responsible for the instability of the two-phase flow.
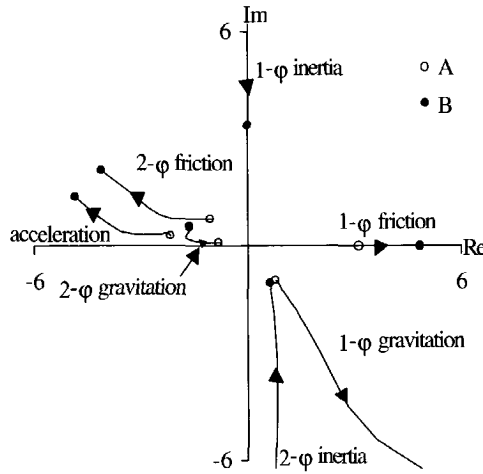
Figure 2.6: The complex vectors representing the gain and phase of the different pressure drop transfer functions obtained at operating conditions along the dynamic (Type-II) SB. Points A and B correspond to those in figure 2.3
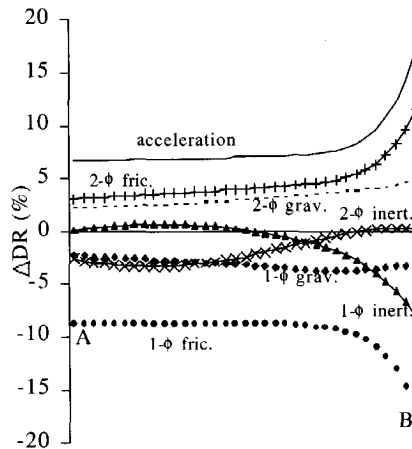
Figure 2.7: Relative change (sensitivity) of the DR of the system for a 5% increase in a pressure drop transfer function along the dynamic SB. Points A and B correspond to those in figure 2.3

The influence of the different pressure drops on the stability of the system can be quantified by examining the sensitivity of the system stability to changes in the magnitude of the individual pressure drop transfer functions. Figure 2.7 shows how the stability of the system would react for a 5% increase in magnitude of a pressure drop transfer function. The relative increase or decrease of the DR of the least stable pole is given as one moves along the dynamic SB (from point A to point B in figure 2.3). One can notice that as the magnitude of the transfer functions increases along the dynamic SB

toward higher subcoolings in figure 2.6, the corresponding sensitivities also increase in figure 2.7. The results show that the system stability is about two times more sensitive to the accelerational than to the two-phase frictional pressure drop. These two are the most important destabilizing terms for the Type-II instability.

2.3.2 Natural-circulation system

In the following, a natural-circulation thermal-hydraulic system is considered with a riser placed on the top of the heated section. The dimensions and the operating pressure are again the same as in Dodewaard.
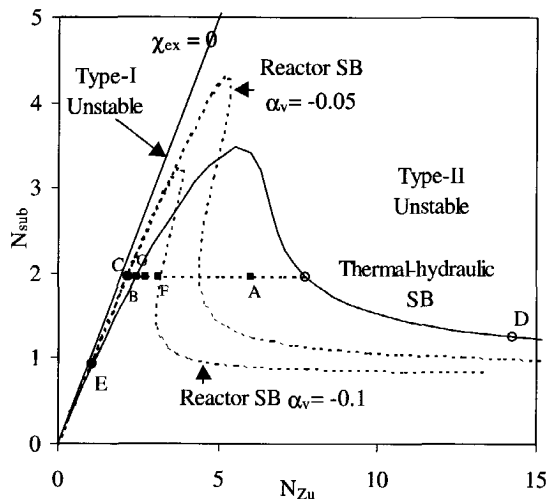
Figure 2.8: Stability map of a natural-circulation system. The thermal-hydraulic SB (solid line) is shown together with the reactor-kinetic SB's for two different void coefficients (α_V) (dotted lines).

The stability map, given in figure 2.8, shows that another region of instability emerges compared to the forced-circulation case close to the zero quality line: the Type-I instability region (Fukuda and Kobori, 1979). For the Type-I instability, the large variations in the gravitational pressure drop in the riser play a very important role. The large variation in the gravitational pressure drop in the riser is due to the abrupt change in void fraction triggered by core exit flow quality fluctuations at low core exit qualities (Fukuda and Kobori, 1979). This is similar to the origin of the Ledinegg instability, except that then other kinds of pressure drops (acceleration and two-phase friction) are influenced just as strongly as the gravitational pressure drop by the void fraction fluctuations (see figure 2.5).

A static SB as shown for a forced-circulation system in figure 2.3 does not appear for a natural-circulation system. To illustrate this, we have calculated the root loci of a natural-circulation system without a riser and with relatively small risers in operating points along a vertical trajectory similar to that in figure 2.3 going up to the zero-quality line. The results are shown in figure 2.9. Because of the symmetry of the root-loci diagrams around the real axis, we plot only the positive imaginary half-plane in the rest of the figures. The natural-circulation system without a riser remains oscillatory up to the limit of the model,

the zero-quality line. If a very short riser (relative to the 1.79-m core height) is added to the system, the system becomes again dynamically (Type-I) unstable before reaching the zero-quality line, and the root loci approach the origin from the positive real half-plane.
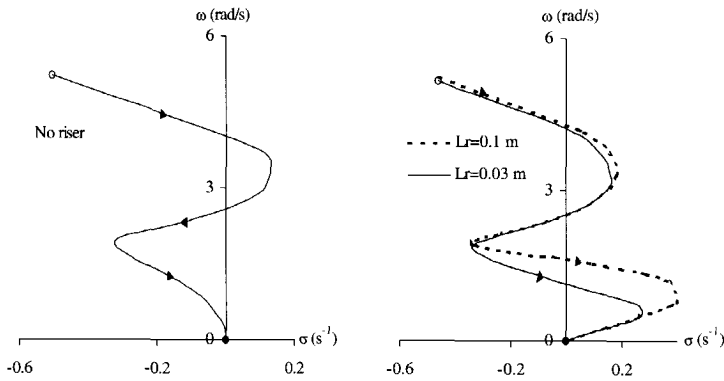
Figure 2.9: Root loci of a natural circulation system without a riser (left figure) and with rather short risers (right figure) along a vertical trajectory of operating points from the N_{Zu} axis up to the zero-quality line (similar to the vertical line in Figure 2.3).A natural-circulation system without a riser remains oscillatory approaching the zero-quality line with the operating conditions. With a relatively small riser (L_r denotes the riser length), the system becomes dynamically (Type-I) unstable just before reaching the zero-quality line.
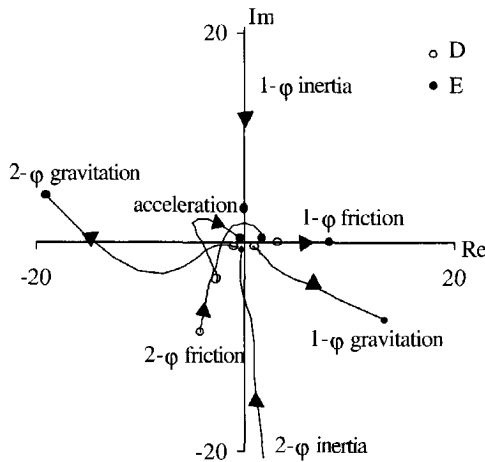
Figure 2.10: The complex values of the pressure drop transfer functions along the SB of the natural-circulation thermal-hydraulic system. The arrows show the direction of moving from the Type-II to the Type-I region (from point D to E in figure 2.8).

    Figure 2.10 shows the contributions of the different pressure-drop transfer functions to the characteristic equation along the SB moving from the Type-II region to the Type-I

region (from point D to point E in figure 2.8). One can see that as the Type-I region is approached, the two-phase gravitational pressure-drop transfer function gradually becomes larger in magnitude and becomes dominating, while the magnitudes of the two-phase frictional and accelerational pressure-drop transfer functions decrease. A similar trend in the behavior of the sensitivity of the system stability with respect to these terms is shown prominently in figure 2.11. The following interesting points can be inferred from figure 2.11:

1. The sensitivity of the stability to the two-phase gravitational term increases tremendously, from practically zero to 20% in the DR, moving from the Type-II to the Type-I region.

2. In the Type-I region, where the core exit flow quality is low, the boiling boundary is situated close to the core exit. Therefore, the influence of the two-phase gravitational pressure drop is due to the change of the gravitational pressure drop in the riser. The riser behaves as an amplifier for the Type-I oscillations.

3. The sensitivities to the other two-phase pressure drop terms that are dominating in the Type-II region decrease to very low values in the Type-I region. The effect of the two-phase frictional and the two-phase inertial pressure drop change from destabilizing to stabilizing.

4. The sensitivity to the one-phase inertial pressure drop is just about the opposite of the sensitivity to the two-phase inertial pressure drop.

5. The one-phase frictional and one-phase gravitational pressure drops are stabilizing in both regions. The latter one has a strongly increasing influence on the stability in the Type-I region, similarly to the increasing (destabilizing!) influence of the two-phase gravitational pressure drop.
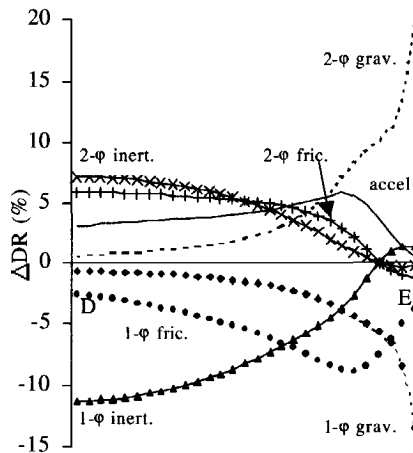
Figure 2.11: Sensitivity of the stability of a natural-circulation two-phase flow system with a riser to a 5% increase in the magnitude of a pressure drop transfer function along the SB. Points D and E correspond to those in figure 2.8.

Figure 2.12 shows typical root loci of the natural-circulation system as one follows trajectories (the horizontal line in Figure 2.6) of operating points leading from the Type-II to the Type-I region. Using four riser nodes, the thermal-hydraulic subsystem is modelled as a seventh order system, which has in this case three complex conjugate pole pairs and one real pole.

The same pole pair remains the least stable one in both instability regions. On the other hand, we have seen that different types of physical mechanisms are responsible for the two types of instabilities. This shows that a pole (pair) of the natural-circulation thermal-hydraulic system cannot be identified with a specific physical phenomenon.
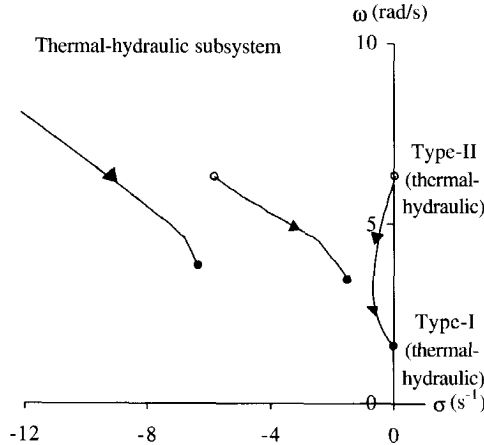
Figure 2.12: Root loci of the natural-circulation thermal-hydraulic system moving along the horizontal trajectory in figure 2.8 from the Type-II to the Type-I region. The single real pole is out of the range on the negative axis.

2.4 Stability analysis of a natural-circulation BWR

In this section, we analyze a natural-circulation reactor by coupling the thermal-hydraulic system studied in Section 2.3.2 with the neutronics and fuel dynamics (see figure 2.2). A detailed description of the void-reactivity feedback is given in Chapter 7. It should be noted, that this study is restricted to the examination of in-phase reactor stability. Figure 2.8 shows the stability maps of a natural-circulation reactor for two different void-reactivity coefficients (α_V). The value of the void-reactivity coefficient is used as a parameter to draw the root loci of the system at two operating points denoted by A ($N_{Zu} = 6.0$, $N_{sub} = 1.96$) and B ($N_{Zu} = 2.44$, $N_{sub} = 1.96$) in figure 2.8. Parts of these root loci are shown in figure 2.13. The locations of the reactor-kinetic SB's in figure 2.8 already show that the Type-II unstable region increases by increasing (in absolute sense) the void coefficient; consequently, point A becomes unstable at a certain, large enough value of the void coefficient. However, the Type-I region decreases, and point B (which was exactly on the Type-I SB for the thermal-hydraulic system) becomes stable. The same can be seen in more detail in the root-loci diagrams in figure 2.13.

It is well known in linear stability analysis that the poles of the so-called open-loop transfer function play an important role in determining the stability and root loci of the
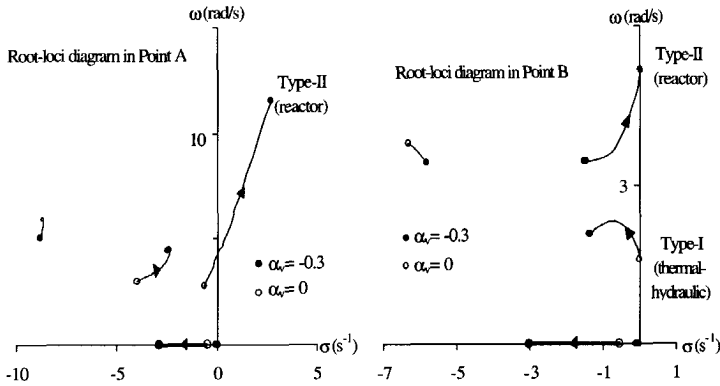
Figure 2.13: Root loci of a natural-circulation reactor using the void coefficient (α_V) as parameter. The Type-II oscillations are destabilized in point A in figure 2.8 (left figure), while in point B the Type-I oscillations are stabilized (right figure) by increasing (in the absolute sense) the void coefficient. At strong void feedback ($\alpha_V = -0.3$), the higher-frequency pole becomes (Type-II) unstable at point B. Arrows indicate the direction of the increasing void coefficient. (The locus of one real pole is restricted within a very small interval close to the origin.) Two real poles are strongly negative and out of the range of the figure.

system. The open-loop transfer function of the reactor system is equal to $G_R G_F [\alpha_D + \alpha_V G_A]$ (see Eq. 2.2). The zero-power reactor transfer function G_R has two real poles (second order) using one group of delayed neutrons (Hetrick, 1971). The locus of one of them is the one very close to the origin in figure 2.13; the other is out of the range on the negative real axis. The G_F fuel heat transfer function has one real pole (the corresponding locus is the longer one on the real axis in figure 2.13), determined by the fuel time constant (first-order process). The thermal-hydraulic transfer function G_A has three complex conjugate pole pairs and one real pole, as is shown in Sec 2.3.2. The root loci of the system approach the poles of the open-loop transfer function if the void and Doppler feedback coefficients approach zero (Hetrick, 1971). It can also be shown that the complex pole pairs of Eq. (3) at $\alpha_V = 0$ in figure 2.13 are just the poles of the thermal-hydraulic subsystem. Their position is gradually changed (and thus also the stability of the system) as α_V is increased.

In the case of point B, the Type-I unstable pole (at the lower frequency) of the thermal-hydraulic system is stabilized by an increasing void coefficient. On the contrary, the pole at a higher frequency, which is thermal-hydraulically stable, becomes unstable at high values of the void coefficient (around $\alpha_V = -0.3$). At this value of α_V, the Type-II SB is shifted past point B. The opposite effects of the void reactivity feedback on the two different types of instabilities can be explained as Van Bragt and Van der Hagen (1998b) have pointed out: At the relative high frequencies of the (thermal-hydraulic) Type-II oscillations, a large phase lag is caused by the fuel transfer function and the thermal-hydraulic subsystem. This large phase lag turns the negative feedback into positive, destabilizing the system. At higher frequencies, the gain of the fuel transfer function is considerably smaller. This is compensated for by a strong feedback, a void coefficient of -0.3, in case of the higher-frequency pole pair in figure 2.13. The frequency of the Type-I

oscillations is generally low; therefore, the phase lags are much smaller, and the negative void reactivity feedback has a stabilizing effect on the thermal-hydraulic oscillations. This is the origin of the interchange of the least stable poles in figure 2.13.

A similar interchange of the stability of two different pole pairs can be found if one follows a trajectory (the horizontal line in figure 2.8) of operating points leading from the Type-II to the Type-I region for different void reactivity coefficients. The results can be seen in figure 2.14. Only the complex poles are plotted there since the real poles are not important for the stability.
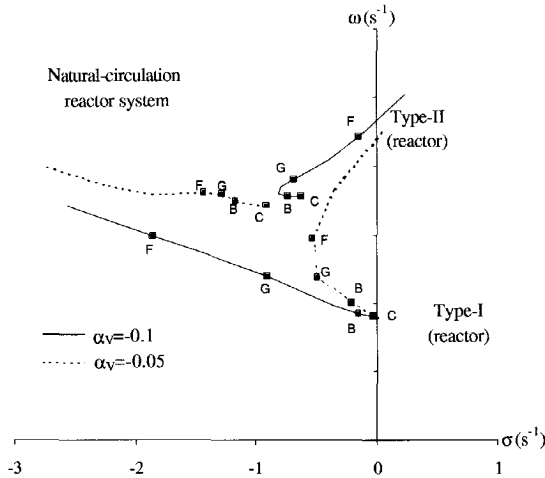
Figure 2.14: Poles of the reactor system along the trajectory of operating points shown in figure 2.8 from point F to point C, for two void reactivity feedback coefficients. Only the relevant poles are plotted. For a stronger void reactivity feedback, there is an interchange between the two pole pairs being the least-stable one.

For a low value of the void reactivity coefficient, a similar behavior can be observed as for the thermal-hydraulic subsystem in figure 2.12: The same pole pair remains the least stable one in both regions. This is plausible because for weak void reactivity feedback, the coupled system behaves more or less in the same manner as the thermal-hydraulic subsystem. However, for a stronger void reactivity feedback, the two pole pairs interchange their stability. First, the higher-frequency pole is the least stable in the Type-II region, whereas in the Type-I region (at point C of the horizontal trajectory in figure 2.8), the lower-frequency pole becomes the least stable one and moves into the right half-plane. Moving from the Type-II region to the Type-I region with the operating point, the void fraction in the core becomes gradually lower (lower core exit quality), and thus, the void feedback becomes gradually weaker [just the same effect as decreasing α_V (in absolute sense) in figure 2.13b]. Eventually, the system behaves again like the thermal-hydraulic subsystem ($\alpha_V = 0$ in figure 2.13b), which is confirmed by the joining of the root loci obtained with different void coefficients as well.

To illustrate the effect of the interchange of the least stable pole pairs on the behavior of the system, figure 2.15 shows the impulse responses of the reactor power at some points along the root loci for $\alpha_V = -0.1$ in figure 2.14. In points 1 and 2, the higher-frequency pole pair is the least stable and dominates in the impulse response. In points 3 and C,
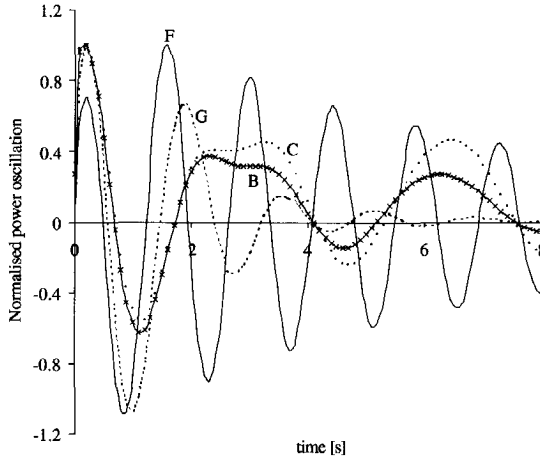
Figure 2.15: Impulse responses of the reactor power at different positions along the root loci marked by 1,2,3 and C in figure 2.14 for the case of $\alpha_V = -0.1$. For a better comparison, each impulse response is normalized with the value of its first positive peak.

its influence can be seen only up to 2 second, after that the lower-frequency pole pair determines the impulse response, which is then the least stable one.

To ascertain the stability of the system correctly, one should be able to find the least stable (dominating) pole of the system for any operating conditions. The interchange of the least stable pole pairs shows us that one has to consider several pole pairs carefully when determining the linear stability.

2.5   Conclusions

A reduced-order dynamic model has been used to examine the root loci of natural-circulation BWRs and the underlying two-phase flow systems.

To gain more insight into the physics of the instability phenomena, the role of the different poles of the system in determining the stability and their relation to the physical instability mechanisms have been examined. By evaluating the contributions of the different pressure drop transfer functions to the characteristic equation, it was reconfirmed that different types of pressure drops are responsible for the two types of instabilities in a natural-circulation (thermal-hydraulic) system. For the Type-II instability the two-phase frictional and the accelerational pressure drop are the main destabilizing terms, whereas for the Type-I, instability the gravitational pressure drop is the most important destabilizing term. It was also demonstrated that the same pole pair of the thermal-hydraulic subsystem determines the stability in both the Type-I and the Type-II instability regions. Thus, a certain pole pair cannot be associated with a specific instability mechanism.

For a reactor with weak void reactivity feedback, the same conclusion can be drawn since the root loci behave similarly as for the thermal-hydraulic system: The same pole pair is the least stable one in both instability regions. For a reactor with strong void reactivity feedback, an exchange of the least stable pole pairs has been found for the transition between the two different instability types: The least stable pole pair in the

Type-II region is not the same as in the Type-I region. This shows that one has to consider the different poles carefully to be able to determine the correct stability characteristics of a natural-circulation BWR using a frequency-domain reduced-order model.

This study demonstrates the usefulness of reduced-order models in understanding and identifying the physics behind the instability phenomena in BWRs.

Chapter 3

Experiments on the stability of the DESIRE facility

3.1 Description of the DESIRE facility

The DESIRE facility is a natural-circulation, boiling two-phase flow loop. It contains a scaled copy of a fuel assembly of the Dutch Dodewaard reactor. The scaling analysis that led to the design of the DESIRE facility, based on using Freon-12 (CCl_2F_2) as working fluid instead of water, is described in Van de Graaf *et al.* (1994a,b). The goal of the scaling analysis was to obtain the same axial void-fraction and flow-quality distribution in DESIRE as it is in an average fuel bundle of the Dodewaard reactor at nominal conditions. The main result of the scaling analysis was a size reduction of a factor of 0.47 in all directions, a reduction of the nominal pressure from 75.5 bar to 11.6 bar, and a reduction of the nominal average assembly power from 1116 kW to 22.3 kW.

Figure 3.1 shows a schematic view of the DESIRE facility. The primary loop consists of the fuel assembly, a riser, a downcomer, and four downcomer loops. At the top of the riser, separation of liquid and vapor takes place at the free surface. The liquid flows into the downcomer, while the vapor flows upward towards the condenser. There it first passes a pressure-controlling valve. The setpoint of this valve determines the pressure in the primary loop. This is a motor-actuated valve controlled by a proportional-integral-derivative (PID) controller. The settings of the PID coefficients were chosen so that the control of the valve is slow enough not to influence the dynamics of the two-phase flow in the facility. The vapor that leaves the facility is condensed in the condenser. Before this liquid is pumped back into the primary loop, it can be cooled to about $-20°C$ by a heat exchanger that is connected to a separate cooling system (see figure 3.1). The temperature and the mass flow rate of the "feedwater" flow are important boundary conditions for the primary circuit. The liquid level in the primary circuit is controlled via the flow rate of freon pumped back to the primary loop. The variable pump speed is controlled using PID controllers.

3.1.1 Heated section

The heated section is a copy of a fuel assembly from the Dodewaard reactor, consisting of the following parts: 35 electrically heated fuel rods, 3 spacers, bottom nozzle, top nozzle, and a dummy (instrumented) fuel rod, all contained in the fuel assembly casing. There are two sets of fuel rods, which can replace one another, one with a flat power profile, the other with a sinus+offset power profile. In the latter, the pitch of the coils of the
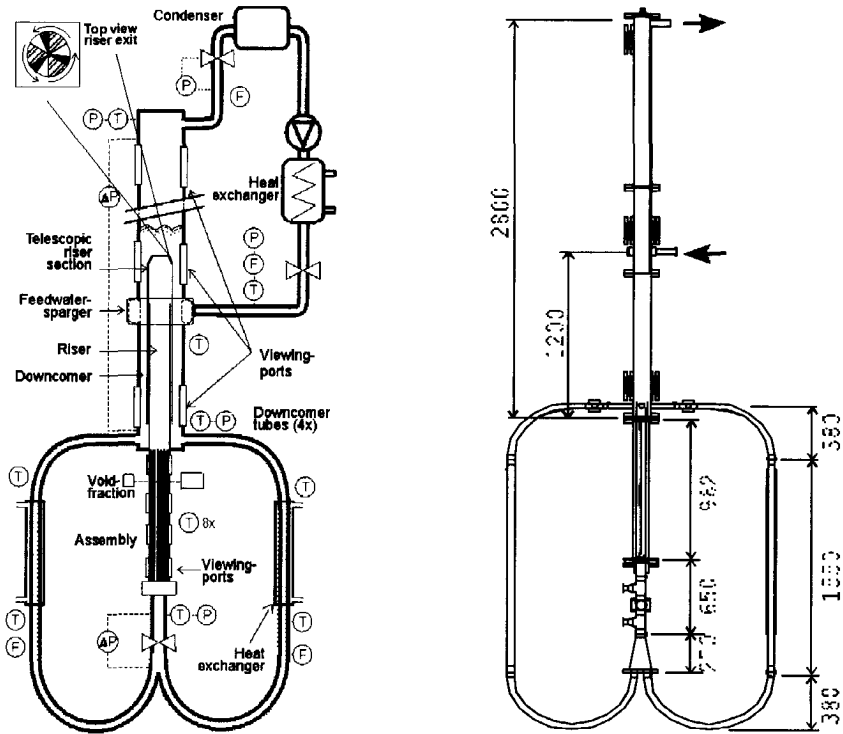
Figure 3.1: Scheme of the DESIRE facility, where P, T and F denote pressure, temperature and flow sensors, respectively (left figure). The dimensions of the facility are shown in the right figure. The length of heated section is at 962 mm and the liquid flows upwards entering at the bottom nozzle. The system parameters are summarized in Appendix B.

resistance wire is a function of the axial position in the rod in such a way that the power profile $P'(z)$ is:

$$P'(z) = P \frac{(1 - \frac{2}{\pi}f_p) + (f_p - 1)\sin(z\frac{\pi}{L_C})}{L_C(1 - \frac{2}{\pi})} \tag{3.1}$$

where f_p is the axial peaking factor that has the value of 1.4, L_C is the height of the assembly and P is the total power. The fuel rods are arranged in a square 6x6 lattice with a pitch of 8.8 mm. One of the four central rods is not a fuel rod but an unheated instrumentation rod with the same dimensions as a heated rod. This corresponds with the Dodewaard fuel assembly, in which one of the four central rods does not contain any uranium but is filled with water.

The fuel assembly is contained in a square-formed stainless steel casing with an inner width of 54 mm. The fuel rods are held in place by three spacers located at 251, 491, and 731 mm from the bottom of the assembly. The spacers are exactly scaled copies of the spacers used in the Dodewaard reactor. The height of the spacers is 24 mm.

The bottom nozzle of the DESIRE fuel assembly is designed to allow each fuel rod to be connected individually to one of six power supplies while retaining the shape of the Dodewaard bottom nozzle. In this way it is possible to create a variety of radial power

profiles.

3.1.2   Riser section

The riser consists of a fixed part and a telescopic part. The fixed part is a square tube with an inner dimension of 54x54 mm. It has a length of 1000 mm and is mounted directly on top of the fuel assembly. The telescopic part also has a length of 1000 mm but has a larger inner dimension of 61x61 mm. The telescopic section fits around the fixed section and can be moved up and down during operation, thus creating a variable riser length between 1.1 and 1.9 m. The riser was made of glass to allow visual inspection of the two-phase flow in the riser through viewing ports in the downcomer casing. A variable flow resistance element is installed at the exit of the riser section. Without this friction element the facility is so stable that it is impossible to study flow instabilities (Section 3.2). A schematic picture of the flow resistance element can be seen in figure 3.2. It consists of two slightly conical shaped metal plates situated on the top of each other, both having a circular cross section. The upper one is fixed to a support plate that fits exactly into the square cross section of the riser, while the lower one can be rotated. Both plates have a threefold orifice arranged in 120° rotational symmetry as is shown on the top view of figure 3.1. By setting the lower plate under different angles, between 0° and 60°, with respect to the upper one, the size of the orifices and thus the flow resistance (friction) of the element can be changed.
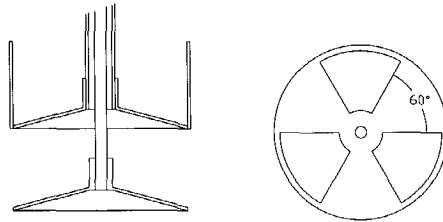
Figure 3.2: Side view of the two metal plates forming the friction element (left figure). Top view of the lower plate (right figure).

3.1.3   Downcomer

The downcomer tube is placed concentrically around the riser. The downcomer does not extend to the bottom of the fuel assembly as in Dodewaard but ends at the top of the fuel assembly, where the flow is diverted into four loops. This enables to place external measurements devices (e.g. gamma-transmission setup) around the assembly. The dimensions of the downcomer loops are chosen such that the extra friction introduced by them is negligible. Moreover, the scaling of the transit times is also taken into account choosing the length of the downcomer loops: the ratio of the transit times in the core

and in the rest of the system is the same as for Dodewaard. Due to the aforementioned scaling constrains, the inertia of the downcomer could not be scaled properly. Namely, the dimensionless equivalent inertia length of DESIRE is more than twice of that of Dodewaard.

The downcomer consists of three lengths of square stainless steel tubing with an inner dimension of 90x90 mm. Total length of the tube is 2.8 m, which leaves 0.9 to 1.7 m above the riser exit. Viewing ports are located at 200, 1300, and 2600 mm above the top of the fuel assembly. The viewing port at 1300 mm is located in the range of the riser exit, so the flow at this point can be inspected visually. The feedwater sparger is located 1200 mm above the top of the fuel assembly. It injects the "feedwater" evenly from all sides into the downcomer flow through thirty-six 2-mm-diameter holes.

The downcomer loops divert the flow away from the fuel assembly. Each of the four loops consists of the following sections, from top to bottom (see figure 3.1):

1. Horizontal straight section with a 380-mm length and 40-mm inner tube diameter.

2. 90° curve with a 380-mm radius and 40-mm inner tube diameter.

3. A heat exchanger consisting of two concentric tubes of 1000-mm length. The inner tube has a diameter of 40 mm. The secondary side of the heat exchanger can be connected to the water mains. Approximately 2 to 3 kW of heat can be extracted from the primary loop, increasing the subcooling by about $3°C$.

4. Straight section for the flowmeters: 550 mm of 30 mm tube.

5. 180° curve with a 380-mm radius and 40-mm inner tube diameter.

The four loops are joined in a conical section with a length of 270 mm, a bottom diameter of 129 mm, and a top diameter of 50 mm. Finally, a section with two T-junctions, a total length of 650 mm and a tube diameter of 50 mm connects the loop to the bottom of the fuel element. Between the T-junctions a valve is installed to be able to influence the inlet flow. On the two T-junctions a pump is coupled which enables to use the facility in forced-circulation mode. It is also used for friction measurements.

3.1.4   Instrumentation

The DESIRE facility is equipped with temperature sensors, flow meters and with absolute and differential pressure sensors. Figure 3.1 shows the approximate positions of the instrumentation. For the measurement of the local void fraction at different axial positions, a gamma-ray transmission set-up is installed on the facility. In the following, the instrumentation is described briefly.

Temperature sensors

Most of the temperature sensors used in DESIRE are chromel-alumel thermocouples with a diameter of 0.5 mm and a sensitivity of 40 $\mu V/°C$. Eight thermocouples are located in the fuel assembly. They are mounted in the instrumented fuel rod and extend into the bulk of the flow. The first one is placed 12 mm from the bottom of the fuel assembly, the rest at 100 mm intervals. Four thermocouples are placed at the bottom of the riser, just above the top nozzle. They are positioned above different subchannels. In the downcomer one thermocouple is located 150 mm from the bottom and one at 1050 mm

from the bottom. The vapor temperature is measured at the very top of the downcomer tube, near the vapor-exit point. One thermocouple is located at the inlet 150 mm below the fuel assembly. The accuracy of such thermocouples is not better than $\pm 1.0°C$.

There are also two PT100 probes (Class B, DIN 43760) - platinum resistance sensors - installed for high-accuracy temperature measurements. One is installed 180 mm below the inlet of the heated assembly, the other is installed in the "feedwater" line. The former one is also used as reference for calibrating the thermocouples in the facility.

There are six so-called temperature-difference sensors installed at points where measuring the temperature difference with relative high accuracy is of interest. Such a sensor consists of two chromel-alumel thermocouples (originating from the same badge) coupled with one side (of the same type) on each other and the voltage between the other sides is amplified. In this way one measures the temperature difference more accurately between the positions of the two thermocouples than by taking the difference of two low-accuracy absolute measurements. Furthermore, there is no need for cold junction compensation and only one amplifier is needed, both of which can increase the accuracy of the measurement. One temperature difference sensor is installed over the heated assembly to measure the inlet subcooling. Four sensors are positioned over the sections with the heat exchangers in the downcomer loops and one measures between the downcomer and the exit of the heated assembly. The last one is used for measuring the carry-under (see section 3.2).

Pressure sensors

Four absolute pressure sensors (PTX 510, measurement range: 0-30 bar) are located at the following positions:

1. at the inlet 210 mm below the fuel assembly

2. in the downcomer 150 mm from the bottom

3. at the top of the downcomer tube near the vapor exit ('steam dome')

4. in the "feedwater" line close to the feedwater sparger

Flow meters

The main circulation flow rate is measured by four vortex flowmeters installed in the downcomer loops. (Endress+Hauser SwingWirl II DMV 6331 with an inner diameter of 26.6 mm.) The feedwater flow rate and the vapor flow rate are also measured by vortex flowmeters. (Endress+Hauser SwingWirl II DMV 6331 with an inner diameter of 14 mm.)

The operation of these flow meters is based on the principle of vortex shedding. The frequency of the vortex shedding is determined by the flow velocity. In a typical velocity range in DESIRE, the vortices are shed at very regular intervals with typical frequencies of 10-20 Hz. This frequency is converted to a 4-20 mA current, which requires an averaging over time of the vortex frequency. The SwingWirl manual states that the time constant of this low-pass filter is 2 seconds. This means that these flow meters are too slow for dynamic measurements. It was found possible to experimentally determine the transfer function of the electronics of the flow meter which converts the vortex shedding frequency to a 4-20 mA current. Using this experimentally determined transfer function the dynamic measurements could be corrected for the low-pass filtering and typical flow rate variations (up to 0.5-0.6 Hz) could be handled.

Differential pressure sensors

Three differential pressure sensors are installed in DESIRE.

One (Endress+Hauser Delatabar S series PMD235, range:6 bar) measures the pressure drop over the inlet valve. The second one (Endress+Hauser Delatabar S series FMD533, range:500 mbar) is connected between the bottom and top of the downcomer tube. This sensors measures the collapsed liquid level above the riser exit. The third one (Endress+Hauser Delatabar S series FMD633, range:160 mbar) is installed over the heated section to measure the average void fraction there. The sensor used to measure the pressure drop over the inlet valve is connected directly to the freon in the primary loop, the other two has indirect connection using a diaphragm seal filling fluid (glycerine oil). The sensor installed over the heated section has a time constant of 2 seconds (specified by the manufacturer). It is important to correct for it in case of dynamic measurements.

Gamma-transmission setup

The gamma source and the detector are mounted on a translation table. The translation table is mounted on a rotation table and the whole setup can be positioned at different heights along the heated assembly. The setup is used with one of the two following sources: a 300 mCi ^{241}Am (60 keV) source or a 250 mCi ^{51}Cr (320 keV) source. The former one can only be used via one of the inspection windows due to the low energy of the gamma ray. The latter one has a gamma energy high enough to measure through the steel casing of the heated section. The detector is a scintillation detector with a 38-mm height and 38-mm diameter BGO (bismuth germanate, $Bi_4Ge_3O_{12}$) crystal. BGO has a high density (7.13 g/cm^3) making it a very efficient gamma absorber. The scintillation flashes are converted to current pulses and amplified by the photo-multiplier tube mounted on the detector. A preamplifier is built in the detector for signal shaping and further amplification. The signal coming from the detector is amplified and passed through a single channel analyzer that converts the pulses into uniform pulses. Depending on the void fraction, the source gives a count rate of about 10.000-20.000 counts per second, which is converted to a continuous signal by a ratemeter with a variable time constant.

3.2   Destabilizing the DESIRE facility

The reduced-order BWR dynamics model (Van Bragt and Van der Hagen, 1998a) has been used to investigate the thermal-hydraulic stability of the DESIRE facility. The frequency-domain version of the model is very suitable for performing fast parametric studies on the stability of the system. It was shown that the model is able to predict the trends on stability as some system parameters are varied (Van Bragt and Van der Hagen, 1998a).

Kok (1998) has concluded, based on his experimental results, that the DESIRE facility is very stable from the thermal-hydraulic point of view. It is in accordance with the results obtained using the reduced-order model, which predicts the linear stability boundary of DESIRE situated far away from the operating range of the facility (figure 3.3). We focus here on the Type-II instability; since the Type-I region cannot be reached in DESIRE due to its limited operating range with relatively low subcooling (see figure 3.3).

To be able to investigate a wide range of dynamic behavior of the system e.g. density-wave oscillations, the stability characteristics of the facility have been changed, namely the facility has been destabilized. An extensive study was performed to examine all the

Figure 3.3: The stability boundary (SB) and the operating range of DESIRE for zero riser-exit friction (left figure). SB's for two increased riser-exit friction values and the corresponding operating ranges (right figure).

possible changes in the system that decreases stability. The practically easiest realizable solution, which also has the largest impact on stability according to the prediction of the model, is to increase the friction at the riser exit. A comparison can be seen in figure 3.3, that shows that increasing the riser-exit friction factor destabilizes considerably the facility. In Chapter 2, it was demonstrated that increasing the two-phase frictional pressure drop the two-phase flow becomes less stable. For an increased riser-exit friction, not only the stable operating region decreases, but also the operating range of the system shifts towards the unstable operating regime. The shift of the operating range in terms of N_{Zu} is due to the lower flow rates caused by the increased friction. At an increased N_{Zu}, assuming steady-state and a constant liquid level in the system, the N_{sub} increases as well (see Eq. 4.1 in Chapter 4).

It must be noted that the friction element built into the exit of the riser in DESIRE can be used to simulate the influence of the friction of the steam-water separator on the stability of a natural circulation system. A steam separator on the top of the riser is also incorporated in the ESBWR design to decrease carry-under (whereas in Dodewaard free-surface separation was utilized). Carry-under is the amount of steam (gas) flow that is dragged by the liquid into the downcomer. It is important for the ESBWR to keep carry-under as low as possible since it decreases the driving force for the natural-circulation flow.

3.3 Experiments on the thermal-hydraulic stability of DESIRE

Extensive experimental series have been carried out to examine the linear stability of the DESIRE facility at two settings of the riser-exit friction element. The measurement series were performed for both a sinus offset and for a flat axial power profile. In each series, measurements were done at various operating conditions, so that practically the whole

interesting operating region of the facility was covered. All the measurements introduced here have been performed at a nominal system pressure of 11.6 bar. First, a short review of the measurement and signal analysis methods is given.

3.3.1   Experimental and signal processing methods

In these measurements, we use two signals to investigate the stability: the local void-fraction and the inlet mass flow rate. The local void-fraction signal obtained by the gamma transmission setup using the ^{241}Am source. Choosing a sufficiently small time constant on the ratemeter, the void-fraction variations are measured without significant attenuation and phase shift at the frequencies of interest (0.2-0.3 Hz). We measured the void fraction via the third inspection window at the core.

To quantify the stability of the system we use the decay ratio (DR), which is widely accepted measure for BWR stability (D'Auria *et al.*, 1997). We already defined the DR for a complex conjugate pole pair of the dynamic model in Chapter 2. In general, the DR is defined as the ratio between two consecutive maxima (or minima) of the impulse response function of the system. The latter is equivalent to the definition given in Chapter 2 for an oscillatory second-order system (i.e. a system with one complex conjugate pole pair). For higher-order systems, the ratio of consecutive maxima or minima can change (see figure 2.15 in Chapter 2). Therefore, the DR is uniquely defined only for a second-order system. To emphasize this, March-Leuba (1984) distinguishes between the *apparent* DR (obtained from the first two maxima) and the *asymptotic* (the actual) DR for a BWR, which is not a second-order system.

There are numerous methods to extract the DR from measured time series (Upadhyaya *et al.*, 1980; Van der Hagen *et al.*, 1995; D'Auria *et al.*, 1997). Many of the methods are based on autoregressive (AR) modelling of the time series. In these methods, the impulse response of the system is reconstructed and the DR is calculated from it. The DR can also be extracted from the autocorrelation function (ACF) of the signal. The ACF of signal $x(t)$ is defined as (Priestley, 1981)

$$ACF_{x(t)}(\tau) \equiv \lim \frac{\frac{1}{T}\int_0^T x(t)x(t+\tau)dt}{\frac{1}{T}\int_0^T x(t)^2 dt}. \tag{3.2}$$

For a second-order system, the ratio of the two consecutive maxima or minima of the ACF is the same as that of the impulse response and thus renders the same DR (Van der Hagen *et al.*, 1995). It is possible to derive the ACF for higher-order systems and to obtain the DR from that. In this thesis, we use a second- or a third-order model to fit the measured ACF to estimate the DR. In most practical cases, the contribution of the least stable pole pair, which determines the stability, dominates in the impulse response and the contributions of other poles die out soon. Therefore, the second-order assumption works reasonably good for higher-order systems too if one ignores the first few peaks of the ACF and determines the DR from peaks at higher τ's. However, one has to make a compromise since at higher τ's the peaks can become too small to be practical for determining the DR. The advantage of using the ACF for DR determination is simplicity and no additional model is needed to reconstruct the underlying system like in case of AR model based methods.

To determine the stability, noise measurements were performed on the system. For the noise analysis technique to work, one needs (real) fluctuations in the physical processes, parasitic (e.g. electronic) noise is not useful. Boiling in a two-phase flow system

interesting operating region of the facility was covered. All the measurements introduced here have been performed at a nominal system pressure of 11.6 bar. First, a short review of the measurement and signal analysis methods is given.

3.3.1   Experimental and signal processing methods

In these measurements, we use two signals to investigate the stability: the local void-fraction and the inlet mass flow rate. The local void-fraction signal obtained by the gamma transmission setup using the ^{241}Am source. Choosing a sufficiently small time constant on the ratemeter, the void-fraction variations are measured without significant attenuation and phase shift at the frequencies of interest (0.2-0.3 Hz). We measured the void fraction via the third inspection window at the core.

To quantify the stability of the system we use the decay ratio (DR), which is widely accepted measure for BWR stability (D'Auria *et al.*, 1997). We already defined the DR for a complex conjugate pole pair of the dynamic model in Chapter 2. In general, the DR is defined as the ratio between two consecutive maxima (or minima) of the impulse response function of the system. The latter is equivalent to the definition given in Chapter 2 for an oscillatory second-order system (i.e. a system with one complex conjugate pole pair). For higher-order systems, the ratio of consecutive maxima or minima can change (see figure 2.15 in Chapter 2). Therefore, the DR is uniquely defined only for a second-order system. To emphasize this, March-Leuba (1984) distinguishes between the *apparent* DR (obtained from the first two maxima) and the *asymptotic* (the actual) DR for a BWR, which is not a second-order system.

There are numerous methods to extract the DR from measured time series (Upadhyaya *et al.*, 1980; Van der Hagen *et al.*, 1995; D'Auria *et al.*, 1997). Many of the methods are based on autoregressive (AR) modelling of the time series. In these methods, the impulse response of the system is reconstructed and the DR is calculated from it. The DR can also be extracted from the autocorrelation function (ACF) of the signal. The ACF of signal $x(t)$ is defined as (Priestley, 1981)

$$ACF_{x(t)}(\tau) \equiv \lim \frac{\frac{1}{T}\int_0^T x(t)x(t+\tau)dt}{\frac{1}{T}\int_0^T x(t)^2 dt}. \tag{3.2}$$

For a second-order system, the ratio of the two consecutive maxima or minima of the ACF is the same as that of the impulse response and thus renders the same DR (Van der Hagen *et al.*, 1995). It is possible to derive the ACF for higher-order systems and to obtain the DR from that. In this thesis, we use a second- or a third-order model to fit the measured ACF to estimate the DR. In most practical cases, the contribution of the least stable pole pair, which determines the stability, dominates in the impulse response and the contributions of other poles die out soon. Therefore, the second-order assumption works reasonably good for higher-order systems too if one ignores the first few peaks of the ACF and determines the DR from peaks at higher τ's. However, one has to make a compromise since at higher τ's the peaks can become too small to be practical for determining the DR. The advantage of using the ACF for DR determination is simplicity and no additional model is needed to reconstruct the underlying system like in case of AR model based methods.

To determine the stability, noise measurements were performed on the system. For the noise analysis technique to work, one needs (real) fluctuations in the physical processes, parasitic (e.g. electronic) noise is not useful. Boiling in a two-phase flow system
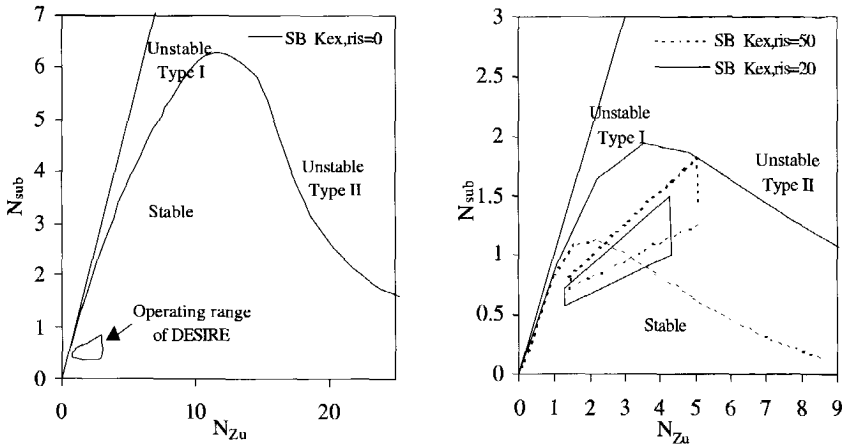
Figure 3.3: The stability boundary (SB) and the operating range of DESIRE for zero riser-exit friction (left figure). SB's for two increased riser-exit friction values and the corresponding operating ranges (right figure).

possible changes in the system that decreases stability. The practically easiest realizable solution, which also has the largest impact on stability according to the prediction of the model, is to increase the friction at the riser exit. A comparison can be seen in figure 3.3, that shows that increasing the riser-exit friction factor destabilizes considerably the facility. In Chapter 2, it was demonstrated that increasing the two-phase frictional pressure drop the two-phase flow becomes less stable. For an increased riser-exit friction, not only the stable operating region decreases, but also the operating range of the system shifts towards the unstable operating regime. The shift of the operating range in terms of N_{Zu} is due to the lower flow rates caused by the increased friction. At an increased N_{Zu}, assuming steady-state and a constant liquid level in the system, the N_{sub} increases as well (see Eq. 4.1 in Chapter 4).

It must be noted that the friction element built into the exit of the riser in DESIRE can be used to simulate the influence of the friction of the steam-water separator on the stability of a natural circulation system. A steam separator on the top of the riser is also incorporated in the ESBWR design to decrease carry-under (whereas in Dodewaard free-surface separation was utilized). Carry-under is the amount of steam (gas) flow that is dragged by the liquid into the downcomer. It is important for the ESBWR to keep carry-under as low as possible since it decreases the driving force for the natural-circulation flow.

3.3 Experiments on the thermal-hydraulic stability of DESIRE

Extensive experimental series have been carried out to examine the linear stability of the DESIRE facility at two settings of the riser-exit friction element. The measurement series were performed for both a sinus+offset and for a flat axial power profile. In each series, measurements were done at various operating conditions, so that practically the whole

Figure 3.4: Several typical ACFs of the measured local void-fraction signal. The examples are taken from the measurements described in Table 3.1.

is a stochastic process, but in a relatively stable operating condition these fluctuations are too small to be practical. In this case, the system has to be disturbed by external noise. For this reason, a wide-band random noise signal is added to the driving signal of the electrically heated rods to enable noise measurements. We must note here that the situation in an actual BWR is somewhat different since the inherent fluctuations caused by boiling (the boiling noise) are amplified by the void reactivity feedback and result in small power fluctuations. These power fluctuations are well measurable and they form a practically usable source of information on the dynamics of BWR's.

Practical experience shows that assuming a second-order system is a quite good approximation for thermal-hydraulic stability measurements in DESIRE (see some typical ACFs of the measured void-fraction signal in figure 3.4). Using this assumption, three methods are applied to calculate the DR from the oscillatory ACFs:

1. Taking the ratio of several consecutive maxima and minima and averaging these ratios.

2. Taking the square root of a neighboring maximum and minimum.

3. Using Lagrange Interpolating Polynomial formula as it is described in D'Auria *et al.* (1997).

The three aforementioned methods give practically the same results. Both the void-fraction and the flow signals give practically identical DR values in all measured cases.

3.3.2   Measurement results and their comparison to the reduced-order model

All the measurements discussed here were carried out at a nominal pressure of 11.6 bar. The operating points at which measurements were carried out are given in the $N_{Zu} - N_{sub}$ plane in figure 3.5. It can be seen from the DR values in the figure, that the two-phase flow loop is less stable at a higher riser-exit friction for both axial power profiles. This result is expected according to the prediction of the reduced-order model.
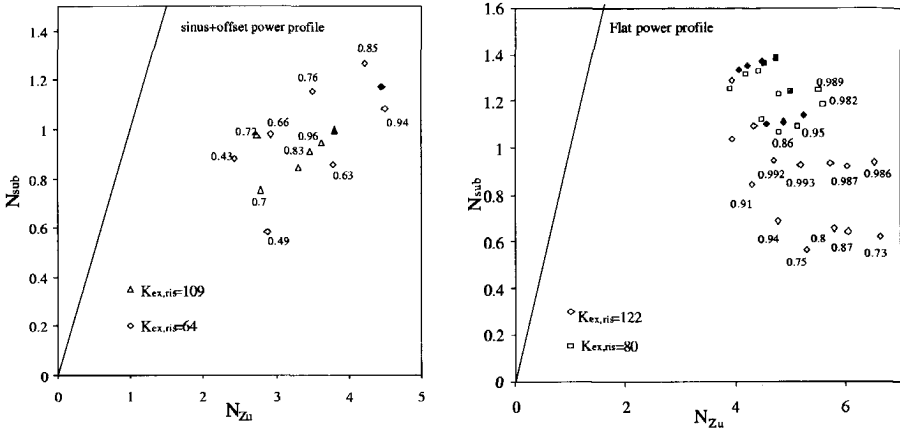
Figure 3.5: Measurement points in the $N_{Zu} - N_{sub}$ plane for the two riser-exit friction settings. The left figure shows the results for a sinus+offset axial power profile, the right figure for a flat power profile. The numerals are the measured DR's indicated near several points. Solid symbols indicate unstable points (limit-cycle oscillations, DR=1), open symbols indicate stable operating points. The operating conditions are detailed in Table 3.1 for the sinus+offset power profile case.

$K_{r,e}$	P	$\Phi_{C,i}$	T_{sub}	T_{fw}	Φ_{fw}	N_{Zu}	N_{sub}
[−]	[kW]	[kg/s]	[°C]	[°C]	[kg/s]		
64	23.3	1.14±0.01	3.9±0.5	-0.9±0.5	0.13±0.01	2.88±0.02	0.58±0.07
±6	19.0	1.10±0.01	5.9±0.5	-9.3±0.5	0.08±0.01	2.43±0.02	0.88±0.07
	23.3	1.11±0.01	6.6±0.5	-9.7±0.5	0.011±0.01	2.94 ± 0.02	0.98 ± 0.07
	30.0	1.11±0.01	5.8±0.5	-1.7±0.5	0.17±0.01	3.80 ± 0.03	0.86 ± 0.07
	27.8	1.11±0.01	7.8±0.5	-10.0±0.5	0.13±0.01	3.52 ± 0.03	1.15 ± 0.07
	32.8	1.09±0.01	8.5±0.5	-8.5±0.5	0.16±0.01	4.22 ± 0.03	1.27 ± 0.07
	34.7	1.08±0.01	7.3±0.5	-1.9±0.5	0.21±0.01	4.5 ± 0.03	1.08 ± 0.07
	35.6	1.12±0.01	7.9±0.5	-6.6±0.5	0.19±0.01	4.45 ± 0.03	1.17 ± 0.07
109	16.7	0.86±0.01	6.6±0.5	-8.0±0.5	0.07±0.01	2.74 ± 0.02	0.98 ± 0.07
±7	18.7	0.88±0.01	5.1±0.5	-9.6±0.5	0.10±0.01	2.75 ± 0.02	0.75 ± 0.07
	20.6	0.87±0.01	5.7±0.5	-9.9±0.5	0.10±0.01	3.30 ± 0.03	0.85 ± 0.07
	21.5	0.87±0.01	6.2±0.5	-10.2±0.5	0.11±0.01	3.46 ± 0.03	0.91 ± 0.07
	22.5	0.87±0.01	6.4±0.5	-10.1±0.5	0.12±0.01	3.62 ± 0.03	0.94 ± 0.07
	23.5	0.87±0.01	6.7±0.5	-10.2±0.5	0.12±0.01	3.80 ± 0.03	1.00 ± 0.07

Table 3.1: Overview of the operating conditions of the stability measurements for the case of sinus+offset power profile shown in figure 3.5. The measurements have been carried out at nominal system pressure, 11.6 bar.

For the case of the sinus+offset power profile, the operating conditions and the correponding values of N_{Zu} and N_{sub} at which the measurements were carried out, are summarized in Table 3.1. The estimated errors in N_{sub} correspond to an uncertainty of about $0.5°C$ in the temperature measurements. The uncertainty in N_{Zu} is determined by the

accuracy of the flow meter as specified by the manufacturer (0.7% full range).

DR	DR	DR	Frequency [Hz]	Frequency [Hz]	Frequency [Hz]	$\Phi_{C,i}$ [kg/s]
Measured	Calc. red.-o. mod.	Calc. MONA	Measured	Calc. red.-o. mod.	Calc. MONA	Calc. MONA
0.53±0.04	0.72±0.09	0.46	0.27±0.01	0.263±0.006	0.30	1.13
0.43±0.02	0.95±0.13	0.46	0.23±0.01	0.233±0.005	0.25	1.11
0.66±0.05	1.32±0.15	0.71	0.25±0.01	0.249±0.006	0.27	1.12
0.63±0.02	1.44±0.16	0.62	0.29±0.01	0.286±0.006	0.35	1.11
0.76±0.04	2.02±0.26	0.73	0.26±0.01	0.249±0.006	0.31	1.11
0.85±0.01	2.83±0.42	-	0.27±0.01	0.271±0.007	-	-
0.95±0.01	2.35±0.33	1.0	0.30±0.01	0.297±0.006	0.30	1.05
0.99±0.01	2.67±0.38	1.0	0.30±0.01	0.295±0.006	0.31	1.04
0.72±0.04	1.94±0.26	0.81	0.19±0.01	0.177±0.005	0.25	0.90
0.70±0.05	1.50±0.19	0.76	0.21±0.01	0.203±0.005	0.24	0.92
0.86±0.03	1.97±0.24	0.71	0.21±0.01	0.211±0.006	0.27	0.90
0.83±0.02	2.31±0.28	0.77	0.21±0.01	0.212±0.005	0.27	0.91
0.96±0.01	2.57±0.33	1.0	0.22±0.01	0.217±0.006	0.26	0.91
1.00	2.96±0.37	1.0	0.23±0.01	0.220±0.006	0.26	0.90

Table 3.2: Comparison of the results of the stability measurements with the results obtained by the reduced-order model and by the MONA code (see next section) for the case of sinus+offset power profile shown in figure 3.5. The corresponding operating conditions are given in Table 3.1.

The results of the stability measurements (the DR's and oscillation frequencies) are shown in Table 3.2. The oscillation frequency was determined from the frequency spectrum of the signals, and the uncertainties in the frequencies correspond to half of the resolution of the frequency spectra. The uncertainties of the DR's are estimated from the uncertainties of the measured ACF values.

First, we compare the measurement results with the prediction of the reduced-order model introduced in Chapter 2. The measured natural-circulation flow rate is not predicted accurately by the reduced-order model. It is partly due to the simple two-phase flow model used, but more importantly it stems from the lack of modelling the carry under (the amount of vapor flow dragged into the downcomer), which plays an important role in DESIRE (Kok, 1998). Therefore, we use the measured flow rate - to which value the dynamics of the system is sensitive as numerical experience shows - as input for the dynamic calculations with the reduced-order model. The same holds for the inlet subcooling, which is not an independent variable of the system either, rather is the feedwater temperature. However, using the feedwater temperature as input without taking into account the carry under would lead to an erroneous estimation of the inlet subcooling. The other two input parameters for the calculations are the system pressure and power. Table 3.2 contains the DR's and oscillation frequencies calculated by the reduced-order model. The influence of the measurement uncertainty in the inlet subcooling is accounted for in the calculated DR's and oscillation frequencies. The effect of the uncertainty in the riser-exit friction factor on the results of the calculation is also taken into account. The standard deviation originating from the combined effect of these uncertainties is given as
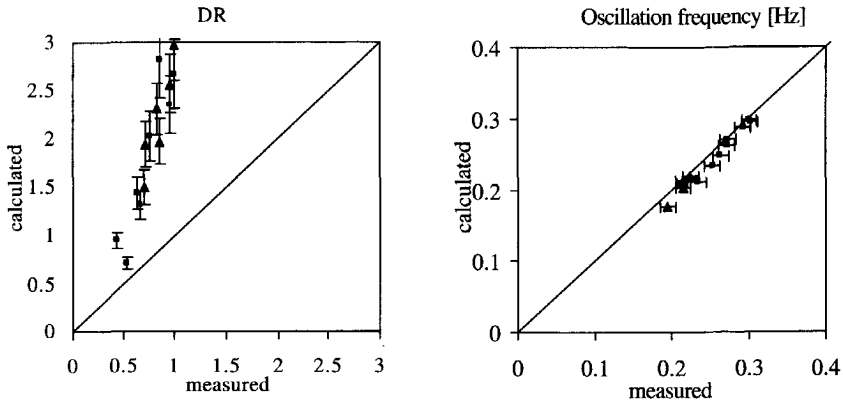
Figure 3.6: Comparison of the results of the stability measurements and those obtained by the reduced-order model for sinus+offset power profile (figures are given in Table 3.2). Prediction of the frequency is excellent, but the DR's are strongly over predicted. The triangles correspond to a friction factor $K_{r,e} = 109$, squares correspond to a friction factor $K_{r,e} = 64$.

the uncertainty of the calculated values in Table 3.2. The influence of uncertainty of the flow rate measurement on the prediction is negligible with respect to the aforementioned two effects.

Figure 3.6 shows the comparison of the results obtained by the reduced-order model to the experimental results in a scatter plot. It can be seen that the oscillation frequencies are predicted very well. Their values agree quantitatively with the measured ones within the uncertainties (only the error bars in the measured frequencies are given since they are significantly larger than those of the calculated results). However, the deviations in the DR's are quite significant: all the DR's are very strongly over predicted by the model. There are several reasons that might be responsible for this discrepancy. The reduced-order model contains a lot of approximations and assumptions (Chapter 2). It captures only the very basic physics of the phenomena involved. Thus, one cannot expect quantitatively precise prediction of the measurements, although there is a clear correlation between measured and calculated DR's.

Remarkably, the larger the actual value of the DR, the larger is the error in the prediction. The following conservative and non-conservative approximations, used in the reduced-order model (see Section 2.2), might have a major influence on the results:

1. A very rough approximation in the model is neglecting the wave phenomena in the heated channel: a quasi-static approximation assuming linear spatial enthalpy and quality profiles is used instead. It is a non-conservative approximation (Karve *et al.*, 1994).

2. The neglecting of subcooled boiling, which results in over-predicting the boiling-boundary oscillation and has a destabilizing influence (Van Bragt, 1998).

3. In calculating the dynamic pressure drop over the heated channel there is a conservative assumption: instead of the true two-phase mass flux profile, the delayed

(and thus destabilizing) channel-exit mass flux is used in integrating the momentum equation.

4. Inlet-temperature variations are neglected although it has a significant influence on the dynamics. Whether it is a conservative or a nonconservative assumption depends on the operating conditions (the phase of inlet-temperature oscillation with respect to inlet-flow oscillations). Its influence is investigated in the next chapter.

Although the first approximation is always strongly non-conservative, the third one is always strongly conservative, it is difficult to estimate the gross effect of the above approximations since it might depend on the operating conditions. One can only speculate. Therefore, in the next section, we evaluate the stability measurements using the thermal-hydraulic system code MONA 1.9, which is based on an advanced two-phase flow model and a much more detailed description of the phenomena than the reduced-order model.

3.4   Evaluation of the measurements using the MONA code

Before discussing the results of the evaluation of the stability experiments using the MONA code, the code and the nodalization of the DESIRE facility are described briefly.

3.4.1   Description of MONA code; the nodalization of DESIRE

MONA 1.9 is a commercial thermal-hydraulic code developed by Scandpower (Hoyer, 1994a) for steam-water/inert gas system. The code has been successfully benchmarked by Scandpower against experiments performed with the FRIGG loop for steady-state conditions and for dynamic conditions with particular emphasis on density wave oscillations (Hoyer, 1994b).

MONA includes a full two-fluid, non-equilibrium, non-homogeneous two-phase flow model. It contains a set of seven conservation equations, based on the modelling of three flow fields: the bulk liquid or liquid film at the wall, the liquid droplet field and the gas or steam phase. From the seven conservation equations three are mass conservation equations. Using a simplifying assumption the momentum conservation equations for gas and droplet are added to yield one combined conservation equation. The same is done with the energy conservation equations for liquid and droplets. The conservation equations are completed with the thermodynamic equation of state for each phase and with closure relations for liquid and gas wall shear, for interfacial shear and for interfacial heat and mass transfer rates. The closure relations depend on the flow regime. The code uses an implicit upwind scheme to solve the discretized conservation equations numerically.

Only the primary loop is considered for the nodalization. The rest of the facility is considered in the definition of the boundary conditions for the primary loop (see below). The first nodalization of the DESIRE facility was done by Adams (1997) and it was modified by Manera (1998). Figure 3.7 shows the nodalization of the DESIRE facility for the MONA code (only one of the four downcomer loops is represented in the figure).

The table in figure 3.8 shows the representation of the different sections of the facility by different number of nodes. The primary loop of the facility is represented by 8 BRANCH components divided into 35 pipes. In the following a brief description of the main parts of the circuit is given.
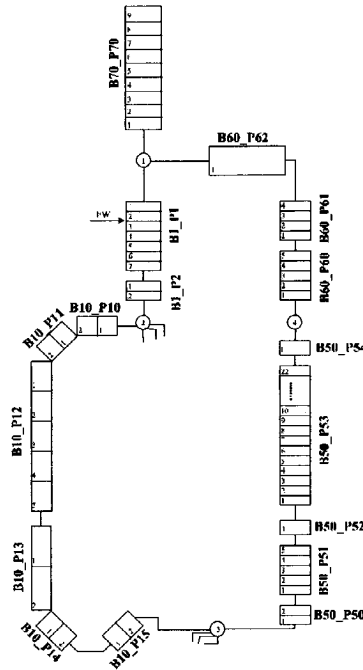
Figure 3.7: DESIRE nodalization for MONA 1.9. The facility is divided into a certain number of pipe components (P) in order to reproduce geometrical changes (all volumes of the same pipe are characterized by the same hydraulic diameter and flow area). The pipes are grouped in branches (B) to simulate the network of connections between the different parts of the loop.

Lower plenum: it is represented by one branch divided into two pipes in order to simulate the abrupt area changes and the valve used to influence the inlet flow (Branch 50, Pipe 50-51).

Fuel assembly: the active part of the fuel assembly is represented by a pipe component (Branch 50, Pipe 53) divided into 22 hydraulic volumes. The corresponding heat structure is modelled by 35 cylindrical pins subdivided into 22 axial nodes, each one corresponding to a hydraulic volume of the fuel assembly nodalization. It is possible to associate a certain amount of the total heating power to each of these nodes, so non-uniform axial power distributions can be simulated.

Feedwater inlet: it is specified by a SOURCE term; external inputs are the feedwater flow rate and its temperature (Branch1, Pipe 1, Volume 2).

Downcomer: it is represented by five branches, one for the region coaxial with the riser section and four for the downcomer loops.

Riser: the riser section is simulated by two different pipes having different flow areas (this is to represent the telescopic riser section).

Steam dome: the steam dome above the riser section is represented by a pipe of 9

GENERAL ZONE	NODES	NAME
Lower plenum	-	Branch 50
	2	Pipe 50
	5	Pipe 51
Valve	-	Pp. 51 Loc. 3
Fuel assembly	1	Pipe 52
	22	Pipe 53
	1	Pipe 54
Riser	-	Branch 60
	5	Pipe 60
	4	Pipe 61
Steam dome	-	Branch 60-70
	1	Pipe 62
	9	Pipe 70
Upper downcomer	-	Branch 1
	7	Pipe 1
	2	Pipe 2
Downcomer loop 1	-	Branch 10
	2	Pipe 10
	2	Pipe 11
	5	Pipe 12
	2	Pipe 13
	2	Pipe 14
	2	Pipe 15
Downcomer loop 2		Branch 20
Downcomer loop 3		Branch 30
Downcomer loop 4		Branch 40

Figure 3.8: Hydraulic volumes in MONA 1.9. nodalization. Table taken from Manera (1998).

hydraulic volumes and by a horizontal pipe needed to simulate the separating surface between liquid and vapor phase. At the top of the steam dome a NODE component is used to fix the system pressure.

The nodalization was benchmarked against steady-state measurement with DESIRE and the results show a good agreement (Manera, 1998). The nodalization was also used to perform pre-test calculations on the dynamics of the system (Manera, 1998).

3.4.2 Numerical simulations

We simulated the stability measurements using the MONA code. MONA is capable of calculating flow regime related two-phase friction and form friction factors. However, as much as it is possible, the same measured friction factors (see Appendix B) are used in the simulations as in case of the reduced-order model.

For the MONA code, the externally controllable parameters of the system: system pressure, power, and feedwater flow and temperature have to be given as input parameters. There is no carry under model in MONA, but one can give an average value of the carry under as input too, and the code takes its influence into account. An example of MONA input file is given in Appendix C for the case of the last measurement above the double horizontal line in Table 3.2.

The results of the MONA calculations are compared to the experimental results in a scatter plot in figure 3.9 (figures are given in Table 3.2). The overall agreement is quite good: the difference between the calculated and measured DR's remains always within ten percent, just like the differences between the oscillation frequencies. The calculated

inlet mass flow rates are also given in Table 3.2. Since the flow rate is a very important dependent variable in a natural-circulation system, comparison of it also qualifies the results. The scatter plot in figure 3.10 shows that the matching of the calculated and measured flow rates is quite good.
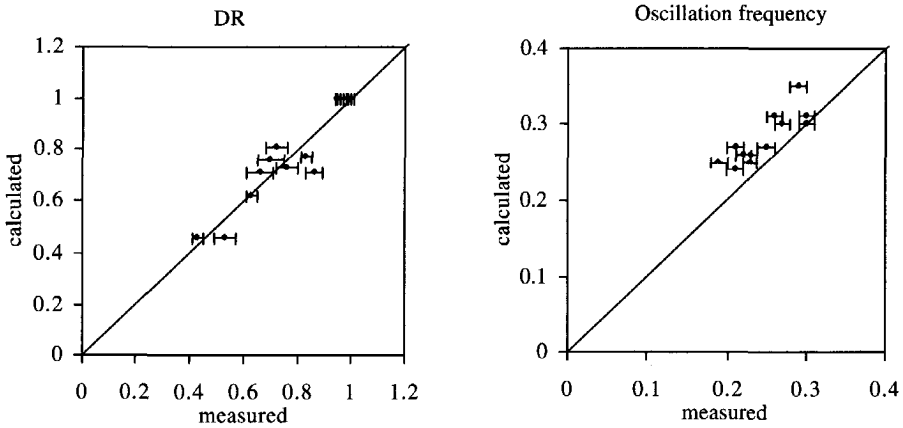
Figure 3.9: Comparison between experimental DR's, oscillation frequencies and those calculated by the MONA code for the linear stability measurements carried out for a sinus+offset power profile.
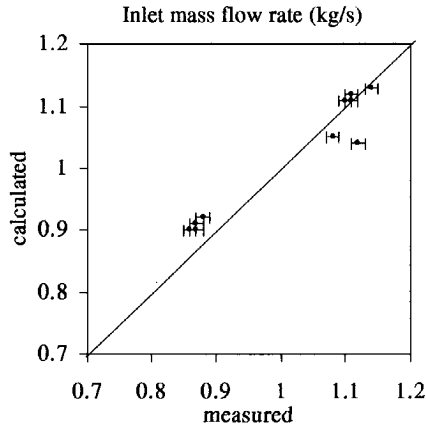
Figure 3.10: Comparison of the experimental values of the inlet mass flow rate and the prediction of it by the MONA code.

In figure 3.5 there are several points indicated that lie in the linearly unstable region of the facility, where constant-amplitude oscillations are measured. These so-called limit-cycle oscillations are typical nonlinear phenomena for which the initially small-amplitude, growing (linearly unstable) oscillations are bounded by nonlinear effects (see Chapter 5). In these conditions, linear analysis is not a valid approximation anymore.

We could simulate these limit-cycle oscillations with the MONA code in most cases, although oscillation amplitudes did not really match with the measured ones. As the operating point gets further away from the linear SB, the oscillation amplitude increases strongly (see Chapter 5 and Chapter 6). These large-amplitude limit cycles resulted in flow reversal (negative flows) in the simulation. The experimental investigations on the nonlinear dynamics of the facility in the unstable operating region are described in Chapter 6.

3.5   Conclusions

In its original design, the DESIRE facility is extremely stable from the thermal-hydraulic point of view, therefore the facility has been "destabilized" on purpose to enable the experimental study of a wider range of dynamic situations. The experiments were preceded with a parametric study on the stability of DESIRE using a reduced-order model. Based on the results of this study a variable flow resistance element has been build into the exit of the riser.

The influence of increasing the friction at the riser exit was examined in the experiments. The results show the same trend as predicted by the reduced-order model: increased friction at riser exit decreases the stability of the two-phase flow.

Quantitative comparison of the results of stability measurement with the prediction of the reduced-order model shows that the model predicts the oscillation frequency very well, however, the DR of the system is very much overpredicted. This is due to the strong approximations applied in the model.

The measurements are simulated using the advanced thermal-hydraulic code MONA 1.9 with more success. A very good agreement has been found with the measured DR's, oscillation frequencies and with an important dependent variable: the natural-circulation flow rate.
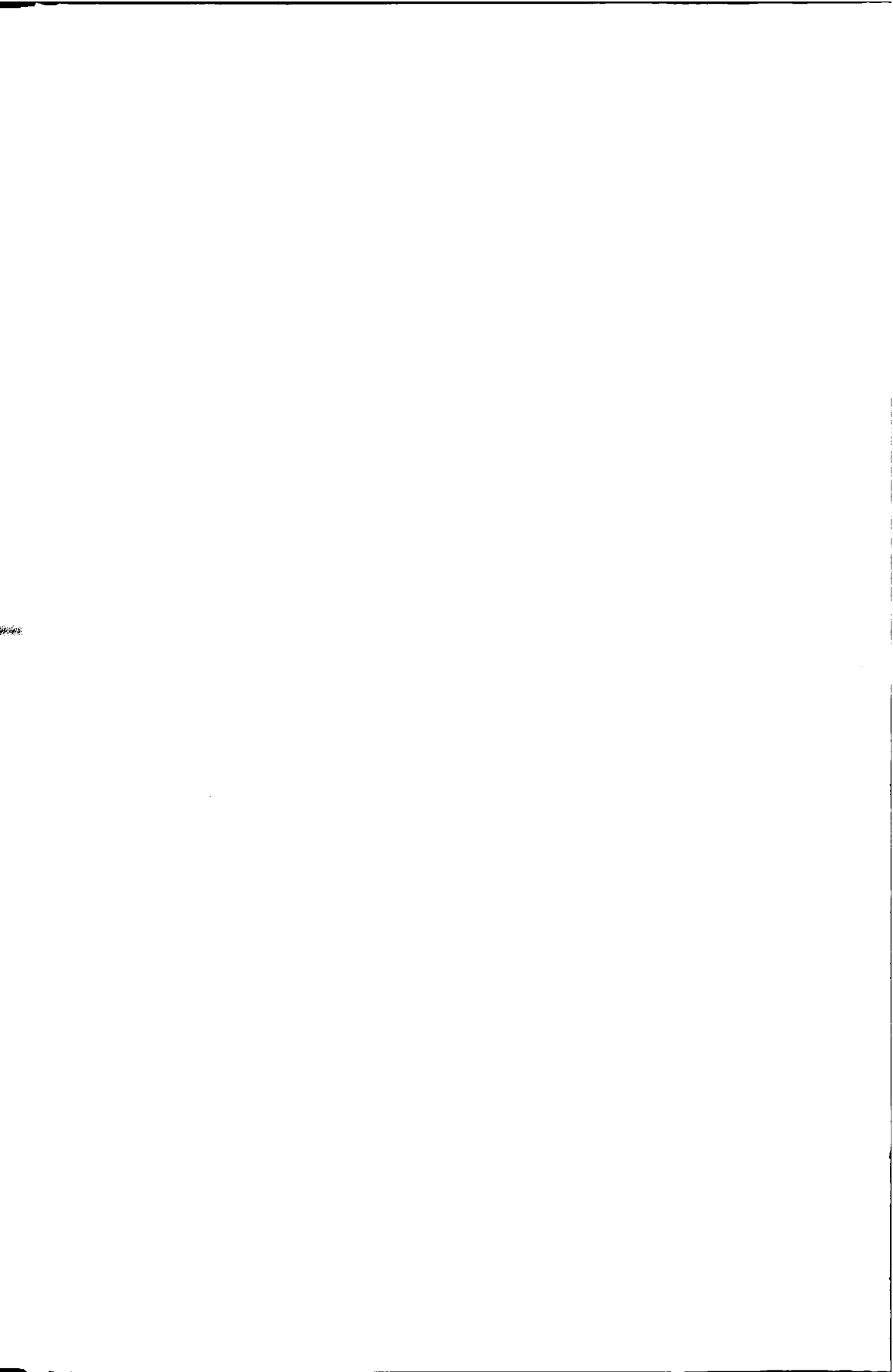
Chapter 4

Applications of the reduced-order model

4.1 Introduction

This chapter consists of two studies carried out using the reduced-order model addressing two quite distinct issues about BWR stability analysis. The first one examines the relation between the DR and operational stability margins and it provides with results that are interesting from the point of view of BWR stability monitoring and operation. The outcome of the other study, which investigates the influence of core-inlet temperature variations on the thermal-hydraulic stability of natural-circulation reactors, might be interesting for the design of future BWRs.

4.2 On the relation between DR and operational stability margins

The decay ratio (DR) is a commonly accepted and widely used parameter for BWR stability monitoring (D'Auria *et al.*, 1997). Present-day commercial BWR plants are usually equipped with a core stability monitoring system, which determines the DR through noise analysis of measured neutron-flux signals. The DR is defined as the ratio of two consecutive maxima of the impulse response of the system. Methods to calculate the DR are given in the previous chapter.

At a given operating condition of the reactor, the DR proves to be a correct measure of the linear stability of the system: in a system with a smaller DR the perturbations are damped more rapidly than in a system with a higher DR. However, relying exclusively on the DR can be misleading since it cannot give reliable information about the operational margin to unstable system behavior. This was pointed out recently by Van der Hagen *et al.* (1997), who have performed a series of stability measurements on the natural-circulation Dodewaard BWR. They showed that a very slight change (less than a few per cents) in the operational conditions might cause a dramatic increase in the DR (from 0.7 to 1.02), supporting the concern expressed above about the feasibility and practicability of the DR as a stability indicator. To gain more insight into this problem, we investigate it using the reduced-order model. It is shown here that a reactor working at an operating point with a smaller DR can be closer to instability than at an operating point with a larger DR in terms of operational variables. This fact is very important from a practical point of view. For the reactor operators it would be useful to know the margin to unstable

reactor behavior expressed in terms of operational parameters (power, system pressure etc.) together with the DR.

4.2.1   Numerical investigations

The geometry and parameters of the Dodewaard reactor are used in this study. In a natural-circulation BWR, the power, the system pressure and the temperature of the feedwater are the externally controllable operating parameters. The relation between the DR and the operational margins to instability, expressed in terms of the aforementioned three variables, is investigated. We use the dimensionless N_{Zu} and N_{sub} numbers to characterize the reactor operating conditions and to plot the stability map. At a certain feedwater temperature, the following simple relationship exists, which determines possible reactor operating conditions in the $N_{Zu} - N_{sub}$ plane:

$$N_{sub} = \frac{h_f - h_{fw}}{h_g - h_{fw}} N_{Zu}, \qquad (4.1)$$

where h_{fw} is the enthalpy of the feedwater at the feedwater sparger.
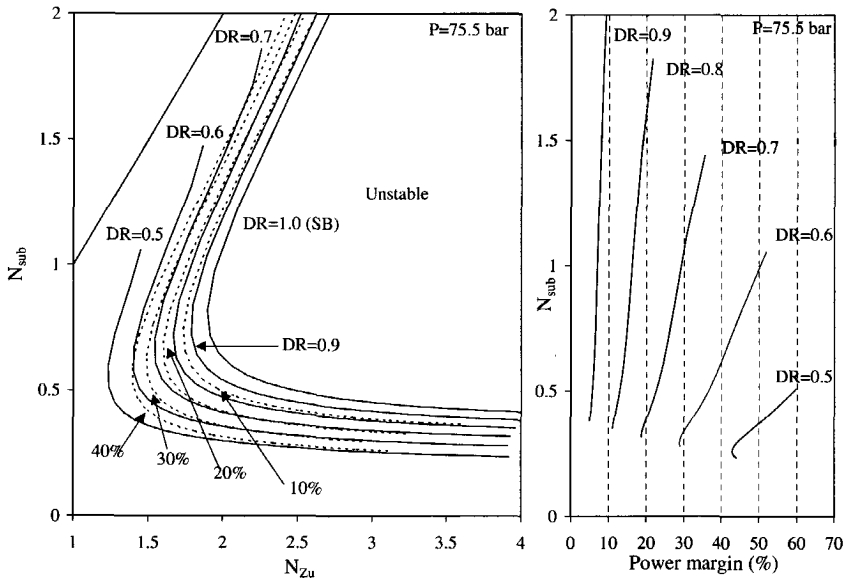
Figure 4.1: Equi-DR lines (solid) and power equi-stability margin lines (dashed) intersect in the $N_{Zu} - N_{sub}$ plane (left figure). This means that the power stability margin changes along the same equi-DR line (right figure). Only those parts of the equi-DR and equi-stability margin lines are depicted on the figure that correspond to the Type-II reactor instability.

The solid lines on the left of figure 4.1 show the linear SB and the lines of operating points with equal DR (equi-DR lines). Only those parts of these lines are shown that correspond to the Type -II instability since this is the region where practically all stability incidents have been encountered in operating plants and therefore the most important for stability monitoring.

The operational margin to instability in terms of the reactor power is defined in an operating point described with a power P_o as

$$powermargin = (P_c - P_o)/P_o, \qquad (4.2)$$

where P_c is the power value at which the threshold of instability (the SB) is reached by gradually changing the power and keeping all other independent variables constant. This (relative) power margin is evaluated in operating points along the different equi-DR lines. Figure 4.1 shows also the lines (dashed) of operating points with equal power stability margin. From figure 4.1 it is obvious that operating points with the same DR can have quite different operational margins to instability. Moreover, the curves show that an operating point with a certain DR may have a larger safety margin to instability than another operating point with a smaller DR. This is shown more clearly in figure 4.2.
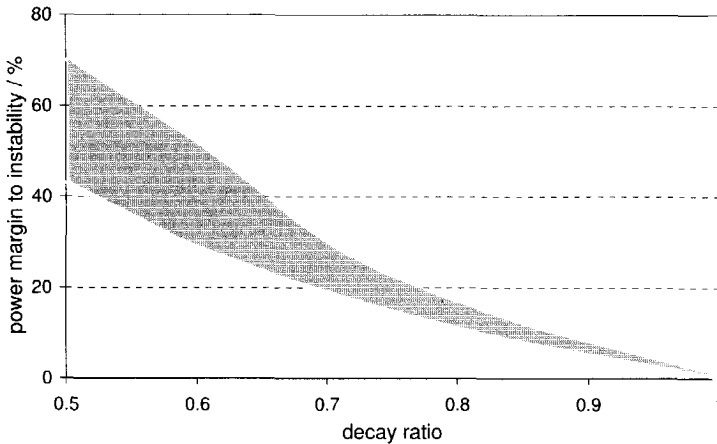
Figure 4.2: Range of possible power margins to instability as a function of decay ratio (for cases with a subcooling number smaller than unity).

The operational stability margins for the other two externally controllable variables are defined in the same way as for the reactor power (except that not relative but absolute margins are given). These are shown as a function of N_{sub} along the equi-DR lines in figure 4.3.

The stability margin in terms of feedwater temperature changes a lot along an equi-DR line. Remarkably, an operating point with DR=0.9 might have a feedwater temperature margin as high as -45°C, while an other point with DR=0.6 has a margin of only -12°C (about a factor four difference in the margin)! This reconfirms our concern about the practicability of the DR as an indicator for the margin to instability.

The pressure margin changes only slightly as a function of operating point along the equi-DR lines and it is always smaller (in absolute sense) for a larger DR. It indicates that for operational changes in the pressure the DR can also be used as an indicator for the margin to instability.

The above reported operational stability margins and equi-stability margin lines have been evaluated at nominal system pressure of the Dodewaard reactor (75.5 bar). Using the $N_{Zu} - N_{sub}$ plane has the advantage that the thermal-hydraulic SB and the equi-DR lines are independent of the system pressure (Van Bragt and Van der Hagen, 1998a). It
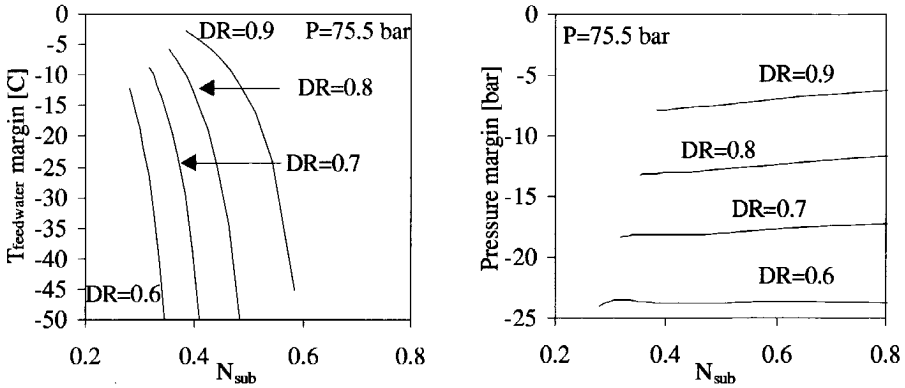
Figure 4.3: Operational stability margins in terms of the feedwater temperature (left figure) and the system pressure (right figure) along different equi-DR lines.
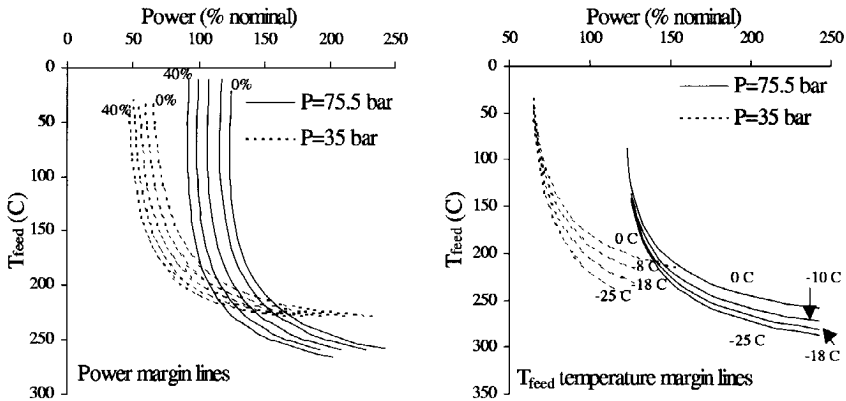
Figure 4.4: The stability margins in terms of the reactor power (left figure) and in terms of the feedwater temperature (right figure) change significantly for different system pressures.

is approximately true for the reactor SB too, since the void- reactivity coefficient is only slightly dependent on the pressure (Van Bragt and Van der Hagen, 1998a). However, the N_{Zu} and N_{sub} numbers themselves depend on the pressure and thus the position of an operating point described with a certain power, flow rate and inlet subcooling depends on the system pressure in the $N_{Zu} - N_{sub}$ plane. Therefore, the operational stability margins also depend on the pressure. The power margin and the feedwater temperature margin lines at nominal pressure are compared with the same equi-margin lines at 35 bar in figure 4.4. The curves are given in the $power - T_{feedwater}$ plane, which is more useful from the practical point of view since these are the externally controllable parameters of the system. The differences are significant, especially the feedwater temperature margins may vary considerably with the system pressure.

4.2.2 Summary

The relation between the DR and the operational stability margins in a natural-circulation BWR has been examined. The margins are expressed in terms of the externally controllable variables of the system: power, pressure and feedwater temperature. It has been found that the system might be closer to instability than the value of the DR would indicate. Therefore, the usage of operational margins in combination with the DR seems to be more practical for stability monitoring.

Of course, the simplicity of the model used here allows only to give indicative results; one should not focus too much on the exact numerical values of its output. Nevertheless, we believe that the results shown here call for a reconsideration of the use of the DR as a sole indicator for BWR stability monitoring.

4.3 The influence of core-inlet temperature variations on BWR stability

In (flow) transient situations, the coolant temperature at the inlet of the core of a natural-circulation BWR can vary. This thermal feedback has an influence on the dynamics and stability of the closed-loop reactor system as is pointed out by Podowski and Pinheiro Rosa (1997). A quite rough approximation in the reduced-order model of Van Bragt and Van der Hagen (1998a) is that fluctuations of the core-inlet temperature (inlet subcooling) are ignored and a constant inlet subcooling is assumed in dynamic situations (see point No. 7 on p. 11). The influence of this approximation is examined with respect to the linear stability of the system by extending the model with a variable core-inlet temperature.

4.3.1 Modelling core-inlet temperature variations

Assuming a constant feedwater temperature and flow rate, we consider the inlet temperature variations that originate from the temperature fluctuations at the feedwater sparger caused by the mixing of the constant (cold) feedwater flow and the fluctuating (warm) circulation flow. We do not consider fluctuations in the feedwater flow or feedwater temperature. First of all, the time dependence of the inlet liquid enthalpy is introduced in the dynamic equation for the position of the boiling boundary (see Appendix A).

$$\frac{dz_{bb}(t)}{dt} = 2\left[\frac{M_{C,i}(t)}{\rho_l} - \frac{q'(t)z_{bb}(t)}{\rho_l A_C(h_f - h_{C,i}(t))}\right] \tag{4.3}$$

A flat axial power profile is assumed here, although other profiles can be introduced easily (see Chapter 5). Since we use a frequency-domain approach for the linear stability analysis, Eq. 5.8 is linearized and Laplace transformed to obtain the normalized transfer function from the core-inlet enthalpy to the boiling-boundary position:

$$G_{z_{bb},h_{C,i}} \equiv \frac{\frac{\delta z_{bb}}{z_{bb,o}}}{\frac{\delta h_{C,i}}{h_{C,i,o}}} = \frac{\frac{h_{C,i,o}}{h_f - h_{C,i,o}}}{1 + \frac{\tau_{nb}s}{2}}, \tag{4.4}$$

where $\tau_{nb} = \frac{z_{bb,o}\rho_l}{M_{C,i}}$ is the single-phase transit time in the core. To describe the dynamics of the inlet temperature (enthalpy), we start with the differential enthalpy-balance equation for the single-phase flow in the downcomer. Using a one-dimensional model (no

radial effects) and neglecting heat losses to the environment and heat diffusion in the downcomer one can write:

$$\frac{\partial \rho_l h(z,t)}{\partial t} + \frac{\partial M_d(t) h(z,t)}{\partial z} = 0, \tag{4.5}$$

where M_d is the mass flux in the downcomer. Linearizing and Laplace transforming, this equation can be integrated from the feedwater sparger to the core inlet to obtain the normalized transfer function from mass flux to inlet enthalpy:

$$G_{h_{C,i}, M_{C,i}} \equiv \frac{\frac{\delta h_{C,i}}{h_{C,i,o}}}{\frac{\delta M_{C,i}}{M_{C,i,o}}} = \frac{h_f - h_{C,i,o}}{h_{C,i,o}} e^{-s\tau_d}, \tag{4.6}$$

where $\tau_d = \frac{\rho_l l_{sp,in}}{M_{d,o}}$ is the transit time of the coolant from the feedwater sparger to the core inlet and $l_{sp,in}$ is the distance between the feedwater sparger and the core inlet. Here, an instantaneous and perfect mixing of the cold feedwater and the down-coming fluid at the sparger is assumed and use is made of Eq. 4.1.
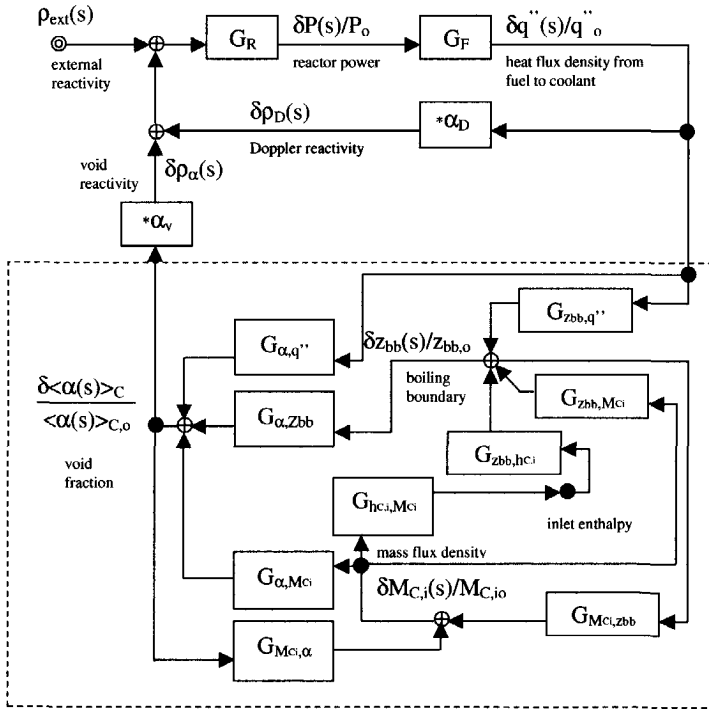
Figure 4.5: The block diagram of the extended model. The core-inlet enthalpy is introduced as a new system variable in the model.

Adding the two aforementioned transfer functions, one can draw the block diagram of the extended model as is shown in figure 4.5. We examine only the thermal-hydraulic stability of the system. The transfer function from heat flux to the core average void fraction can be derived as (compare to Eq. 2.1)

$$\frac{\frac{\delta<\alpha(s)>_C}{<\alpha>_{C,o}}}{\frac{\delta q''(s)}{q_o''}} = \frac{G_1 - G_1 G_3 + G_0 G_3}{1 + G_1 G_2 + G_0 G_2}, \tag{4.7}$$

where

$$G_0 = G_{z_{bb},h_{C,i}} G_{h_{C,i},M_{C,i}} G_{<\alpha>,z_{bb}}$$

$$G_2 = \frac{G_{M_{C,i},<\alpha>}}{1 + G_{M_{C,i},z_{bb}} G_{z_{bb},q''} - G_{M_{C,i},z_{bb}} G_{z_{bb},h_{C,i}} G_{h_{C,i},M_{C,i}}}$$

$$G_3 = \frac{G_{M_{C,i},z_{bb}} G_{z_{bb},q''}}{G_{M_{C,i},<\alpha>}} G_2$$

and G_1 has already been defined in Chapter 2 (Eq. 2.1).
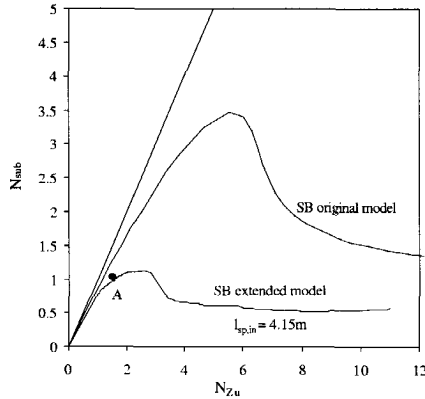
Figure 4.6: Thermal-hydraulic stability map of the Dodewaard reactor obtained by the original and the extended model. The extended model predicts a significantly less stable system. The feedwater sparger is placed at 4.15 m distance from the core inlet in the Dodewaard reactor.

The thermal-hydraulic SB's of the Dodewaard reactor obtained by the original and the extended model are compared in figure 4.6. The figure shows that ignoring the core-inlet temperature variations has a significant influence on the prediction of the stability.

Adding the transfer function in Eq. 4.6 to the model, introduces an extra complex exponential (delay) term. Since transport delays are crucial for density-wave oscillations (see Chapter 1), we expect this transfer function to play an important role in the thermal-hydraulic stability. The phase shift of this transfer function is determined by the coolant transit time τ_d, which, at a certain operating condition, depends only on the distance between the feedwater sparger and the core inlet. We study the role of the phase of the aforementioned transfer function in determining the thermal-hydraulic stability by changing the sparger position.
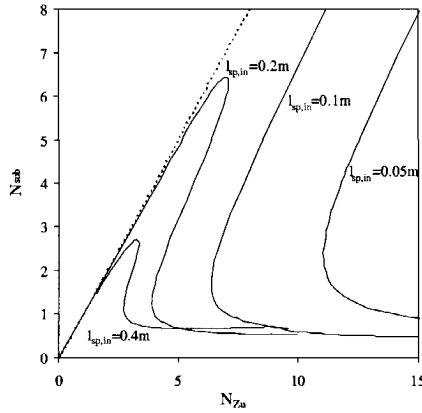
Figure 4.7: Thermal-hydraulic stability of the Dodewaard reactor for various positions of the feedwater sparger obtained by the extended model. As the position of the feedwater sparger approaches the core inlet the system becomes more stable. If the sparger is placed at the core inlet, the model predicts a stable system in the entire $N_{Zu} - N_{sub}$ plane.

4.3.2   Influence of the sparger position on the stability

The results on the stability map of the reactor found by changing the sparger position (the $l_{sp,in}$ distance) are shown on figure 4.7.

The thermal-hydraulic system becomes more stable as the sparger position approaches the core inlet. At the limit of zero sparger-core inlet distance, the system becomes stable in the entire operating region (unconditionally stable). This is because the influence of flow variations on the boiling-boundary position is just cancelled by the influence of the inlet-temperature variations. This follows from $G_{z_{bb},M_{C,i}} = -G_{z_{bb},h_{C,i}}G_{h_{C,i},M_{C,i}}$ for $\tau_d = 0$. In other words, if the sparger is at the core inlet, the right side of the linearized boiling boundary equation, (Eq. 5.8), becomes independent of the instantaneous value of the inlet mass flux and the inlet enthalpy, i.e. the boiling-boundary oscillations are cancelled. Van Bragt (1995) has shown that ignoring the boiling-boundary oscillations in the reduced-order model, it reduces to a damped oscillator like the model of March-Leuba (1984) and predicts an unconditionally stable thermal-hydraulic system,. This is because only two nodes (one single-phase and one two-phase) are considered in the core and within the nodes a quasi-static approximation is used for the enthalpy and quality profiles. For more details on the influence of the number of nodes used for modelling the core see D'Auria et al. (1997).

What happens with the stability as $l_{sp,in}$ increases is explained via the following illustrative example. The DR's and frequencies of several (dominant) pole pairs of the system (see Chapter 2) are shown in figure 4.8 as a function of the distance between the sparger and the core inlet calculated in an operating point marked with A in figure 4.6. Figure 4.8 also shows the phase of the $G_{h_{C,i},M_{C,i}}$ transfer function as a function of the sparger core-inlet distance for the frequencies (f_p) of the different poles $(phase = -2\pi f_p \tau_d$ from Eq. 4.6).

The important role of the phase of the $G_{h_{C,i},M_{C,i}}$ transfer function can be inferred from the figure: for frequencies and $l_{sp,in}$ distances where the phase is close to zero, the DR of the pole pairs is small (minimal). In these cases, the inlet-temperature oscillations are

just in-phase with the inlet-flow oscillations and therefore compensate the influence of the latter on the boiling-boundary oscillations. If the phase is close to $-180°$, i.e. the inlet-temperature oscillations are out-of-phase with the inlet-flow oscillations and therefore reinforce their influence on the boiling-boundary oscillations, then the corresponding DR has a (local) maxima. The matching of the maxima (minima) of the DR curves with the $-180°$ ($0°$) crossings of the corresponding phase curves is not fully perfect because the DR of a pole pair of the system is influenced also by other processes than the relative phase between inlet-flow and inlet-temperature oscillations. The number of local minima and maxima in the DR curves corresponds to the number of crossings of the phase $0°$ and $-180°$, respectively, which in turn is determined by the frequency of the pole.
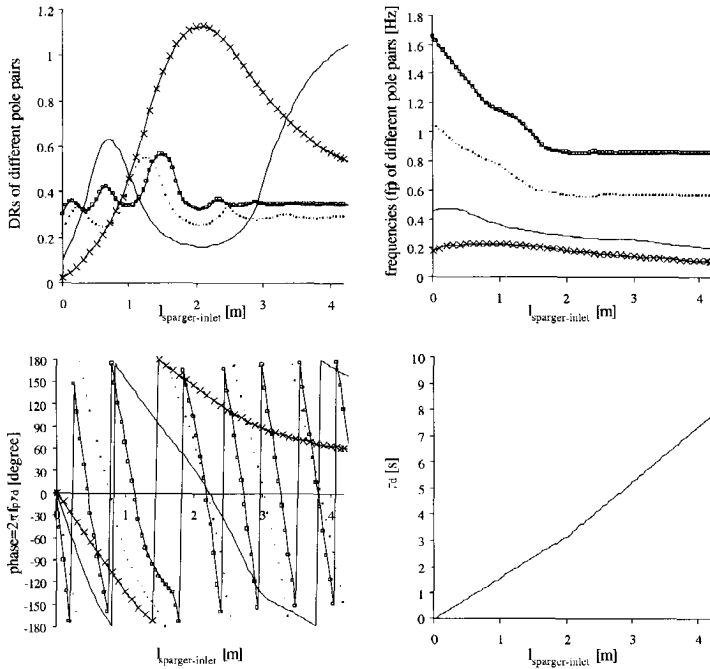
Figure 4.8: The upper figures show the DR's and the frequencies of several (dominant) pole pairs of the thermal-hydraulic system as a function of the distance between the feedwater sparger and the core inlet ($l_{sp,in}$) in operating point A from figure 4.6. The lower-left figure shows the phase shift of the $G_{h_{C,i},M_{C,i}}$ transfer function ($\phi = 2\pi f_p \tau_d$) as a function of $l_{sp,in}$ and the frequency of the different poles. The important influence of the $G_{h_{C,i},M_{C,i}}$ transfer function is clear from the figures: where its phase is close to zero the DR of the corresponding pole is small (minimal), where the phase is close to $-180°$ the DR of the pole has a (local) maxima. The lower-right figure shows the transit time from sparger to core inlet as a function of the distance between the sparger and the core inlet. There is a change in the slope of this line at around $l_{sp,in} = 2$, which is due to change of the area of the downcomer of Dodewaard at a certain height; it has no significance for the results shown here.

The stability of the system is determined by the least-stable pole pair. It is only at $l_{sp,in} = 0$ (when the phase of $G_{h_{C,i},M_{C,i}}$ is zero for all frequencies) that all the pole pairs

have minimal DR's. If $l_{sp,in}$ increases, there is an interchange between the different poles being the least-stable one as shown in figure 4.8. Therefore, the DR of the system is a sort "envelope" of the curves (at each $l_{sp,in}$ the maximal DR must be taken) shown in figure 4.8.

Investigations using the MONA code

It is due to the simplicity of the reduced-order model that it predicts an unconditionally stable system, when the sparger is at the core inlet. Considering the steady state, it is plausible physically that e.g. an increase in the flow would raise the boiling-boundary position just as much as the increase in the inlet temperature - caused by the increase in the flow - would pull it down; i.e. the boiling boundary position remains constant. In dynamic situations, the trend of decreasing DR as the sparger approaches the inlet, predicted by the reduced-order model, deserves further investigations. We use the MONA 1.9 code to study the influence of the position of the feedwater sparger on the thermal-hydraulic stability of the system. To enable subsequent comparison with experimental data, the nodalization of the DESIRE facility (see Chapter 3) is used for this study, since from a thermal-hydraulic point of view DESIRE is just a scaled copy of Dodewaard.

MONA is an advanced thermal-hydraulic code and 22 nodes are used to model the core section of the DESIRE facility. In this way we can circumvent the limitations of the reduced-order model and expect more reliable results.
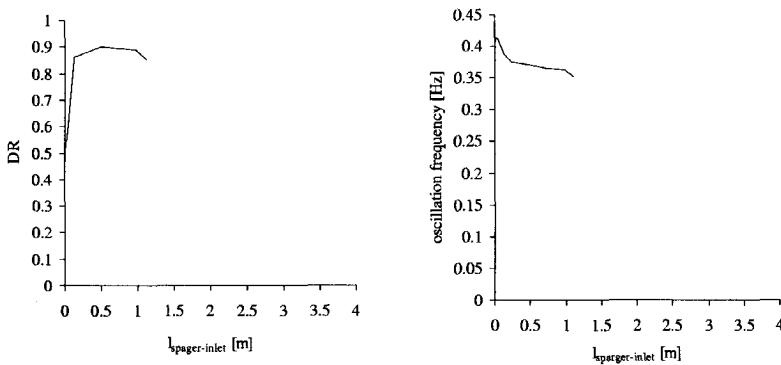
Figure 4.9: The influence of the feedwater sparger position on the stability of the DESIRE facility as predicted by MONA. There is a trend of stabilizing as the sparger position approaches the core inlet. the results are shown only for relatively small sparger-inlet distance.

The influence of the distance between the sparger and the core inlet on the stability of the system is examined by MONA in an operating point with a N_{Zu} and N_{sub} number close to that of point A in figure 4.6. The result in figure 4.9 shows a similar trend as found by the reduced-order model. The system becomes more stable as the sparger approaches the core inlet. Unfortunately, the investigations using MONA were not completely successful. This is due to the strong numerical diffusion in calculating the propagation of temperature oscillations in the downcomer of DESIRE as illustrated in figure 4.10.
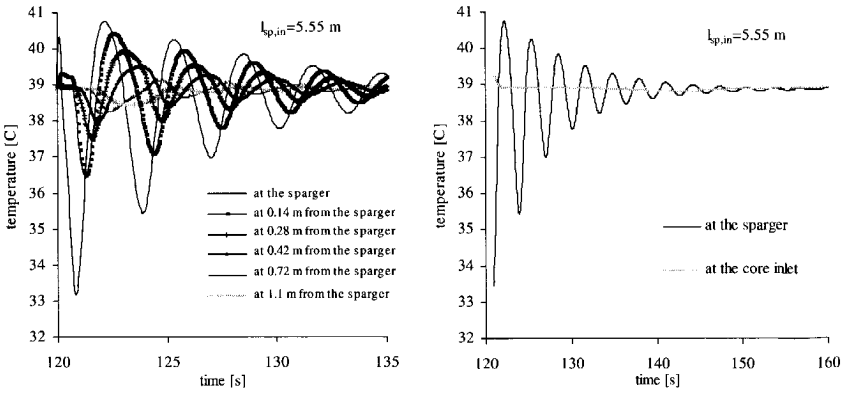
Figure 4.10: The temperature oscillations in the downcomer of DESIRE predicted by MONA. Due to numerical diffusion the temperature oscillations are strongly damped already within a relatively small distance downstream from the sparger (left figure). The oscillations do not appear at the core inlet (right figure). The distance between the sparger and the assembly inlet in DESIRE is 5.55 m, which corresponds to about 22 s transit time.

The figure shows that the temperature oscillations created at the sparger are strongly damped as they propagate towards the core inlet. Arriving at the core inlet the oscillations are died out completely due to the numerical diffusion in solving the discretized conservation equations over the nodes.
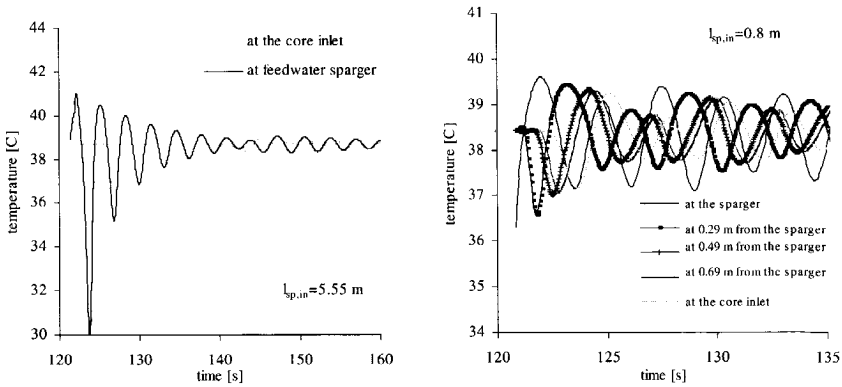
Figure 4.11: The temperature oscillations in the downcomer of DESIRE predicted by a refined nodalization (eight times more hydrodynamic volumes in each node in the downcomer) are still damped by numerical diffusion although temperature oscillations appear at the core inlet (left figure). The damping of temperature oscillations is less severe only if the sparger is close (<1m) to the core inlet (right figure).

The nodalization of DESIRE in the downcomer is quite rough. MONA uses an implicit upwind numerical scheme for solving the governing equations, which usually needs a quite fine nodalization (small hydrodynamic volumes) to decrease numerical diffusion. Therefore the nodalization of the downcomer is refined. The results are shown for an

eight times finer mesh, i.e. each original node is divided into eight nodes equidistantly, in figure 4.11. Using the refined nodalization, the results do not improve very much. The damping by numerical diffusion is not so significant only if the sparger is placed less than about 1 m from the core inlet. The curves (DR, frequency) in figure 4.9 are calculated with the refined nodalization. Some tests showed that refining further the nodalization does not improve the results satisfactory. Moreover, it has the drawback that the calculations become unpractically time-consuming.

These results indicate that one should be aware of the importance of proper modelling of core-inlet temperature oscillations and the influence of numerical diffusion when using thermal-hydraulic codes for stability investigations.

4.3.3   Examining the influence of turbulent diffusion on inlet-temperature variations

Turbulent heat diffusion has also a smearing out, damping influence on the temperature oscillations in the downcomer in actual cases, which is neglected in Eq. 4.5.

To get an idea how important (strong) the inlet-temperature variations actually are, we examine them measured in the DESIRE facility at transient flow conditions.
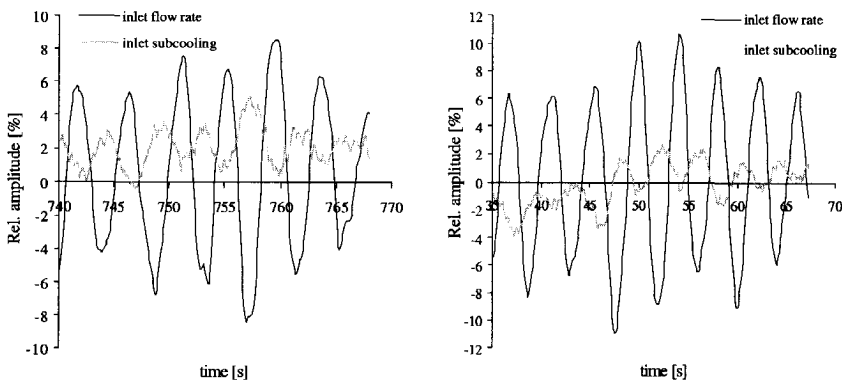
Figure 4.12: Inlet subcooling oscillations during typical transient flow conditions are well observable in the DESIRE facility. The measurements are carried out for a linearly stable system DR's of 0.79 (left figure) and of 0.92 (right figure).

Figure 4.12 shows that the inlet temperature (subcooling) variations are well detectable during flow transients (2 − 4% relative amplitude).

To get an idea how strong the damping of the temperature oscillations in the downcomer of DESIRE is, figure 4.13 shows the temperature oscillations measured in the downcomer just below the sparger and at the core inlet for a typical flow transient case. the data shows that, on average, the amplitude of temperature oscillations at the core inlet is around 30-32% of that at the sparger.
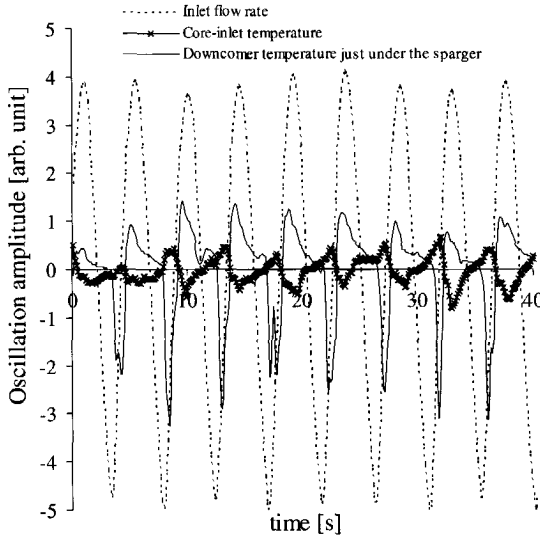
Figure 4.13: Temperature oscillations measured in DESIRE just under the feedwater sparger in the downcomer and at the core inlet for transient flow conditions. The flow rate oscillations are also depicted.

To estimate the damping of the temperature oscillations by turbulent diffusion, the one-dimensional heat convection-diffusion equation is considered:

$$\frac{\partial T(z,t)}{\partial t} + u\frac{\partial T(z,t)}{\partial z} = a\frac{\partial^2 T(z,t)}{\partial z^2}, \tag{4.8}$$

where $a = \frac{k}{c_p \rho_l}$ is the thermal diffusivity and k is the thermal conductivity. It is assumed that the flow velocity, u, is constant which is a reasonable approximation if the flow variations are relatively small. Laplace transforming and integrating Eq. 4.8, one obtains the temperature fluctuations at a distance z from the sparger by taking only the physically meaningful solution as:

$$T(z,s) = T_{sp}(s)e^{\frac{uz}{2a}\left(1-\sqrt{1+4as/u^2}\right)}, \tag{4.9}$$

where $T_{sp}(s)$ is the Laplace transform of the temperature oscillations at the sparger. Substituting $s = i\omega$ into Eq. 4.9, the ratio of the amplitude of temperature oscillations at the core inlet and at the sparger can be calculated in the frequency range of interest. In highly turbulent flows, as in the DESIRE facility, an effective diffusivity must be used in Eq. 4.8 instead of the molecular (material) diffusivity. This turbulent diffusivity can be several orders of magnitude higher than the molecular diffusivity and it strongly depends on the flow. Although there are correlations for the diffusivity in turbulent pipe flows obtained by e.g. $k - \varepsilon$ model (Wilcox, 1993) experimental values of the diffusivity, measured in the DESIRE facility (Van der Hagen, 1996), are used here. The value of $a = 2.8cm^2/s$ for flow in a cylindrical and the value of $a = 46cm^2/s$ for flow in between two square tubes is given by Van der Hagen (1996) for DESIRE. Since the downcomer of DESIRE is a combination of square and cylindrical geometries, we estimate and effective turbulent diffusivity as a weighted average (weighted by the relative lengths of the two

sections) of the aforementioned two diffusivity values: $a = 10.97 cm^2/s$. Using this value, the amplitude of the temperature oscillations at the core inlet is estimated to be around 30% of that at the sparger for the measured oscillation frequency (0.2 Hz) in DESIRE. This is in good agreement with the measured value.

Using Eq. 4.8 instead of Eq. 4.5 would lead to the following transfer function from mass flux to inlet enthalpy in Eq. 4.6:

$$G_{h_{C,i},M_{C,i}} \equiv \frac{\frac{\delta h_{C,i}}{h_{C,i,o}}}{\frac{\delta M_{C,i}}{M_{C,i,o}}} = \frac{h_f - h_{C,i,o}}{h_{C,i,o}} e^{\frac{ul_{sp,in}}{2a}(1-\sqrt{1+4as/u^2})}. \tag{4.10}$$

The gain and the phase of this transfer function are compared with those of the transfer function in figure 4.14 using the above value of the turbulent diffusivity for DESIRE. The figure shows that the difference between the gain of the two transfer functions is less than 20% up to a sparger to core-inlet distance of 1 m, for the the measured oscillations frequencies (around 0.2 Hz). The difference in the phases is negligible. This confirms that the turbulent diffusion has a relative small influence and neglecting it has practically no consequence on the results of the previous section, i.e. the stabilizing influence of nearing the sparger to the core inlet.
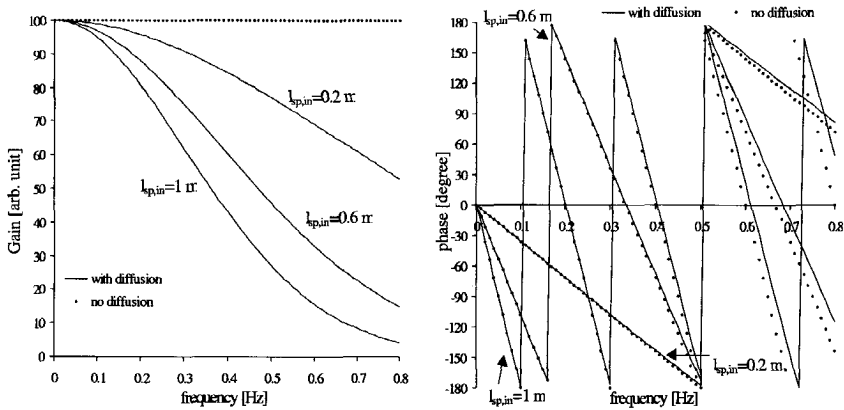
Figure 4.14: Comparison of the gain and the phase of the transfer functions in Eq. 4.6, the exponential delay term (no turbulent diffusion is modelled), and in Eq. 4.10 (with turbulent diffusion) for different sparger to core inlet distances.

4.3.4   Discussion

It has been shown that neglecting the influence of core-inlet temperature variations leads to erroneous results on the thermal-hydraulic stability of natural-circulation BWRs. Applying frequency-domain analysis of the reduced-order model, it was found that the phase at which the temperature oscillations, created at the feedwater sparger, reach the core inlet has a significant influence on the stability. This phase can be adjusted by positioning the sparger and it was found that approaching the sparger to the core inlet has a stabilizing influence. At the limit, when the sparger is at the core inlet, the system becomes unconditionally stable. The unconditional stability is due to the simplifications

in the reduced-order model. The MONA code was used to obtain more reliable results. A stabilizing trend is found with MONA too as the sparger approaches the inlet.

The stabilizing effect of positioning the sparger at the core inlet might be interesting for the design of the new generation of BWRs. The following important items should be thoroughly considered with respect to effects on reactor operation and consequences on the design if the sparger is placed at the core inlet (Challberg, 2002):

- There can be a decrease in the driving force of the natural-circulation flow if there is a significant carry-under (like in the Dodewaard reactor with free-surface steam-water separation). In a design with a steam-water separator (like the ESBWR), where the carry-under is small, the flow decreasing influence is presumably minor.

- In case of a (feedwater) pipe-line break, the reactor core would not remain covered with water if the sparger is at the height of the core inlet. However, this could be circumvented by using internal piping in the downcomer: starting from a high vessel entry position travelling downward to the core inlet (lower plenum). This internal piping in the downcomer should be accommodated in a way that relatively low extra friction is added.

- An advantage of a high sparger position is that one obtains a thorough mixing of the feedwater and the down-coming saturated liquid, which in turn, provides consistent temperatures or better yet, known conditions at the entrance to the core. Placing the sparger near the core inlet can have an undesirable effect creating not well-mixed, separate streams of cold and saturated liquid at the core inlet. This is an important practical issue that should be thoroughly examined using multi-dimensional analysis to see whether sufficient mixing can be achieved in the lower plenum if the sparger is placed in the vicinity of the core inlet.

- There is practical consideration of access to the lower annulus primarily for vessel material test specimens.

As another approach, one could try to optimize the length/area ratio of the downcomer, i.e. the transit time in the downcomer, so that for typical operating conditions oscillations in a certain (expected) frequency range are damped.

Examining further the influence of positioning the sparger at the core inlet on the stability remains an interesting issue.

Thermal-hydraulic codes implemented with other numerical scheme than implicit upwind scheme could be used for further numerical investigations. For example, numerical schemes based on the so-called time-splitting technique are very efficient in solving diffusion-convection type of equations that are involved in the present problem Press *et al.* (1986).

To enable a simple experimental investigation of the problem, an extra sparger could be added to the core inlet of the DESIRE facility, which could be alternatively used with the original one for stability investigation.

Chapter 5

Numerical analysis of the nonlinear dynamics of BWRs

5.1 Introduction

The understanding of density-wave oscillations and nuclear-coupled density-wave insta-bilities in BWRs is fairly good for linear phenomena, however, more work is needed to understand nonlinear dynamics and unstable behavior. As in the case of linear stabil-ity analysis, reduced-order models are more attractive for parametric studies on non-linear BWR dynamics than complicated system codes. The work by March-Leuba *et al.* (1986a,b) was the first significant attempt to investigate the nonlinear dynamics of BWRs using a simplified model. Similar, entirely numerical studies have also been carried out on the stability of boiling channels (Rizwan-uddin and Dorning, 1990; Clausse and Lahey, 1991; Pinheiro Rosa and Podowski, 1994; Garea *et al.*, 1994). Such numerical analyses are time consuming and therefore restricted to small regions of the parameter space. A better alternative is to perform analytical bifurcation analysis, which was first done by Achard *et al.* (1985) for a boiling channel using the homogeneous-equilibrium model. It was extended later by Rizwan-uddin and Dorning (1987) using the drift-flux model and nonuniform heater profiles. The application of these analytical techniques, developed in the field of nonlinear dynamics, for BWR stability analysis gradually gained attention. A "fully analytical" approach, based on the Hopf theory, was applied by Munoz-Cobo and Verdú (1991) for coupled neutronic-thermohydraulics using March-Leuba's model. The disadvantage of such an analytic approach is that algebraic complexity increases tremen-dously with the number of equations. To circumvent this difficulty, Tsuji *et al.* (1993) performed bifurcation analysis of forced-circulation BWRs using the numerical bifurcation code BIFOR2.

The present study employs the latter - numerical bifurcation analysis - approach to examine the influence of a special operating parameter, namely the axial power distribu-tion, on the nonlinear dynamics of natural- and forced-circulation BWRs. The influence of asymmetrical axial power profiles on the linear and non-linear stability of a simple heated channel has been investigated by Rizwan-uddin and Dorning (1986, 1987) using the drift-flux model. They concluded that (for the same total heating power) a bottom-peaked power distribution results in the lowest and a top-peaked profile results in the highest stability in the region of practical interest. This result was confirmed by Narayanan *et al.* (1997), who reported on the effect of linear and exponential variations of the axial power profile on the stability boundary. However, only thermal-hydraulic stability was investi-gated in the aforementioned papers. Since the natural-circulation BWR is a promising

candidate for the next generation of BWRs, Van Bragt *et al.* (1999) performed stability and bifurcation analysis of natural-circulation BWRs. They used the reduced-order BWR model introduced in Chapter 2 and the numerical Hopf-bifurcation code BifDD. Nevertheless, only symmetrical axial power profiles have been analyzed there, whereas in reality the axial power distribution can be quite asymmetrical. To broaden the insight into the influence of the axial power profile on the nonlinear dynamics of BWRs, Hopf bifurcation analysis is performed here on four different types of systems. Two purely thermal-hydraulic systems are investigated: a forced-circulation and a natural-circulation boiling channel. The corresponding reactor (coupled) systems are examined as well. Numerical time-domain simulations are also carried out to determine the range of validity of the bifurcation analysis.

5.2   The Hopf bifurcation

The Hopf bifurcation proved to be one of the most important bifurcation type in BWR dynamic analysis (Achard *et al.*, 1985; Rizwan-uddin and Dorning, 1986; Tsuji *et al.*, 1993). The Hopf bifurcation theorem guarantees the existence of family of a periodic solutions of a set of nonlinear ordinary differential equations (Hassard *et al.*, 1981; Hale and Kocak, 1991). Consider the autonomous system

$$\frac{d\vec{x}}{dt} = F(\vec{x}, \nu), \tag{5.1}$$

where ν is a so-called bifurcation parameter, and suppose that for a certain ν_c, $\vec{x}(\nu_c)=0$ and $\vec{x}=0$ is an equilibrium point of the system, i.e.

$$F(\vec{x}, \nu_c) = 0 \tag{5.2}$$

According to the theorem, a family of periodic solutions of Eq. 5.1 exists in the vicinity of ν_c if the following conditions are fulfilled (Hassard *et al.*, 1981; Hale and Kocak, 1991):

1. Let $DF(\vec{x}, \nu) = \frac{dF}{d\vec{x}}(\vec{x}, \nu)$ denote the Jacobian matrix of F and $\lambda(\nu) = \sigma(\nu) + i\omega(\nu)$ the eigenvalues of it. $DF(\vec{x}, \nu_c)$ has a pair of complex conjugate eigenvalues lying on the imaginary axis, i.e. $\sigma(\nu_c) = 0$ and $\omega(\nu_c) = \omega_c > 0$ and all the other eigenvalues have strictly negative real parts.

2. The real parts of the eigenvalues cross the imaginary axis with a non-zero speed, i.e. $\frac{d\sigma(\nu_c)}{d\nu} \neq 0$.

Obviously, at the ν_c critical value, the stability of the system changes, with other words it undergoes a bifurcation. The critical value ν_c, (the linear stability boundary value) can be easily determined using linear stability analysis. However, bifurcation analysis is needed to determine the amplitude of the linearly unstable, oscillatory solutions close to the stability boundary. The bifurcation can be studied either by integrating numerically the governing differential equations for different ν values around ν_c or by performing analytical bifurcation analysis. The latter one usually involves some form of asymptotic expansion methods. In such a case, the periodic solution is expanded in terms of a small parameter ϵ:

$$\vec{x}(t, \nu) = \vec{x}(\nu_c) + \epsilon Re(e^{\frac{2\pi i t}{T(\epsilon)}} \vec{v}_1) + O(\epsilon^2), \tag{5.3}$$

where $\vec{v}_1$ is the eigenvector of the linearized system on the stability boundary. Similarly, the nonlinear oscillation period $T(\epsilon)$ and the bifurcation parameter ν are also expanded in powers of ϵ:

$$T(\epsilon) = \frac{2\pi}{\omega_o}[1 + \tau_2\epsilon^2 + O(\epsilon^4)], \tag{5.4}$$

$$\nu(\epsilon) = \nu_c + \mu_2\epsilon^2 + O(\epsilon^4). \tag{5.5}$$

The stability of the periodic solutions can be determined by the Floquet theory of differential equations with periodic components (Hassard *et al.*, 1981; Hale and Kocak, 1991). Let $\vec{p}(t)$ be a T-periodic, $\vec{\psi}(t)$ be an arbitrary solution of 5.1. Suppose that $\vec{y}(t) = \vec{\psi}(t) - \vec{p}(t)$ is small, and we form the following linear variational system:

$$\frac{d\vec{y}}{dt} = F(\vec{p} + \vec{y}) - F(\vec{p}) \simeq A(t)\vec{y}, \tag{5.6}$$

where $A(t) = DF(\vec{p}(t))$ is a matrix with T-periodic components. The stability of $\vec{p}(t)$ is largely determined by the behavior of the aforementioned linear variational system. The Flouqet theorem states that every fundamental matrix solution of $\frac{d\vec{y}}{dt} = A(t)\vec{y}$ has the form: $Y(t) = P(t)e^{Bt}$, where $P(t)$ is a T-periodic matrix and B is a constant matrix. The β_i eigenvalues of B are called the characteristics or Floquet exponents.

The Floquet exponent describing the stability of the periodic solutions can be written as $\beta(\epsilon) = \beta_2\epsilon^2 + O(\epsilon^4)$ (Hassard *et al.*, 1981). The Floquet exponents describe the asymptotic decay of the transients to the periodic solution in Eq. 5.3. Depending on the sign of the Floquet exponent the periodic solution attracts neighboring state-space trajectories and is thus orbitally stable (a limit cycle) for $\beta(\epsilon) < 0$; or repels trajectories in his vicinity and is thus orbitally unstable for $\beta(\epsilon) > 0$. Detailed analysis of the Hopf theorem shows that if periodic solutions exist in the linearly unstable region, i.e. the Hopf bifurcation is *supercritical*, the periodic solutions are stable. If periodic solutions exist in the linearly stable region, i.e. the bifurcation is *subcritical*, the periodic solutions are unstable.

In principle, one can derive so-called bifurcation formulae for the expansion coefficients μ_i, τ_i, β_i. However, one usually stops already at μ_2, τ_2, β_2. (Detailed analysis shows (Hassard *et al.*, 1981) that $\mu_1 = 0, \tau_1 = 0, \beta_1 = 0$ always; and $\mu_3 = 0, \tau_3 = 0, \beta_3 = 0$ with an appropriate choice of the variables.) The analytical calculation of the expansion coefficients is only practical for a very limited class of reasonably simple systems. For more complex systems it becomes quickly cumbersome. A practical alternative is to evaluate the bifurcation formulae numerically.

This analytic-numeric alternative is used in the the numerical Hopf-bifurcation code BifDD (Hassard, 1987), which is applied here for bifurcation analysis of the reduced-order BWR model. The BifDD code enables to calculate the aforementioned critical value of the bifurcation parameter in the model at given values of all other system parameters. Thus, by incrementally varying another parameter of the system, the entire stability boundary in a two-dimensional space can be determined. The main result of the bifurcation calculation with BifDD is the set of expansion coefficients, μ_2, τ_2, β_2 for each point along the SB.

One has to bear in mind that the result of the Hopf theorem is local in nature and is only valid in the vicinity of the SB (Hassard *et al.*, 1981). Therefore, we have also performed direct numerical integration of the model equations for several cases to check the range of validity of the prediction of BifDD and to determine the system dynamics further away from the SB. The NDSolve subroutine in the Mathematica package has been

used for this purpose (Wolfram, 1996). The NDSolve routine uses the Adams predictor-corrector method for non-stiff differential equations and backward difference formulas (Gear method) for stiff differential equations with a default accuracy of ten digits. All calculations are performed with double precision using the BifDD code.

5.3   Modelling of asymmetrical axial power profiles

The reduced-order BWR dynamic model has been already introduced in Chapter 2, and further details of the model are given in Van Bragt and Van der Hagen (1998a), and in Van Bragt *et al.* (1999). Only the slight modifications, which have been made to this model to perform the present study, are mentioned in the following. For the simulation of asymmetrical axial power profiles, the $AP(z^*) = f_p \sin(A + Bz^*)$ power profile has been added to the model, where z^* is the axial position (relative to the core height), and f_p is the power peaking factor. The axial position of the power peak z_p^* and the value of the peaking factor can be given as an input to the model, relating A and B to each other as $A + Bz_p^* = \frac{\pi}{2}$. The values of the constants A, B then follow from the normalization condition:

$$\int_0^1 AP(z^*)dz^* = 1. \tag{5.7}$$

Note that for each z_p^* there is an upper limit for f_p for which a still physically meaningful profile exist (e.g. $f_p = \frac{\pi}{2}$ for $z_p^* = 0$).
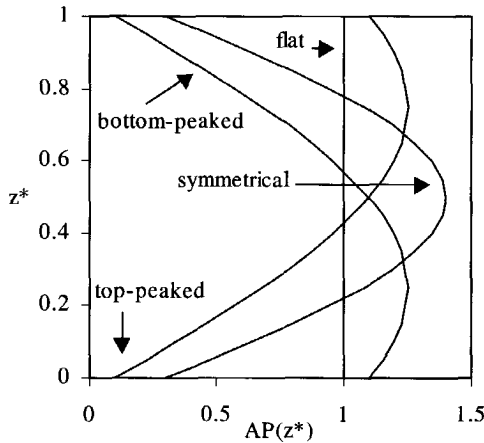
Figure 5.1: Typical axial power profiles used in the model. The areas under the different curves are normalized to unity.

Some typical axial power distributions used in the model are depicted in figure 5.1. The dynamics equation describing the boiling-boundary position (Van Bragt *et al.*, 1999) is strongly dependent on the actual power distribution in the one-phase region:

$$\frac{dz_{bb}^*}{dt^*} = \frac{1}{P_d}[M_{C,e}^*(1 + J_{2,C}^*) - (1 - z_{bb}^*) < q''^* >_{2\phi} N_{Zu} - z_{bb}^* < q''^* >_{1\phi} \frac{N_{Zu}}{N_{sub}}]), \tag{5.8}$$

where the factor P_d characterizes the influence of the axial power profile on the dynamics of the boiling boundary:

$$P_d = \frac{[z_{bb}^* B \cdot \cos A + \sin A - \sin(A + B z_{bb}^*)] \sin(A + B z_{bb}^*)}{[\cos A - \cos(A + B z_{bb}^*)]^2} \tag{5.9}$$

The asterisk in Eq. 5.8 and in Eq. 5.9 means that the quantities are made dimensionless (Van Bragt and Van der Hagen, 1998a).

5.4   Thermal-hydraulic systems

5.4.1   Forced-circulation system

An elementary thermal-hydraulic system, consisting of a vertical heated channel and a downcomer is investigated first in this section. The circulation in the loop is sustained by an external pressure drop imposed over the downcomer section.

The stability map of the heated channel system are shown in figure 5.2 in the N_{Zu} − N_{sub} plane for the four axial power profiles depicted in figure 5.1.
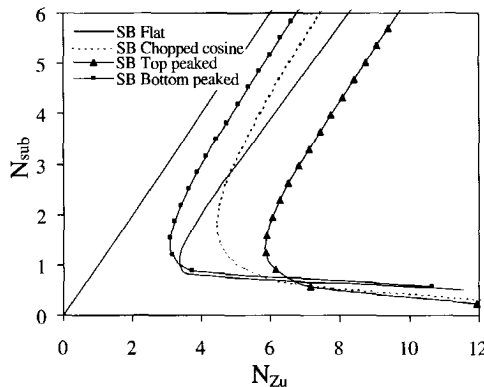
Figure 5.2: Stability map of a simple heated channel for the four different axial power profiles depicted in figure 5.1. A bottom-peaked profile yields the least, and a top-peaked profile yields the most stable system for relatively low N_{Zu} and N_{sub} numbers.

As it was shown in Chapter 2, for a forced-circulation system the most important type of instability is the Type-II density-wave oscillation. The mutual positions of the SBs agree with previous results by Rizwan-uddin and Dorning (1987), obtained for a similar heated channel system. In figure 5.3, SBs of a typical top- ($z_p^* = 0.75, f_p = 1.39$) and bottom-peaked ($z_p^* = 0.25, f_p = 1.39$) profile are given. The dashed lines connect operating points for which equal-amplitude periodic solutions exist, where ϵ is the oscillation amplitude (half of the peak-to-peak value) of the channel-exit mass-flux density relative to its equilibrium value. (The eigenvector $\vec{v}_1$ in Eq. 5.3 is normalized with respect to the first component, i.e. the normalized core-exit mass-flux density $M_{C,e}^*$, of the state vector $\vec{x}(t, \nu)$.) Figure 5.3 shows that in case of a top-peaked profile the periodic nonlinear solutions are located to the right of the SB, i.e. in the Type-II unstable region. This means that the bifurcation is supercritical for a top-peaked profile and the periodic

solutions are orbitally stable, limit-cycle oscillations. On the other hand, in case of bottom
peaked profile, the $\epsilon = 0.3$ line crosses the SB at about $N_{sub} = 3.0$ and penetrates into
the (linearly) stable region at high values of the subcooling number. When the periodic
nonlinear solutions are located in the linearly stable region, the bifurcation is subcritical
and unstable periodic solutions exist. As long as perturbations in the core-exit mass-
flux density do not exceed the value of the corresponding ϵ in that operating point, the
oscillations are damped and the system settles to equilibrium. As the magnitude of the
perturbations exceed ϵ diverging oscillations develop. Subcritical bifurcations are therefore
rather dangerous, since they might result in diverging oscillations in the linearly stable
operating regime.
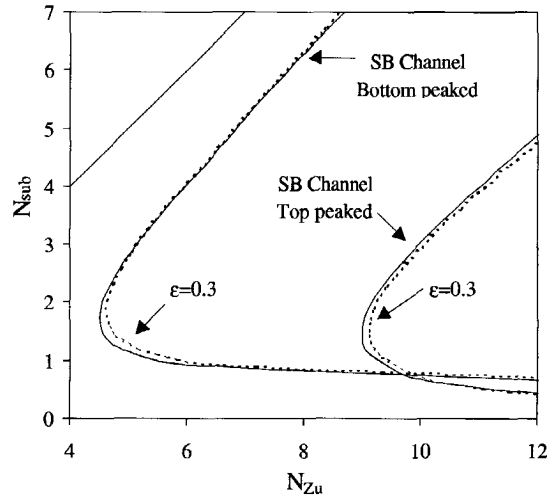
Figure 5.3: SBs and lines of equal-amplitude oscillation ($\epsilon = 0.3$) for a typical top- and
bottom-peaked profile (see figure 5.1). The bifurcation is subcritical for high values of the
subcooling in case of a bottom-peaked profile, whereas, bifurcation is supercritical for a
top-peaked profile.

Note that a linear analysis cannot predict the existence of this kind of diverging non-
linear oscillations. This phenomenon therefore deserves a more detailed analysis. The
detailed bifurcation analyses are carried out at N_{sub}=4.0 using N_{Zu} as bifurcation param-
eter for different axial power peak positions and peaking factors. The results are shown
in figure 5.4. The horizontal coordinate in figure 5.4 - $\delta N_{Zu} = (N_{Zu} - N_{Zu,SB})/N_{Zu,SB}$
- is the relative distance of the $\epsilon = 0.3$ curve from the SB, the vertical coordinate is the
relative axial power peak position. For positive values of δN_{Zu}, a bifurcation is supercrit-
ical, whereas a bifurcation is subcritical for $\delta N_{Zu} < 0$. Figure 5.4 clearly shows the strong
impact of the axial power profile on the Hopf-bifurcation characteristics. The bifurcation
is supercritical if $z_p^* \geq 0.3$. Only for strongly bottom-peaked profiles ($z_p^* < 0.3$), with a
high peaking factor, subcritical bifurcations may occur. Note also that the $\epsilon = 0.3$ curves
depicted in figure 5.4 cross in the same point regardless of f_p. The reason for this is not
known and it needs further investigations.

The influence of the peaking factor f_p on the oscillation amplitude is also apparent; the
equal amplitude curves shift away from the SB as a function of f_p. A similar observation
was made by Van Bragt et al. (1998) with respect to symmetrical power profiles. Figure 5.4
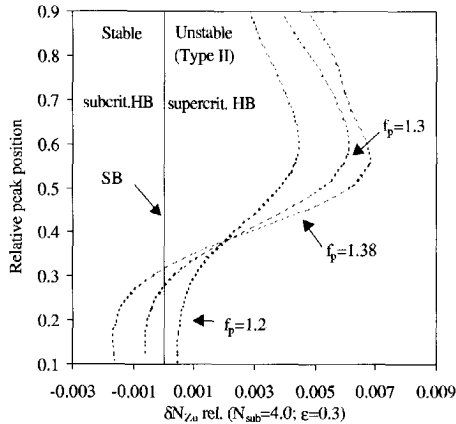
Figure 5.4: Relative distances from the SB for different peak positions and different peaking factors. The lines of equal oscillation amplitude ($\epsilon = 0.3$) are located quite close to the SB (the oscillation amplitude rises rapidly as a function of the distance from the boundary).

shows that a shift of only 0.1% in N_{Zu} (from the SB) results in limit-cycle oscillations with a relative large amplitude of 30% for a slightly bottom-peaked profile ($z_p^* \cong 0.4$). Supercritical bifurcations result in orbitally stable oscillations, however, from safety point of view it is also very important to notice how fast the amplitude of the limit cycle increases as the SB is crossed.

5.4.2 Natural-circulation system

The next system under consideration is a natural-circulation boiling loop. In natural-circulation BWRs the flow rate is enhanced by installing a tall riser section on the top of the core. The system considered consists of a heated channel, an unheated riser and a downcomer. For such a natural-circulation system the SB is depicted for a typical bottom- and top-peaked profile in figure 5.5. Due to the presence of a riser, the additional unstable region of the Type-I instability appears close to the one-phase boundary (see Chapter 2). The corresponding $\epsilon = 0.3$ lines are also presented in figure 5.5.

The bifurcation type changes from supercritical to subcritical in the Type-I region in case of a bottom-peaked profile, while it remains supercritical for a top-peaked profile. A detailed study has been performed again to examine the influence of the peak position on the bifurcation characteristics (for different peaking factors), both in the Type-I and Type-II regions. The result of this analysis is shown in figure 5.6. It is again obvious from the figure that the asymmetry of the power distribution significantly influences the Hopf-bifurcation characteristics (cf. figure 5.4).

One should notice that in figure 5.6, in case of the Type-I region, the locations of the stable and unstable regions are just opposite to those in the Type-II region. This implies that in this case subcritical bifurcation occurs for $\delta N_{Zu} > 0$ and supercritical bifurcation for $\delta N_{Zu} < 0$. The right side of figure 5.6 shows that bottom-peaked profiles with a high peaking factor can cause the occurrence of unstable oscillations in the Type-I region (subcritical bifurcation). The left side of figure 5.6 shows that in the Type-II region no

subcritical bifurcation occurs in contrast to the forced-circulation case (figure 5.4).
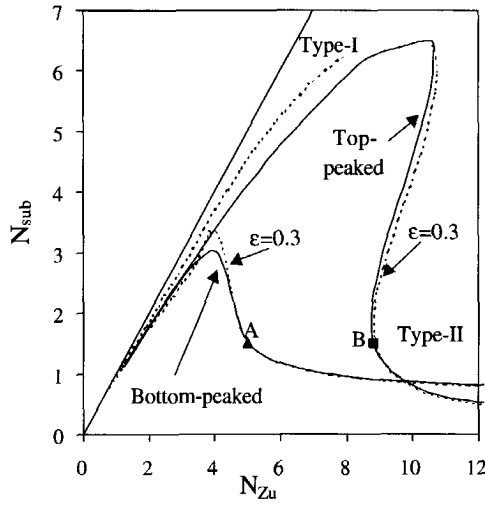
Figure 5.5: Bifurcation and stability map of a natural-circulation loop, for bottom- and top-peaked power profiles. The mutual position of the boundaries in the Type-II region is approximately the same as for a forced-circulation system. Bifurcation is subcritical in the Type-I region for a bottom-peaked profile, whereas bifurcation is supercritical for a top-peaked profile.
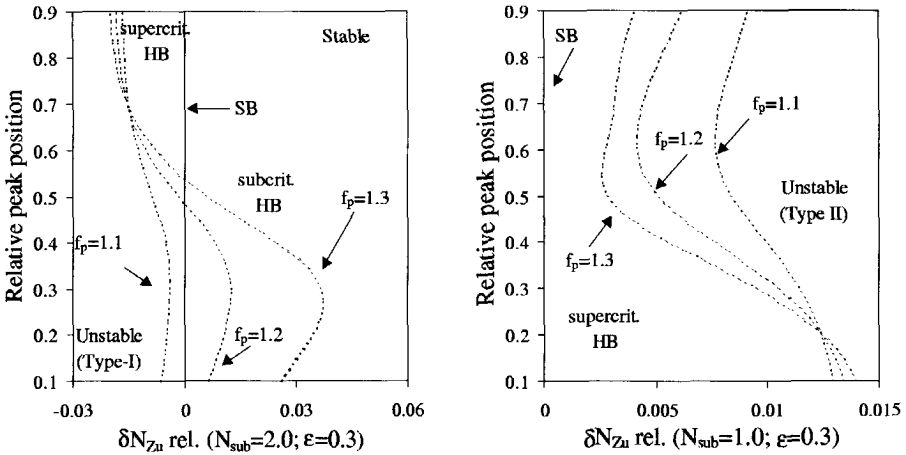
Figure 5.6: Influence of the axial peak position on the Hopf bifurcation characteristics in a natural-circulation loop in the Type-I (left figure) and in the Type-II (right figure) region.

In the Type-II region in figure 5.6, the oscillation amplitude rises the slowest for the lowest peaking factor and the fastest for the highest peaking factor as a function of the

distance from the SB for the natural circulation system. This is just the opposite for the forced-circulation system in figure 5.4.

To examine this behavior further and to validate the prediction of the oscillation amplitude made by BifDD, the model equations have been integrated numerically using the NDSolve subroutine in the Mathematica package. The calculations have been carried out for bottom and top-peaked profiles in several points in the vicinity of the points A and B indicated in the stability map in figure 5.5. The oscillation amplitudes are given in figure 5.7 as a function of the relative distance from the SB. For practical reasons, this distance is expressed as a function of the subcooling number (for $N_{Zu} = 5.0$) in the vicinity of point A in figure 5.5. The oscillation amplitude increases as the square root of the distance from the SB according to the prediction of the BifDD code (see Eq. 5.5). This prediction agrees very well with numerical time-domain results up to about $\epsilon = 0.6$ (60% relative amplitude) for a top-peaked profile in point B. BifDD predicts the relative amplitude accurately only up to about 0.3 in case of a bottom-peaked profile.
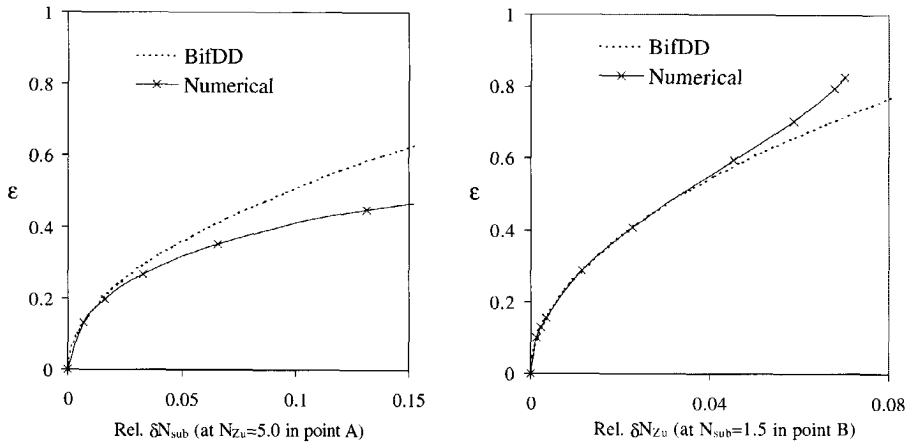
Figure 5.7: Comparison between the Hopf prediction of the oscillation amplitude made by BifDD and direct time-domain results in the Type-II region. Simulations with a bottom-peaked profile (left figure) are carried out in points in the vicinity of point A in figure 5.5. Simulations with a top-peaked profile (right figure) are performed in the vicinity of point B in figure 5.5.

5.5   Reactor systems

This section investigates the impact of the axial power profile on the Hopf-bifurcation characteristics of BWRs. It is shown in Chapter 2 that void-reactivity feedback influences strongly the linear stability. Recently, Van Bragt *et al.* (1998) have examined the influence of the strength of the void reactivity feedback on the Hopf bifurcation. They found that the actual value of the void-reactivity feedback coefficient (α_v) can significantly influence the type of bifurcation. However, only axially symmetrical profiles have been investigated there. We present here a similar analysis using different asymmetrical profiles. Results in figure 5.8 are obtained for a forced-circulation BWR.

The curves, plotted in the $\alpha_v - N_{Zu}$ plane, are the $\epsilon = 0.3$ lines calculated by BifDD. It must be noted that ϵ here means the relative (half peak-to-peak) oscillation amplitude of the reactor power. Different top- and bottom-peaked profiles are used in the calculations. The results are similar to the results reported in the aforementioned paper of Van Bragt *et al.* As the reactivity coefficient is increased (in absolute sense), the bifurcation type changes from supercritical to subcritical (around $\alpha_v = -0.05$) and again back to supercritical for larger (negative) values of α_v as is shown on the left side of figure 5.8.
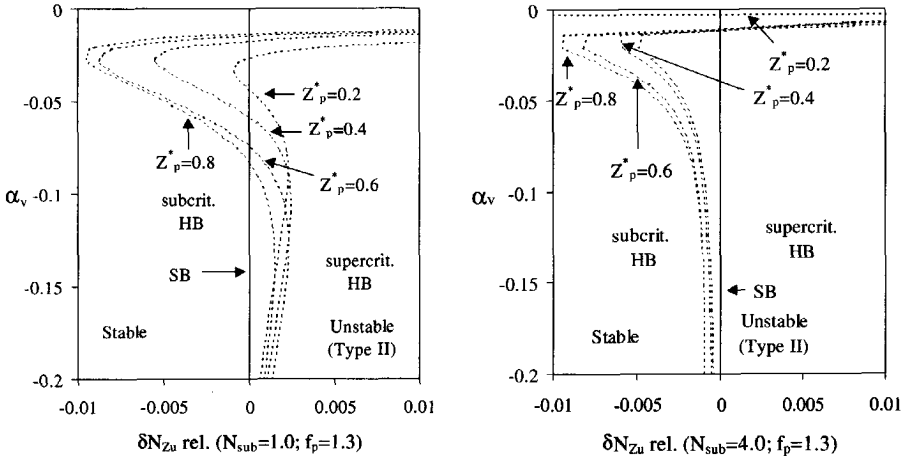
Figure 5.8: Influence of the void-reactivity coefficient (α_v) on the Hopf bifurcation curves of a forced-circulation reactor with different asymmetrical power profiles for $N_{sub} = 1.0$ (left figure), and for $N_{sub} = 4.0$ (right figure). The peaking factor was kept constant $(f_p = 1.3)$.
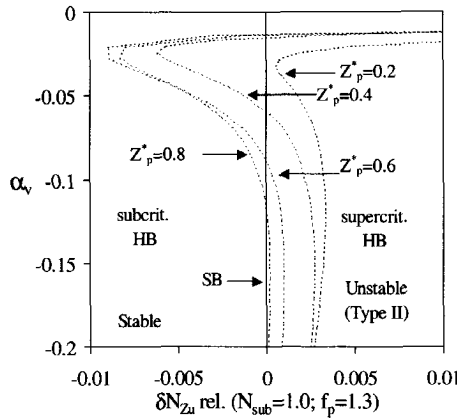
Figure 5.9: Influence of the void-reactivity coefficient on the Hopf bifurcation for a natural-circulation reactor with asymmetrical power profiles. The peaking factor was kept constant $(f_p = 1.3)$.

Note that for a strongly bottom-peaked profile the region where subcritical bifurcations occur is reduced very much. For strong void reactivity feedback (large negative α_v), the equal amplitude lines approach the SB for each profile. This means that the oscillation amplitude grows very rapidly away from the SB for a strong void-reactivity feedback for each different power profiles. For a higher value of N_{sub}, on the right side of figure 5.8, the bifurcations are always subcritical except for small absolute values of α_v. The uppermost curve - belonging to $z_p^* = 0.2$ - takes a very sharp turn and returns to the subcritical region as α_v approaches zero (the case of a boiling channel) while the others remain on the supercritical side (this is not depicted for a better visualization). This is in agreement with the result in figure 5.4. For large negative α_v, the curves are squeezed to the SB again.

Finally, the same analysis has been performed for a natural-circulation BWR. Results are shown in figure 5.9. The bifurcation curves show the same qualitative behavior as on the left side of figure 5.8. It appears that for a strongly bottom-peaked profile the bifurcation remains supercritical for all values of the void-reactivity coefficient examined. For α_v approaching zero, the bifurcation is supercritical for each profile, in correspondence with the previous results in figure 5.6.

5.6 Conclusions

The influence of asymmetrical axial power distributions on nonlinear BWR dynamics has been investigated using a reduced-order BWR dynamics model. Both forced- and natural-circulation two-phase flow channels and reactor systems have been evaluated. Hopf-bifurcation analyses of these systems have been performed using the numerical Hopf-bifurcation code BifDD. Both fundamental Hopf bifurcation types, the sub- and the supercritical bifurcation, are encountered depending on the actual power distribution. Bottom-peaked profiles (with a high peaking factor) typically induce subcritical bifurcations in the Type-II regime for high values of the core-inlet subcooling. For top-peaked profiles the bifurcation is supercritical in practically the whole operating range for a forced-circulation channel. In case of a natural-circulation boiling channel, subcritical bifurcations occur again for bottom-peaked profiles but in the Type-I instability region. Top-peaked profiles result in supercritical bifurcations in both unstable regions. In case of reactor systems, the strength of the void-reactivity feedback has a significant impact on the bifurcation characteristics. With increasing void-reactivity coefficient (in an absolute sense), the Hopf bifurcation changes from supercritical to subcritical and then back again to supercritical for practically interesting (relatively low) values of the inlet subcooling. This bifurcation-changing effect is strongly attenuated in case of low power-peak positions. In case of very strong reactivity feedback, the lines of equal-amplitude oscillations are squeezed to the SB for each axial power profile and the limit-cycle amplitude grows very rapidly as a function of the distance from the SB.

Chapter 6

Experiments on the nonlinear dynamics of natural-circulation two-phase flows

6.1 Introduction

This chapter presents comprehensive experimental investigations on the nonlinear dynamics of natural-circulation, boiling two-phase flows using the DESIRE facility. The investigations can be divided into two distinct studies. One study concentrates on examining the character of nonlinear density-wave oscillations measured in the neighborhood of the SB. The other tries to map the system behavior over a larger domain of operating conditions focusing on what happens "deep" in the unstable region.

6.2 Experiments on the character of density-wave oscillations

6.2.1 Previous work

Density-wave oscillations in heated channels have been studied for long being of a vital importance for the safe operation of industrial boiling, two-phase flow systems like heat exchangers, boilers and BWRs. The progress in this field has continuously been reviewed (Bouré *et al.*, 1973; Yadigaroglu, 1981; Kakac and Liu, 1991; Lahey and Moody, 1993). Thanks to the considerable research effort, significant success has been achieved in explaining and identifying the main physical mechanisms involved in density-wave oscillations (see Chapter 1 section 1.4).

Several papers discussed the relation between the oscillation period and transit time of the fluid through the system. The period was traditionally reported to be one to two times the channel transit time (Stenning and Veziroglu, 1965; Bouré *et al.*, 1973; Kakac and Liu, 1991).

Some years ago, Rizwan-uddin restarted the discussion about the physical mechanism of density-wave oscillations (Rizwan-uddin, 1994). He pointed out, based on numerical simulations for high channel-inlet subcooling, that density-wave oscillations may persist with mixture-density variations occurring almost simultaneously along the system (i.e. with very weak "density-waves"). He showed that variations in mixture velocity play a more important role than variations in the mixture density in determining the channel pressure-drop characteristics. He found the oscillation period to be between three-to-four times the channel transit time. He found the same using earlier experimental data of Saha

et al. (1976), calculating channel residence times and comparing them to the measured oscillation periods.

Inspired by the work of Rizwan-uddin, Ambrosini *et al.* (1998) have performed a comprehensive analysis of density-wave oscillations using nonlinear analytical tools. They have mapped the oscillation-period to transit-time ratio for the whole operating parameter plane in terms of N_{Zu} and N_{sub}. They found a continuous distribution of the oscillation-period to transit-time ratio from very low values (<1) at low subcooling to infinity at the threshold of the Ledinegg (excursive) instability at high subcooling. In the low-subcooling region generally, a strong propagating (wave) character of the mixture-density oscillations is found and the period of the oscillations is generally close to twice the transit time of the fluid. At high-subcooling conditions they draw the same conclusions as Rizwan-uddin (1994).

The continuing discussion shows that there is still obscurity in the physical interpretation of density-wave oscillations and a complete consensus has not been reached yet. Density-wave oscillations involve a complex combination of void propagation (transport) and local void production effects. Inlet-flow fluctuations result in an instantaneous variation in heating rate along the channel, which result in variations in the local enthalpy (in the single-phase region) and in the local void production (in the two-phase region). This is accompanied by the propagation of these enthalpy and void-fraction perturbations with the flow from lower elevations to higher elevations in the channel. It seems extremely difficult, if not impossible, to disentangle these two effects. Which one of the two characters of mixture-density variations - the instantaneous or the propagating - dominates during the oscillations, depends on the operating parameters as pointed out numerically by Ambrosini *et al.* (1998).

We have investigated the problem experimentally using the DESIRE facility. As a new approach, we examine the character of the mixture-density variations by measuring the phase shift (and the associated time lag) between the inlet-flow oscillations and the void-fraction oscillations at different heights. Furthermore, the time lag between the inlet-flow oscillations and riser-exit void-fraction oscillations is compared to the oscillation period. The time lag between the inlet-flow oscillations and riser-exit void-fraction oscillations is a dynamic variable that we expect to reflect more from the dynamic characteristics of the oscillating two-phase flow than the steady-state fluid transit time. We show that this time lag cannot be interpreted simply as the transit time of mixture-density waves propagating through the system, which is due to the aforementioned complex nature of the density-wave oscillations. To compare the experimental results with the aforementioned numerical studies, we also examine the relation of the measured oscillation period to the steady-state fluid transit time estimated from the model of Rizwan-uddin.

6.2.2   Experimental results

The experiments have been carried out in the unstable operating region of the facility, relatively close to the SB, where it exhibits large, constant-amplitude density-wave oscillations. For these experiments two gamma-transmission setup have been used to measure the mixture density (void fraction) at different elevations.

Taking the Cross-Correlation Function (CCF) between the inlet-flow oscillations and the void-fraction oscillations at different elevations, we can extract the phase shift between them and the time lag associated with the phase shift. For periodic oscillations, the CCF will also be periodic as it is shown in figure 6.1.
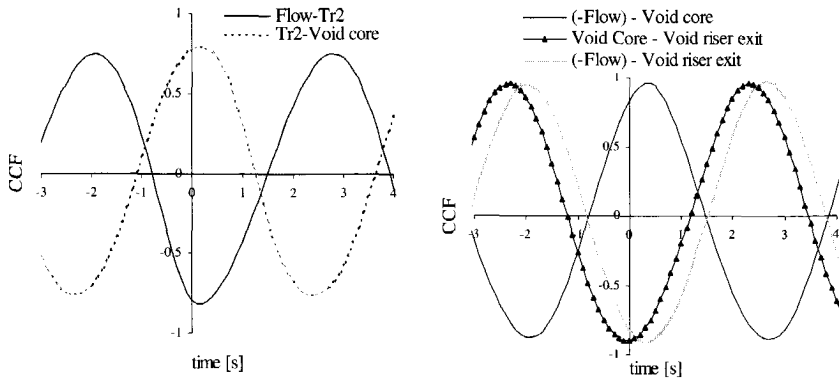
Figure 6.1: Left figure: the solid line, the CCF between the inlet-flow and the temperature (Tr2) oscillations measured at 10 cm elevation from the inlet, shows a minimum (negative correlation) while the dashed line, the CCF between the temperature and void-fraction oscillations (at 50 cm above the inlet), shows a maximum (positive correlation) for positive times. Right figure: CCFs obtained combining the inlet flow oscillations, riser-exit void-fraction oscillations and the void-fraction oscillations measured in the core (The negative of the flow signal was taken!). The time lag between the inlet-flow and riser-exit void-fraction oscillations is estimated to be around 2.6 s from the grey line.

On the left side of figure 6.1 the solid line shows the CCF between the inlet flow and the temperature at about 10 cm elevation above the inlet of the heated section (still in the single-phase region). One can see a negative correlation with a minimum of the CCF at about 0.1 s. This is plausible, since a positive inlet-flow perturbation triggers an enthalpy fluctuation with the opposite sign. The 0.1 s time lag is associated with the phase shift between the enthalpy oscillations at 10 cm height and the triggering flow oscillations at the inlet. The dashed line shows the CCF between the temperature and the void-fraction signal (this latter is measured in the two-phase region at about 50 cm above the inlet). Since the void-fraction oscillation has the same sign as the enthalpy perturbation it originates from, this CCF has a positive peak at about 0.2 s that corresponds to the phase shift between the void-fraction oscillations and the temperature (enthalpy) oscillations. The right side of figure 6.1 shows the CCFs obtained combining the inlet-flow signal, the riser-exit void-fraction signal and the void-fraction signal measured in the core. To eliminate the effect of opposite sign between inlet-flow and enthalpy oscillations and to facilitate the comparison of these CCFs, we took the negative of the flow signal (we do similarly in the rest of the section). The figure shows the considerable phase shift and consequently the large time lag between the inlet-flow fluctuations and the riser-exit void-fraction fluctuations. Taking the CCF between the void-fraction oscillations at the outlet of the system and the inlet-flow oscillations should be sufficient to estimate the time lag between them. However, in case of periodic signals one has to identify the cause-and-effect relations and the phase shift with care. Using two void-fraction signals obtained at different locations is helpful for this.

Two extensive series of measurements have been carried out at two different settings of the riser-exit flow resistance element with the friction factors $K_{r,e} = 122$ (Set I) and $K_{r,e} = 80$ (Set II), respectively. At both settings, diverse operating conditions have been chosen to cover a region of the operating plane as large as possible. For the DESIRE

No.	Set I		Set II	
	N_{Zu}	N_{sub}	N_{Zu}	N_{sub}
1	3.93±0.17	1.29±0.05	3.89±0.14	1.25±0.04
2	3.94±0.18	1.04±0.05	4.19±0.15	1.31±0.05
3	4.07±0.17	1.34±0.06	4.43±0.16	1.33±0.05
4	4.32±0.19	1.10±0.05	4.47±0.16	1.12±0.04
5	4.30±0.19	0.85±0.04	4.54±0.16	1.36±0.06
6	4.22±0.17	1.35±0.07	4.79±0.18	1.23±0.05
7	4.56±0.20	1.10±0.05	4.80±0.18	1.07±0.05
8	4.68±0.21	0.94±0.07	4.75±0.16	1.38±0.06
9	4.76±0.22	0.69±0.05	4.98±0.18	1.24±0.06
10	4.48±0.18	1.37±0.07	5.14±0.19	1.09±0.05
11	4.87±0.21	1.11±0.06	5.51±0.21	1.24±0.05
12	5.18±0.24	0.93±0.06	5.59±0.21	1.19±0.05
13	5.29±0.25	0.56±0.05		
14	5.23±0.23	1.14±0.06		
15	5.71±0.27	0.93±0.05		
16	5.80±0.28	0.65±0.05		
17	6.03±0.29	0.92±0.06		
18	6.03±0.30	0.64±0.05		
19	6.54±0.33	0.94±0.06		
20	6.62±0.33	0.62±0.07		

Table 6.1: Operating conditions for Set I and Set II. The numbers marking the measurements corresponds with those in Table 6.2 and Table 6.3.

facility this region is limited to relatively low subcoolings. The operating conditions are given for both measurement sets in Table 6.1.

First, we examine the results of a typical measurement (No. 3 in Table 6.1) of Set I in detail. The CCFs, shown in figure 6.2 are measured moving the lower gamma-transmission setup to different elevations while the facility is kept in the same operating condition. The figure shows a significantly increasing phase shift between inlet-flow oscillations and local void-fraction oscillations at increasing elevations in the core. This indicates a strong propagating (wave) character of the mixture-density (void-fraction) variations in the core. The same qualitative behavior is found practically in the whole measured operating region that is characterized with a relatively low inlet subcooling. This is in good qualitative agreement with the results of Ambrosini et al. (1998), who also found a strong propagating character of the density-waves at low-subcooling conditions.

There is, in general, a large time lag between the riser-inlet and riser-exit void-fraction oscillations. Due to the lack of void production in the unheated riser, the time lag between the riser-inlet and riser-exit void-fraction oscillations can be interpreted as the transit time of the void-fraction wave through the riser (pure propagation effect).

Table 6.2 and Table 6.3 contain the values of the oscillation period and the time lag between inlet-flow and riser-exit void-fraction oscillations for all the measurements in Set I and Set II, respectively. In both cases, we also compare the oscillation period with the estimated steady-state transit time of the fluid.
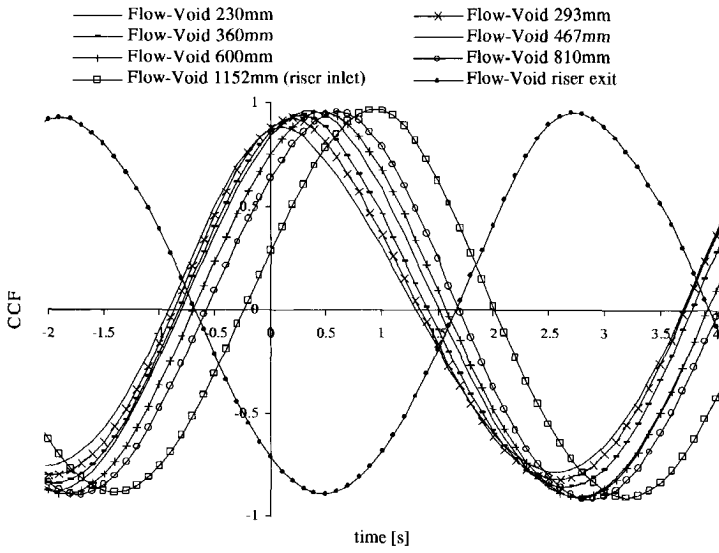
Figure 6.2: The curves from left to right are the CCFs between the inlet-flow and the void-fraction oscillations measured at increasing elevations (elevations are measured in mm's from the inlet of the heated section). The time lag between the inlet-flow oscillations and the void-fraction oscillations significantly increases with increasing elevation.

The steady-state transit time of the fluid is estimated from the operating conditions using the model of Rizwan-uddin (1994). The model is based on the assumption of incompressible single-phase flow and uses the homogeneous equilibrium model for the two-phase flow. It contains two integro-differential equations that are obtained by integrating the mass and energy balance equations along their characteristics to find the kinetic variables as a function of inlet velocity. Substituting the kinetic variables into the momentum equation, it is integrated along the total length of the system to get the equation for the total pressure drop. The dimensionless steady-state transit time for the single-phase region is given as:

$$\tau_{1-\phi} = \frac{N_{sub}}{N_{Zu}}. \tag{6.1}$$

For the two-phase region in the heated section it is given as

$$\tau_{2-\phi} = \frac{1}{N_{Zu}} ln(1 + N_{Zu} - N_{sub}) \tag{6.2}$$

Although it is not given in the paper of Rizwan-uddin (1994), one can derive the steady-state transit time for the riser section in a similar fashion as for the two-phase region in the heated section without taking heating into account. This transit time is given as

$$\tau_r = \frac{L_r^* A_r^*}{1 + N_{Zu} - N_{sub}} \tag{6.3}$$

No.	$T_{osc.period}$ [s] (measured)	$T_{time\ lag}$ [s] (measured)	$\frac{T_{osc.per}}{T_{time\ lag}}$	$T_{transit\ time}$ [s] (estimated)	$\frac{T_{osc.per}}{T_{trans}}$
1	4.88±0.06	2.70±0.05	1.81±0.06	3.54±0.20	1.38±0.05
2	4.55±0.05	2.50±0.05	1.82±0.06	3.31±0.19	1.37±0.05
3	4.76±0.06	2.70±0.05	1.76±0.05	3.33±0.18	1.43±0.05
4	4.55±0.05	2.80±0.05	1.63±0.05	3.15±0.17	1.45±0.05
5	4.36±0.05	2.40±0.05	1.82±0.06	2.93±0.15	1.49±0.04
6	4.66±0.05	2.60±0.05	1.79±0.06	3.10±0.17	1.50±0.04
7	4.45±0.05	2.60±0.05	1.71±0.05	2.94±0.15	1.51±0.04
8	4.36±0.05	2.30±0.05	1.89±0.06	2.84±0.16	1.54±0.04
9	4.18±0.04	2.30±0.05	1.82±0.06	2.66±0.14	1.57±0.04
10	4.55±0.05	2.60±0.05	1.75±0.05	2.93±0.15	1.55±0.04
11	4.36±0.05	2.70±0.05	1.61±0.05	2.77±0.14	1.57±0.04
12	4.27±0.04	2.70±0.05	1.58±0.05	2.68±0.14	1.59±0.04
13	4.10±0.04	2.10±0.05	1.95±0.07	2.45±0.12	1.67±0.04
14	4.27±0.04	2.70±0.05	1.58±0.05	2.65±0.13	1.61±0.04
15	4.18±0.04	3.00±0.05	1.39±0.04	2.56±0.12	1.63±0.04
16	4.10±0.04	2.90±0.05	1.41±0.04	2.40±0.11	1.71±0.03
17	4.18±0.04	3.00±0.05	1.39±0.04	2.50±0.13	1.67±0.04
18	4.02±0.04	2.90±0.05	1.38±0.04	2.34±0.11	1.71±0.03
19	4.10±0.04	3.00±0.05	1.37±0.04	2.40±0.12	1.71±0.04
20	4.10±0.04	2.90±0.05	1.41±0.04	2.24±0.14	1.83±0.04

Table 6.2: Ratio of the oscillation period and the time lag between inlet-flow and riser-exit void-fraction oscillations for measurement Set I. In the last column, the oscillation period is also compared to the steady-state transit time of the fluid estimated from the operating conditions using the model of Rizwan-uddin (1994).

No.	$T_{osc.period}$ [s] (measured)	$T_{time\ lag}$ [s] (measured)	$\frac{T_{osc.per}}{T_{time\ lag}}$	$T_{transit\ time}$ [s] (estimated)	$\frac{T_{osc.per}}{T_{trans}}$
1	3.94±0.04	2.30±0.05	1.71±0.05	2.87±0.14	1.37±0.04
2	3.86±0.04	2.50±0.05	1.55±0.05	2.76±0.13	1.40±0.04
3	3.79±0.04	2.40±0.05	1.58±0.05	2.62±0.13	1.45±0.04
4	3.59±0.03	2.30±0.05	1.56±0.05	2.48±0.11	1.45±0.04
5	3.66±0.03	2.20±0.05	1.66±0.05	2.50±0.11	1.46±0.04
6	3.59±0.03	2.30±0.05	1.56±0.05	2.43±0.12	1.48±0.04
7	3.47±0.03	2.20±0.05	1.58±0.05	2.34±0.11	1.48±0.04
8	3.59±0.03	2.10±0.05	1.71±0.06	2.38±0.11	1.51±0.04
9	3.53±0.03	2.20±0.05	1.61±0.05	2.33±0.11	1.52±0.04
10	3.47±0.03	2.20±0.05	1.58±0.05	2.24±0.10	1.55±0.03
11	3.47±0.03	2.10±0.05	1.65±0.05	2.24±0.10	1.55±0.04
12	3.47±0.03	2.20±0.05	1.58±0.05	2.21±0.10	1.57±0.03

Table 6.3: The results for measurement Set II.

The total steady-state transit time is $\tau_{1-\phi} + \tau_{2-\phi} + \tau_r$. The variables are made dimensionless as follows:

$$t^* = \frac{t}{L/v_{i,o}}, \; L_r^* = \frac{L_r}{L}, \; A_r^* = \frac{A_r}{A},$$

where L is length of the heated channel, A is the cross section and $v_{i,o}$ is the steady state velocity at the inlet of the heated section.

The uncertainty of the measured oscillation frequencies in Table 6.2 and Table 6.3 corresponds to the half of the frequency spacing of the Fourier spectrum of the oscillations. The uncertainty in the time lag between inlet-flow oscillations and riser-exit void-fraction oscillations is estimated as the half of the time spacing of the CCF. The uncertainty of the estimated transit time of the fluid stems from the uncertainties in the operating conditions, N_{Zu} and N_{sub}.
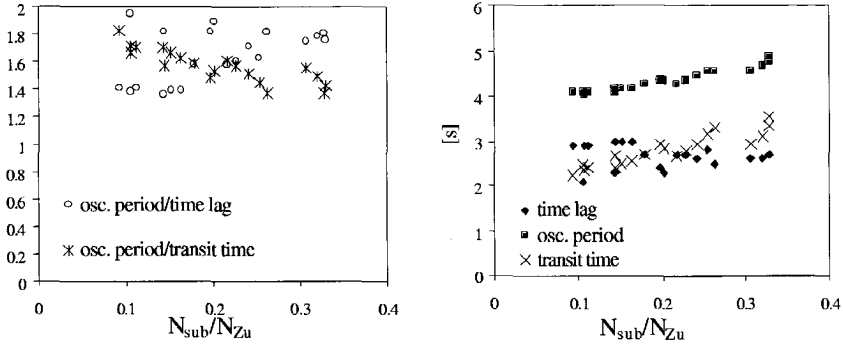
Figure 6.3: Ratios of the oscillation period and the time lag between inlet-flow and riser-exit void-fraction oscillations and the ratios of the oscillation period and the steady-state transit time for measurement Set I as a function of N_{sub}/N_{Zu} (left figure). The measured oscillation period and time lag and the estimated transit time of the fluid are compared in the right figure.
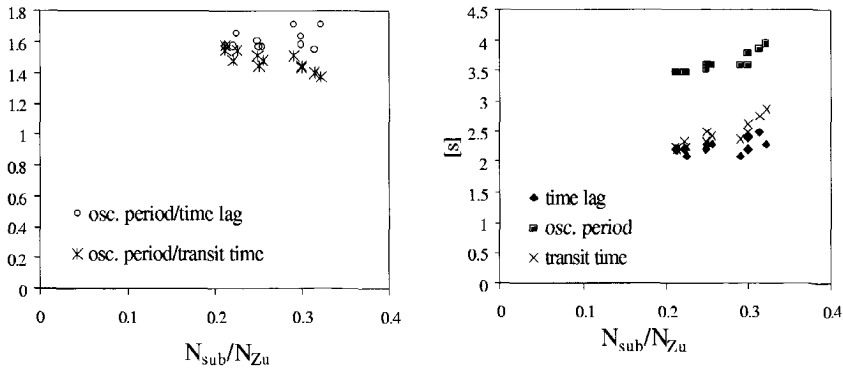
Figure 6.4: The results for measurement Set II plotted similarly as in figure 6.3.

The measured ratio of the oscillation period and the time lag between inlet-flow and riser-exit void-fraction oscillations varies from 1.35 to 1.95 for the different measurements. The ratio of the oscillation period and the estimated steady-state transit time of the fluid

varies between similar values (1.37 - 1.83). These latter values are in accordance with the results obtained by Ambrosini *et al.* (1998) in the low-subcooling operating region.

The results given in Table 6.2 and Table 6.3 are plotted in figure 6.3 and figure 6.4. All values are plotted there as a function of the ratio N_{sub}/N_{Zu}, which is just the dimensionless single-phase transit time and also equal to the dimensionless position of the boiling boundary (Rizwan-uddin, 1994).

The transit time increases with an increasing N_{sub}/N_{Zu} ratio, as it is also inferred from Eqs. 6.1 to 6.3, since the length of the lower velocity single-phase region increases relative to the higher velocity two-phase region. The measured oscillation period behaves similarly to the transit time. A trend of increasing can be seen for the time lag in case of Set II for increasing N_{sub}/N_{Zu} ratio as well. However, in case of Set I, the time lag shows a more complex behavior: at low N_{sub}/N_{Zu} ratios a significantly larger transit time is obtained for certain cases than for others measured at almost the same N_{sub}/N_{Zu} ratio. These points are measured at relatively higher power, therefore at relatively higher void fractions and for the higher riser-exit friction setting (Set I) as is indicated in figure 6.5 comparing the time lag and the transit time. Although the propagating character of the void fraction oscillations dominates, this figure shows that the measured time lag between inlet-flow and riser-exit oscillations can not be interpreted as a transit time of mixture-density waves propagating along the system. It is a complex dynamic variable of the system. To the author's knowledge there is no analytical model that can predict the behavior of the time lag between inlet-flow and riser-exit oscillations directly as a function of operating conditions. Its behavior could be examined using advanced thermal-hydraulic codes by simulating the measured density-wave oscillations.
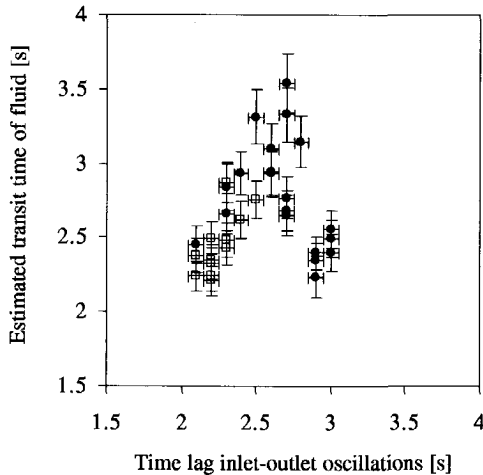
Figure 6.5: Comparison of the measured time lag between inlet-flow and riser-exit void-fraction oscillations with the estimated transit time of the fluid shows a complex relationship. The solid dots denote the results for Set I, the open squares those for Set II.

6.2.3   Summary

The characteristics of mixture-density variations during density-wave oscillations have been investigated experimentally using a natural-circulation, boiling, two-phase flow loop.

The void-fraction oscillations measured at different elevations along the system are correlated with the inlet-flow oscillations and a significantly increasing time lag has been found between them with increasing elevation. This indicates, in accordance with the results of previous numerical studies, that in the operating region with low inlet subcooling the mixture-density (void-fraction) oscillations exhibit a strong propagating character and the instantaneous variations in the local void production induced by inlet-flow oscillations seem to be less significant.

The oscillation period has been compared to the time lag between system outlet (riser-exit) void-fraction oscillations and the inlet-flow oscillations. Their ratio has been found between roughly one and a half to two. The steady-state transit time of the fluid has been estimated from the operating conditions using a model based on assuming homogeneous equilibrium two-phase flow. The oscillation period is also between one and a half to twice the estimated transit time for each measurement case. This is in agreement with previous findings.

The comparison of the estimated steady-state transit time of the fluid with the measured time lag between inlet-flow and riser-exit void-fraction oscillations shows a complex relation and that the time lag cannot be interpreted simply as the transit time of mixture-density waves propagating through the system. This is because density-wave oscillations involve a combination of variation in void propagation and variation in the local void production.

6.3 Nonlinear dynamics deep in the unstable region

The nonlinear dynamics of the natural-circulation two-phase flow is investigated further away from the SB, deep in the unstable operating region. Before starting to discuss the experimental results, we introduce shortly the so-called Feigenbaum scenario from the field of dynamics of nonlinear systems.

6.3.1 The Feigenbaum scenario

In this scenario, a cascade of successive period-doubling bifurcations takes place as a system parameter (the bifurcation parameter) is being varied in a nonlinear system and the aperiodic (chaotic) behavior starts off as the bifurcation parameter is varied past a critical value. At each period-doubling bifurcation, the period of the oscillation becomes twice as before and the number of different oscillation amplitudes is also doubled. This is accompanied by the appearance of successive subharmonics in the frequency spectrum of the oscillations. According to Feigenbaum's theory (Feigenbaum, 1980), this scenario possesses certain universal features that are independent of the actual form of the equations governing the dynamics of the nonlinear system. Namely, the ratio of successive increments (or decrements) in the bifurcation parameter at which the consecutive bifurcations occur approach asymptotically a universal number, the Feigenbaum-delta (δ). In other words, the sequence of consecutive bifurcation points converges asymptotically in a geometric manner with δ towards the limit of aperiodic behavior. The value of δ was found to be 4.6692... by mathematical models. Another universal scaling feature of this scenario is that the ratio of the amplitudes of the consecutive subharmonic components in the spectrum converges to: $\mu = 6.5573...$.

Since the discovery of the universality features of the period-doubling route towards chaotic behavior, this scenario has been observed experimentally in a broad variety of

small scale physical systems (Lauternborn *et al.*, 1997) including e.g. nonlinear electronic circuits (Linsay, 1981), Rayleigh-Bénard cells (Giglio *et al.*, 1981), optically bistable laser cavities (Gibbs *et al.*, 1981) and superfluid helium (Smith *et al.*, 1982). However, in large-scale physical, mechanical systems prone to high noise levels even the onset of the scenario (the first period-doubling) has not been reported. For example, although predicted with theoretical models by Clausse and Lahey (1991) and by Chang and Lahey (1997), it has not been observed yet in boiling two-phase flow systems. To the author's knowledge the results presented here are the first experimental observations of the Feigenbaum scenario in a large, boiling two-phase flow system.

6.3.2   Experimental observations

The experiments were carried out for different system pressures and for various distributions of the frictional pressure drops in single- and two-phase regions. The latter was achieved by varying the friction coefficient of an adjustable flow resistance element at the riser exit. The following procedure has been followed in all cases: starting from a stable operating condition, the heating power was gradually increased, in steps, while all other controllable system parameters were kept constant. At each power step a measurement was carried out after waiting long enough for the system to settle down to its asymptotic state. The following scenario has been observed in all cases with different system pressures and with various friction at the riser exit: as the power reaches the threshold of stability, the fixed point becomes unstable, undergoes a supercritical Hopf bifurcation and constant amplitude flow oscillations result. As the power reaches another critical value, the system undergoes a next bifurcation: a period-doubling bifurcation. At this point, oscillations with two different amplitudes and with a period twice the period of the original oscillations arise. These two bifurcations are the onset of the Feigenbaum scenario.

Representative oscillation patterns and the corresponding Fourier spectra for the onset of the Feigenbaum scenario measured at a system pressure of 11.6 bar are shown in figure 6.6a and figure 6.6b, respectively.

After the first period doubling, with a relatively small increase in the power, the system becomes chaotic in accordance with the universal scaling with δ. A representative chaotic oscillation pattern, recorded at 11.6 bar, and the corresponding spectrum are shown in figure 6.6c. The oscillation amplitude (maxima and minima) as a function of the power is shown in the bifurcation diagram of figure 6.7.

The finer details of the Feigenbaum scenario - the cascade of period-doubling bifurcations - could not be detected conclusively. Because of the relative large value of δ, the consecutive bifurcation points - after the first few period-doublings - cannot be distinguished from each other in terms of the bifurcation parameter due to the finite resolution of the measurement. Due to the scaling with μ, the amplitude of the successive subharmonics becomes very small for practical (measurement) purposes after a few period-doublings as well. Obviously, the presence of measurement noise diminishes further the possibility to identify subsequent bifurcations. The small spectral peaks corresponding to higher-order bifurcations disappear in the noisy background spectrum. Noise has in our two-phase flow system a very strong inherent source, namely boiling. Nevertheless, in all cases, a gradual and clear change can be observed in the measured oscillation patterns and in the corresponding spectra (a gradual broadening of the peaks and a peculiar increase in the broad-band background; see e.g. figure 6.6c) as the power is increased past the first period-doubling bifurcation point.
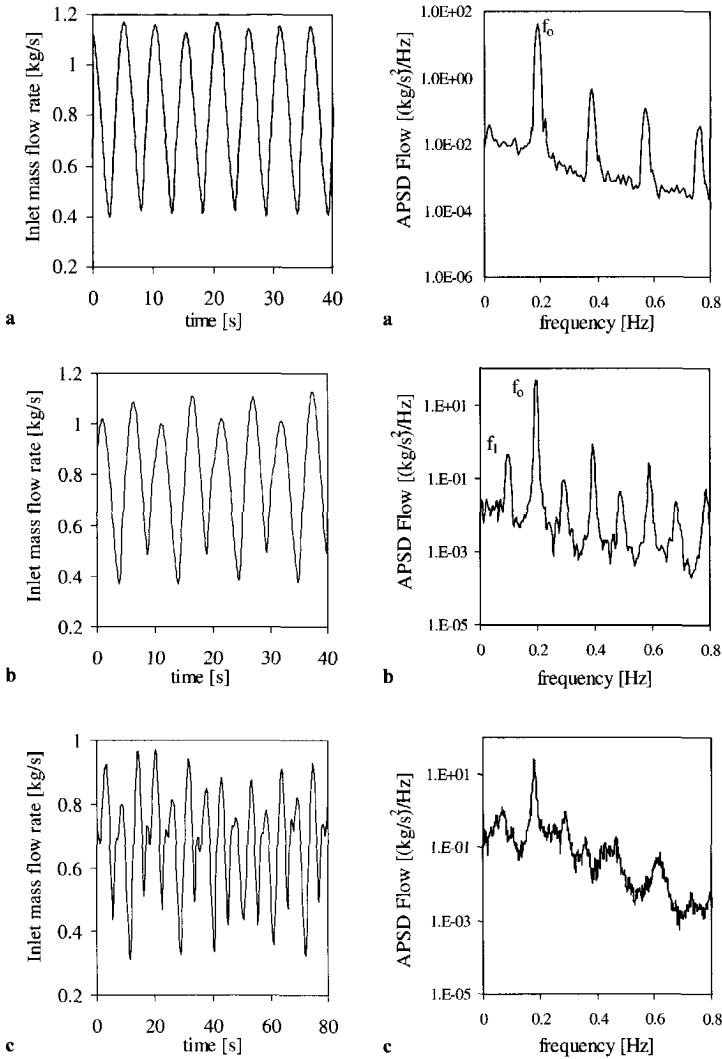
Figure 6.6: Inlet flow oscillation patterns and the corresponding APSD (Auto Power Spectral Density) for a system pressure of 11.6 bar and for a friction factor at the riser exit of 118 ± 18. a.) Beyond the threshold of stability (at 25.5 kW power). The appearance of numerous higher harmonic components in the APSD indicates the strongly nonlinear character of the oscillations. b.) Just beyond the first period- doubling point (at 28.4 kW power). The oscillation period is twice of that in a. Correspondingly, a halved frequency component (f_1, the first subharmonic) appears in the spectrum next to f_o. c.) Further beyond the first period-doubling bifurcation (at 32.3 kW power) the oscillations are chaotic.
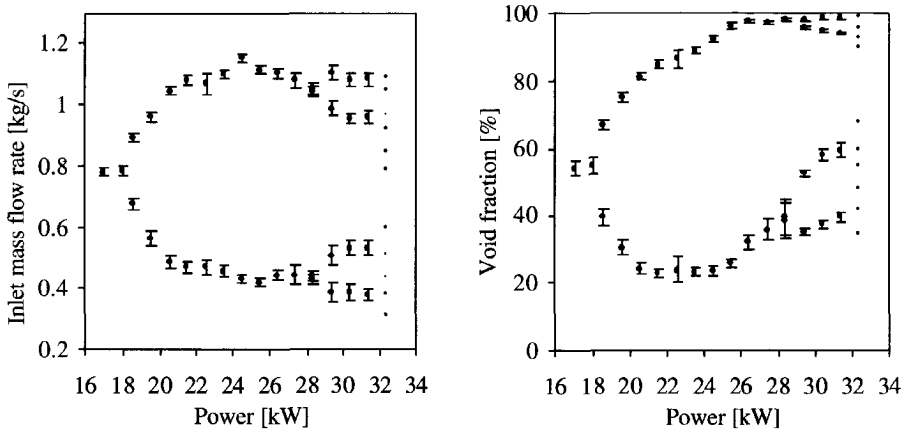
Figure 6.7: The bifurcation diagram shows the minima and maxima of the flow-rate and void-fraction oscillations as a function of power measured at a system pressure 11.6 bar and with a riser-exit friction factor of 118±18. Points at 32.3 kW show chaotic oscillations with random amplitudes

Series	Pressure [bar]	$K_{r,e}$ [-]	P_0 [kW]	P_1 [kW]	P_∞ [kW]	P_∞^{est} [kW]
1	11.6	118 ± 8	18.0 ± 0.3	27.4 ± 1.0	32.3	30.0 ± 1.3
2	8.4	145 ± 17	15.2 ± 0.3	24.6 ± 1.0	29.3	27.1 ± 1.4
3	11.2	145 ± 17	16.2 ± 0.5	n.a.	31.3	n.a.
4	12.2	110 ± 7	24.0 ± 0.4	38.2 ± 1.0	45.9	42.1 ± 1.4

Table 6.4: Critical values of heating power at the transition to oscillatory behavior (P_0), at the first period- doubling bifurcation (P_1) and for chaotic oscillations (P_∞). Also shown are the estimated threshold values for the transition to chaos (P_∞^{est}). Experimental conditions (pressure, riser-exit friction factor) are given in the table as well.

The effect of system pressure on the bifurcation sequence was studied by repeating the experiments for two different values of system pressure at the same riser-exit friction factor (series 2 and 3 in Table 6.4). However, period doubling in experiment series 3 could not be detected clearly and hence the effect of system pressure on the bifurcation sequence is not clear. The effect of changing the fraction of total pressure drop in the two-phase region was studied by varying the riser-exit friction factor while keeping the system pressure approximately constant (series 1 and 4). Decreasing the frictional pressure drop at the riser exit tends to increase the critical bifurcation values, and also tends to stretch the interval between the first bifurcation and the period-doubling bifurcation. Table 6.4 summarizes the experimental conditions: system pressure, riser-exit friction factor ($K_{r,e}$), the values of the power at the bifurcations points and the measured and estimated chaotic limit for each measurement series. The critical value of the power at the chaotic limit is estimated (assuming geometric convergence with δ) from the first two measured bifurcation points, the threshold of stability, P_0, and the value of the power at the first period-doubling bifurcation, P_1 as:

$$P_\infty^{est} = P_1 + \frac{P_1 - P_0}{\delta - 1} \tag{6.4}$$

The estimated values of the chaotic limit are somewhat lower than the observed chaotic limit (Table 6.4). The discrepancy is believed to be due to the fact that in reality the convergence is only asymptotically geometric. It should also be noted that the measured chaotic limits in Table 6.4 are not really accurate being actually the lowest power values at which chaotic signals are measured (see next section).

It is difficult to quantify the system behavior close to and in the chaotic region by only looking at the Fourier spectrum. Autoregressive (AR) based methods would not work better for these extremely nonlinear signals either, since they assume linearity and claim that all non-linearities have effects indistinguishable from noise. To qualify and quantify the system behavior in the presumed chaotic region, we apply special methods developed for nonlinear and chaotic time series analysis. The void-fraction and the mass flow rate signals measured at a power indicated in the P_∞ column in Table 6.4 are analyzed in the next section.

6.3.3   Nonlinear time series analysis

A vast literature exists on the different methods to detect and quantify chaos in measured time series (Eckmann and Ruelle, 1985; Grassberger *et al.*, 1991). To substantiate the overview of the methods that we use to analyze the measurements, first, the basic concepts of strange attractor and time delay embedding are introduced. The attractor is a subset of the state space of the dynamical system on which the system remains moving after the transients die out. It can be e.g. a fixed point or an attracting periodic orbit for a linearly stable or a periodic system. Because a chaotic system is aperiodic, the system's trajectory never settles to a point or a closed curve but it rather fills a subset of the state space in a complicated manner. This subset is also called a *strange attractor*. To map the attractor, we should measure all the system variables representing each state space dimension. In practice, however, one measures only a few well accessible system variables. To circumvent this problem, a basic technique was introduced: the *time-delay embedding* (Takens, 1981). This technique enables the reconstruction of the dynamics (the attractor) of a multidimensional system from a single measured variable of it. Given the measured time series $x(i)$ with i=1,..,N and sampling time τ, the reconstruction vectors of dimension d are formed as

$$\vec{X}(i) = [x(i), x(i+T), ..., x(i + (d-1)T)], \tag{6.5}$$

T and d being the time delay and the embedding dimension, respectively. The firm mathematical base of the method was formulated by Takens (1981). He showed that an embedding in $d = 2D + 1$ dimension (where D is the dimension of the attractor) captures completely the dynamics of the system.

All the algorithms introduced below, except for determining the Lyapunov exponent, are implemented in a menu driven software package RRCHAOS (Schouten and Van den Bleek, 1994). This package is used to evaluate chaos quantifiers for the different measurement series. Each algorithm in RRCHAOS starts with the reconstruction of the attractor using time-delay embedding. Schouten *et al.* (1994a) argue that the average cycle time of the oscillations, T_C, provides a robust and characteristic measure for the length of the embedding time window (i.e. $d \cdot T \cdot \tau$). The average cycle time is defined as

$$T_C = \frac{\text{length of time series [s]}}{(\text{number of crossings the average of the time series})/2}$$

They also suggest to choose the sampling frequency so that the embedding dimension, d - the number of sample points in one T_C - is at least of the order of 50-200 points per time window.

First, we perform a statistical test, which was developed to distinguish between possible deterministic chaos and colored random noise or more generally between nonlinear deterministic time series and linear stochastic time series.

Statistical test for non-linearities

The main idea behind most methods used to distinguish chaos from noise is to make use of the *short-term predictability* of chaotic signals. It is (in theory) impossible to predict the time evolution of a random signal. This short-term predictability is described by so-called characteristic exponents in a chaotic system (see Kolmogorov entropy and Lyapunov exponent below). These exponents measure the average rate of divergence or convergence of two initially close points on nearby orbits in the state space. For a random noise signal the rate of divergence is infinite corresponding to unpredictability. The analysis relies on the time-delay reconstruction of the system's attractor in state space and it assumes that the system is in stationary condition. The method uses a statistical test, which compares the measured time series with a linear, random surrogate time series that are created with the same autocorrelation coefficients as the original time series. This way the surrogate data series have the same spectral properties as the original signal (isospectral random signals). The test is a combination of the method proposed by Takens (1981) and by Kennel and Isabelle (1992). First an AR-model of the measured time series is composed according to

$$x_i^p = \sum_{j=1}^{k} a_j x_{i-j}, \tag{6.6}$$

where k is the order of the AR model. For these analyses k is taken typically 20. The coefficients a_j are estimated from the measured series using Burg's method. The noise, r_i is modelled as

$$r_i = x_i - x_i^p, \tag{6.7}$$

A random time series, w_i, is created by using the AR coefficients of the original series and the noise, r, chosen randomly from the set of residues r_i, as

$$w_i = r + \sum_{j=1}^{k} a_j w_{i-j}, \tag{6.8}$$

so it has the same spectral properties as the original signal. To compare the short-term predictability in the original, x_i, with that in the random series, w_i, the (exponential) growth of the interpoint distances are examined in the two series. A set of interpoint distances in the reconstructed state space are created by randomly choosing N_1 number of pairs that are closer than a certain distance. The distances between the reconstruction vectors are followed for a fixed amount of time T_{track}, and the distances at $t = T_{track}$ are gathered in set A. Set B is created by repeating the same for M number of surrogate data sets being N_2 distances collected in each of them (so the total number of elements in B is $N_3 = N_2 * M$). With sets A and B the Mann-Whitney rank-sum statistic is formed as

$$U = \sum_{i=1}^{N_1} \sum_{j=1}^{N_3} \Theta(A_i - B_i), \tag{6.9}$$

where Θ is the Heaviside operator. For large enough N_1, the quantity

$$Z = \frac{U - N_1 N_3/2}{\sqrt{\frac{1}{12} N_1 N_3 (N_1 + N_3 + 1)}}, \tag{6.10}$$

is normally distributed with zero mean and unit variance under the *null hypothesis* that both sets A and B come from the same distribution (which is only true when the original time series is linear stochastic). On the other hand, if the original series (set A) has short-time predictability originating from deterministic chaos, then the distances in set A are smaller than the distances in set B (short term predictability originating from randomness) in a statistically significant way and we will observe a Z-value smaller than zero. To disprove the null hypothesis at 99% confidence level a Z-value smaller than -3 is required.

Series	Power [kW]	Flow rate Z_{max}	Z_{min}	$<Z>$	Void fraction Z_{max}	Z_{min}	$<Z>$
1	32.3	-5.65	-8.62	-6.69	-5.64	-7.97	-6.92
2	29.3	-7.23	-10.89	-8.99	-6.45	-11.3	-9.7
3	31.3	-7.38	-13.9	-11.01	-9.06	-11.26	-9.86
4	45.9	-7.72	-8.98	-8.53	-6.95	-10.4	-8.32

Table 6.5: Results of the non-linearity test. A $< Z >$ value smaller than -3 indicates the presence of non-linearities and short term predictability.

The calculation of the Z-value defined in Eq. 6.10 is repeated ten times in the analysis with RRCHAOS using the same set A. The results, shown in Table 6.5 are the maximum, minimum and the average value of Z in each case. The considerably smaller values of $< Z >$ than -3 for both the void-fraction and flow signals show that there is a very high level of non-linearity and short-term predictability in the measured time series. It can also be considered as a sign of chaotic behavior. Although no general rule exists for that, some authors, e.g. Kennel and Isabelle (1992) and Van der Hagen *et al.* (1996), found that Z is around or smaller than -10 for chaotic systems.

The Kolmogorov entropy

The Kolmogorov entropy, K, characterizes the *dynamics* (time evolution) of chaotic behavior. One divides the state space into small cells and follows the time evolution of the system using a collection of initial conditions located all within one cell. After N time steps of length τ, the trajectories generally are already spread out over a large number of cells, the entropy S_N is calculated:

$$S_N = -\sum_r p_r ln p_r, \tag{6.11}$$

where p_r, is the probability (the relative frequency) that a trajectory is in cell r after N steps. The Kolmogorov entropy characterizes the rate of change in S_N

$$K_N = \frac{S_{N+1} - S_N}{\tau}. \tag{6.12}$$

The precise definition of K is the average of K_N over the whole attractor (as $N \to \infty$) in the limit of infinite small cells size and time steps ($\tau \to 0$). A more general definition can be found in Eckmann and Ruelle (1985). To illustrate the meaning of K, consider one of the most fundamental features of a chaotic system, the *divergence of nearby trajectories*. This manifests itself as an exponential separation of initially close trajectories as times goes on. As a result, two different initial conditions, that are not distinguishable (they are in the same cell) within a certain experimental precision, will evolve into distinguishable states (into separate cells) after a finite time. In this way, extra information about the state of the system is produced as it evolves. This process can also be interpreted as information loss, since the state of a single initial point specified with a certain accuracy will not be predictable after evolving for a finite time. The Kolmogorov entropy measures the rate of information loss (or gain) along the attractor. It is usually expressed in bits/seconds. A positive, finite K is considered as the conclusive proof that the time series and the underlying system are chaotic. K equal to zero represents a regular, cyclic or constant motion. An infinite K refers to a stochastic, random phenomenon.

The maximum-likelihood estimation of K as proposed by Schouten *et al.* (1994b) is used in this study. This has the advantage that the uncertainty of the entropy can be estimated easily. The essence of the method is as follows. According to Grassberger and Procaccia (1983b), the separation of nearby points on different orbits is exponential, and the time interval t_o required for two initially nearby points to separate by a distance larger than l_o will be exponentially distributed:

$$C(t_o) \sim e^{-Kt_o}. \tag{6.13}$$

This can be transformed into a discrete cumulative distribution function as

$$C(b) \sim e^{-Kb\tau}. \tag{6.14}$$

with b=1,2,3... and τ the sampling interval in the time series. The variable b is the number of sequential pairs of points on the attractor for which the interpoint distance is for the first time larger than l_o (given that the initial pair of points were within the distance l_o). For determining the distance of two reconstruction vectors the maximum norm is used. The probability of finding a distance larger than l_o after exactly b interpoint distances is

$$p(b) = C(b-1) - C(b). \tag{6.15}$$

Using this probability distribution of b, a maximum-likelihood estimation of K can be derived. The probability of finding exactly the sample $(b_1, b_2, b_3, ..., b_M)$, depending on K, from a random drawing of M pairs of independent points on the attractor, is

$$p_K = P(b_1, b_2, ..., b_M; K) = \prod_{i=1}^{M} p(b_i). \tag{6.16}$$

Applying the maximum-likelihood method for this probability distribution as a function of K one can find a maximum-likelihood estimation of K as (Schouten *et al.*, 1994b):

$$K_{ML} = -\frac{1}{\tau} ln(1 - \frac{1}{\bar{b}}), \tag{6.17}$$

with

$$\bar{b} = \frac{1}{M} \sum_{i=1}^{M} b_i,$$ (6.18)

which is the average value of the b's in the sample $(b_1, b_2, b_3, ..., b_M)$, with sample size M. The relative standard deviation of K_{ML} is approximately proportional to $1/M$ (Schouten *et al.*, 1994b). Thus, requiring a certain accuracy for K_{ML}, the necessary number M of samples of b's (the number of initially close point pairs for which t_o should be evaluated from the time series) can be determined.

Figure 6.8: The influence of the choice of the embedding time window (normalized with T_C) on the estimated Kolmogorov entropy for Series 4 (left figure). The influence of the choice of l_o (normalized with the average absolute deviation of the time series) on K_{ML} for Series 2 (right figure).

First, the influence of the embedding time window (embedding dimension) on the estimation of K_{ML} is examined and the results are shown in figure 6.8a. For embedding windows larger than two cycle time, the estimated K_{ML} is independent of the embedding time window. Generally, it is expected that the quantifiers of the reconstructed attractor does not change as a function of the size of the embedding window once the window size necessary to accommodate the attractor is reached (Hilborn, 1994). Choosing the embedding window as twice the cycle time seems to be correct for the entropy estimation.

Figure 6.8b shows the influence of the choice of l_o on K_{ML}. The figure shows that lowering l_o at small $l'_o s$ increases the entropy estimate significantly. According to Eq. 6.17, K_{ML} depends only on the average value of time steps, that is needed for an initially small interpoint distance to grow larger than l_o, i.e. on $\bar{b}$. If there is an approximately constant rate at which the interpoint distances grow on the attractor (see also the Lyapunov exponents), then the smaller l_o is chosen, the smaller $\bar{b}$ is. This results in a larger entropy estimate. On the other hand, for increasing l_o, K_{ML} slowly drops. Using the same argument, increasing l_o will result in a larger $\bar{b}$ and, in turn, a smaller K_{ML}. Choosing l_o around unity seems to be a good compromise between the two extremes.

Using the above values of the embedding window and l_o, the K_{ML} values evaluated for the different measurement in the four experimental series are summarized in Table 6.6.

Series	Power	Void fraction K_{ML}	Rel. st.dev.	Flow rate K_{ML}	Rel. st. dev.
	[kW]	[bits/sec]	[%]	[bits/sec]	[%]
1	32.3	0.256	0.96	0.211	0.94
2	29.3	0.127	0.93	0.139	0.93
3	31.3	0.044	0.93	0.049	0.91
4	45.9	0.189	0.94	0.116	0.89

Table 6.6: Maximum-likelihood estimation of the Kolmogorov entropy (K_{ML}).

The positive values of the estimated Kolmogorov entropy confirm that the system behavior is chaotic.

The correlation dimension

The correlation dimension is a *geometric* type of chaos quantifier. It emphasizes the geometric nature of the trajectories in state space and it is closely related to the concept of fractals. The correlation dimension was proposed by Grassberger and Procaccia (1983a) based on the behavior of the so-called correlation sum. If one lets the system trajectory evolve for a longer time and collects N trajectory points, then the *correlation sum* is defined as

$$C(R) = \frac{1}{N(N-1)} \sum_{i=1}^{N} \sum_{j=1, i \neq j}^{N} \Theta(R - |x_i - x_j|), \qquad (6.19)$$

where Θ is the Heaviside function. The correlation sum, $C(R)$, gives the relative number of trajectory points in the state space that are within a distance R from each other. If R is about the size of the attractor, then $C(R) \rightarrow 1$. If R is smaller than the smallest distance between the trajectory points, then $C(R) = 0$. The correlation dimension, D_C, is defined to be the number that satisfies

$$C(R) = \lim_{R \to 0} k R^{D_C}. \qquad (6.20)$$

or equivalently

$$D_C = \lim_{R \to 0} \frac{\log C(R)}{\log R}. \qquad (6.21)$$

D_C is also called scaling index since $C(R)$ scales with it as a function of R. This generalized dimension definition can give dimensionalities that are not integers for special objects, which are called fractals. Fractals play an important role in the dynamics of chaotic systems since a strange attractor, per definition, has a non-integer dimension.

Generally, measurement noise induces a bias in the observed distances of trajectories and corrupts the scaling behavior expressed in Eq. 6.21. To calculate D_C, we use the method proposed by Schouten *et al.* (1994a) for the case of noisy attractors. This method can disentangle the dimension of the underlying (uncorrupted) attractor by rescaling the correlation integral assuming a noise strictly bounded in amplitude. The scheme of the procedure is as follows. One must embed the time series, then choose randomly point pairs $(\vec{Z}_i, \vec{Z}_j)$ from the reconstructed attractor. The kth component of the vector $\vec{Z}_i$ is $z_{i,k} = x_{i,k} + \delta x_{i,k}$, where $x_{i,k}$'s are the components of the uncorrupted (noise free) vector and $-\delta x_{max}/2 \leq \delta x_{i,k} \leq +\delta x_{max}/2$ is the bounded noise component. An upper

limit for the scaling distance should be chosen, note it by l_o (l_o is chosen as the average absolute deviation of the time series following Schouten *et al.* (1994a)). The maximum-norm distance, l_z, between $\vec{Z}_i$ and $\vec{Z}_j$ is determined for each pair and a histogram of the number of pairs with $l_z \leq l_o$ is created. Due to the usage of the maximum norm the corrupted distance $l_z = l_x + l_n$, where l_x is the noise free distance and $l_n = \delta x_{max}$ the maximum noise distance. Then the corrupted l_z distances are rescaled in order to let the correlation integral obey the power scaling law. For the noise free distance: $C(l_x) \sim l_x^{D_C}$, then we can write that

$$C(l_z | l_z > l_n) \sim (l_z - l_n)^{D_C}, \tag{6.22}$$

because $l_x = l_z - l_n$. With the requirements that $C(l_z \leq l_n) = 0$ and $C(l_z = l_o) = 1$ one obtains that

$$C(l_z) = \left(\frac{l_z - l_n}{l_o - l_n}\right)^{D_C}, l_n \leq l_z \leq l_o. \tag{6.23}$$

Then all the distances are normalized with respect to l_o, using $r = l_z/l_o$ and $r_n = l_n/l_o$ from which it follows that

$$C(r) = \left(\frac{r - r_n}{1 - r_n}\right)^{D_C}, r_n \leq r \leq 1. \tag{6.24}$$

Thus, calculating the normalized cumulative histogram from the aforementioned histogram of number of the experimental point pairs with distance $l_z \leq l_o$, one gets the correlation integral $C(r)$. Applying a nonlinear least-squares fit to this in the form of Eq. 6.24, the correlation dimension, D_C, and the minimum scaling length (maximum noise level), r_n, are estimated.

We examined the influence of the choice of the embedding parameters and the maximal scaling distance, l_o, on the estimated correlation dimension. Examples of it are shown in figure 6.9. For normalized embedding windows larger than 1.5 - 2, the value of D_C, apart from small deviations, does not change as function of the embedding time window. This is consistent with the results obtained for the Kolmogorov entropy (see above).

For $l_o's$ larger than about 0.6-0.7 times the average deviation D_C becomes practically independent of the value of l_o. For lower values of l_o, the correlation dimension estimates are becoming higher. As l_o approaches the noise level (the scaling region decreases), the influence of the noise on the $C(r)$ distribution function and on dimension estimation obtained from it increases (especially if the noise is in reality not bounded in amplitude in contrast to the assumption in the method). The random measurement noise tends to make the trajectories spread out more uniformly in the state space and thus increases the estimated dimension.

The correlation dimensions for the four measurement series are given in Table 6.7 evaluated using the same embedding window as for the Kolmogorov entropy in Table 6.6.

The estimated dimension of the attractor varies around 1.4 -1.8 in almost all of the cases, which indicates low-dimensional chaotic behavior. The estimated noise levels (r_n) are relatively high, about 20% of the average absolute deviation. In Schouten *et al.* (1994a), it is pointed out that at such noise levels the rescaled correlation integral might underestimate the real dimension.
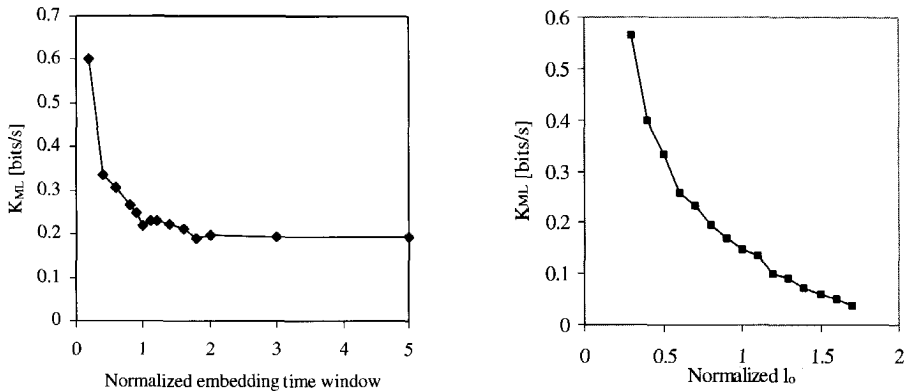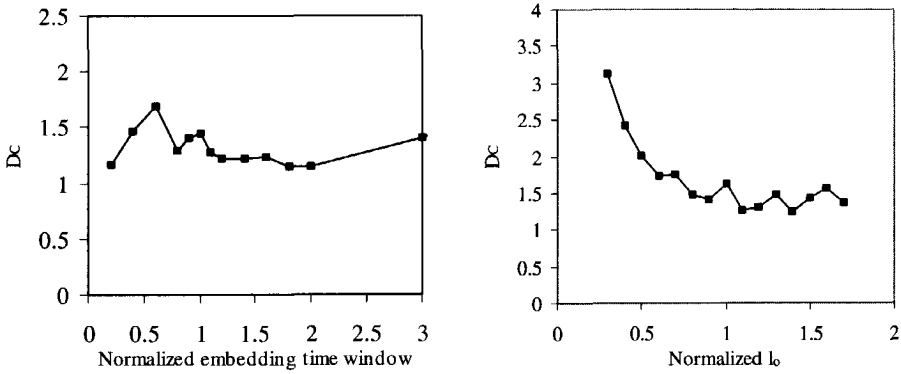
Figure 6.9: The influence of the choice of the embedding time window (normalized with T_C) on the correlation dimension for Series 4 (left figure). The influence of the choice of l_o (normalized with the average absolute deviation of the time series) on D_C for Series2 (right figure).

		Void fraction		Flow rate	
Series	Power [kW]	D_C	r_n	D_C	r_n
1	32.3	1.738	0.158	1.796	0.206
2	29.3	1.746	0.273	1.831	0.242
3	31.3	1.576	0.287	1.615	0.194
4	45.9	1.203	0.345	1.405	0.301

Table 6.7: The estimated values of the correlation dimension and the noise level.

The Lyapunov exponents

The Lyapunov exponents measure the average exponential rate of divergence or convergence of nearby orbits in state space. It is very closely related to the Kolmogorov entropy. Any system containing at least one positive Lyapunov exponent is defined to be chaotic and the magnitude of the exponent reflects the time scale on which system dynamics become unpredictable (loss of information). Given a dynamical system in a n-dimensional state space, one monitors the time evolution of an infinitesimal n-sphere. After time t it will be transformed to an n-ellipsoid with principal axes $p_i(t)$. The ith Lyapunov exponent is defined in terms of $p_i(t)$ as

$$\lambda_i = \lim_{t \to \infty} \frac{1}{t} \log_2 \frac{p_i(t)}{p(0)}. \tag{6.25}$$

Thus, the Lyapunov exponents are related to the expanding and contracting nature of different directions in state space. Motion on a periodic attractor results in a zero largest Lyapunov exponent corresponding to the neither converging nor diverging nature of the motion. For a stable fixed point, all the Lyapunov exponents are negative. Similar to the Kolmogorov entropy, the units of Lyapunov exponents are bits/sec. It should be noted here, that there is a mathematical theory for differentiable map functions (Packard et al., 1980), which establishes the relation between the Kolmogorov entropy and the Lyapunov exponents stating that $K \leq \sum_i positive \lambda_i$. This result is believed to be true for continuous

Series	Power [kW]	Void fraction λ [bits/sec]	St. dev. [bit/sec]	Flow rate λ [bits/sec]	St. dev. [bit/sec]
1	32.3	0.71	0.44	0.74	0.50
2	29.3	0.05	0.19	0.16	0.29
3	31.3	0.03	0.12	0.11	0.21
4	45.9	0.06	0.21	0.13	0.27

Table 6.8: The estimated values of the largest Lyapunov exponent using the algorithm in Wolf *et al.* (1985).

systems as well (Packard *et al.*, 1980). This means that a positive Kolmogorov entropy indicates the existence of at least one positive Lyapunov exponent.

The method of Wolf *et al.* (1985) is be used to extract the largest Lyapunov exponents from the measured time series. The straightforward idea of the method is to follow the evolution of two points on nearby orbits of the reconstructed attractor. The nearest neighbor (in the Euclidean sense) of the first point of the embedded time series is located first. These two points can be considered to define the early state of the first principal axis. Denote the distance of the initial points by $L(t_o)$. At time t_1, this distance increases to $L(t_1)$ as the two points evolve along their trajectories. As the separation between the two points becomes large, the algorithm applies a simple replacement of the second point, which attempts to preserve orientation and minimizes the distance between the evolved first point and the replacement point. In this way one monitors the evolution of a single principal axis vector. From this evolution a Lyapunov exponent is estimated at each replacement. The evolution+replacement procedure is repeated until the end of the time series is reached. Then the set of estimated Lyapunov exponents is averaged to get

$$\lambda_1 = \frac{1}{t_M - t_o} \sum_{k=1}^{M} \log_2 \frac{L(t_k)}{L(t_{k-1})}, \qquad (6.26)$$

where M is the total number of replacement steps. The idea behind preserving the orientation at replacement is that one keeps following the evolution of the principal axis always in an expanding direction. For this reason, the angle between the replacement point and the replaced point is minimized.

In the algorithm proposed by Wolf *et al.* (1985), the evolution time $t_k - t_{k-1}$ is chosen to be constant, so that only the small scale attractor structure is examined. This is because for bounded attractors, the distance L cannot grow unlimited. If the evolution time is chosen to be too long, L can even shrink as the two trajectories pass a folding region of the attractor. This would lead to an underestimation of λ_1. The evolution time is chosen, taking into account this effect, somewhat less than half of the average cycle time. The values for the largest Lyapunov exponent obtained by the above method are summarized in Table 6.8.

The largest Lyapunov exponents are estimated to be around 0.05 for the void-fraction signal and 0.12-16 for the flow signal except for Series 1, where it is considerably larger. The standard deviations are usually two-to-three times larger than the estimated exponents themselves (again, except for Series 1). This shows that the algorithm, although appealing for its simplicity, does not work really well in our case. The method is for example not robust against the influence of measurement noise. However, the most severe

Series	Power [kW]	Void fraction λ [bits/sec]	St. dev. [bit/sec]	Flow rate λ [bit/sec]	St. dev. [bit/sec]
1	32.3	0.23	0.13	0.21	0.12
2	29.3	0.33	0.25	0.30	0.29
3	31.3	0.29	0.19	0.25	0.21
4	45.9	0.36	0.24	0.26	0.18

Table 6.9: The estimated values of the largest Lyapunov exponent using the modified algorithm.

handicap is presumably the constant evolution time that might make the method 'stiff'. Depending on the position on the attractor, a fixed evolution can be sometimes so long that one passes from a expanding region to a folding region of the attractor, which results in underestimation or even negative exponent estimates. On the other hand, choosing the evolution time short increases the necessary number of replacement steps, which can lead more frequently to the loss of following the direction of expansion or to the accumulation of small errors in the direction at replacement steps. The orientation is usually preserved at replacement within a certain limit, however, if no possible replacement point is found, then this constraint is automatically loosened in the algorithm.

A quite straightforward modification of the algorithm in order to try to circumvent the above problems is to use variable evolution times. The variable evolution time is determined in the following way: after each replacement we follow the evolution of the distance between the two trajectories until it start to decrease. At that point, the next replacement step follows. In this way, one always follows the trajectories in the stretching region of the attractor and the necessary number of replacement steps is decreased as well. To reduce the effect of noise, we reject in the calculation of the Lyapunov exponent those evolutions that are shorter than a few time steps (thus, probably only due to noise). The largest Lyapunov exponents estimated with the modified algorithm are summarized in Table 6.9. The results are considerably improved compared to the ones obtained with the original algorithm. The exponent estimates are increased (except for series 1), while their (relative) standard deviations are significantly decreased.

More sophisticated methods, as proposed by Sano and Sawada (1985) and by Eckmann et al. (1986) examining the growth of the tangent vectors in the tangent space of the original trajectories, could also be used to improve the results. Moreover, those methods are capable of predicting all the positive Lyapunov exponents of the system.

6.3.4   Summary

The nonlinear dynamics of natural-circulation two-phase flow has been investigated. It is found that the two-phase flow undergoes, first, a supercritical Hopf bifurcation at the threshold of linear stability, followed by a period-doubling bifurcation as the heating power is increased. The finer details of the well-known Feigenbaum scenario, i.e. the cascade of period-doubling bifurcations, could not be detected presumably due to the presence of strong experimental noise. The oscillations, detected further on after the first period-doubling point, exhibit a peculiar, chaos-like behavior. To analyze those measurements, nonlinear time sequence analysis methods were applied. A statistical test shows that there is a strong short-term predictability and non-linearity in the time series with possible

chaotic behavior.

Quantifier:	K_{ML} [bit/sec]	D_C -	λ [bit/sec]
Void fraction	0.256	1.738	0.23
Flow rate	0.211	1.796	0.21

Table 6.10: Summarizing the three different chaos quantifiers found for measurement at 32.3 kW in Series 1. The values are typical of a system exhibiting low-dimensional chaotic behavior.

Several types of chaos quantifiers have been determined for the different measurement series including the Kolmogorov entropy, the largest Ljapunov exponent and the correlation dimension of the attractor. To find the correct embedding parameters the influence of the embedding window is examined on the estimated Kolmogorov entropy and correlation dimension. For both cases, it was found that choosing the embedding time window as about twice the average cycle time or larger the attractor is reconstructed correctly. The estimated values of the quantifiers obtained by using these embedding parameters are summarized for the measurement in Series 1 in Table 6.10. They indicate, just as in case of the other measurement series, low-dimensional chaotic behavior.

Chapter 7

Experiments on the neutronic-thermalhydraulic stability

7.1   Introduction

To be able to develop reliable BWR stability models and codes, extensive experimental databases for code validation are inevitably needed. In spite of this, considerable more work has been devoted to modelling of BWR stability than to experimental studies. Experimental activities are limited to a few reactor tests and event records (D'Auria *et al.*, 1997). This is mainly because experimental possibilities on BWRs are quite restricted. Valuable experimental data can be gathered by using thermal-hydraulic facilities, however, these all lack the neutronic feedback. This problem can be solved by providing a thermal-hydraulic facility with a simulated neutronic feedback (Rao *et al.*, 1996; Kok and Van der Hagen, 1999). Such a hybrid system that is flexible and comprises the most important physics of a real BWR, enables the investigations of coupled neutronic-thermalhydraulic stability. The idea behind this type of hybrid facilities with real thermalhydraulics and simulated neutronics is that the difficulty and uncertainty of modelling the thermalhydraulics is much larger than of the neutronics. The opposite and probably less feasible approach has been reported by Turso *et al.* (1995) using a university research reactor coupled with a reduced-order model for the thermalhydraulics. The calculated void reactivity effect of the thermalhydraulics was realized by control rod movements. The underlying thermal-hydraulic model was improved later to account better for the two-phase flow phenomena (Huang and Edwards, 2000). Recently, the same authors proposed the coupling of a two-phase flow loop with a research reactor in order to minimize the need for computer simulation (Edwards *et al.*, 2000).

The DESIRE natural-circulation two-phase flow facility has been extended with simulated neutronics (Kok and Van der Hagen, 1999). The void-reactivity feedback simulation is implemented in the form of a digital controller (DC) on a PC. The DC controls the power of the electrically heated rods based on the simulated reactivity effect of the measured void-fraction fluctuations. The flexible design of the digital controller allows to study BWR dynamics with the possibility to vary the fuel time constant and other reactor physical parameters like the void-reactivity coefficient, the delayed-neutron fraction and decay constant (e.g. important for predicting the influence of using MOX fuel). These parameters can all be given to the simulation as input.

The details of implementation of the void-feedback simulation are described in Kok and Van der Hagen (1999). The most crucial point in the simulation of the void-reactivity

feedback is the reconstruction of the average void fraction in the heated assembly. This reconstruction is based on a quite simplified approach with several assumptions (see section 7.3). Presumably due to these strong simplifying assumptions, the first test measurements with the simulated feedback gave results contradictory to those of the reduced-order model of Van Bragt and Van der Hagen (1998a); even qualitative agreement was not found at all (Kok, 1998). The reduced-order model is not suitable for quantitative comparison with measurements, however, it predicts the stability trends qualitatively well (as is shown in Chapter 4). Therefore the void-reactivity feedback simulation needs to be improved. In the following, the theoretical background of the void-reactivity feedback simulation is given. Thereafter, the improvements in the feedback simulation and the measurement results obtained with the improved system are presented.

7.2   Theoretical background

A brief overview of the theoretical background of the void-reactivity feedback simulation is given here. The simulation is based on the well-known point-kinetic equations to describe the dynamics of the neutron population in the reactor (Ott and Neuhold, 1985):

$$\frac{dn(t)}{dt} = \frac{\rho(t) - \beta}{\Lambda}n(t) + \sum_{i=1}^{6}\lambda_i c_i(t) \tag{7.1}$$

and

$$\frac{dc_i(t)}{dt} = \frac{\beta_i}{\Lambda}n(t) - \lambda_i c_i(t), \quad (i = 1, .., 6), \tag{7.2}$$

where the symbols have their usual meaning.

Generally, point kinetics is a good approximation for reactor dynamics when the spatial flux shape does not vary strongly as a function of time. This is the case for small, tightly coupled reactor cores, or for transient situations in large reactors that involve fairly uniform perturbations throughout the core. The latter one is practically true for in-phase oscillations in BWRs. We assume small variations in the reactor properties (cross sections) around the equilibrium values at which the reactor is critical. Then the reactivity changes are given with respect to a critical reactor using a first-order approximation as (Ott and Neuhold, 1985)

$$\delta\rho = \frac{<\phi^+|(\delta\widehat{P} - \delta\widehat{D})\phi_o>}{<\phi^+|\widehat{P}_o\phi_o>}, \tag{7.3}$$

where $\widehat{P}$ is the production operator, $\widehat{D}$ is the destruction operator and the subscript o denotes the equilibrium (critical reactor) state. The actual form of these operators depends on whether the transport equation or one of its diffusion approximations is used for deriving the point-kinetic equations. The $<|>$ scalar product is defined as:

$$< f|g >= \int fg d\mathbf{x},$$

where $\mathbf{x}$ denotes all the phase space variables. The function ϕ^+ appearing in Eq. 7.3 is a weighting function and ϕ_o is the critical flux shape:

$$\widehat{P}_o\phi_o = \widehat{D}_o\phi_o, \tag{7.4}$$

The solution of the point-kinetic equations is particularly sensitive to uncertainties in the reactivity. Therefore, it is desired to choose the ϕ^+ weighting function so that

one gets an optimal estimation of the reactivity. It can be shown that using the static adjoint function as weighting function, Eq. 7.3 for the reactivity is stationary (Ott and Neuhold, 1985). It means that first-order errors in the flux result only in second-order uncertainties in the reactivity. The static adjoint function, ϕ_o^+, is defined to satisfy the adjoint to Eq. 7.4:

$$\widehat{P_o^+}\phi_o^+ = \widehat{D_o^+}\phi_o^+. \tag{7.5}$$

For the physical meaning of the adjoint function we refer to the book of Ott and Neuhold (1985).

We simplify the treatment by applying one energy group diffusion approximation, for which the flux is self-adjoint. The two feedback effects that give rise to reactivity variations in a BWR are the variations in fuel temperature (Doppler effect) and in the moderator void fraction. Confining our attention only to the void reactivity variations Eq. 7.3 can be written as (Ott and Neuhold, 1985):

$$\delta\rho_\alpha(t) = \frac{\int_V (\nu\delta\Sigma_f - \delta\Sigma_a)\phi_o^2 - \delta D(\nabla\phi_o)^2 dV}{\int_V \nu\Sigma_f\phi_o^2 dV}, \tag{7.6}$$

where Σ_f, Σ_a and D are the one-group fission, the one-group absorption cross sections and the diffusion coefficient, respectively. We ignore the leakage term in Eq. 7.6, which is reasonable approximation. Using a one-dimensional, axial, model of the reactor and assuming small variations in the cross sections around the equilibrium value, i.e. assuming a linear dependence on the variations in the void fraction, the void-reactivity variation is given as:

$$\delta\rho_\alpha(t) = C \int_0^{L_C} \phi_o^2(z)\delta\alpha(z,t)dz, \tag{7.7}$$

where C is a constant of proportionality.

7.3 Improving the void-reactivity feedback simulation

Eq. 7.7 is taken as a basis to calculate the void reactivity for the simulation. The Doppler-reactivity effect is not simulated. Since flat-profile heater rods are installed in DESIRE, we do not apply the flux shape weighting for the void-reactivity calculation in the measurements reported here. However, it is quite straightforward to add the flux shape weighting for non-flat profiles (e.g. for chopped-cosine) to the methods introduced below. Eq. 7.7 shows that to calculate the reactivity the time evolution of the axial void-fraction profile must be known. Concerning the feedback simulation in the DESIRE facility, it means that the axial void-fraction distribution in the heated part must be measured real time. If the local void fraction is simultaneously measured at different heights using e.g. several gamma-transmission set-ups, the axial void-fraction profile could be approximated. However, this is practically not feasible. Reconstructing the void-fraction profile from fewer local measurements using some assumptions is a practical alternative.

This approach was chosen by Kok and Van der Hagen (1999), measuring the local void fraction at a certain height by gamma-transmission technique. It was converted to quality using the HEM model:

$$\chi(z_{mes}, t) = \frac{1}{\frac{1}{\alpha(z_{mes},t)}\frac{\rho_l}{\rho_g} + (1 - \frac{\rho_l}{\rho_g})}, \tag{7.8}$$

where z_{mes} is the elevation of the void measurement. They applied a quasi-static approximation for the thermodynamic equilibrium quality $(\chi(z,t))$ assuming a linear axial

quality profile. The linear quality profile is calculated at each time instant from the measured local quality and the channel-inlet quality as:

$$\chi(z,t) = \frac{\chi(z_{mes,t}) - \chi_{C,i}}{z_{mes}} z + \chi_{C,i}. \tag{7.9}$$

From the quality profile the core-averaged void fraction was calculated, then multiplied by the void-reactivity coefficient to obtain the void reactivity (no flux shape weighting was used). This quasi-static approach is a quite rough approximation of the actual, wavy character of the void production and propagation in DESIRE (see Chapter 6). There is both a considerable magnitude and phase difference between the actual core-average void fraction and the one obtained by the linear, quasi-static approximation.

To improve the void-fraction profile reconstruction, we introduce six methods in the following.

The quality profile method

In this method, we apply a polynomial expansion of the axial quality profile up to a second-degree approximation. For this, we use two gamma setups and measure the void fraction at two elevations simultaneously. These are converted to quality values using the HEM model and together with the measured instantaneous value of the core-inlet temperature (quality) are used to obtain a quadratic polynomial approximation of $\chi(z,t)$ in the from:

$$\chi(z,t) = a_0(t) + a_1(t)z + a_2(t)z^2, \tag{7.10}$$

where the parameters a_0, a_1 and a_2 are determined at each sampling instant using Eq. 7.10. A quadratic quality profile with time dependent coefficients has also been used in a reduced-order BWR model by Karve et al. (1994). They compared stability maps obtained using linear and quadratic quality profiles with the exact solution and showed that using a quadratic profile instead of a linear profile considerably improves the results. A similar conclusion was drawn by Shanathanan (1964), who developed a BWR model applying an expansion of $\alpha(z,t)$ in a series of orthogonal functions (Legendre polynomials) of the axial position with time dependent coefficients similarly to Eq. 7.10. He concluded that changing from a first-degree to a second-degree approximation in the expansion has the largest influence on the results. Applying higher-degree approximations increases the calculational labor considerably, however, the results do not change significantly. Based on these numerical results, we expect that using Eq. 7.10 will also improve the performance of the feedback simulation in DESIRE.

The instantaneous position of the boiling boundary, $z_{bb}(t)$, is estimated from Eq. 7.10 by setting $\chi(z_{bb}(t)) = 0$ and taking the physically meaningful root of the equation. Then inverting Eq. 7.8 the axial void-fraction profile is reconstructed. At this step, we suppose thermal equilibrium and neglect the influence of subcooled boiling on the void-fraction profile. Integrating the void-fraction profile over the two-phase region the core-averaged void fraction, denoted by $< \alpha >_{pro,\chi}$, can be calculated as:

$$< \alpha >_{pro,\chi} = \frac{1 - \frac{z_{bb}}{L_C}}{1 - \frac{\rho_g}{\rho_l}} - \frac{1}{a_2(\frac{\rho_l}{\rho_g} + \frac{\rho_g}{\rho_l} - 2)\sqrt{K}L_C} arctan(\frac{(L_c - z_{bb})}{\sqrt{K} + \frac{(L_C + \frac{a_1}{2a_2})(z_{bb} + \frac{a_1}{2a_2})}{\sqrt{K}}}), \tag{7.11}$$

$$\text{if } K > 0, \text{ where } K = \sqrt{\frac{a_0}{a_2} - \frac{a_1^2}{4a_2^2} + \frac{1}{a_2(\rho_l/\rho_g - 1)}}$$

or

$$< \alpha >_{pro,\chi} = \frac{1 - \frac{z_{bb}}{L_C}}{1 - \frac{\rho_g}{\rho_l}} - \frac{1}{a_2\left(\frac{\rho_l}{\rho_g} + \frac{\rho_g}{\rho_l} - 2\right)\sqrt{|K|}L_C} arth(K_1), \quad (7.12)$$

if $K < 0$ and $K_1 < 1$ and $|\frac{L_C + \frac{a_1}{2a_2}}{\sqrt{|K|}}| < 1$ and $|\frac{z_{bb} + \frac{a_1}{2a_2}}{\sqrt{|K|}}| < 1$,

where $K_1 = \frac{(L_C - z_{bb})}{\sqrt{|K|} - \frac{(L_C + \frac{a_1}{2a_2})(z_{bb} + \frac{a_1}{2a_2})}{\sqrt{|K|}}}$

or otherwise

$$< \alpha >_{pro,\chi} = \frac{1 - \frac{z_{bb}}{L_C}}{1 - \frac{\rho_g}{\rho_l}} - \frac{1}{a_2\left(\frac{\rho_l}{\rho_g} + \frac{\rho_g}{\rho_l} - 2\right)\sqrt{K}L_C} ln\left(\frac{|\frac{L_C + \frac{a_1}{2a_2} - \sqrt{|K|}}{L_C + \frac{a_1}{2a_2} + \sqrt{|K|}}|}{|\frac{z_{bb} + \frac{a_1}{2a_2} - \sqrt{|K|}}{z_{bb} + \frac{a_1}{2a_2} + \sqrt{|K|}}|}\right). \quad (7.13)$$

These formulas can be used in combination with the void reactivity coefficient to calculate the simulated void reactivity.

The void profile method

Instead of using the quality, as in Eq. 7.10, one can apply a second-degree polynomial expansion to the axial void-fraction profile as well:

$$\alpha(z,t) = a_0(t) + a_1(t)z + a_2(t)z^2. \quad (7.14)$$

Eq. 7.14 applies only in the two-phase region, therefore we use it with the constrain $\alpha(z_{bb}, t) = 0$. The coefficients in Eq. 7.14 are determined from the two local void-fraction measurements and the estimated instantaneous position of the boiling boundary. The boiling-boundary position can be estimated using the second-degree approximation in Eq. 7.10. The influence of subcooled boiling is neglected here as well. The core-averaged void fraction, denoted by $< \alpha >_{pro,\alpha}$, is obtained using Eq. 7.14 as

$$< \alpha >_{pro,\alpha} = \frac{L_C - z_{bb}}{L_C}[a_0(t) + \frac{a_1(t)}{2}(L_c + z_{bb}) + \frac{a_2(t)}{3}(L_C^2 + L_C z_{bb} + z_{bb}^2)]. \quad (7.15)$$

The ΔP methods

Another way of improving the simulation of reactivity feedback is to use a different (not local) void-fraction measurement technique. One possibility, that was chosen for DESIRE, is to use a differential pressure sensor over the core. The core-averaged void fraction can be estimated from the measured pressure drop. Obviously, this technique gives only integral information about the axial void-fraction distribution. A drawback of this method is that the contribution of the non-gravitational pressure drops in the measured signal can spoil the estimation of the average void fraction. Rao *et al.* (1996) reported on experiments with a hybrid thermal-hydraulic loop where the simulated void reactivity was calculated based on the pressure drop measured over the heated section. They argued that the contribution of the inertial, frictional and accelerational pressure drops were so small due to the very low flow rate in their experiments that they could ignore them.

The simplest method, which neglects the non-gravitational pressure drops, estimates the core-averaged void fraction (denoted by $< \alpha >_{\Delta P,grav}$) as:

$$< \alpha >_{\Delta P,gr} = \frac{\rho_l L_C g - \Delta P_{mes}}{L_C g (\rho_l - \rho_g)}, \tag{7.16}$$

where ΔP_{mes} is the measured pressure drop over the heated section.

However, the non-gravitational pressure drops are not always negligible in DESIRE (see next section). Therefore we use two other methods, which correct for these terms in the measured core pressure drop. To account for the frictional, inertial and accelerational pressure drop correctly, one should know the dynamic behavior of the void-fraction and flow-quality distribution and the mass flux along the heated section. Since these are not known, the contributions of the non-gravitational pressure drops are estimated in a quasi-static fashion from the measured or estimated instantaneous values of mass flux, quality, void fraction and the boiling-boundary position as:

$$\Delta P_{fr,1-\phi}(t) = z_{bb}(t)\frac{f M_{C,i}(t)^2}{2 D_C \rho_l}, \tag{7.17}$$

$$\Delta P_{fr,2-\phi} = (L_C - z_{bb}(t))\frac{f M_{C,i}(t)^2}{2 D_C \rho_l}\varphi, \tag{7.18}$$

where the two-phase multiplier φ using the HEM model is given as

$$\varphi = 1 + \left(\frac{\rho_l}{\rho_g} - 1\right) < \chi >_{2-\phi}(t)$$

$$\Delta P_{acc} = M_{C,i}(t)^2\left(\frac{1}{\rho_l} - \frac{\chi_{ex}^2(t)}{\alpha_{ex}(t)\rho_g} - \frac{(1 - \chi_{ex}(t))^2}{(1 - \alpha_{ex}(t))\rho_l}\right), \tag{7.19}$$

The instantaneous values of z_{bb}, α_{ex} and χ_{ex} in the above equations can be obtained either using the quality profile from Eq. 7.10, or using the void profile from Eq. 7.14. The core-averaged void fraction is denoted by $< \alpha >_{\Delta P,\chi}$ for the former method, and by $< \alpha >_{\Delta P,\alpha}$ for the latter method. It is calculated as

$$< \alpha >_{\Delta P,..} = \frac{\rho_l L_C g - (\Delta P_{mes} - \Delta P_{fr,1-\phi} - \Delta P_{fr,2-\phi} - \Delta P_{acc})}{L_C g (\rho_l - \rho_g)}. \tag{7.20}$$

In the quasi-static approach we ignore the contribution of the inertial pressure drop in Eq. 7.20, which is a quite reasonable approximation for linearly stable situations in DESIRE.

The factor f in Eq. 7.17 and in Eq. 7.18 is the wall friction factor (Fanning friction factor) and it can be estimated with the empirical Blasius formula (Todreas and Kazimi, 1989) for circular pipe or bundle geometries. However, in the heated bundle in DESIRE there are three spacers whose influence cannot be accounted for with the Blasius formula. Therefore an effective wall friction factor incorporating the friction of the spacers was determined experimentally for a range of flow rate, which is typical in DESIRE. It is found to be $f = 0.039 \pm 0.003$. In the next section, we show the importance of the non-gravitational pressure drop correction terms to obtain a reasonable estimate of the core-averaged void fraction.

The combined void profile method

A straightforward way to combine the local (gamma transmission) and the integral (pressure drop) measurements of the void fraction is to apply a third-degree polynomial expansion of either the quality or the void-fraction profile instead of the aforementioned second-degree approximations. The coefficients are determined from the two local measured void

fractions, the estimated position of the boiling boundary (obtained from Eq. 7.10) and from the estimated core-averaged void fraction obtained from the pressure drop measurement. Because of the latter the third-degree polynomial has to be integrated, which would lead, in case of expansion of the quality profile, to a system of transcendent equations for the coefficients containing cumbersome formulas like in Eq. 7.11, Eq. 7.12 and Eq. 7.13. This would pose difficulties and possibly problems for the real-time simulation. Therefore a third-degree expansion to the axial void-fraction profile is applied in the form:

$$\alpha(z, t) = a_0(t) + a_1(t)z + a_2(t)z^2 + a_3(t)z^3. \tag{7.21}$$

In this case, finding the coefficients reduces to a linear problem. From Eq. 7.21 the core-averaged void fraction, denoted by $< \alpha >_{com}$, is obtained as

$$< \alpha >_{com} = a_0(t)\frac{L_C - z_{bb}}{L_C} + a_1(t)\frac{L_C^2 - z_{bb}^2}{2L_C} + a_2(t)\frac{L_C^3 - z_{bb}^3}{3L_C} + a_3(t)\frac{L_C^4 - z_{bb}^4}{4L_C}. \tag{7.22}$$

7.3.1 Implementation of the feedback simulation

Because of the major changes (new methods, new instrumentation) the whole void-reactivity simulation has been newly implemented in DESIRE. It is now realized in LAB-VIEW environment (LABVIEW, 2000) on a powerful PC.
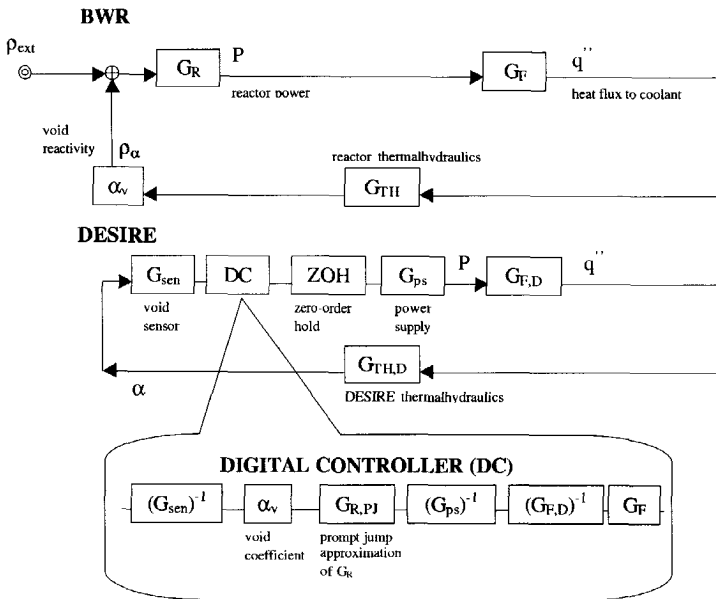
Figure 7.1: Comparison of the block schema of a BWR and DESIRE extended with the artificial void-reactivity feedback simulation. G_R denotes the zero-power reactivity-to-power transfer function, G_F is the fuel-to-coolant heat transfer function and G_{TH} is the thermalhydraulics (heat flux to average void fraction) transfer function. The transfer function in the DC are in discrete time, the rest is in continuous time.

The simulation was implemented in a flexible way that the user can choose among the aforementioned void fraction reconstruction methods. In figure 7.1 the void-reactivity

feedback scheme of a BWR and the artificial void-reactivity simulation in DESIRE is compared.

The transfer functions in the digital controller (DC) are all in discrete time, while the rest of the transfer functions in the figure are all in continuous time. The DESIRE system contains some elements that are not present in a BWR, however, one cannot avoid them in the feedback simulation. Such element is the zero-order hold (ZOH). It couples the discrete-time simulation in the DC with the rest of the continuous-time system. This is the most common used reconstruction filter, which takes into account the effect of sampling the data (Ogata, 1987). The output signal of the DC is kept constant by the ZOH during one sample interval.

G_{sen} symbolizes the transfer function of the void measurement sensor - both the transfer function of the gamma-transmission setup (the ratemeter) and the transfer function of the differential pressure sensor. G_{ps} is the transfer function of the power supplies of DESIRE. In order to avoid the undesired phase shift and attenuation of the signal in these elements, the transfer functions G_{sen}^{-1} and G_{ps}^{-1} are included in the DC to correct for them in the simulation. Experimental experience shows that correcting for the transfer function of the ratemeter of the gamma setup is not necessary if the time constant of the ratemeter is small enough ($\leq 0.1s$). Then the attenuation and the phase shift of the ratemeter is negligible in the frequency range of interest ($< 1Hz$). However, we must correct for the attenuation and the phase shift caused by the differential pressure sensor since it has a quite large time constant of 2 s as specified by the manufacturer. Similarly, we have to compensate for the power supply.
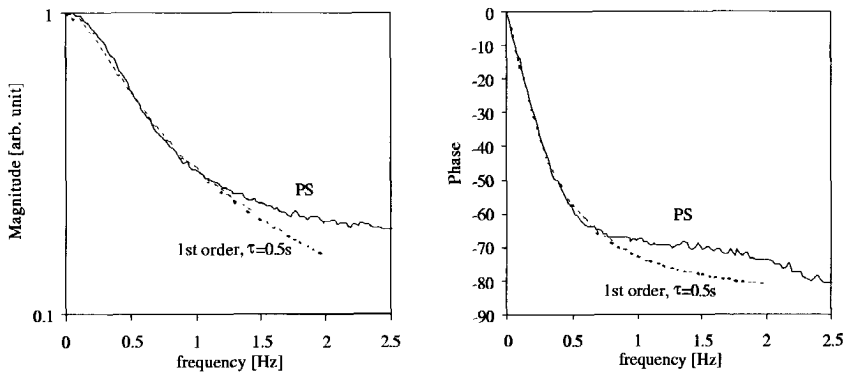
Figure 7.2: The magnitude and the phase of the transfer function of the power supply of DESIRE (solid line). Although the power supply is not a first-order system, it behaves like a first-order system with a time constant of 0.5 s (dashed line) up to about 1 Hz.

The experimentally determined transfer function of the power supply is shown in figure 7.2. The figure shows that the behavior of the power supply is of a first order system with a time constant of 0.5 s up to about 1 Hz. In principle, one can compensate for the low-pass filtering effect of both the pressure sensor and the power supply using the inverted transfer functions with the appropriate time constants. However, this would amplify high frequencies too much. The input to the DC contains a considerable level of relatively high-frequency measurement noise (e.g. originating from the Poisson statistics of the gamma measurement). Although this high-frequency noise has practically no effect on the dynamics of the system, it can saturate the control signal driving the power supply since

the latter has a limited range. Therefore, in the transfer functions G_{sen}^{-1} and G_{ps}^{-1} besides the compensating zero we apply a pole that filters out the disturbing high-frequency noise:

$$G^{-1} = \frac{1 + s\tau_{sen}}{1 + s\tau_p}, \qquad (7.23)$$

where τ_{sen} is the time constant of the sensor. The τ_p time constant is chosen such (0.05 s - 0.1 s) that filtering (suppression) occurs only above the frequency range of our interest. Applying Z-transform (Ogata, 1987), Eq. 7.23 corresponds in discrete time to

$$(G^z)^{-1} = \frac{1 - e^{\frac{\Delta t}{\tau_p}}}{1 - e^{\frac{\Delta t}{\tau_{sen}}}} \frac{1 - e^{\frac{\Delta t}{\tau_{sen}}} z^{-1}}{1 - e^{\frac{\Delta t}{\tau_p}} z^{-1}}, \qquad (7.24)$$

where Δt is the sampling time of the DC. In case of the power supply, an ARMA(2,2) model was fitted to the transfer function and its inverse was originally proposed to be used for compensating in the DC by Kok and Van der Hagen (1999). This is replaced by an Eq. 7.24 type of correction not only to achieve the aforementioned noise reduction but the ARMA model has also a slight negative bias at zero frequency. Eq. 7.24 does not have this problem.

Another compensating transfer function in the DC is $(G_{F,D})^{-1}$. This is implemented in combination with G_F to enable the simulation of systems with various fuel time constants. The time constant of the fuel rods in DESIRE was found to be about 0.5 s (Kok, 1998). The combined effect of compensating for the DESIRE fuel time constant and simulating an arbitrary fuel time constant is also implemented in the form of Eq. 7.24 in the DC. In that case, τ_{sen} is the DESIRE fuel time constant and τ_p is the fuel time constant of the simulated system.

To simplify the simulation of the neutronics, the prompt-jump approximation to the point-kinetic equations with one effective group of delayed neutrons is implemented in DESIRE (Kok and Van der Hagen, 1999). In the prompt-jump approximation the dn/dt term in Eq. 7.1 is neglected, which is valid for the low-frequency region interesting for BWR stability and for reactivities smaller than 1$ ($\rho = \beta_{eff}$) (Hetrick, 1971). This limits the maximum void-reactivity coefficient that can be validly used during the simulation. Under this conditions of limited reactivity changes, the small sampling interval of $\Delta t = 25$ ms applied in the DC ensures a sufficiently small time step for solving numerically the neutronic equations.

An important point is the scaling of the neutronics when one simulates an actual BWR with DESIRE using the artificial feedback as discussed by Kok and Van der Hagen (1999). Due to the different channel transit times - the characteristic time that plays an important role for density-wave oscillations - in DESIRE and in the BWR that is simulated, one has to scale the point-kinetic equations. This can be done by setting the $N_t = \lambda t$ dimensionless group for the simulation to the same value as for the reactor (Kok and Van der Hagen, 1999). For example, a proper scaling is achieved for the Dodewaard reactor if one uses a λ in the simulation that is 1.47 times larger than in Dodewaard, since the transit time in DESIRE is smaller by a factor of 0.68 (Kok and Van der Hagen, 1999).

7.4   Experimental results

We have carried out measurements to test the different void-fraction reconstruction methods proposed in the previous section and to test how the artificial void-reactivity feedback

simulation works with these methods. As a reminder, the six void reconstruction methods, introduced in the previous section, are summarized in Table 7.1:

Method	Based on	non-gravitational pressure drops	$< \alpha >_C$ is given by
$\alpha_{pro,\chi}$	$\chi(z,t) = a_0 + a_1 z + a_2 z^2$	-	Eqs. 7.11 to 7.13
$\alpha_{pro,\alpha}$	$\alpha(z,t) = a_0 + a_1 z + a_2 z^2$	-	Eq. 7.14
$\alpha_{\Delta P,gr}$	ΔP_{mes}	-	Eq. 7.16
$\alpha_{\Delta P,\chi}$	ΔP_{mes}	from $\chi_{pro,\chi}(z,t)$	Eq. 7.20
$\alpha_{\Delta P,\alpha}$	ΔP_{mes}	from $\alpha_{pro,\alpha}(z,t)$	Eq. 7.20
α_{com}	$\alpha(z,t) = a_0 + a_1 z + a_2 z^2 + a_3 z^3$	from $\alpha_{pro,\alpha}(z,t)$	Eq. 7.21

Table 7.1: Summary of the six void-fraction reconstruction methods.

The experiments have been carried out for three friction distributions in the facility to represent all possible thermal-hydraulic stability conditions in DESIRE. These three cases are:

1. A high friction setting ($K_{r,e} = 80$) of the riser-exit resistance element in combination with a zero-friction setting at the core-inlet valve ($K_{C,i} = 0$) representing the least stable situation from the thermal-hydraulic point of view (see Chapter 3), with a relatively low coolant flow rate.

2. The lowest possible friction setting at the riser-exit ($K_{r,e} = 15$), a high-friction setting at the core-inlet valve ($K_{C,i} = 65$) representing an extremely stable thermal-hydraulic system with a relatively low coolant flow rate.

3. The lowest possible friction setting at the riser-exit ($K_{r,e} = 15$), a zero-friction setting at the core-inlet valve ($K_{C,i} = 0$) representing an intermediate stability in between the above two cases - practically a very stable thermal-hydraulic system - with a relatively high coolant flow rate.

We concentrate on the question how good the different methods can reproduce the core-averaged void fraction in *dynamic situations*. As it was mentioned in section 7.3., the method proposed previously by Kok and Van der Hagen (1999) had the deficiency to introduce a significant phase and magnitude difference with respect to the actual core-averaged void-fraction variations. Considering the latter one, we have to realize that it is not the absolute value (magnitude) of the core-averaged void fraction that is important to be predicted correctly. Rather the *fluctuations*, more precisely the *dynamics* of the core-averaged void fraction that must be reconstructed properly for a correct simulation of coupled neutronic-thermalhydraulic oscillations. We qualify the methods with respect to this. However, for entirety, first the reconstruction of the steady-state void fraction using the different methods is discussed briefly.

7.4.1   Reconstruction of the steady-state void fraction

We examine how the steady-state axial void-fraction profile and the steady-state core-averaged void fraction is reconstructed. The six methods, listed in Table 7.1 are compared to each other and to the actual core-averaged void fraction, $< \alpha >$.
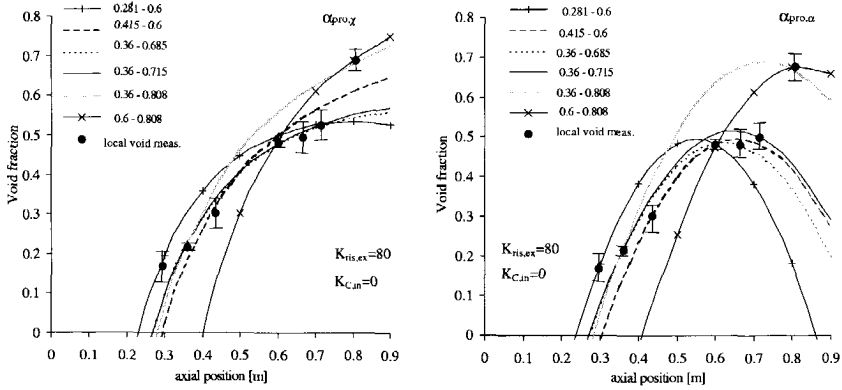
Figure 7.3: The influence of the void-measurement heights on the reconstruction of the steady-state void-fraction profile. The left figure shows the results obtained by the $\alpha_{pro,\chi}$ method, the right figure corresponds to those of the $\alpha_{pro,\alpha}$ method. The different curves corresponds to different combinations of the heights (given in meters) of the two gamma sensors. A typical case for $K_{r,e} = 80$, $K_{C,i} = 0$ is depicted.

To be able to estimate $< \alpha >$, measurements were carried out changing the elevation of the two gamma-transmission setups while keeping the facility in the same operating condition. The core-averaged void fraction is estimated from the local void-fraction measurements as

$$< \alpha >= \sum_i \frac{z_{i+1} - z_i}{L_C} \alpha(z_i), \tag{7.25}$$

where z_i is the elevation of the ith local void-fraction measurement point.
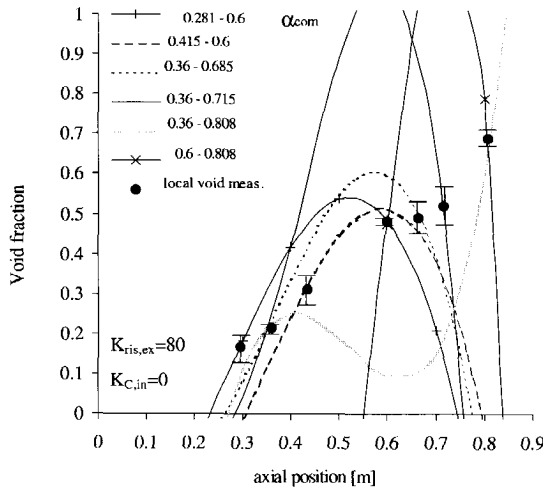
Figure 7.4: The reconstructed steady-state void-fraction profile using the α_{com} method. The measurements for $K_{r,e} = 80$, $K_{C,i} = 0$ are shown.

Figure 7.3 and figure 7.4 show the results for a typical case for the friction distribution, $K_{r,e} = 80$ and $K_{C,i} = 0$, which represents relatively low inlet flow rate conditions. The axial void-fraction profile is obtained for the $\alpha_{pro,\chi}$, the $\alpha_{pro,\alpha}$ and the α_{com} methods. Figure 7.5 shows the corresponding predictions of the core-averaged void fraction for the six methods.
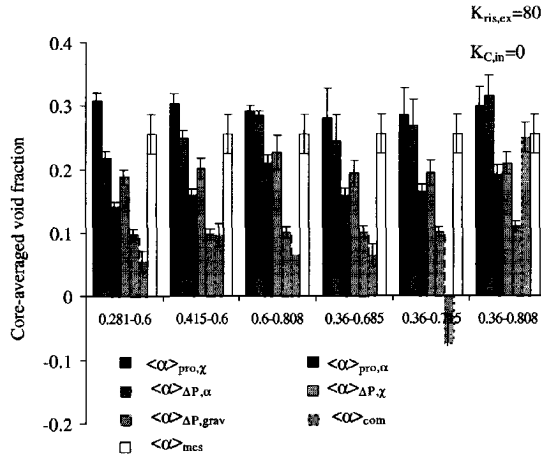
Figure 7.5: The core-averaged void fraction predicted by the six methods for all void-measurement height combinations. The actual core-averaged void fraction estimated from the local measurements is shown as well. The $\alpha_{pro,\chi}$ and the $\alpha_{pro,\alpha}$ methods predict the average void fraction within the uncertainty of the measurements. The ΔP based methods underpredict it. The prediction of the α_{com} method shows a strong dependence on the height of the gamma sensors. The same measurement case is depicted as in figure 7.3 and in figure 7.4.

The $\alpha_{pro,\chi}$ method seems to predict the most realistic steady-state axial void-fraction profile. The void-fraction profile predicted by the $\alpha_{pro,\alpha}$ method is only a second-degree approximation of the actual void-fraction profile. This is not a very realistic description since the actual profile is obviously not a second-degree polynomial of the axial position. Since only two local void-fraction values are used to fit the profile at a time, the profile depends on the void-fraction measurement heights. However, the differences in the prediction of the core-averaged void fraction for the various measurement heights are small. The core-averaged void fraction, although usually slightly overestimated, is predicted always within the uncertainties of the measurements using the aforementioned two methods.

The α_{com} method does not work properly for the steady-state. This is because the average void fraction that would be obtained only from the measured local void fractions and the one extracted from the pressure-drop measurement differs in the most cases significantly. The former usually overestimates the actual average void fraction (see $< \alpha >_{pro,\alpha}$ in figure 7.5), the latter usually underestimates it (see $< \alpha >_{\Delta P,\alpha}$ in figure 7.5). In Eq. 7.21, basically, we try to match these two which can lead, depending on the local void-fraction measurement positions, to non-physical void-fraction profiles and to an erroneous core-average void fraction prediction as shown in figure 7.5.

The $\alpha_{\Delta P,\alpha}$ and the $\alpha_{\Delta P,\chi}$ methods usually underestimate the actual core-averaged void fraction. However, they predict significantly better then if one only considers the gravi-
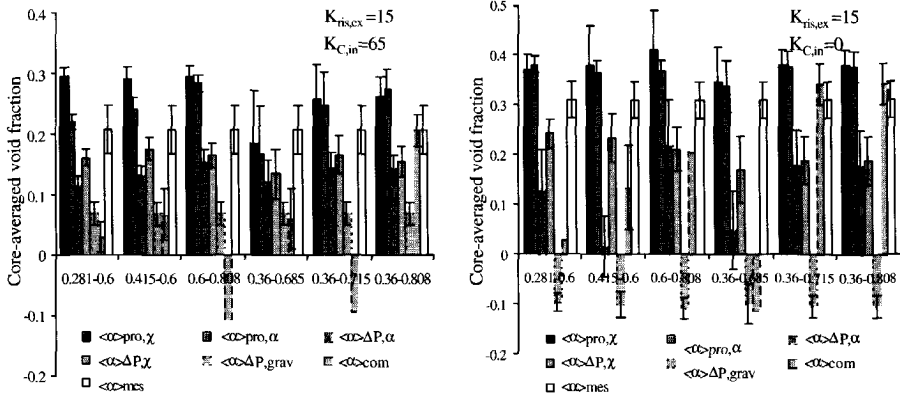
Figure 7.6: The core-averaged void-fraction prediction for the other two friction settings at the core-inlet and at the riser-exit. Qualitatively, the results for $K_{r,e} = 15$, $K_{C,i} = 65$ are similar to those in figure 7.5 (left figure). In case of $K_{r,e} = 15$ and $K_{C,i} = 0$ (high flow rate conditions) the prediction of the ΔP based methods is relatively worse, the $\alpha_{\Delta P,gr}$ method gives a negative void fraction (right figure).

tational pressure drop ($< \alpha >_{\Delta P,gr}$) without correcting for the non-gravitational pressure drops. The performance of the pressure drop based methods could be, in principle, further improved using a more sophisticated two-phase model instead of the HEM for estimating the correction terms for the two-phase frictional and accelerational pressure drops.

The results of a typical case for the other two friction distributions are given in figure 7.6. It can be seen that for the $K_{r,e} = 15$ and $K_{C,i} = 0$ case the corrections for the non-gravitational pressure drops is absolutely necessary otherwise negative void fraction is predicted. This is because at this friction distribution the flow rate is relatively high and the relative contributions of non-gravitational pressure drops to the total pressure drop is much higher than for the other two friction distributions. For $K_{r,e} = 15$ and $K_{C,i} = 65$, the predictions of the core-averaged void fraction by the different methods are comparable to those obtained for $K_{r,e} = 80$, $K_{C,i} = 0$.

7.4.2 The dynamics of reconstructed average void fraction

In this subsection, we examine how the *dynamics* of the core-averaged void fraction is reconstructed using the six methods without turning the feedback on. The *phase differences* between the actual and the different reconstructed core-averaged void fractions are examined and their *stability indicators*: the DR and the oscillation frequency are compared.

Measurements were performed changing the position of the two gamma sensors keeping the facility around the same equilibrium point. We propose to use the asymmetry of the cross correlation function (CCF) between the reconstructed and the actual core-averaged void fraction with respect to the Y-axis to extract the phase difference. At zero phase difference the CCF should be symmetrical around the Y-axis. First, the CCF between the actual core-averaged void fraction and the core-averaged void fraction obtained by

the $\alpha_{\Delta P,gr}$ method is estimated as

$$CCF_{<\alpha(t)>,<\alpha(t)>_{\Delta P,gr}} = \sum_i \frac{z_{i+1} - z_i}{L_C} CCF_{\alpha(z_i,t),<\alpha(t)>_{\Delta P,gr}}, \qquad (7.26)$$

It is assumed here that the system is stationary and that the CCFs on the right-hand side represent the same system behavior (the same dynamics). We will see later that this is approximately true (figure 7.8). The measurements were carried out at the $K_{r,e} = 80$ and $K_{C,i} = 0$ friction settings for which the thermal-hydraulic stability is low enough to obtain usable CCFs. The value of the phase difference is obtained by fitting the $A sin(\omega t + \phi)$ function to the measured CCFs using a nonlinear least-square method, where ϕ is the phase difference.

	at P = 31 kW	at P = 27 kW
$\phi_{<\alpha>,<\alpha>_{\Delta P,gr}}$	-9.21°±0.56°	-3.1°±0.83°

Table 7.2: The measured phase difference between the estimated core-averaged void fraction and the average void fraction reconstructed by the $\alpha_{\Delta P,gr}$ method. The measurements are done for the least stable thermal-hydraulic system, $K_{r,e} = 80$, $K_{C,i} = 0$.

Small phase differences are measured between the estimated core-averaged void fraction and the average void fraction reconstructed by the $\alpha_{\Delta P,gr}$ method as shown in Table 7.2. This shows that the phase of the ΔP_{mes} signal, and thus that of $< \alpha >_{\Delta P,gr}$ too, with good approximation is the same as of the core-averaged void fraction.

For the $\alpha_{\Delta P,gr}$ method, the phase of the reconstructed core-averaged void fraction does not depend on the local void-measurement heights, since it is based exclusively on the pressure drop measurement. However, for the other methods it might depend on the local void measurement height (see figure 7.7). Therefore, we estimate the phase differences between the actual core-averaged void fraction and the reconstructed core-averaged void fractions by taking the phase difference between $< \alpha >_{\Delta P,gr}$ and the other reconstructed average void fractions ($< \alpha >_{rec}$) as

$$\phi_{<\alpha>,<\alpha>_{rec}} = \phi_{<\alpha>,<\alpha>_{\Delta P,gr}} + \phi_{<\alpha>_{\Delta P,gr},<\alpha>_{rec}}. \qquad (7.27)$$

These values are shown in figure 7.7. The figure shows a significant dependence of the phase differences on the height of the local void-fraction measurements for the methods based exclusively on these local measurements. The same trend is observed for both measurement cases : when both gamma sensors are at low positions, there is a small phase difference between the reconstructed average void fraction and the core-averaged void fraction. As one of the gamma sensors is placed higher, the phase difference (phase delay) increases. As both sensors are placed at higher positions, the phase differences decrease and become small. For the other methods, based on the pressure drop measurement or on a combination of pressure drop and gamma measurements, the phase difference is significantly less dependent on the void-fraction measurement height and remains small for each height combinations.
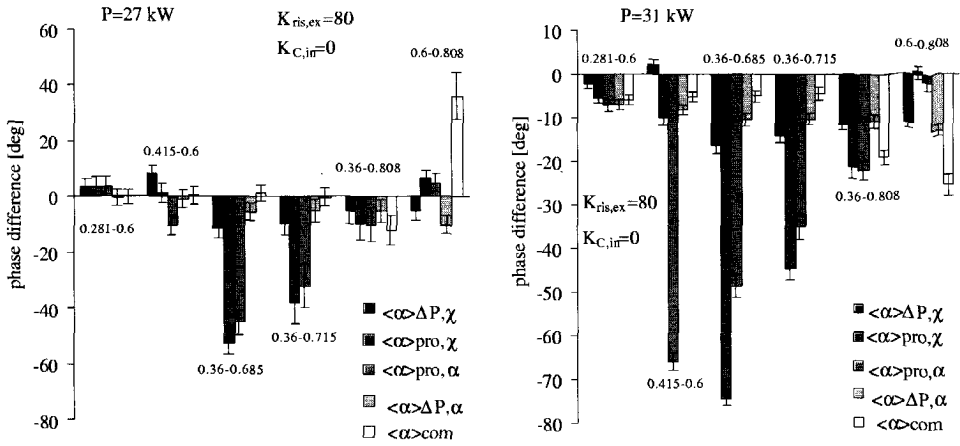
Figure 7.7: The phase differences between the actual core-averaged void fraction and the reconstructed core-averaged void fractions (except for $< \alpha >_{\Delta P,gr}$). The measurements are carried out at 27 kW and 31 kW power for $K_{r,e} = 80$, $K_{C,i} = 0$. The phase differences for methods based exclusively on the local void-fraction measurements show a significant dependence on the height of the gamma sensors. The methods based on the pressure drop measurement give generally a small phase difference with respect to the actual core-averaged void fraction.

Next, we compare the stability indicators of the core-averaged void fractions obtained by the different methods. The stability indicators of the actual core-averaged void fraction are obtained from its autocorrelation function (ACF) that is estimated similarly to Eq. 7.26 as

$$ACF_{<\alpha(t)>} = \sum_i \frac{z_{i+1} - z_i}{L_C} ACF_{\alpha(z_i,t)}, \qquad (7.28)$$

and compared with the DR and oscillation frequency of the reconstructed core-averaged void fractions.

The DR's are shown in figure 7.8 for all the combinations of the measurement heights of the two gamma sensors. The DR's and oscillation frequencies are obtained by fitting the ACF of a third-order system to the measured ACFs using a nonlinear least-square method (see Chapter 3).

The figure shows that the differences between the DR's of the reconstructed and the estimated actual core-averaged void fraction are small (less than 2% for P=31kW and less than 6% for P=27kW). For the oscillation frequency it is always less than 0.5%, which is not depicted for brevity. These results show that with respect to stability (indicators) all reconstruction methods perform very similar. We note that the DR's calculated from the $< \alpha >_{\Delta P,gr}$ signal for the different void-measurement height combinations are practically constant, which confirms our assumption made for calculating the CCF in Eq. 7.26 that approximately the same dynamics has been measured for all measurement height combinations.
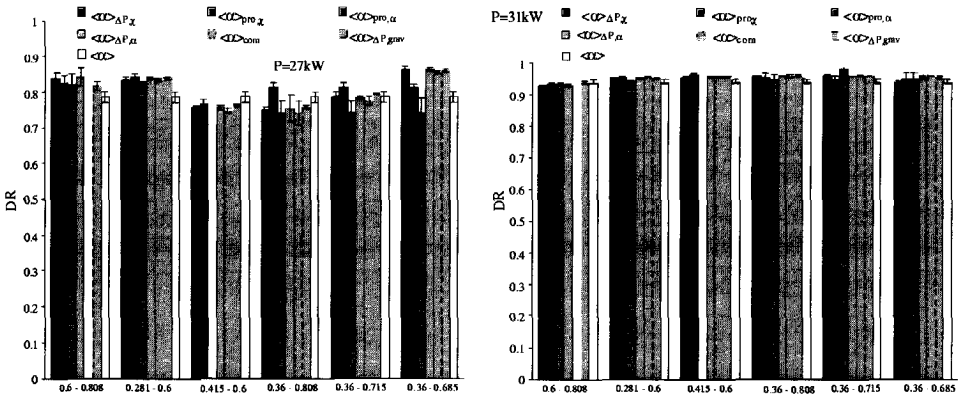
Figure 7.8: The DR's determined from the reconstructed average-void-fraction signals obtained by the different methods for all combinations of the measurement heights of the two gamma detectors at 31 kW power and at 27 kW power. The DR of the estimated core-averaged void fraction is also shown. The differences between the DR's obtained by the different methods are very small.

7.4.3 Dynamics with feedback simulation

The reconstruction methods are compared in this section by studying the dynamics of the simulated reactor. We examine the results of measurements performed with the simulated feedback turned on for the friction distribution $K_{r,e} = 15, K_{C,i} = 65$ and positioning the gamma sensors at 0.36 m and at 0.715 m. Table 7.3 shows the DR's of the simulated reactor using the $< \alpha >_{\Delta P,\chi}$ and the $< \alpha >_{pro,\chi}$ void-fraction reconstruction methods with various void-reactivity coefficients. The table contains the DR's calculated with the reduced-order model too, showing the same trend - increasing DR with increasing magnitude of α_V - as the measurements.

α_V	DR $\alpha_{\Delta P,\chi}$	DR $\alpha_{pro,\chi}$	DR model
0	-	-	0.07
-0.01	0.14±0.04	0.082±0.04	0.08
-0.015	0.18±0.03	-	0.09
-0.05	-	0.19±0.03	0.22
-0.06	-	0.29±0.03	0.28

Table 7.3: Measured DR's of the simulated reactor using the $\alpha_{\Delta P,\chi}$ and the $\alpha_{pro,\chi}$ void-fraction reconstruction methods with the void-reactivity feedback on. Measurements are done for the friction distribution $K_{r,e} = 15$, $K_{C,i} = 65$ at P=22 kW with the gamma-transmission sensors positioned at 0.36 m and at 0.715 m elevations. DR's calculated with the reduced-order model are shown in the last column.

The results show that a void-reactivity coefficient with about three times higher magnitude (-0.015 and -0.05) is needed for the $< \alpha >_{pro,\chi}$ method to obtain about the same DR (0.18 and 0.19) as with the $< \alpha >_{\Delta P,\chi}$. To explain this one has to consider that the

stability of the coupled system is determined by the poles of the characteristic equation (see Eq. 2.2 in Chapter 2):

$$1 + G_R G_F |\alpha_V| G_A = 0, \tag{7.29}$$

where the Doppler feedback is omitted and we take into account that the void coefficient, α_V, is negative in a BWR. Examining $|\alpha_V| G_R G_F G_A$ as a function of the complex frequency, $i\omega$, one can define the phase margin to instability as $\Delta\phi = 180° - arg(|\alpha_V| G_R G_F G_A)$ at the frequency where $|\alpha_V G_R G_F G_A| = 1$. Similarly, one can define the gain margin to instability as $1 - |\alpha_V G_R G_F G_A|$ at the frequency where $arg(|\alpha_V| G_R G_F G_A) = 180°$. Since G_R is always the same in the feedback simulation, it is enough to examine the phase and the magnitude of $G_F G_A$, which is actually the normalized transfer function from the power to the core-averaged void fraction ($G_{<\alpha>_{rec},P}$). The phase and the gain of this transfer function is shown in figure 7.9 for a measurement case of Table 7.3.
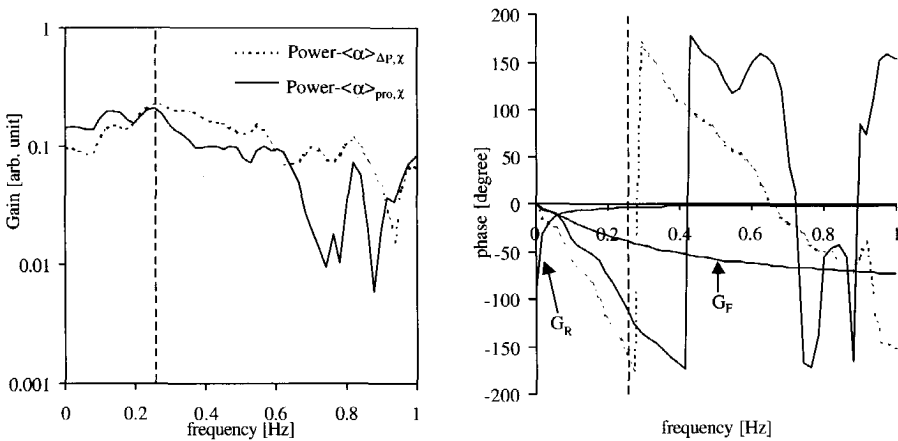
Figure 7.9: The measured gain and phase of the $G_{<\alpha>_{\Delta P,\chi},P}$ and the $G_{<\alpha>_{pro,\chi},P}$ transfer functions for the measurement at $\alpha_V = -0.015$ from Table 7.3. The vertical dashed line marks the resonance frequency of the simulated reactor, which is approximately the same for both methods. The two extra solid lines in the phase diagram are the phase of G_R (from the prompt-jump approximation) and the phase of G_F (obtained with 0.5 s time constant of the DESIRE rods) from Eq. 7.29. The gain at the resonance frequency is approximately the same for both methods, however there is a significant difference in the phase.

The gain of the two transfer functions at the resonance frequency are practically the same. The phase shift of the transfer function for $< \alpha >_{\Delta P,\chi}$ is however significantly larger (with about 48°) and thus the phase margin is considerably smaller for that method. Therefore, the difference in stability in this case is attributed mainly to the difference in the phase of $G_{<\alpha>_{rec},P}$. Note that similar phase differences are found between the $< \alpha >_{\Delta P,\chi}$ and $< \alpha >_{pro,\chi}$ for the thermal-hydraulic measurements in figure 7.7 at the 0.36 m - 0.715 m void-measurement height combination as here between the $G_{<\alpha>_{\Delta P,\chi},P}$ and the $G_{<\alpha>_{pro,\chi},P}$ transfer functions at the resonance frequency of the simulated reactor. We must keep in mind that the difference between the phase of the different $G_{<\alpha>_{rec},P}$

transfer functions depends on the resonance frequency of the simulated reactor, which is, in general, different from the resonance frequency of the thermalhydraulics.

This example shows that concerning the stability and dynamics of the simulated reactor, it is better to qualify the different void reconstruction methods by comparing the phase and gain of the $G_{<\alpha>_{rec},P}$ transfer function obtained by the different reconstructions. To examine this transfer function, measurements were carried out (again for different void-fraction measurement height combinations) with the feedback switched off and adding a random noise signal to the constant heating power (this option is also implemented in the DC). The transfer function from the power to the actual core-averaged void fraction is estimated as

$$G_{<\alpha(t)>,P} = \sum_i \frac{\frac{z_{i+1}-z_i}{L_C} CPSD_{\alpha(z_i,t),P}}{\frac{z_{i+1}-z_i}{L_C} APSD_P}, \tag{7.30}$$

where $CPSD_{x,y}$ is the cross power spectral density between signal x and y.

The phase shift and the gain of the $G_{<\alpha>_{rec},P}$ transfer functions are compared for the different methods with the one obtained from Eq. 7.30 in figure 7.10 and in figure 7.11.

As pointed out above, the phase depends on the frequency and one should look at the phase at the resonance frequency of the simulated reactor (the coupled system). Therefore phases of the transfer function are compared in a ± 0.1 Hz frequency range around the resonance frequency of the thermal-hydraulic system. In general, for the gamma-transmission sensor positions shown in figure 7.10 the phase shift of the $G_{<\alpha>_{rec},P}$ is somewhat larger in the 0.2 Hz - 0.3 Hz range than for the gamma sensor positions in figure 7.11. This corresponds with the trend shown in figure 7.7 on the dependence of the phase differences on the local void-fraction measurement heights for the different methods.

Considering the gain, $G_{<\alpha>_{\Delta P,\alpha},P}$ and $G_{<\alpha>_{\Delta P,\chi},P}$ lie closest to the gain of $G_{<\alpha>,P}$ for the most sensor height combinations, although the differences with other methods are small. Only the gain of $G_{<\alpha>_{\Delta P,gr},P}$ is considerably higher than the rest. This is because the transfer functions are normalized and $< \alpha >_{\Delta P,gr}$ always significantly underestimates the steady-state core-averaged void fraction (see the section 7.4.1). The same occurs at certain combinations of the height of the gamma-transmission sensors with the gain of $G_{<\alpha>_{com},P}$ for the same reason (see also figure 7.5).
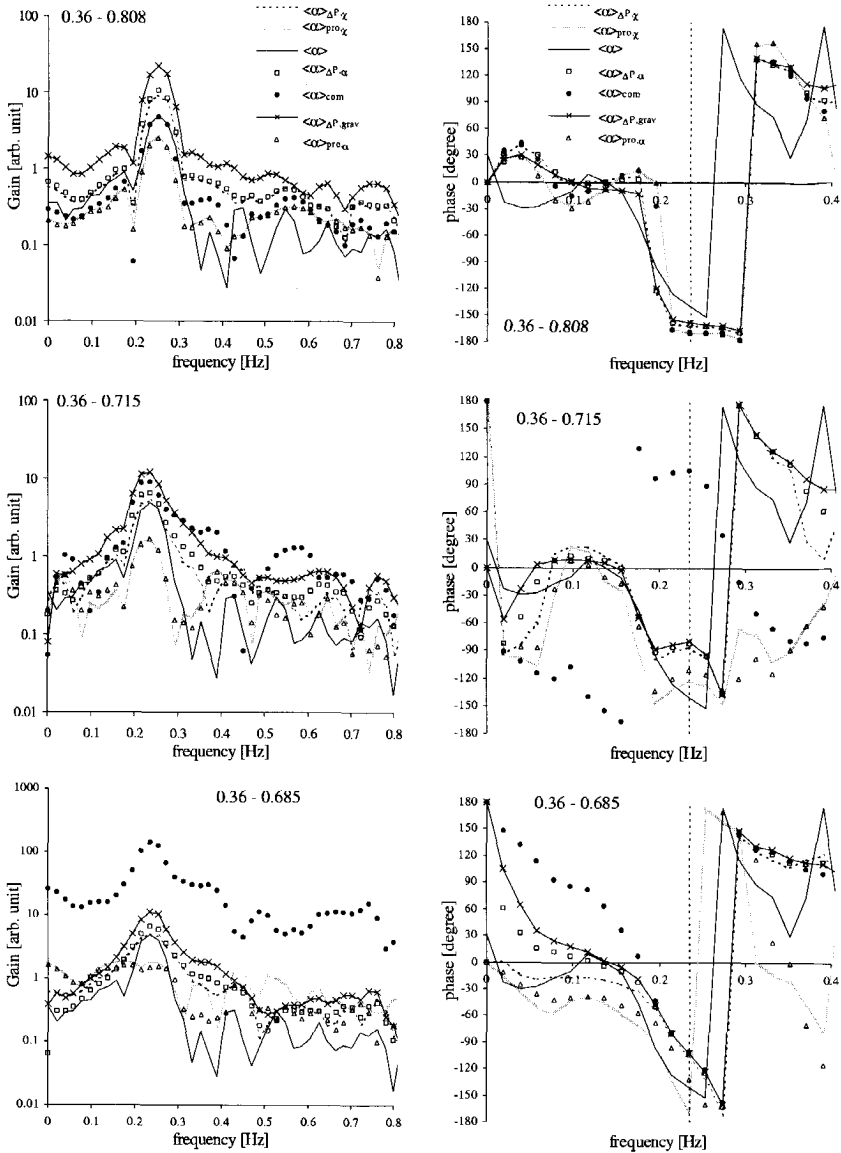
Figure 7.10: The gain and the phase of the measured power to core-averaged void fraction transfer functions for all the reconstruction methods. The phase curves are shown in a frequency range where there is a reasonable coherence between the power and the void-fraction oscillations. The dashed vertical lines in the phase diagrams indicate the resonance frequency of the thermalhydraulics. The measurement are carried out at 31 kW power for $K_{ex,ris} = 80$, $K_{C,i} = 0$. The results for three combinations of the height of the gamma-transmission sensors are shown here, for other three are shown in figure 7.11. The relative standard deviation of the phase values (depending on the coherence) is estimated to be around 10%, for the gain it is estimated to be around 22%.
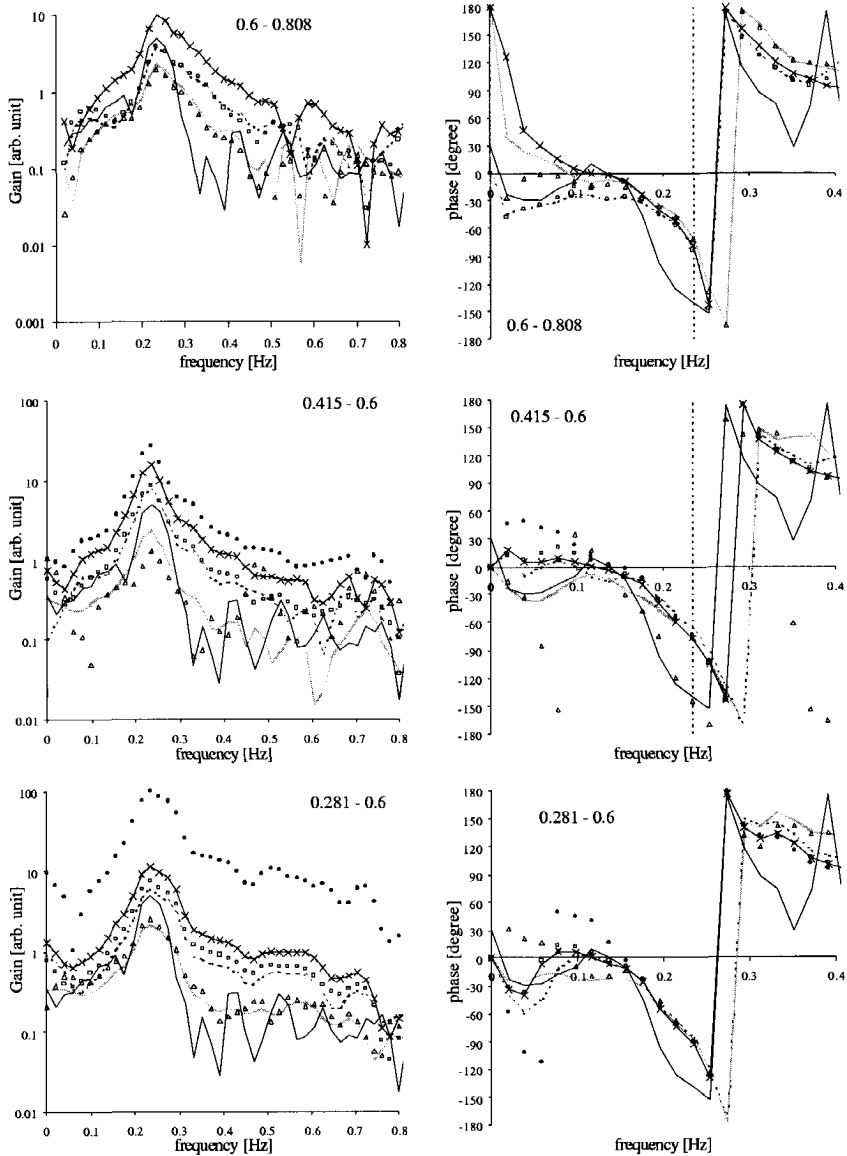
Figure 7.11: The continuation of figure 7.10.

Finally, we show the results of stability measurements with the simulated reactor using all the reconstruction methods. The measurements were carried out for various void coefficients at 19 kW power for the friction distribution $K_{r,e} = 80$, $K_{C,i} = 0$. The measured DR's are summarized in Table 7.4.

Unlike for the measurements shown in Table 7.3, the DR does not increase monotonous with increasing magnitude of the void coefficient but shows a more peculiar behavior. For the reconstruction $\alpha_{\Delta P,\alpha}$, $\alpha_{pro,\alpha}$ and α_{com} the DR first decreases, then it starts to increase. This, at first sight surprising, trend is also predicted by the reduced-order model (see the

α_V	DR α_{com}	DR $\alpha_{pro,\alpha}$	DR $\alpha_{pro,\chi}$	DR $\alpha_{\Delta P,\alpha}$	DR $\alpha_{\Delta P,\chi}$	DR model
-0.002	-	-	-	0.57±0.02	-	1.13
-0.004	0.61±0.02	-	-	0.42±0.03	-	0.96
-0.005	-	-	0.69±0.02	-	0.70±0.02	0.88
-0.006	0.24±0.04	-	-	0.63±0.02	-	0.81
-0.007	-	0.76±0.01	0.74±0.02	-	-	0.74
-0.008	0.27±0.03	-	-	0.75±0.01	0.55±0.02	0.69
-0.009	-	0.70±0.01	0.86±0.01	-	-	0.64
-0.010	0.45±0.03	-	-	-	-	0.64
-0.011	-	0.86±0.01	0.88±0.01	-	0.43±0.03	0.65
-0.012	-	-	-	-	-	0.68
-0.013	-	-	-	-	-	0.71

Table 7.4: Measured DR's of the simulated reactor using the different void-fraction reconstruction methods for the void feedback. Measurements are done for the friction distribution $K_{r,e} = 80$, $K_{C,i} = 0$ at P=19 kW. The DR's predicted by the reduced-order model are shown in the last column. A trend of decreasing and then increasing DR with increasing (absolute) value of the void coefficient is shown for both the predicted and for the measured DR's (except for $\alpha_{\Delta P,\chi}$ and for $\alpha_{pro,\chi}$).

table) and it is attributed to the interchange in the stability of the two least stable pole pairs as is shown in figure 2.13 in Chapter 2. The reduced-order model is used here only for qualitative comparison. In case of the $\alpha_{\Delta P,\chi}$ reconstruction method the DR decreases, for the $\alpha_{pro,\chi}$ method it increases monotonous for the range of void coefficients at which measurements were carried out.

7.5 Summary

The DESIRE two-phase flow facility has been extended with an artificial void-reactivity feedback simulation to enable the study of coupled netutronic-thermalhydraulic stability of natural-circulation BWRs. In the first version of the void-feedback simulation a very simple linear, quasi-static approach has been used to reconstruct the axial void-fraction profile and to calculate the core-averaged void fraction. The first results obtained using the simulated feedback with this simple approach were unsatisfactory. Therefore, more sophisticated methods have been introduced to improve the most crucial point in the simulation, the real-time reconstruction of the axial void profile.

Two methods are based on a second-degree polynomial expansion of the axial quality profile $(\alpha_{pro,\chi})$ and the axial void-fraction profile $(\alpha_{pro,\alpha})$, using two simultaneous, local gamma-transmission measurements of the void fraction and the measured inlet quality (temperature). Three other methods are based on the measurement of the pressure drop over the heated section. One of them $(\alpha_{\Delta P,gr})$ directly obtains the core-averaged void fraction from the measured pressure drop. The other two corrects for the non-gravitational pressure drops using the profile information either from $\alpha_{pro,\chi}$ $(\alpha_{\Delta P,\chi})$ or from $\alpha_{pro,\alpha}$ $(\alpha_{\Delta P,\alpha})$. A sixth method, combining the local gamma-transmission measurements and the pressure drop measurement, applies a third-degree polynomial expansion of the axial void-fraction profile (α_{com}).

Since for the stability of a BWR the fluctuations (the dynamics) in the void fraction and in the void reactivity are important, we examined how the different methods reconstruct the core-averaged void fraction in dynamics situation.

The two local void measurement based methods are discussed together. The same is done for the three pressure drop based methods. We summarize the findings about the performance of the different methods with respect to the following items:

1. Reconstruction of the core-averaged void-fraction fluctuations (without turning the feedback on), considering the phase differences and differences in stability indicators (DR, oscillation frequency) with respect to the estimated actual core-averaged void fraction.

2. Reconstruction of the power to core-averaged void-fraction transfer function, with respect to phase and gain in a frequency range around the resonance frequency of the thermal-hydraulic system. The gain and the phase of the power to core-averaged void-fraction transfer function are the most important parameters determining the stability when one turns on the void-reactivity feedback simulation.

Methods based on the local void-fraction measurements

1. In dynamic situations, the $\alpha_{pro,\alpha}$ and $\alpha_{pro,\chi}$ methods predict the core-averaged void fraction reasonably well. For both methods, the phase difference with respect to the actual core averaged-void fraction depends on the local void-fraction measurement heights and shows the same trend as a function of those for both methods. For certain height combinations: 0.36-0.685, 0.36-0.715 the phase delay is significant. The differences in stability indicators are less than a few percent for both methods.

2. Considering this item the gain is usually slightly underestimated. The phase shift shows a similar trend as mentioned in the previous item for the different height combinations of the local void-fraction sensors.

Methods based on the pressure drop measurement

1. For the methods $\alpha_{\Delta P,\alpha}, \alpha_{\Delta P,\chi}$ and $\alpha_{\Delta P,gr}$, the phase difference with respect to the actual core-averaged void fraction is much less dependent on the local void-fraction sensor heights (for $\alpha_{\Delta P,gr}$ is independent) than for the methods based exclusively on the local void-fraction measurements. This phase difference remains always small. The differences in stability indicators with respect to the actual core-averaged void fraction are less than a few percent for each method. A disadvantage of the $\alpha_{\Delta P,gr}$ method is that it does not work under relatively high flow rate conditions.

2. The estimation of the gain and the phase of the power to core-averaged void-fraction transfer function is reasonably good and the phase depends only very slightly on the local void-fraction measurement heights.

The combined method

1. Considering the phase difference with respect to the actual core-averaged void fraction the α_{com} method behaves, in general, similarly to the local void-fraction based methods. However, for certain void sensor height combinations this method gives very unphysical results and for these cases the phase difference is large. The stability indicators are predicted well, within a few percent.

2. The gain is overpredicted for the aforementioned unphysical cases. For these cases the phase shift is also considerably different than that for the actual core-averaged void fraction for these cases.

Comparing the overall performance of the six methods, it is not straightforward to choose a single one that is the best. Two methods based exclusively on the local gamma measurements ($\alpha_{pro,\alpha}$ and $\alpha_{pro,\chi}$) perform quite similarly to each other. The two pressure drop based methods ($\alpha_{\Delta P,\alpha}$ and $\alpha_{\Delta P,\chi}$) give also similar results to each other. Considering that the phase difference with respect to the actual core-averaged void fraction is always small and only slightly depends on the local void-fraction measurement heights for the $\alpha_{\Delta P,\alpha}$ and $\alpha_{\Delta P,\chi}$ methods, these methods are favored. However, they do not provide the axial void-fraction profile, while the $\alpha_{pro,\alpha}$ and $\alpha_{pro,\chi}$ methods do, which is advantageous if one wants to include flux weighting for the reactivity calculation.

Keeping these comments in mind, either one of the former two methods or one of the latter two methods could be used for stability experiments. If the α_{com} method is chosen then the experimenter should take care because it does not work for certain height combinations of the local void-fraction sensors. This method should be further improved.

Using all the methods, we performed several stability measurements on the simulated coupled neutronic-thermalhydraulic system. The DR is found to decrease first and then to increase with an increasing magnitude of the void coefficient. This behavior is also predicted qualitatively by the reduced-order model in the measured operating conditions and it is attributed to an interchange in the stability of the two least stable pole pairs of the system.
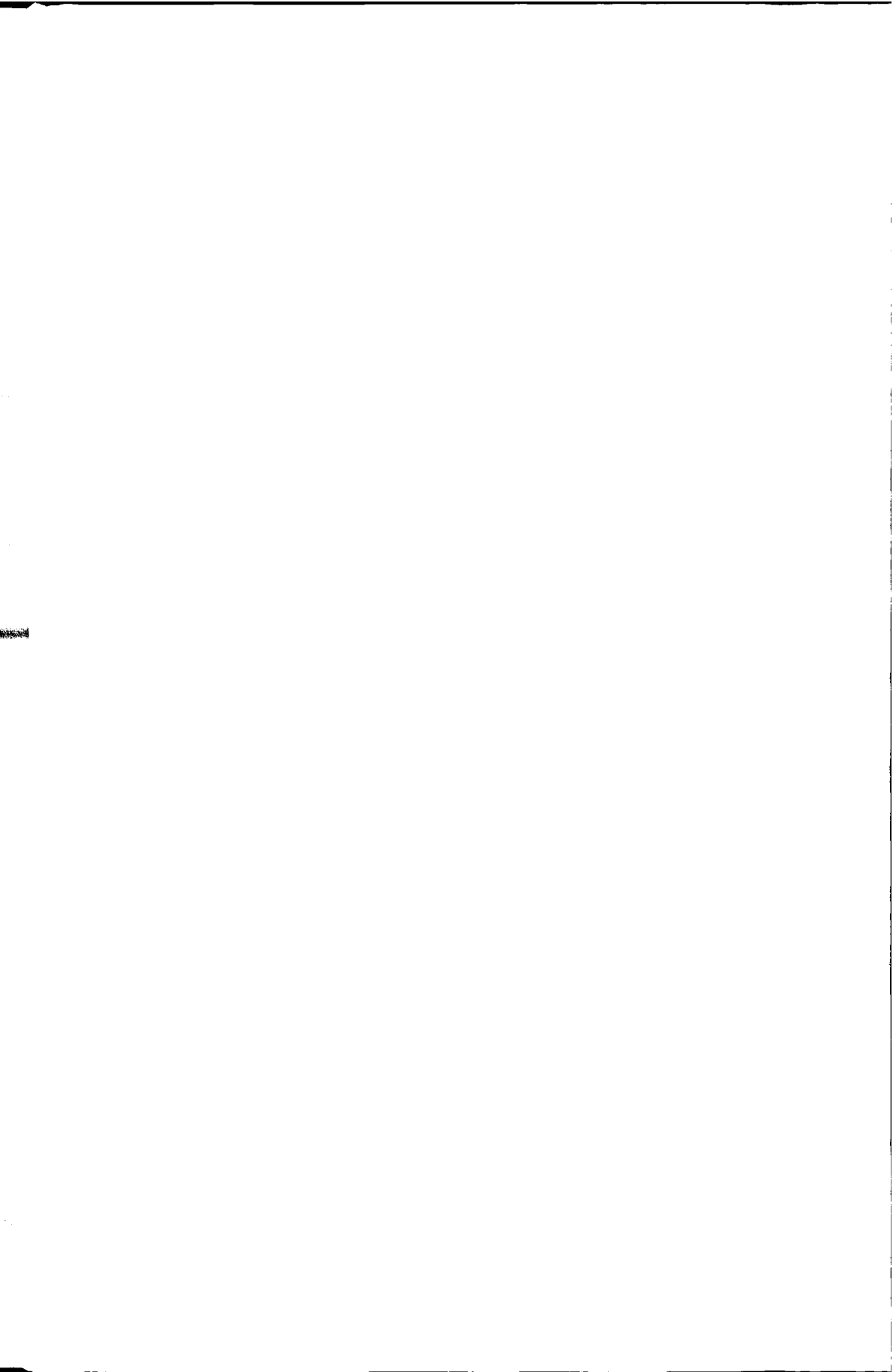
Chapter 8

Conclusions and discussion

In this thesis, several aspects of the dynamics and stability of natural-circulation BWRs have been studied using three powerful tools: an experimental facility, a reduced-order model and a thermal-hydraulic system code.

The linear stability of natural-circulation BWRs has been investigated extensively using a reduced-order model. The reduced-order model has been developed concentrating only on the most important physical processes determining the dynamics of BWRs and neglecting less important phenomena. This model is very suitable for fast parametric studies on the stability of BWRs. It has the capability to increase the insight into the role of the relevant physical processes responsible for the different kinds of instabilities. The sensitivity of the stability (the decay ratio) of the natural-circulation two-phase flow to the different types of pressure drops present in the system has been examined. It has been found that the accelerational and the two-phase frictional pressure drops are the most important destabilizing terms for the Type-II instability and the gravitational pressure drop in the riser is the most important destabilizing term for the Type-I instability. Using frequency-domain analysis, the poles of a natural-circulation BWR have been identified with neutronic, heat transfer and thermal-hydraulic processes. It is shown that it depends on the strength of the void-reactivity feedback which pole pair determines the stability of the reactor in the Type-II and in the Type-I instability region: for a strong void-reactivity feedback there is an interchange between two pole pairs moving from the Type-II to the Type-I region.

The reduced-order model has been extended to take into account core-inlet temperature variations. It is shown that it has a significant effect on the thermal-hydraulic stability of the system. It is found that moving the feedwater sparger to the core inlet the thermal-hydraulic stability increases. If the sparger is at the core inlet the reduced-order model predicts a unconditionally stable system, which is due to the simplification in the reduced-order model. On physical basis the stabilizing effect is plausible. A similar stabilizing trend is obtained by the advanced thermal-hydraulic code MONA as the sparger approaches the core inlet. Unfortunately, as the sparger core-inlet distance increases there is a strong numerical diffusion in modelling the propagation of temperature oscillations in the downcomer. The influence of the sparger position on the thermal-hydraulic stability deserves further investigations, if the effect is significant enough then new reactor designs might benefit from it. With a simple modification, adding an alternative extra feedwater sparger connected to the inlet of the heated assembly, the DESIRE facility could be used to investigate the effect experimentally. Further numerical investigations should be

performed using a thermal-hydraulic code provided with an advanced numerical scheme.

As an application of the reduced-order model, the problem of the practicability of using the decay ratio as a sole stability indicator for BWR stability monitoring is examined. It is shown that the system can be much closer to unstable behavior in terms of operational parameters like power, pressure and feedwater temperature than the value of the decay ratio would indicate. Therefore, relying only on the value of the decay ratio can be misleading in judging the stability margin. It would be more practical to use the operational margins together with the decay ratio. Due to the simplicity of the reduced-order model, the results given here are only indicative. Advanced thermal-hydraulic codes could be used to obtain more reliable results on the relation of decay ratio and operational margins. Experimental investigation of the problem using the DESIRE facility is also advocated.

The influence of the axial power profile on the nonlinear dynamics of BWRs has been examined using a numerical Hopf bifurcation code based on the reduced-order model. It is shown that bifurcation characteristics of the thermal-hydraulic system are sensitive to the axial power profile and both sub- and supercritical bifurcations are encountered. Generally, strongly bottom-peaked profiles might result in subcritical bifurcations (accompanied by diverging oscillations), for top-peaked profiles the bifurcation is supercritical (constant-amplitude oscillations). The type of bifurcation occurring in the reactor is found, in accordance with earlier studies, to be predominantly influenced by the strength of the void-reactivity feedback. The influence of the power profile in that case is not so significant. As for further investigation on the the nonlinear dynamics of BWR it would be of interest examining the role of the different nonlinear physical processes in the occurrence of subcritical and supercritical bifurcations, a similar (but nonlinear) study as described in Chapter 2 of this thesis.

The experimental facility, the DESIRE natural-circulation boiling two-phase flow loop, has been modified, based on a study with the reduced-order model. Installing a variable friction at the riser exit enables the study of unstable situations (density-wave) oscillations.

The thermal-hydraulic stability of natural-circulation two-phase flows have been investigated by performing extensive sets of stability measurements e.g. for different friction distributions, for different axial power profiles. Valuable experimental data has been gathered, which can be indicative for innovative, natural-circulation BWR designs (like the ESBWR) and it can be used for code validation as well. The measured stability indicators (decay ratio, oscillation frequency) are predicted fairly well by the MONA code, however, the reduced-order model is able to predict only the trends in the stability indicators correctly.

The nonlinear dynamics of the natural-circulation two-phase flow is investigated performing measurements at unstable operating conditions. The characteristics of the nonlinear density-wave oscillations in the vicinity of the stability boundary are examined and it is shown that the oscillations are dominated by the strong propagating mixture-density variations confirming earlier numerical results. It is found that the natural-circulation two-phase flow undergoes the so-called Feigenbaum scenario, the period-doubling route towards chaotic behavior as one penetrates into the unstable operating region of the system. To the author's knowledge, this is the first occasion that this phenomenon has been experimentally observed in (boiling) two-phase flow systems.

The prediction of highly nonlinear, unstable behavior is usually very sensitive to modelling assumptions and the empirical correlations applied in thermal-hydraulic codes. Therefore the pertinence of correlations and modelling assumptions could be efficiently checked by benchmarking the numerical results of the code against the aforementioned type of experimental data on nonlinear oscillations.

As an extension of the experimental possibilities of the thermal-hydraulic facility, the DESIRE loop is equipped with an artificial void-reactivity simulation implemented on a PC. This hybrid system is used to investigate the stability of natural-circulation BWRs experimentally. The most crucial point in the simulation is the real-time reconstruction of the axial void-fraction profile in the heated assembly of DESIRE. New void-fraction reconstruction methods have been introduced into the simulator to improve its performance. These methods are based on the measured pressure drop over the heated assembly (integral measurement), or on local gamma-transmission void-fraction measurements applying improved models or on the combination of the local void-fraction and pressure drop measurements. The performance of the different methods have been compared with respect to reconstructing the dynamics of the actual core-averaged void fraction without turning the feedback on. Comparison of the methods is also made for reactor stability measurements. In general, all methods perform reasonable well in dynamic situations except the combined method, which does not work for certain height combinations of the local void sensors. The phase difference with respect to the actual core-averaged void fraction might be higher for void-profile based methods depending on the height of the local void-fraction measurements. The phase difference for the pressure-drop based methods is always small and only very slightly dependent on the local void-fraction measurement height. The disadvantage of the pressure-drop based methods is that they do not provide with information on the void-profile. Moreover, one must apply corrections for the non-gravitational pressured drop terms, which might spoil the prediction of the core-averaged void fraction.

Dynamic measurements using the improved void-feedback simulation reveal stability trends that are also predicted by the reduced-order model.

Systematic experimental investigation on the neutronic-thermohydraulic stability can be performed in the future using the void-feedback simulation methods described here. The correction terms for the non-gravitational pressure drops should be improved and in this way the performance of the pressure-drop based and the combined reconstruction methods could be improved. The pressure-drop measurement methods with the improved correction terms could be the most practical to use if the heated assembly of the system is split into two (or more) parallel channels for investigating out-of-phase stability.
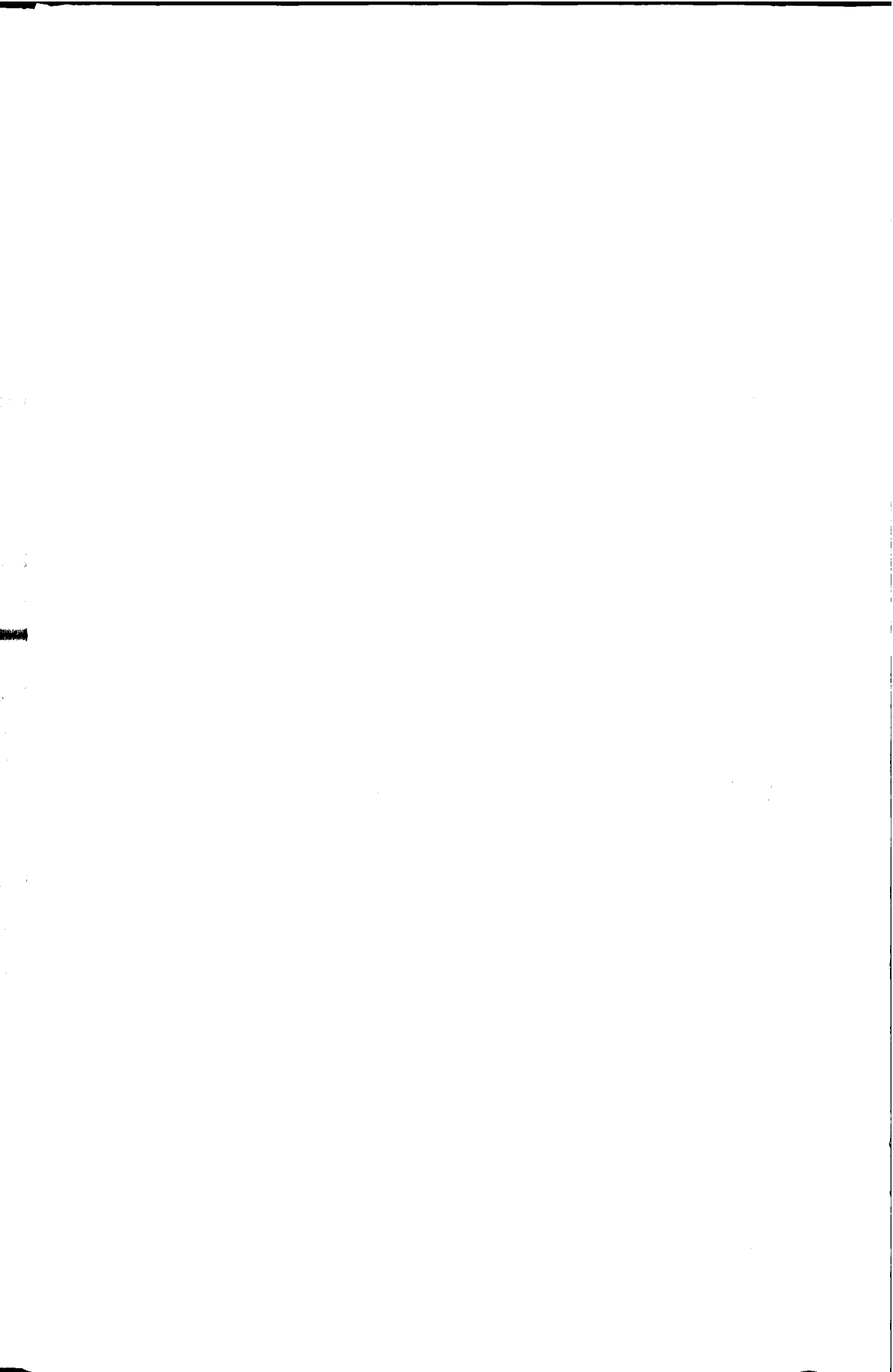
Appendix A

The reduced-order model

A.1 Model equations

The following equations constitute the reduced-order model of Van Bragt and Van der Hagen (1998a).

Neutron kinetics

Using one effective delayed neutron group:

$$\frac{dn(t)}{dt} = \frac{\rho(t) - \beta}{\Lambda} n(t) + \lambda c(t), \tag{A.1}$$

$$\frac{dc(t)}{dt} = \frac{\beta}{\Lambda} n(t) - \lambda c(t). \tag{A.2}$$

Fuel dynamics

$$\frac{d}{dt} \frac{q''(t)}{q_o''} = \frac{1}{\tau_f} [\frac{q'(t)}{q_o'} - \frac{q''}{q_o''}], \tag{A.3}$$

where $q''(t) = k_f [T_f(t) - T_{sat}]$.

Boiling boundary dynamics

$$\frac{dz_{bb}(t)}{dt} = 2[\frac{M_{C,i}(t)}{\rho_l} - \frac{q'(t) z_{bb}(t)}{\rho_l A_C (h_f - h_{C,i})}]. \tag{A.4}$$

Core void dynamics

$$\frac{d < \alpha(t) >_C}{dt} = \frac{M_{C,e}(t) - M_{C,i}(t)}{(\rho_f - \rho_g) L_C}, \tag{A.5}$$

$$M_{C,i}(t) = M_{C,e}(t)[1 + \frac{\rho_f - \rho_g}{\rho_g} \chi_{C,e}(t)] - \frac{(\rho_f - \rho_g)}{\rho_g} \frac{[L_C - z_{bb}(t)] q'(t)}{A_C (h_g - h_f)}, \tag{A.6}$$

$$< \alpha(t) >_C = \frac{L_C - z_{bb}(t)}{L_C} \frac{\rho_f}{\rho_f - \rho_g} \{1 - \frac{\rho_g}{(\rho_f - \rho_g) \chi_{C,e}(t)} ln[1 + \frac{\rho_f - \rho_g}{\rho_g} \chi_{C,e}(t)] \}. \tag{A.7}$$

Riser void dynamics

For the nth riser node

$$\frac{d < \alpha(t) >_{r,n}}{dt} = \frac{M_{r,n}(t) - M_{r,n-1}(t)}{\rho_f - \rho_g} \frac{N_r}{L_r}, \tag{A.8}$$

$$M_{r,n-1}(t)[1 + \frac{\rho_f - \rho_g}{\rho_g}\chi_{r,n-1}(t)] = M_{r,n}(t)[1 + \frac{\rho_f - \rho_g}{\rho_g}\chi_{r,n}(t)], \tag{A.9}$$

$$< \alpha(t) >_{r,n} = \frac{\rho_f}{\rho_f - \rho_g}\{1 - \frac{\rho_g}{(\rho_f - \rho_g)(\chi_{r,n}(t) - \chi_{r,n-1}(t))} ln[1 + \frac{\rho_f - \rho_g}{\rho_g}\frac{\chi_{r,n}(t) - \chi_{r,n-1}(t)}{1 + \chi_{r,n-1}(t)\frac{\rho_f - \rho_g}{\rho_g}}]\}, \tag{A.10}$$

where N_r is the number of riser nodes.

Mass-flux density dynamics

The mass-flux density equation is given implicitly by the integral momentum equation along the closed natural-circulation loop:

$$\Delta P_C(t) + \Delta P_r(t) + \Delta P_d(t) = 0, \tag{A.11}$$

where the different types of pressure drops accounted for in the model are summarized in the following table:

Inertia core	$z_{bb}(t)\frac{dM_{C,i}(t)}{dt} + [L_C - z_{bb}(t)]\frac{dM_{C,e}(t)}{dt} +$ $[M_{C,i}(t) - M_{C,e}(t)]\frac{dz_{bb}(t)}{dt}$
Inertia riser	$\sum_{n=1}^{N_r} \frac{L_r}{N_r}\frac{d<M>(t)_{r,n}}{dt}$
Inertia downcomer	$(\frac{L}{A})\frac{d\Phi(t)}{dt}$
Acceleration core	$\frac{M_{C,e}^2(t)}{\rho_f}\varphi^2[\chi_{C,e}(t)] - \frac{M_{C,i}^2(t)}{\rho_f}$
Acceleration riser	$\frac{M_{r,e}^2(t)}{\rho_f}\varphi^2[\chi_{r,e}(t)] - \frac{M_{r,i}^2(t)}{\rho_f}\varphi^2[\chi_{r,i}(t)]$
Acceleration downcomer	$\frac{\Phi^2(t)}{2\rho_f}(\frac{1}{A_{d,e}^2} - \frac{1}{A_{d,i}^2})$
Gravity core	$L_C g[\rho_f(1- < \alpha(t) >_C) + \rho_g < \alpha(t) >_C]$
Gravity riser	$\sum_{n=1}^{N_r} L_r g[\rho_f(1- < \alpha(t) >_{r,n}) + \rho_g < \alpha(t) >_{r,n}]$
Gravity downcomer	$-\rho_f g(L_C + L_r)$
Distributed friction core	$z_{bb}(t)\frac{f_C}{2D_C}\frac{M_{C,i}^2(t)}{\rho_f} + [L_C - z_{bb}(t)]\frac{f_C}{2D_C}\frac{M_{C,e}^2(t)}{\rho_f}\varphi^2[\frac{1}{2}\chi_{C,e}(t)]$
Distributed friction riser	$\sum_{n=1}^{N_r}\frac{L_r}{N_r}\frac{f_r}{2D_r}\frac{<M(t)>_{r,n}^2}{\rho_f}\varphi^2[< \chi(t) >_{r,n}]$
Local friction inlet core	$K_{C,i}\frac{M_{C,i}^2(t)}{2\rho_f}$
Local friction exit core	$K_{C,e}\frac{M_{C,e}^2(t)}{2\rho_f}\varphi^2[\chi_{C,e}(t)]$
Local friction exit riser	$K_{r,e}\frac{M_{r,e}^2(t)}{2\rho_f}\varphi^2[\chi_{r,e}(t)]$
Local friction inlet downcomer	$K_{d,i}\frac{M_{d,i}^2(t)}{2\rho_f}$

A.2 Transfer functions used in the frequency-domain approach

The following transfer functions appearing in the block diagram of figure 2.2 can be derived from the above equations. The zero-power reactivity transfer function derived from the point-kinetic equations is given as follows:

$$G_R = \frac{\frac{\delta P}{P_o}}{\delta \rho} = \frac{s + \lambda}{\Lambda s^2 + (\lambda \Lambda + \beta)s}. \tag{A.12}$$

The transfer function describing the heat transfer from fuel to coolant is

$$G_F = \frac{\frac{\delta q''}{q_o''}}{\frac{\delta P}{P_o}} = \frac{1}{\tau_f} \frac{1}{s + \frac{1}{\tau_f}}; \tag{A.13}$$

The transfer function from the heat flux and from the core-inlet mass flux to the boiling-boundary position are

$$G_{z_{bb},q''} = \frac{\frac{\delta z_{bb}}{z_{bb,o}}}{\frac{\delta q''}{q_o''}} = \frac{2}{\tau_{nb}} \frac{1}{s + \frac{1}{\tau_{nb}}}, \tag{A.14}$$

where

$$\tau_{nb} = \frac{z_{bb,o}\rho_l}{M_{C,i}};$$

and

$$G_{z_{bb},M_{C,i}} = -G_{z_{bb},q''}; \tag{A.15}$$

The transfer function from the heat flux and from the core-inlet mass flux to the core-averaged void fraction are

$$G_{\alpha,q''} = \frac{\frac{\delta <\alpha>_C}{<\alpha>_{C,o}}}{\frac{\delta q''}{q_o''}} = \frac{q_o''}{A_C H <\alpha>_o} \frac{1}{s + \frac{1}{\tau_{bb}}}, \tag{A.16}$$

where

$$\tau_{bb} = \frac{-H(L - z_{bb,o})}{2 M_{C,i}(h_l - h_g)\frac{\partial <x>}{\partial <\alpha>}},$$

$$H = (\rho_g h_g - \rho_l h_l) + [(1 - 2 <\chi>_o)h_l + 2 <\chi>_o h_g](\rho_l - \rho_g);$$

and

$$G_{\alpha,M_{C,i}} = -G_{\alpha,q''}; \tag{A.17}$$

The transfer function from the boiling-boundary position to the core-averaged void fraction is

$$G_{\alpha,z_{bb}} = \frac{\frac{\delta <\alpha>_C}{<\alpha>_{C,o}}}{\frac{\delta z_{bb}}{z_{bb,o}}} = \frac{z_{bb,o}}{L_C - z_{bb,o}} \frac{-\mu - \frac{1}{\tau_{bb}}}{s + \frac{1}{\tau_{bb}}}, \tag{A.18}$$

where

$$\mu = \frac{q_o'}{A_C H <\alpha>_o};$$

The transfer function from the core-averaged void fraction and from the boiling-boundary position to the core-inlet mass flux are

$$
G_{M_C,i,\alpha} = \frac{\frac{\delta M_{C,i}}{M_{C,i,o}}}{\frac{\delta <\alpha>_C}{<\alpha>_{C,o}}} = \frac{[(L_C - z_{bb,o} + L_r \frac{A_C}{A_r})s + K1]\frac{\partial M_{C,e}}{\partial <\alpha>_C} + Core + Riser}{(z_{bb,o} + (L - z_{bb,o})\frac{\partial M_{C,e}}{\partial M_{C,i}} + L_r \frac{A_C}{A_r} + \frac{L}{A_d}A_C)s + K1\frac{\partial M_{C,e}}{\partial M_{C,i}} + K2} \quad \text{(A.19)}
$$

and

$$
G_{M_C,i,z_{bb}} = \frac{\frac{\delta M_{C,i}}{M_{C,i,o}}}{\frac{\delta z_{bb}}{z_{bb,o}}} = \frac{[(L_C - z_{bb,o} + L_r \frac{A_C}{A_r})s + K1]\frac{\partial M_{C,e}}{\partial z_{bb}} + \frac{\partial \Delta P_{fr,C}}{\partial z_{bb}} + \frac{\partial \Delta P_{gr,C}}{\partial z_{bb}}}{(z_{bb,o} + (L - z_{bb,o})\frac{\partial M_{C,e}}{\partial M_{C,i}} + L_r \frac{A_C}{A_r} + \frac{L}{A_d}A_C)s + K1\frac{\partial M_{C,e}}{\partial M_{C,i}} + K2},
$$

$$\text{(A.20)}$$

where

$$
Core = \frac{\partial \Delta P_{acc,C}}{\partial <\alpha>_C} + \frac{\partial \Delta P_{fr,C}}{\partial <\alpha>_C} + \frac{\partial \Delta P_{gr,C}}{\partial <\alpha>_C} + \frac{\partial \Delta P_{fr,C,e}}{\partial <\alpha>_C},
$$

$$
Riser = (\frac{\partial \Delta P_{fr,r,e}}{\partial <\alpha>_r} + \frac{\partial \Delta P_{fr,r}}{\partial <\alpha>_r} + \frac{\partial \Delta P_{acc,r}}{\partial <\alpha>_r} + \frac{\partial \Delta P_{gr,r}}{\partial <\alpha>_r} + \frac{\partial \Delta P_{in,r}}{\partial <\alpha>_r})\frac{\partial <\alpha>_r}{\partial <\alpha>_C},
$$

$$
K1 = \frac{\partial \Delta P_{acc,C}}{\partial M_{C,e}} + \frac{\partial \Delta P_{fr,C}}{\partial M_{C,e}} + \frac{\partial \Delta P_{fr,C,e}}{\partial M_{C,e}} + (\frac{\partial \Delta P_{fr,r}}{\partial M_{C,e}} + \frac{\partial \Delta P_{fr,r,e}}{\partial M_{C,e}})\frac{A_C}{A_r},
$$

$$
K2 = \frac{\partial \Delta P_{acc,C}}{\partial M_{C,i}} + \frac{\partial \Delta P_{fr,C}}{\partial M_{C,i}} + \frac{\partial \Delta P_{acc,d}}{\partial M_{C,i}} + \frac{\partial \Delta P_{fr,d,i}}{\partial M_{C,i}}.
$$

The $\frac{\partial \Delta P}{\partial M}$, $\frac{\partial \Delta P}{\partial <\alpha>}$, $\frac{\partial \Delta P}{\partial z_{bb}}$ dynamic pressure drop derivatives appearing in $G_{M_C,i,\alpha}$ and $G_{M_C,i,z_{bb}}$ can be derived from the dynamic pressure drop terms listed in the above table in a straightforward manner.

Appendix B

System parameters

Dimensions

	Dodewaard	DESIRE
length of fuel rod $[mm]$	1800	830
diameter rod $[mm]$	13.5	6.23
area of a fuel assembly $[m^2]$	0.006981	0.001776
number of assemblies	164	1
riser length $[m]$	2.84	variable between 1.1 and 1.9
area riser $[m^2]$	2.58	0.003237
length downcomer $[m]$:		
along riser	2.84	variable between 1.1 and 1.9
along core	2.01	(see Section 3.1.3)
area downcomer $[m^2]$:		
along riser	3.52	varying (see Section 3.1.3)
along core	2.62	varying (see Section 3.1.3)
elevation of feedwater sparger from top of the core $[m]$	2.14	1.2

Friction coefficients

	Dodewaard	DESIRE
core inlet, $K_{C,i}$	3.46	variable: $3.0 - \infty$ (inlet valve)
core exit, $K_{C,e}$	3.02	3.02
riser exit, $K_{r,e}$	1.0	variable: $15.7 - \infty$ (exit valve)
downcomer inlet, $K_{d,i}$	1.0	1.155
distributed friction factor core, f_C	0.0164	0.021
distributed friction factor riser, f_r	0.0164	0.039

Nominal operating parameters

	Dodewaard	DESIRE
pressure $[bar]$	75.5	11.6
mass flux per assembly $[kgm^{-2}s^{-1}]$	1006	1137
average assembly power $[kW]$	1116	22.3
core inlet subcooling $[K]$	5	2
feedwater temperature $[K]$	408	268
inlet velocity $[ms^{-1}]$	1.37	0.93
channel transit time $[s]$	1.31	0.89

Netronic and fuel data set

	Dodewaard	DESIRE
fuel time constant $[s]$	2.11	0.5
$\xi k_f \; [Js^{-1}m^{-1}K^{-1}]$	$9.33 \cdot 10^5$	$5.69 \cdot 10^3$
β	0.0061	-
$\lambda \; [s^{-1}]$	0.084	-
$\Lambda \; [s^{-1}]$	$5 \cdot 10^{-5}$	-
$r_D \; [K^{-1}]$	$-2 \cdot 10^{-5}$	-

Appendix C

MONA input file example for DESIRE

```
!-------------------------------------------------------------
! MONA model of DESIRE
! This version of the input deck incorporates revised loss coefficient
! Change position for the valve
! 22 nodes for fuel assembly nodalization
! FINAL VERSION (used for dynamics experiments)
!-------------------------------------------------------------

CASE PROJECT = "Mona model of DESIRE"
!
!-------------------------------------------------------------
! Branch Data
!-------------------------------------------------------------

BRANCH ID=1
! Downcomer
PIPE  ID=1, DH=0.023, AREA=0.003611, LENGTH=1.000, ELEVATION=-
1.000, \
    EPSABS=5.0E-6,  NSEG=7, DZ = (0.05, 0.1, 0.15, 0.2, 0.2, 0.2, \
    0.1)          ! Upper Downcomer (fixed length)
!
PIPE  ID=2,  DH=0.030, AREA=0.004500, LENGTH=0.248, ELEVATION=-
0.248, \
    EPSABS=5.0E-6,  NSEG=2, DZ = (0.150, 0.098)
!
BRANCH ID=10
! Downcomer Loop 1
! An entrance loss coefficient for the horizontal section of each
! loop must be defined to account for the 90 degree flow redirection
! from the lower downcomer.
!
PIPE  ID=10, DH=0.040, AREA=0.001257, LENGTH=0.350, ELEVATION=
0.000, \
    EPSABS=5.0E-6,  NSEG=2 ! Horizontal section
PIPE  ID=11, DH=0.040, AREA=0.001257, LENGTH=0.550, ELEVATION=-
0.350, \
    EPSABS=5.0E-6,  NSEG=2 ! 90 Degree bend
PIPE  ID=12, DH=0.040, AREA=0.001257, LENGTH=1.000, ELEVATION=-
1.000, \
    EPSABS=5.0E-6,  NSEG=5 ! Upper vertical section
PIPE  ID=13, DH=0.030, AREA=0.000707, LENGTH=0.550, ELEVATION=-
0.550, \
    EPSABS=5.0E-6,  NSEG=2 ! Lower vertical section
PIPE  ID=14, DH=0.040, AREA=0.001257, LENGTH=0.550, ELEVATION=-
0.350, \
    EPSABS=5.0E-6,  NSEG=2 ! 90 Degree bend down
PIPE  ID=15, DH=0.040, AREA=0.001257, LENGTH=0.550, ELEVATION=
0.350, \
    EPSABS=5.0E-6,  NSEG=2 ! 90 Degree bend up
!
BRANCH ID=20
! Downcomer Loop 2
PIPE  ID=20, DH=0.040, AREA=0.001257, LENGTH=0.350, ELEVATION=
0.000, \
    EPSABS=5.0E 6,  NSEG=2 ! Horizontal section
PIPE  ID=21, DH=0.040, AREA=0.001257, LENGTH=0.550, ELEVATION=-
0.350, \
    EPSABS=5.0E-6,  NSEG=2 ! 90 Degree bend
PIPE  ID=22, DH=0.040, AREA=0.001257, LENGTH=1.000, ELEVATION=-
1.000, \
    EPSABS=5.0E-6,  NSEG=5 ! Upper vertical section
PIPE  ID=23, DH=0.030, AREA=0.000707, LENGTH=0.550, ELEVATION=-
0.550, \
    EPSABS=5.0E-6,  NSEG=2 ! Lower vertical section
PIPE  ID=24, DH=0.040, AREA=0.001257, LENGTH=0.550, ELEVATION=-
0.350, \
    EPSABS=5.0E-6,  NSEG=2 ! 90 Degree bend down
PIPE  ID=25, DH=0.040, AREA=0.001257, LENGTH=0.550, ELEVATION=
0.350, \
    EPSABS=5.0E-6,  NSEG=2 ! 90 Degree bend up
!
BRANCH ID=30
! Downcomer Loop 3
PIPE  ID=30, DH=0.040, AREA=0.001257, LENGTH=0.350, ELEVATION=
0.000, \

    EPSABS=5.0E-6,  NSEG=2 ! Horizontal section
PIPE  ID=31, DH=0.040, AREA=0.001257, LENGTH=0.550, ELEVATION=-
0.350, \
    EPSABS=5.0E-6,  NSEG=2 ! 90 Degree bend
PIPE  ID=32, DH=0.040, AREA=0.001257, LENGTH=1.000, ELEVATION=-
1.000, \
    EPSABS=5.0E-6,  NSEG=5 ! Upper vertical section
PIPE  ID=33, DH=0.030, AREA=0.000707, LENGTH=0.550, ELEVATION=-
0.550, \
    EPSABS=5.0E-6,  NSEG=2 ! Lower vertical section
PIPE  ID=34, DH=0.040, AREA=0.001257, LENGTH=0.550, ELEVATION=-
0.350, \
    EPSABS=5.0E-6,  NSEG=2 ! 90 Degree bend down
PIPE  ID=35, DH=0.040, AREA=0.001257, LENGTH=0.550, ELEVATION=
0.350, \
    EPSABS=5.0E-6,  NSEG=2 ! 90 Degree bend up
!
BRANCH ID=40
! Downcomer Loop 4
PIPE  ID=40, DH=0.040, AREA=0.001257, LENGTH=0.350, ELEVATION=
0.000, \
    EPSABS=5.0E-6,  NSEG=2 ! Horizontal section
PIPE  ID=41, DH=0.040, AREA=0.001257, LENGTH=0.550, ELEVATION=-
0.350, \
    EPSABS=5.0E-6,  NSEG=2 ! 90 Degree bend
PIPE  ID=42, DH=0.040, AREA=0.001257, LENGTH=1.000, ELEVATION=-
1.000, \
    EPSABS=5.0E-6,  NSEG=5 ! Upper vertical section
PIPE  ID=43, DH=0.030, AREA=0.000707, LENGTH=0.550, ELEVATION=-
0.550, \
    EPSABS=5.0E-6,  NSEG=2 ! Lower vertical section
PIPE  ID=44, DH=0.040, AREA=0.001257, LENGTH=0.550, ELEVATION=-
0.350, \
    EPSABS=5.0E-6,  NSEG=2 ! 90 Degree bend down
PIPE  ID=45, DH=0.040, AREA=0.001257, LENGTH=0.550, ELEVATION=
0.350, \
    EPSABS=5.0E-6,  NSEG=2 ! 90 Degree bend up
!
BRANCH ID=50
! Lower Plenum, Upper Plenum, Assembly
!
PIPE ID=50, DH=0.0895, AREA=0.006291, LENGTH=0.290, ELEVATION=
0.290, \
    EPSABS=5.0E-6,  NSEG=2 ! Lower plenum
PIPE ID=51, DH=0.050, AREA=0.001964, LENGTH=0.600, ELEVATION=
0.600, \
    EPSABS=5.0E-6,  NSEG=5, DZ=(0.08, 0.12 ,0.12 ,0.08 ,0.2 ) ! Upper plenum
PIPE ID=52, DH=0.00764, AREA=0.001776, LENGTH=0.012, ELEVATION=
0.012, \
    EPSABS=5.0E-6,  NSEG=1 ! Assembly unheated section
PIPE ID=53, DH=0.00764, AREA=0.001776, LENGTH=0.880, ELEVATION=
0.880, \
    EPSABS=5.0E-6,  NSEG=22! Assembly heated section
PIPE ID=54, DH=0.00764, AREA=0.001776, LENGTH=0.066, ELEVATION=
0.066, \
    EPSABS=5.0E-6,  NSEG=1 ! Assembly unheated section
!
BRANCH ID=60
! Riser
PIPE  ID=60, DH=0.054, AREA=0.002916, LENGTH=1.000, ELEVATION=
1.000, \
    EPSABS=5.0E-7,  NSEG=5 ! Lower Riser (fixed length)
PIPE  ID=61, DH=0.061, AREA=0.003721, LENGTH=0.300, ELEVATION=
0.300, \
    EPSABS=5.0E-7,  NSEG=4, DZ = (0.1, 0.1, 0.05, 0.05)
!                    Upper Riser (variable length)
!
PIPE  ID=62, DH=0.3281, AREA=0.165096, LENGTH=0.03925,
ELEVATION= 0.000, \
                 NSEG=1 ! horizontal connecting pipe.
!
BRANCH ID=70
! Steam Dome
PIPE  ID=70, DH=0.090, AREA=0.008100, LENGTH=1.100, ELEVATION=
1.100, \
```

```
EPSABS=5.0E-6,  NSEG=9, DZ = (0.05, 0.05, 0.1, 0.1, 0.1, 0.1, \
     0.2, 0.2, 0.2)
!                    Steam Dome (variable length)
!
!-------------------------------------------------------------------
! Network Data
!-------------------------------------------------------------------
!
TABLE LABEL=PEAK, X = TIME, F= PT
TABLE POINT = (0.,  11.60E+5)
TABLE POINT = (200., 11.60E+5)
!TABLE POINT = (45.1, 12.4E+5)
!TABLE POINT = (45.2, 11.60E+5)
!TABLE POINT = (300., 11.60E+5)
NETWOR NODE=1, TYPE=SPLIT ! Downcomer, Riser, Steam Dome (reference
Riser)
NETWOR NODE=2, TYPE=SPLIT ! Downcomer to Downcomer Loops
(reference Downcomer)
NETWOR NODE=3, TYPE=MERGE ! Downcomer Loops to Lower Plenum
(reference L.P.)
NETWOR NODE=4, TYPE=MERGE ! Assembly to Lower Riser (reference
Lower Riser)
NETWOR NODE=5, TYPE=TERMINAL, PTTAB = PEAK, \
     TL = 48.00 C, TG = 48.00 C ! Steam "Outlet"
NETWOR BRANCH= 1, ORIGIN = 1, DESTINATION = 2, OANG= 90 ! D.C. -
Inlet to Exit
NETWOR BRANCH=10, ORIGIN = 2, DESTINATION = 3 ! Loop 1 Inlet to
Exit
NETWOR BRANCH=20, ORIGIN = 2, DESTINATION = 3 ! Loop 2 "      "
NETWOR BRANCH=30, ORIGIN = 2, DESTINATION = 3 ! Loop 3 "      "
NETWOR BRANCH=40, ORIGIN = 2, DESTINATION = 3 ! Loop 4 "      "
NETWOR BRANCH=50, ORIGIN = 3, DESTINATION = 4 ! Lower Plenum to
Lower Riser
NETWOR BRANCH=60, ORIGIN = 4, DESTINATION = 1 ! Lower Riser to
Steam Dome
NETWOR BRANCH=70, ORIGIN = 1, DESTINATION = 5 ! Steam Dome to
Outlet
!
!-------------------------------------------------------------------
! Fluid
!-------------------------------------------------------------------
!
FLUID  PROP=R12, FILE="dka11:[zboray]R12.DAT"
!
!-------------------------------------------------------------------
! Special components
!-------------------------------------------------------------------
!
! Define an entrance loss coefficient for the inlet to the upper
! downcomer.  Treat the entrance as square-edged (Reference Fox &
! McDonald, "Introduction to Fluid Mechanics", Table 8.1, page 366).
!
LOSS BRANCH=1, PIPE=1, LOC=1, BPOS=0.5 ! Upper Downcomer inlet
!
! Define an entrance loss coefficient for the exit of the upper
! downcomer.  Treat the entrance as an expansion (Reference Fox &
! McDonald, "Introduction to Fluid Mechanics", Fig. 8.17 page 367).
!
LOSS BRANCH=1, PIPE=2, LOC=1, BPOS=0.05 ! Upper Downcomer exit
!
TABLE LABEL=BEND, X = REYN, F = BPOS
TABLE POINT = (8.5E+3,  0.4181)
TABLE POINT = (1E+4,    0.4050)
TABLE POINT = (2E+4,    0.3371)
TABLE POINT = (4E+4,    0.2874)
TABLE POINT = (6E+4,    0.26132)
TABLE POINT = (1E+5,    0.23519)
TABLE POINT = (3.5E+5, 0.1829)
!
LOSS BRANCH=10, PIPE=14, LOC=1, BPOS=19.73 ! Experimental value,
lumped coeff.
!
LOSS BRANCH=20, PIPE=24, LOC=1, BPOS=15.95 ! Experimental value,
lumped coeff
!
```

```
LOSS BRANCH=30, PIPE=34, LOC=1, BPOS=19.01 ! Experimental value,
lumped coeff.
!
LOSS BRANCH=40, PIPE=44, LOC=1, BPOS=19.68 ! Experimental value,
lumped coeff.
!
! The contraction of the lower plenum from 129 mm diameter to a 50 mm
! diameter is modeled as a reversible pressure loss.  Treat the loss
! coefficient as a gradual contraction (Reference Fox & McDonald,
! "Introduction to Fluid Mechanics", Table 8.2, page 367).
!
! It was changed here to branch=50 extraction at cone inlet
!
LOSS BRANCH=50, PIPE=50, LOC=2, BPOS=0.79   ! Lower plenum inlet
LOSS BRANCH=50, PIPE=51, DPAREA=ON, BPOS=0.1 ! Lower plenum
!
! The flow control valve in the upper plenum is modeled directly.
! The valve discharge coefficient is defined assuming a gate valve
! (Reference Fox & McDonald, "Introduction to Fluid Mechanics",
! Table 8.3, page 371). The valve relative flow area can be varied
! to match experimentally measured recirculation flows.
!
VALVE BRANCH=50, PIPE=51, LOC=3, CD=1.0, DMAX=0.050, AREL=1.0
!
! Assembly entrance loss coefficient as provided by KEMA from
! their TRAC input deck.
!
LOSS BRANCH=50, PIPE=52, LOC=1, BPOS=3.343 ! Assembly inlet (3.343)
!
! The spacers in the assembly are modeled by a pressure loss.  The
! spacers are located 251, 491, and 731 mm from the bottom of the
! fuel assembly.  With 14 axial sections, these locations correspond
! approximately to sections 4, 8, and 11. The loss coefficient (BPOS)
! needs to be adjusted to yield the proper pressure drop across the
! spacers. Spacer value as provided by KEMA from their TRAC input deck.
!
LOSS BRANCH=50, PIPE=53, LOC=(6,12,18), BPOS=0.775 ! Assembly
spacers.
!
! Assembly exit loss coefficient as provided by KEMA from their TRAC
! input deck (note that their value includes the assembly upper tie
! and the chimney, so these values are combined herein)
!
LOSS BRANCH=50, PIPE=54, LOC=1, BPOS=0.87 ! Assembly outlet
!
! Define an entrance loss coefficient for the outlet of the lower
! riser.  Treat the outlet as an expansion (Reference Fox & McDonald,
! "Introduction to Fluid Mechanics", Fig. 8.17 page 367).
!
LOSS BRANCH=60, PIPE=61, LOC=1, BPOS=0.07 ! Upper riser inlet
!
LOSS BRANCH=60, PIPE=61, LOC=4, BPOS=64.  ! Riser exit
!
LOSS BRANCH=60, PIPE=62, LOC=1, BPOS=0.28 ! Steam dome inlet
!
! The steam dome is currently modeled in MONA as a split node with a
! stagnant water level.  The carry under and carry over volume fractions
! are user input, not calculated.
!
SEPARATOR MODEL=DOME, NODE=1, GASLEG=70, CAROV=0,
CARUN=0.110
!
!-------------------------------------------------------------------
! initial conditions
!
!-------------------------------------------------------------------
INITIAL BRANCH=1,  TL=44.70 C, TG=48.00 C, AL=0.0000, PT=11.65E+5,
WT=1.122
INITIAL BRANCH=10, TL=44.60 C, TG=48.00 C, AL=0.0000, PT=11.90E+5,
WT=0.273
INITIAL BRANCH=20, TL=44.60 C, TG=48.00 C, AL=0.0000, PT=11.90E+5,
WT=0.273
INITIAL BRANCH=30, TL=44.60 C, TG=48.00 C, AL=0.0000, PT=11.90E+5,
WT=0.273
```

```
INITIAL BRANCH=40, TL=44.60 C, TG=48.00 C, AL=0.0000, PT=11.90E+5,
WT=0.273
INITIAL BRANCH=50, PIPE=50-52,\
        TL=44.47 C, TG=49.00 C, AL=0.0000, PT=11.88E+5, WT=1.123
INITIAL BRANCH=50, PIPE=53, LOC= 1-6, \
        TL=46.00 C, TG=48.80 C, AL=0.0300, PT=11.84E+5, WT=1.123
INITIAL BRANCH=50, PIPE=53, LOC= 7-8, \
        TL=48.0 C, TG=48.77 C, AL=0.100, PT=11.82E+5, WT=1.123
INITIAL BRANCH=50, PIPE=53, LOC= 9-10, \
        TL=48.70 C, TG=48.74 C, AL=0.2000, PT=11.81E+5, WT=1.123
INITIAL BRANCH=50, PIPE=53, LOC= 11-12, \
        TL=48.85 C, TG=48.71 C, AL=0.3200, PT=11.80E+5, WT=1.123
INITIAL BRANCH=50, PIPE=53, LOC= 13-14, \
        TL=48.82 C, TG=48.69 C, AL=0.4000, PT=11.79E+5, WT=1.123
INITIAL BRANCH=50, PIPE=53, LOC= 15-16, \
        TL=48.79 C, TG=48.66 C, AL=0.4700, PT=11.78E+5, WT=1.123
INITIAL BRANCH=50, PIPE=53, LOC=17-18, \
        TL=48.74 C, TG=48.64 C, AL=0.5100, PT=11.78E+5, WT=1.123
INITIAL BRANCH=50, PIPE=53, LOC=19, \
        TL=48.71 C, TG=48.62 C, AL=0.5300, PT=11.77E+5, WT=1.123
INITIAL BRANCH=50, PIPE=53, LOC=20, \
        TL=48.69 C, TG=48.61 C, AL=0.5450, PT=11.77E+5, WT=1.123
INITIAL BRANCH=50, PIPE=53, LOC=21, \
        TL=48.67 C, TG=48.59 C, AL=0.5540, PT=11.77E+5, WT=1.123
INITIAL BRANCH=50, PIPE=53, LOC=22, \
        TL=48.64 C, TG=48.58 C, AL=0.5590, PT=11.76E+5, WT=1.123
INITIAL BRANCH=50, PIPE=54, \
        TL=48.57 C, TG=48.55 C, AL=0.5600, PT=11.76E+5, WT=1.123
INITIAL BRANCH=60, TL=48.30 C, TG=48.30 C, AL=0.5000, PT=11.70E+5,
WT=1.123
INITIAL BRANCH=70, TL=48.00 C, TG=48.0 C, AL=1.0000, PT=11.60E+5,
WT=0.113


!
!-----------------------------
! Heat Structure Material Data
!-----------------------------
!
! The "fuel rods" consist of 6.35 mm O.D. Incoloy 800 tubes with a wall
! thickness of 0.3 mm. The tube is filled with boron nitrate.
!
MATERI LABEL = INCOLOY, COND = 13.968, CP = 502.4, DENS = 8025.25
MATERI LABEL = BORNITR, COND = 1.8025, CP = 1381.6, DENS = 2274.62
!
!--------------------------------
! End of Heat Structure Material Data
!--------------------------------
!
!
!-----------------------------------------------------------
! Heat Structure Geometry Data
!-----------------------------------------------------------
GEOMET LABEL = FRODS , TYPE = CYLIND , ORIGIN = 0.
ZONE NSEG = 5, SEGTY = ERAD, MATERI = BORNITR, ENDCOO =
.002875, RELPOW = 1
ZONE NSEG = 2, SEGTY = ERAD, MATERI = INCOLOY, ENDCOO =
.003175, RELPOW = 0
!-----------------------------------------------------------
! Heat Structure Coupling
!-----------------------------------------------------------
WALL HS=FRODS,IDHS= 1,RIGHT=PIPE,RBRANCH=50,RPIPE=53,RLOC=
1,SURMUL=35
WALL HS=FRODS,IDHS= 2,RIGHT=PIPE,RBRANCH=50,RPIPE=53,RLOC=
2,SURMUL=35
WALL HS=FRODS,IDHS= 3,RIGHT=PIPE,RBRANCH=50,RPIPE=53,RLOC=
3,SURMUL=35
WALL HS=FRODS,IDHS= 4,RIGHT=PIPE,RBRANCH=50,RPIPE=53,RLOC=
4,SURMUL=35
WALL HS=FRODS,IDHS= 5,RIGHT=PIPE,RBRANCH=50,RPIPE=53,RLOC=
5,SURMUL=35
WALL HS=FRODS,IDHS= 6,RIGHT=PIPE,RBRANCH=50,RPIPE=53,RLOC=
6,SURMUL=35
WALL HS=FRODS,IDHS= 7,RIGHT=PIPE,RBRANCH=50,RPIPE=53,RLOC=
7,SURMUL=35
WALL HS=FRODS,IDHS= 8,RIGHT=PIPE,RBRANCH=50,RPIPE=53,RLOC=
8,SURMUL=35
WALL HS=FRODS,IDHS= 9,RIGHT=PIPE,RBRANCH=50,RPIPE=53,RLOC=
9,SURMUL=35
WALL
HS=FRODS,IDHS=10,RIGHT=PIPE,RBRANCH=50,RPIPE=53,RLOC=10,SUR
MUL=35
WALL
HS=FRODS,IDHS=11,RIGHT=PIPE,RBRANCH=50,RPIPE=53,RLOC=11,SUR
MUL=35
WALL
HS=FRODS,IDHS=12,RIGHT=PIPE,RBRANCH=50,RPIPE=53,RLOC=12,SUR
MUL=35
WALL
HS=FRODS,IDHS=13,RIGHT=PIPE,RBRANCH=50,RPIPE=53,RLOC=13,SUR
MUL=35
WALL
HS=FRODS,IDHS=14,RIGHT=PIPE,RBRANCH=50,RPIPE=53,RLOC=14,SUR
MUL=35
WALL
HS=FRODS,IDHS=15,RIGHT=PIPE,RBRANCH=50,RPIPE=53,RLOC=15,SUR
MUL=35
WALL
HS=FRODS,IDHS=16,RIGHT=PIPE,RBRANCH=50,RPIPE=53,RLOC=16,SUR
MUL=35
WALL
HS=FRODS,IDHS=17,RIGHT=PIPE,RBRANCH=50,RPIPE=53,RLOC=17,SUR
MUL=35
WALL
HS=FRODS,IDHS=18,RIGHT=PIPE,RBRANCH=50,RPIPE=53,RLOC=18,SUR
MUL=35
WALL
HS=FRODS,IDHS=19,RIGHT=PIPE,RBRANCH=50,RPIPE=53,RLOC=19,SUR
MUL=35
WALL
HS=FRODS,IDHS=20,RIGHT=PIPE,RBRANCH=50,RPIPE=53,RLOC=20,SUR
MUL=35
WALL
HS=FRODS,IDHS=21,RIGHT=PIPE,RBRANCH=50,RPIPE=53,RLOC=21,SUR
MUL=35
WALL
HS=FRODS,IDHS=22,RIGHT=PIPE,RBRANCH=50,RPIPE=53,RLOC=22,SUR
MUL=35
!-----------------------------------------------------------------------
! Heat Structure Power - Define an axial cosine+offset distribution
!-----------------------------------------------------------------------
TABLE LABEL = RAMP, X= TIME, F=POWER
TABLE POINT = (0., 24444)
TABLE POINT = (60., 28000)
POWER POWER = 35590, STRUCTURE=1
POWER HSPOWER= 0.017167560, IDHS = 1
POWER HSPOWER= 0.024227842, IDHS = 2
POWER HSPOWER= 0.031071793, IDHS = 3
POWER HSPOWER= 0.037560090, IDHS = 4
POWER HSPOWER= 0.043560654, IDHS = 5
POWER HSPOWER= 0.048951327, IDHS = 6
POWER HSPOWER= 0.053622372, IDHS = 7
POWER HSPOWER= 0.057478699, IDHS = 8
POWER HSPOWER= 0.060441806, IDHS = 9
POWER HSPOWER= 0.062451371, IDHS = 10
POWER HSPOWER= 0.063466486, IDHS = 11
POWER HSPOWER= 0.063466486, IDHS = 12
POWER HSPOWER= 0.062451371, IDHS = 13
POWER HSPOWER= 0.060441806, IDHS = 14
POWER HSPOWER= 0.057478699, IDHS = 15
POWER HSPOWER= 0.053622372, IDHS = 16
POWER HSPOWER= 0.048951327, IDHS = 17
POWER HSPOWER= 0.043560654, IDHS = 18
POWER HSPOWER= 0.037560090, IDHS = 19
POWER HSPOWER= 0.031071793, IDHS = 20
POWER HSPOWER= 0.024227842, IDHS = 21
POWER HSPOWER= 0.017167560, IDHS = 22
!--------------------------------------------------------------------
! operational conditions and execution mode
!--------------------------------------------------------------------
!
! The source defines the location and flow rate of the "feedwater". Note
```

```
! that the source location can be either in the horizontal riser section
! (with the telescoping riser extended less than 2 cm ) or in the upper
! downcomer (with the telescoping riser extended beyond 2 cm).
!
SOURCE BRANCH=1, PIPE=1, LOC=2, STL= -6.60 C, LFL1 = 0.188
!
INTEGRATION TBEG=0., TEND=200., DTSTART=.001, DTMAX=1.,
STABLIMIT=ON
!
!--------------------------------------------------------------------------------
! output declarations
!--------------------------------------------------------------------------------
!
TABLE  LABEL = PRNTOUT, X = TIME, F = DTOUT
TABLE  POINT = (0., 10.)
OUTPUT BRANCH=1, DTOUTTAB = PRNTOUT, \
     VAR= (GG, GL, GD, WG, WL, WD, WT, AL, GA, TL C, TG C, PT, \
     ID, VOL, DZ, ZZ, ZZVOL, STL, COSAF)
OUTPUT BRANCH=10, DTOUTTAB = PRNTOUT, \
     VAR= (GG, GL, GD, WG, WL, WD, WT, AL, GA, TL C, TG C, PT, \
     ID, VOL, DZ, ZZ, ZZVOL, STL, COSAF)
OUTPUT BRANCH=50, DTOUTTAB = PRNTOUT, \
     VAR= (GG, GL, GD, WG, WL, WD, WT, AL, GA, TL C, TSAT C, TG C, \
        PT, ID, VOL, DZ, ZZ, ZZVOL, STL, COSAF, UG, UL)
OUTPUT BRANCH=60, DTOUTTAB = PRNTOUT, \
     VAR= (GG, GL, GD, WG, WL, WD, WT, AL, GA, TL C, TG C, PT, \
     ID, VOL, DZ, ZZ, ZZVOL, STL, COSAF, UG, UL)
OUTPUT IDHS = 1-22, DTOUTTAB = PRNTOUT, \
     VAR= (IDHR, RHFL, RTEM C)
OUTPUT BRANCH=70, DTOUTTAB = PRNTOUT, \
     VAR= (GG, GL, GD, WG, WL, WD, WT, AL, GA, TL C, TG C, PT, \
     ID, VOL, DZ, ZZ, ZZVOL, STL, COSAF)
OUTPUT VAR= (RMERR, RMOUT, RMTOT, RM0TOT, \
        EERR, EOUT, QOUTW, ETOT, E0TOT, VOLGBL )
!
!--------------------------------------------------------------------------------
! plot file declarations
!--------------------------------------------------------------------------------
!
TABLE LABEL = PLTOUT, X= TIME, F = DTPLO
TABLE POINT = (0., .04)
TABLE POINT = (200., .04)
TABLE POINT = (201., 0.04)
TABLE POINT = (300., 0.04)
!TABLE POINT = (111., 0.8)
!TABLE POINT = (120., 0.8)
!PLOT TYPE=TRACE, DTPLOTAB = PLTOUT, BRANCH=1, \
!   VAR= (AL, GD, GG, GL, \
!      ROG, ROL, WG, WL, WD, WT, UD, UG, UL, \
!        PT, TL C, TG C, TSAT C,)
!PLOT TYPE=TRACE,DTPLOTAB = PLTOUT,  BRANCH=10, \
!   VAR= (AL, GD, GG, GL, \
!      ROG, ROL, WG, WL, WD, WT, UD, UG, UL, \
!        PT, TL C, TG C, TSAT C,)
PLOT TYPE=TRACE,DTPLOTAB = PLTOUT,  BRANCH=50, PIPE=53, \
     VAR= (AL, GD, GG, GL, ID, \
        ROG, ROL, WG, WL, WD, WT, UD, UG, UL, \
        PT, TL C, TG C, TSAT C,HL,HG,)
PLOT TYPE=TRACE,DTPLOTAB = PLTOUT,  BRANCH=60, \
     VAR= (AL, GD, GG, GL, ID, \
        ROG, ROL, WG, WL, WD, WT, UD, UG, UL, \
        PT, TL C, TG C, TSAT C,)
!PLOT TYPE=TRACE,DTPLOTAB = PLTOUT,  BRANCH=70, \
!   VAR= (AL, GD, GG, GL, \
!      ROG, ROL, WG, WL, WD, WT, UD, UG, UL, \
!        PT, TL C, TG C, TSAT C,)
PLOT TYPE=trace, DTPLOTAB = PLTOUT,  VAR= (VOLGBL)
ENDCASE
```

Nomenclature

a	thermal diffusivity	m^2s^{-1}
A	cross-sectional flow area	m^2
	constant of proportionality	–
a_i	autoregressive coefficients	–
	auxiliary parameter	–
B	auxiliary parameter	–
c	delayed neutron precursor population	m^{-3}
C	constant of proportionality	–
$C(R)$	correlation sum	–
C_D	correlation dimension	–
d	embedding dimension	–
D	dimension of the attractor	–
	one-group diffusion coefficient	m
	hydraulic diameter	m
$\widehat{D}$	destruction operator	–
f_p	axial power peaking factor	–
f	frequency	s^{-1}
	Fanning friction factor	–
g	gravitational acceleration	ms^{-2}
G_0	auxiliary transfer function	–
G_1	auxiliary transfer function	–
G_2	auxiliary transfer function	–
G_3	auxiliary transfer function	–
G_A	normalized transfer function from heat flux to void fraction	–
G_F	normalized transfer function from power to heat flux	–
G_R	zero power reactivity transfer function	–
G_T	closed-loop transfer function from external reactivity to power	–
$G_{x,y}$	transfer function from y to x	–
h	specific enthalpy	Jkg^{-1}
H	auxiliary variable	Jm^{-3}
J_2	dimensionless auxiliary functions	–
k	thermal conductivity	$Js^{-1}K^{-1}$
k_f	fuel heat transfer coefficient	$Js^{-1}K^{-1}m^{-2}$
K	friction factor	–
	Kolmogorov entropy	$bits^{-1}$
K	auxiliary function	–
K_1	auxiliary function	m
l_o	maximal scaling distance	–
L	length	m

M	mass flux density	$kgm^{-2}s^{-1}$
n	neutron population	m^{-3}
p	probability distribution function	—
P	pressure	$kgm^{-1}s^{-2}$
	power	Js^{-1}
P_d	dimensionless auxiliary functions	—
$\widehat{P}$	production operator	—
q'	linear power production in the fuel	$Jm^{-1}s^{-1}$
q''	heat flux density from fuel to coolant	$Jm^{-2}s^{-1}$
r_D	Doppler reactivity coefficient	K^{-1}
r_n	minimal scaling distance	—
s	Laplace variable	s^{-1}
S	entropy	—
u	velocity	ms^{-1}
U	Mann-Whitney rank sum	—
t	time	s
T	oscillation period	s^{-1}
	average cycle time	s^{-1}
	temperature	K
$\vec{v}$	state vector	—
v	velocity	ms^{-1}
V	volume	m^3
$\boldsymbol{x}$	state space vector	—
x_i	time series	—
z	axial position	m
	Z-transform variable	—
Z	statistical variable	—

Greek symbols

α	void fraction	—
α_D	normalized Doppler reactivity coefficient	—
α_v	void reactivity coefficients	—
β	delayed neutron fraction	—
	Floquet exponent	—
β_2	Hopf bifurcation parameter	—
χ	flow quality, thermodynamic equilibrium quality	—
δ	Feigenbaum's constant	—
ϵ	auxiliary parameter	—
λ	eigenvalue	—
	Lyapunov exponent	$bits^{-1}$
	delayed neutron precursor decay constant	s^{-1}
Λ	neutron generation time	s
μ	Feigenbaum's constant	—
μ_2	Hopf bifurcation parameter	—
ν	bifurcation parameter	—
	average number of neutrons released per fission	—
ω	the imaginary part of s	s^{-1}
	angular frequency	s^{-1}

ρ	density	kgm^{-3}
	reactivity	—
σ	the real part of s	s^{-1}
Σ_a	one-group absorption cross section	m^{-1}
Σ_a	one-group fission cross section	m^{-1}
τ	time constant	s
	sampling time	s
	transit time	s
τ_2	Hopf bifurcation parameter	—
Θ	Heaviside operator	—
ϕ	neutron flux	$m^{-2}s^{-1}$
	phase difference	rad
Φ	mass flow rate	kgs^{-1}
φ	two-phase friction multiplier	—
ξ	heated perimeter	m

Subscripts

∞	chaotic limit	
$1-\phi$	one phase	
$2-\phi$	two phase	
acc	acceleration	
bb	boiling boundary	
C	core	
c	critical	
com	combined	
d	downcomer	
eff	effective	
e	exit	
f	saturated liquid	
	fuel	
fr	friction	
fw	feed water	
g	saturated gas	
g	gravitation	
i	inlet	
in	inertia	
l	property of the liquid phase	
mes	measured	
ML	maximum-likelihood	
nb	non-boiling	
o	steady state	
p	peak	
pro	profile	
ps	power supply	
r	riser	
rec	reconstructed	
sat	saturation	
sen	sensor	

sub	subcooling
sp	sparger
v	void
z	transfer function in discrete time

Superscripts

$+$	adjoint
$*$	dimensionless

Operators

Δ	difference
δ	fluctuating part level
∇	nabla operator
$<>$	spatial average
	ensemble average

Dimensionless numbers

N_{Fr}	Froude number
N_{sub}	Subcooling number
N_{Zu}	Zuber (phase change) number
N_t	dimensionless group to scale the neutronics for the artificial void-reactivity feedback simulation

Abbreviations

ACF	auto-correlation function
ANL	Argonne National Laboratory
APSD	auto power spectral density
AR	autoregressive
ARMA	autoregressive moving average
BifDD	bifurcation analysis of delay-differential equations, code
BIFOR	bifurcation formula, code
BORAX	Boiling water reactor experiments
BGO	bismuth germanate oxide
BWR	boiling water reactor
CCF	cross-correlation function
CPSD	cross-power spectral density
DESIRE	Delft Simulated Reactor
DC	digital controller
DR	decay ratio
EBWR	Experimental boiling water reactor
ESBWR	European simplified boiling water reactor
GE	General Electric Company
HEM	homogeneous equilibrium mixture model
MONA	thermal-hydraulic system code
NACUSP	Natural circulation and stability performance of BWRs
ODE	ordinary differential equation
OECD	Organization for Economic Co-operation and Development
PID	proportional integral derivative

PS   power supply
RAMONA reactor transient code
SB   stability boundary
SBWR   Simplified boiling water reactor
ZOH   zero-order hold

List of publications

R. Zboray, W.J.M. de Kruijf and T.H.J.J. van der Hagen, "Stabilising boiling water reactors by optimising the position of the feedwater sparger", To be published in *Nucl. Eng. Des.*

R. Zboray, W.J.M. de Kruijf, T.H.J.J. van der Hagen and Rizwan-uddin, "Investigating the nonlinear dynamics of natural-circulation, boiling two-phase flows", To be published in *Int. Journal of Multiphase Flow*

Manera, A., R. Zboray, T.H.J.J. van der Hagen, "Assessment of linear and nonlinear auto-regressive methods for BWR stability monitoring", *Symposium on Nuclear Reactor Surveillance and Diagnostics, SMORN VIII* (2002)

R. Zboray, W.J.M. de Kruijf, T.H.J.J. van der Hagen and H. van Dam, "Investigating on the Stability Characteristics of Natural Circulation Boiling Water Reactors Using Root Loci of a Reduced-order Model", *Nucl. Technol.*, **136**, No.3, p. 301-3014, (2001)

R. Zboray, W.J.M. de Kruijf, T.H.J.J. van der Hagen, "Experiments on the relation between the transit time and the oscillation period of density-waves", *Proceedings of the 4th International Conference on Multiphase Flow, May 27- June 1. (2001), New Orleans, USA*. Also accepted for publication in the special issue of the International Journal of Multiphase Flow, February 2002.

R. Zboray, W.J.M. de Kruijf, T.H.J.J. van der Hagen and H. van Dam, "On the Qualification of Boiling Water Reactor Stability Margin Indicators Using Linear Stability Analysis", *Proc. of Physor 2000, May 7-11*, 2000, Pittsburg, Pennsylvania, USA

R. Zboray, T.H.J.J. van der Hagen, W.J.M. de Kruijf and H. van Dam, "Numerical investigations on the relation between the decay ratio and operational margins for monitoring BWR stability", *Proc. of Jahrestagung Kerntechnik 2000, Annual meeting on nuclear technology '00*, May 23-25, Bonn, Germany, (2000)

T.H.J.J. van der Hagen, R. Zboray and W.J.M. de Kruijf, "Questioning the use of the decay ratio in BWR stability monitoring", *Ann. Nucl. Energy*, 27, p. 727-732 (2000).

W.J.M. de Kruijf, R. Zboray and T.H.J.J. van der Hagen, "Including the Travelling of Density Waves in the Analytical Modeling of Coupled Neutronic-Thermohydraulic Power Oscillations", *Proc. of Physor 2000, May 7-11*, 2000, Pittsburg, Pennsylvania, USA

W.J.M. de Kruijf, R. Zboray, A. Manera, T.H.J.J. van der Hagen, H. van Dam and R.F. Mudde, "Non-linear characteristics of thermohydraulic instabilities in innovative BWRs", *Proc. of ICENES 2000, 10th International Conference on Emerging Nuclear Energy Systems*, September 25-28, 2000, Petten, The Netherlands (2000)

R. Zboray, A. Manera, W.J.M. de Kruijf, T.H.J.J. van der Hagen, D.D.B. van Bragt and H. van Dam, "Experiments on Non-linear Density-Wave Oscillations in the DE-SIRE Facility", *Proc. of 9th Int. Topical Mtg. On Nuclear Reactor Thermal Hydraulics (NURETH-9)*, San Francisco, USA, October 3-8, 1999 (1999)

R. Zboray, D.D.B. van Bragt, Rizwan-uddin, T.H.J.J. van der Hagen and H. van Dam, "Influence of Asymmetrical Axial Power Distributions on Nonlinear BWR Dynamics", *Proc. of 9th Int. Topical Mtg. on Nuclear Reactor Thermal Hydraulics (NURETH-9)*, San Francisco, USA, October 3-8, 1999 (1999)

T.H.J.J. van der Hagen, D.D.B. van Bragt, R. Zboray, Rizwan-uddin and W.J.M. de Kruijf, "Analytical parametric studies on BWR nonlinear dynamics" (keynote paper). *Proc. of the 2nd International Conference on Heat Transfer and Transport Phenomena in Multiphase Systems (Heat'99)*, Kielce, Poland, May 18-22, 1999, (1999) 61-70.

R. Zboray, A. Manera, T.H.J.J. van der Hagen and W.J.M. de Kruijf, "Destabilizing the DESIRE facility by increasing the riser exit pressure drop", *Proc. of Jahrestagung Kerntechnik '99, Annual meeting on nuclear technology '99*, May 18-21, 1999, Karlsruhe, Germany, (1999) 79-82.

T.H.J.J. van der Hagen, D.D.B. van Bragt, R.Zboray, Rizwan-udding and W.J.M. de Kruijf, "The importance of non-linear effects in estimating BWR stability margins", *Proc. of Jahrestagung Kerntechnik '99, Annual meeting on nuclear technology '99*, May 18-21, 1999, Karlsruhe, Germany, (1999) 83-86.

Bibliography

Achard, J. L., Drew, D. A., and Lahey, R. T. (1985). The Analysis of Nonlinear Density-Wave Oscillations in Boiling Channels. *J. Fluid Mech.*, 155:213.

Adams, B. T. (1997). A scaling law verification of the Delft Simulated Reactor. In *Proc. 20th Nuclear Simulation Symposium*, Ontario , Canada. Canadian Nuclear Society.

Ambrosini, W., Di Marco, P., and Ferreri, J. C. (1998). Analysis of density-wave instability phenomena by means of nonlinear analytical tools. In *XVI UIT National Heat Transfer Conference*, Siena, Italy.

Beckjord, E. S. (1957). Dresden Reactor Stability Test. Technical Report ANL-5799, Argonne National Laboratory.

Bouré, J. A., Bergles, A. E., and Tong, L. (1973). Review of Two-phase Flow Instability. *Nucl. Eng. Des.*, 25:165–192.

Challberg, R. C. (2002). *Personal communication.*

Challberg, R. C., Cheung, Y. K., Khorana, S. S., and Upton, H. A. (1998). ESBWR Evolution of Passive Features. In *Proc. ICONE-6 (6th Int. Conf. Nucl. Eng.), San Diego, USA*, Illinois, USA. ASME.

Chang, C. J. and Lahey, R. T. (1997). Analysis of chaotic instabilities in boiling systems. *Nucl. Eng. Des.*, 167:307.

Cheung, Y. K., Shiralkar, B. S., and Rao, A. S. (1998). Design Evolution of Natural Circulation in ESBWR. In *Proc. ICONE-6 (6th Int. Conf. Nucl. Eng.), San Diego, USA*, Illinois, USA. ASME.

Clausse, A. and Lahey, R. T. (1991). The Analysis of Periodic and Strange Attractors During Density-Wave Oscillations in Boiling Flows. *Chaos, Solitons and Fractals*, 1:167.

D'Auria, F., Anegawa, T., Blomstrand, J., In de Betou, J., Langenbuch, S., Lefvert, T., and Valtonen, K. (1997). State of the Art Report on Boiling Water Reactor Stability. Technical Report CSNI-OECD NEA.

DeShong, J. A. and Lipinski, W. C. (1958). Analyses of Experimental Power-reactivity Feed-back Transfer Functions for a Natural Circulation Boiling Water Reactor. Technical Report ANL-5850, Argonne National Laboratory.

Eckmann, J. P., Oliffson-Kamphorst, S., Ruelle, D., and Cilibreto, S. (1986). Liapunov exponents from time series. *Phys. Rev. A*, 34:4971–4979.

Eckmann, J. P. and Ruelle, D. (1985). Ergodic theory of chaos and strange attractors. *Rev. Mod. Phys.*, 57:617–656.

Edwards, R. M., Huang, Z., and Weidong, H. (2000). Integration of a Thermal-hydraulic Test-loop and University Research Reactor for Advanced Monitoring and Control Research. In *Proc. International Topical Meeting on Nuclear Plant Instrumentation, Controls, and Human-Machine Interface Technologies*, Washington, DC.

Feigenbaum, M. J. (1980). The transition to aperiodic behavior in turbulent systems. *Commun. Math. Phys.*, 77:65–86.

Fukuda, K. and Kobori, T. (1979). Classification of Two-Phase Instability by Density Wave Oscillation Model. *J. Nucl. Sci. Technol.*, 16:95.

Garea, V. B., Chang, C. J., Bonetto, F. J., Drew, D. A., and Lahey, R. T. (1994). The analysis of nonlinear instabilities in boiling systems. In *New Trends in Nuclear System Thermohydraulics, Pisa, Italy.*

GE (1983). Evaluation of Caorso scram 73. Technical Report NEDO-30112-1, General Electric Company.

Gibbs, H. M., Hopf, F. A., Kaplan, D. L., and Shoemaker, R. L. (1981). Observation of chaos in optical bistability. *Phys. Rev. Lett.*, 46:1349–1352.

Giglio, M., Musazzi, S., and Perini, U. (1981). Transition to chaotic behavior via a reproducible sequence of period-doubling bifurcations. *Phys. Rev. Lett.*, 47:243–246.

Grassberger, P. and Procaccia, I. (1983a). Characterisation of strange attractors. *Phys. Rev. Lett.*, 50:346–349.

Grassberger, P. and Procaccia, I. (1983b). Estimation of the Kolmogorov entropy from a chaotic signal. *Phys. Rev. A*, 28:2591–2593.

Grassberger, P., Schreiber, T., and Schaffrath, C. (1991). Nonlinear time sequence analysis. *Int. J. Bif .and Chaos*, 1:521–547.

Hale, J. and Kocak, H. (1991). *Dynamics and Bifurcations.* Springer-Verlag, New York.

Hassard, B. D. (1987). A code for Hopf Bifurcation Analysis of Autonomous Delay-Differential Equations. In *Proc. Of Oscillation, Bifurcation and Chaos*, page 441. Canadian Mathematical Society.

Hassard, B. D., Kazarinoff, N. D., and Wan, Y. H. (1981). *Theory and Application of Hopf Bifurcation, London Mathematical Society Lecture Note Series 41.* Cambridge University Press.

Hetrick, D. L. (1971). *Dynamics of nuclear reactors.* The University of Chicago Press, Chicago.

Hilborn, R. C. (1994). *Chaos and Nonlinear Dynamics.* Oxford University Press, New York.

Hoyer, N. (1994a). MONA, a 7-Equation Transient Two-Phase Flow Model for LWR Dynamics. In *Proc. Int. Conf. on New Trends in Nuclear System Thermohydraulics*, pages 271–280.

Hoyer, N. (1994b). Validation of the Transient Two-phase Flow Model MONA Against Density Wave Oscillations. In *Proc. First Inetrnational Symposium on Two-Phase Flow Modelling and Experimentation*, Rome , Italy. Edizioni ETS.

Huang, Z. and Edwards, R. M. (2000). Hybrid Reactor Simulation of BWR Using a First Principle Boiling Channel Model. In *Proc. International Topical Meeting on Nuclear Plant Instrumentation, Controls, and Human-Machine Interface Technologies*, Washington, DC.

IRS (1988). Loss of recirculation pumps accompanied by severe power oscillations at La Salle unit 2. Technical Report 880309 IRS-887.0.

Kakac, S. and Liu, H. T. (1991). Two-phase flow dynamics instabilities in boiling systems. In *Multiphase Flow and Heat Transfer, Second International Symposium*, pages 403–444, Washington, DC. Hemisphere.

Karve, A. A., Rizwan-uddin, and Dorning, J. J. (1994). On Spatial Approximations for Liquid Enthalpy and Two-phase Quality During Density-Wave Oscillations. *Trans. Am. Nucl. Soc.*, 71:533.

Karve, A. A., Rizwan-uddin, and Dorning, J. J. (1997). Stability analysis of BWR nuclear-coupled thermal-hydraulics using a simple model. *Nucl. Eng. Des.*, 177:155.

Kennel, M. B. and Isabelle, S. (1992). Method to distinguish possible chaos from colored noise and to determine embedding parameters. *Phys. Rev. A*, 46:3111–3118.

Kok, H. V. (1998). *Experiments on a Natural Circulation Loop - from Void-fraction to Coupled Nuclear Thermal-hydraulics*. PhD thesis, Delft University of Technology, Delft, The Netherlands.

Kok, H. V. and Van der Hagen, T. H. J. J. (1999). Design of a Simulated Void-Reactivity Feedback in a Boiling Water Reactor Loop. *Nucl. Technol.*, 128:1–11.

Kramer, A. W. (1958). *Boiling Water Reactors*. Addison-Wesley Publishing Company.

LABVIEW (2000). *User Manual, National Instruments LABVIEW*. National Insturments Corporation.

Lahey, R. T. and Moody, F. J. (1993). *The thermal-hydraulics of a boiling water reactor*. American Nuclear Society.

Lahey, R. T. and Yadigaroglu, G. (1982). On the relationship between Ledinegg and density wave instability analysis. *Trans. Am. Nucl. Soc.*, 41:689.

Lauternborn, W., Kurz, T., and Parlitz, U. (1997). Experimental Nonlinear Physics. *Int.J.Bif.and Chaos*, 7:2003–2033.

Lee, S. Y. and Lee, D. W. (1991). Linear analysis of flow instabilities in an open two-phase natural circulation loop. *Nucl. Eng. Des.*, 128:317.

Linsay, P. S. (1981). Period-doubling and chaotic behavior in a driven anharmonic oscillator. *Phys. Rev. Lett.*, 47:1349–1352.

Manera, A. (1998). Stability Analysis of the DESIRE facility with MONA 1.9 and with a frequency-doamin code. Technical Report IRI-131-98-012, IRI, TU Delft.

March-Leuba, J. (1984). *Dynamic Behavior of Boiling Water Reactors.* PhD thesis, University of Tennessee, Knoxville,Tennessee,USA.

March-Leuba, J., Cacuci, D. G., and Perez, R. B. (1986a). Nonlinear Dynamics and Stability of Boiling Water Reactors: Part 1 - Qualitative Analysis. *Nucl. Sci. Eng.*, 93:111–123.

March-Leuba, J., Cacuci, D. G., and Perez, R. B. (1986b). Nonlinear Dynamics and Stability of Boiling Water Reactors: Part 2 - Quantitative Analysis. *Nucl. Sci. Eng.*, 93:124–.

March-Leuba, J. and Rey, J. M. (1993). Coupled Thermalhydraulic-Neutronic Instabilities in Boiling Water Nuclear Reactors: A Review of the State of the Arts. *Nucl. Eng. Des.*, 145:99.

McCandless, R. J. and Redding, J. R. (1989). Simplicity: the key to improved safety, performance and economics (SBWR reactor). *Nucl. Eng Int.*, 34:20–24.

Miida, J. and Suda, N. (1963). Derivation of transfer functions of natural circulation boiling water reactor. Technical Report JAERI-1044, JAERI.

Munoz-Cobo, J. L. and Verdú, G. (1991). Application of Hopf bifurcation Theory and Variational Methods to the study of Limit Cycles in boiling Water Reactors. *Ann. Nucl. Energy*, 18:269–302.

Murley, T. E. (1990). Developments in nuclear safety. *Nucl. Safety*, 31:1–19.

Narayanan, S., Srinivas, B., Pushpavanam, S., and Murty Bhallamudi, S. (1997). Nonlinear dynamics of a Two-phase Flow System in an evaporator: The Effects of (i) A Time Varying Pressure Drop (ii) An Axially Varying Heat Flux. *Nucl. Eng. Des.*, 92:253.

Ogata, K. (1987). *Discrete-time Control Systmes.* Engelewood Cliffs: Prentice-Hall.

Ott, K. O. and Neuhold, R. J. (1985). *Nuclear Reactor Dynamics.* American Nuclear Society, La Grange Park, Illinois, USA.

Packard, N. H., Crutchfield, J. P., Farmer, J. D., and Shaw, R. S. (1980). Geometry from a Time series. *Phys. Rev. Lett.*, 45:712–716.

Pinheiro Rosa, M. and Podowski, M. Z. (1994). Nonlinear effects in two-phase flow dynamics. *Nucl. Eng. Des.*, 146:277–288.

Podowski, M. Z. and Pinheiro Rosa, M. (1997). Modeling and numerical simulation of oscillatory two-phase flows, with application to boiling water nuclear reactors. *Nucl. Eng. Des.*, 177:179–188.

Press, W. H., Flannery, B. P., Teukolsky, S. A., and Vetterling, W. T. (1986). *Numerical Recipies; The art of Scientific Computing.* Cambridge University Press.

Priestley, M. B. (1981). *Spectral analysis and time series.* Academic Press, London.

Rao, Y. F., Fukuda, K., and Hashii, N. (1996). Experimental Study of Coupled Thermal and Neutronic Instabilities of Two-phase Flows in a boiling channel. In *Proc. of the ASME Heat Transfer Division*, pages 373–379. ASME.

Rao, Y. F., Fukuda, K., and Kaneshima, R. (1995). Analytical study of coupled neutronic and thermodynamic instabilities in a boiling channel. *Nucl. Eng. Des.*, 154:133.

Rizwan-uddin (1994). On Density-Wave Oscillations in Two-Phase Flows. *Int. J. Multiphase Flow*, 20:721–737.

Rizwan-uddin and Dorning, J. J. (1986). Stability Analyses of Density Wave Oscillations in Channels with Nonuniform Heat Fluxes. *Trans. Am. Nucl. Soc.*, 52:404–405.

Rizwan-uddin and Dorning, J. J. (1987). Nonlinear Stability Analyses of Density-Wave Oscillations in Nonuniformly Heated Channnels. *Trans. Am. Nucl. Soc.*, 54:172–173.

Rizwan-uddin and Dorning, J. J. (1990). Chaotic Dynamics of a Triply-Forced Two-Phase Flow System. *Nucl. Sci. Eng.*, 105:123–135.

Saha, P., Ishii, M., and Zuber, N. (1976). An Experimental Investigation of the Thermally Induced Flow Oscillations in Two-Phase Systems. *Journal of Heat Transfer*, November:616–622.

Sano, M. and Sawada, Y. (1985). Measurement of the Lyapunov spectrum from a chaotic time series. *Phys. Rev. Lett.*, 55:1082–1085.

Schouten, J. C., Takens, F., and Van den Bleek, C. M. (1994a). Estimation of the dimension of a noisy attractor. *Phys. Rev. E*, 50:1851–1861.

Schouten, J. C., Takens, F., and Van den Bleek, C. M. (1994b). Maximum-likelihood estimation of the entropy of an attractor. *Phys. Rev. E*, 49:126–129.

Schouten, J. C. and Van den Bleek, C. M. (1994). RRCHAOS: A Menu-driven Software Package for chaotic time Series Analysis. Technical report.

Shanathanan, C. K. (1964). Dynamic Analysis of Coolant Circulation in Boiling Water Nuclear Reactors. Technical Report ANL-6847, Argonne National Laboratory.

Smith, C. W., Tejwani, M. J., and Farris, D. A. (1982). Bifurcation universiality for first-sound subharmonic generation in superfluid helium-4. *Phys. Rev. Lett.*, 48:492–494.

Stenning, A. H. and Veziroglu, T. N. (1965). Flow oscillations modes in forced convection boiling. In *Proc. 1965 Heat Transfer and Fluid Mech. Inst.*, pages 301–316. Stanford University Press, CA.

Takens, F. (1981). *Detecting strange attractors in turbulence*, page 366. Springer-Verlag, Berlin.

Taylor, J. J. (1989). Improved and safer nuclear power. *Science*, 244:318–325.

Thie, J. A. (1957). EBWR Physiscs Experiments. Technical Report ANL-5711, Argonne National Laboratory.

Thie, J. A. (1958). Theoretical Reactor Statics and Kinetics of Boiling Reactors. In *Proc.Geneva Conf.*, page 440, Geneva, Switzerland. Stanford University Press, CA.

Todreas, N. E. and Kazimi, M. S. (1989). *Nuclear Systems I, Thermalhydraulic Fundamentals*. Hemisphere Publishing Corporation.

Tsuji, M., Nishio, K., and Narita, M. (1993). Stability Analysis of BWRs Using Bifurcation Theory. *Journ. Of Nucl. Sci. and Tech.*, 30:1107–1119.

Turso, J. A., Edwards, R. M., and March-Leuba, J. (1995). Hybrid simulation of Boiling Water Reactor Dynamics using a university Research Reactor. *Nucl. Technol.*, 110:132–144.

Upadhyaya, B. R., Kitamura, M., and Kerlin, T. W. (1980). Multivariate Signal Analysis Algorithms for Process Monitoring and Parameter Estimation in Nuclear Reactors. *Ann. Nucl. Eng.*, 7:1–1.

Van Bragt, D. D. B. (1995). A theoretical model for coupled neutronic-thermohydraulic out-of-phase oscillations in Boiling Water Reactor. Technical Report IRI-131-95-015, IRI, TU Delft.

Van Bragt, D. D. B. (1998). *Analytical Modelling of Boiling Water Reactor Dynamics*. PhD thesis, Delft University of Technology, Delft, The Netherlands.

Van Bragt, D. D. B., Rizwan-uddin, and Van der Hagen, T. H. J. J. (1998). Effect of Void Distribution Parameter and Axial Power Profile on BWR Bifurcation Characteristics. In *Proc. Int. Conf. on the Physics of Nucl. Science and Technology, Long Island, NY*.

Van Bragt, D. D. B., Rizwan-uddin, and Van der Hagen, T. H. J. J. (1999). Nonlinear analysis of a natural circulation boiling water reactor. *Nucl. Sci. Eng.*, 131:23–44.

Van Bragt, D. D. B. and Van der Hagen, T. H. J. J. (1998a). Stability of Natural Circulation Boiling Water Reactors: Part I - Description Stability Model and Theoretical Analysis in Terms of Dimensionless Groups. *Nucl. Technol.*, 121:40–51.

Van Bragt, D. D. B. and Van der Hagen, T. H. J. J. (1998b). Stability of Natural Circulation Boiling Water Reactors: Part I - Parametric study of coupled neutronic-thermohydraulic stability. *Nucl. Technol.*, 121:52.

Van de Graaf, R., Van der Hagen, T. H. J. J., and Mudde, R. F. (1994a). Scaling Laws and Design Aspects of a Natural-Circulation-Cooled Simulated Boiling Water Reactor Fuel Assembly. *Nucl. Technol.*, 105:190–199.

Van de Graaf, R., Van der Hagen, T. H. J. J., and Mudde, R. F. (1994b). Two-phase scaling laws for a simulated BWR assembly. *Nucl. Eng. Design*, 148:455–462.

Van der Hagen, T. H. J. J. (1996). The effect of turbulent diffusion on transit-time dtermination by cross correlation of temperature fluctuations. *Ann. Nucl. Energy*, 23:47–58.

Van der Hagen, T. H. J. J., Pazsit, I., and Thomson, O. (1995). Methods for the Determination of the In-phase and Out-of-phase Stability Characteristics of a Boiling Water Reactor. *Nucl. Technol.*, 107:193–214.

Van der Hagen, T. H. J. J., Stekelenburg, A. J. C., Kaart, S., and Schouten, J. C. (1996). Investigation on Start-Up Flow oscillations in Natural Circulation BWRs. In *Proceedings of National Heat Transfer Conference*, pages 188–197. ANS.

Van der Hagen, T. H. J. J., Van Bragt, D. D. B., Van der Kaa, F. J., Karuza, J., Kilian, D., Nissen, W. H. M., Stekelenburg, A. J. C., and Wouters, J. A. A. (1997). Exploring the Dodewaard Type-I and Type-II stability; from start-up to shut-down, from stable to unstable. *Ann. Nucl. Energy.*, 24:659–669.

Wang, F. S., Hu, L. W., and Pan, C. (1994). Thermal and Stability Analysis of a Two-Phase Natural Circulation Loop. *Nucl. Sci. Eng.*, 117:33.

Wilcox, D. C. (1993). *Turbulence modelling for CFD*. DCW Industries, La Canada, California.

Wolf, A., Swift, J. B., Swinney, H. L., and Vastano, J. A. (1985). Determining Lyapunov exponents from time series. *Physica D*, 16:285–317.

Wolfram, S. (1996). *The Mathematica book*. Cambridge University Press.

Yadigaroglu, G. (1981). *Two-phase flow instabilities and propagation phenomena*, chapter 17, pages 353–403. Hemisphere Publishing Corporation.

Summary

The dynamics and stability of natural-circulation boiling water reactors (BWRs) have been studied in this thesis using diverse tools: a reduced-order analytical model, an advanced thermal-hydraulic system code (MONA) and a natural-circulation two-phase flow loop, the DESIRE facility.

The *linear stability* of natural-circulation BWRs has been investigated extensively using the reduced-order model. This *reduced-order model* is very suitable for fast parametric studies on the stability of BWRs. It has the capability to increase the insight into the relevant physical processes responsible for the occurrence of instabilities. The sensitivity of the stability of the natural-circulation, boiling two-phase flow has been examined to the different types of pressure drops present in the system. It has been found that the accelerational and the two-phase frictional pressure drops are the most important destabilizing terms for the Type-II instability and that the gravitational pressure drop in the riser is the most important destabilizing term for the Type-I instability. Using frequency-domain analysis, the poles of a natural-circulation BWR have been identified with neutronic, heat transfer and thermal-hydraulic processes. It is shown that the strength of the void-reactivity feedback influences which pole pair of the reactor determines the stability in the Type-II and in the Type-I region.

The reduced-order model has been extended with taking into account core-inlet temperature variations. It is shown that it has a significant effect on the thermal-hydraulic stability of the system. It is found that *moving the feedwater sparger to the core inlet* strongly stabilizes the thermalhydraulics. Similar result have been found using the MONA code for relatively small core-inlet to feedwater sparger distances.

The reduced-order model has been used to examine the practicability of using solely the *decay ratio* in BWR stability monitoring. It was shown that the system can be much closer to unstable behavior in terms of operational variables than the value of the decay ratio would indicate. Therefore, relying only on the value of decay ratio can be misleading in judging the stability margin in terms of operational variables.

The influence of the axial power profile on the *nonlinear dynamics* of BWRs has been examined using a numerical Hopf bifurcation code based on the reduced-order model. It is shown that *bifurcation characteristics* of the thermal-hydraulic system are sensitive to the axial power profile. Both sub- and supercritical bifurcations are encountered. Generally, strongly bottom-peaked profiles might result in subcritical bifurcations (accompanied by diverging oscillations). The bifurcation characteristics of the reactor are found, in accordance with earlier studies, to be strongly influenced by the strength of the void-reactivity feedback, which overrules the influence of the power profile.

Using the experimental tool, the *DESIRE facility*, first, the *thermal-hydraulic stability* of this natural-circulation system has been mapped. Valuable experimental data has been gathered, which can be indicative for innovative, natural-circulation BWR designs as well. The measured stability indicators are predicted fairly well by the MONA code, however, the reduced-order model predicts only the trends in the stability indicators correctly.

Next, the nonlinear dynamics of the natural-circulation two-phase flow has been investigated using the facility. It is demonstrated that the two-phase flow undergoes the so-called Feigenbaum scenario, the *period-doubling route towards chaotic behavior* as one penetrates into the unstable operating region of the system. To the author's knowledge, this is the first occasion that this phenomenon has been experimentally observed in (boiling) two-phase flow systems.

As an extension of the experimental possibilities of the thermal-hydraulic facility, the DESIRE facility is equipped with an *artificial void-reactivity feedback simulation*. This hybrid system is used to investigate the stability of natural-circulation BWRs experimentally. The most crucial point in the simulation is the *real-time reconstruction of the axial void-fraction profile* in the heated assembly. New void-fraction reconstruction methods have been introduced into the simulator to improve its performance. These methods are based on the measured pressure drop over the heated assembly (integral measurement), or on local gamma-transmission void-fraction measurements applying improved models (higher-degree polynomial expansion of the void-fraction profile) or on a combination of these. The performance of the different methods have been compared with respect to reconstructing the dynamics of the actual core-averaged void fraction. In general, all methods perform reasonably in dynamic situations. Comparison of the methods is also made for reactor stability measurements.

Dynamic measurements using the improved void-feedback simulation reveal stability trends that are also predicted by the reduced-order model.

Samenvatting

Dit proefschrift beschrijft een zowel experimenteel als modelering onderzoek aan de dynamica van natuurlijke-circulatie kokendwaterreactoren (BWRs). Het onderzoek is uitgevoerd met behulp van: een vereenvoudigd analytische model, een thermohydraulische systeemcode (MONA) en een natuurlijke-circulatie experimentele opstelling, DESIRE.

De *lineaire stabiliteit* van natuurlijke-circulatie BWRs is grondig onderzocht met behulp van het *vereenvoudigd analytische model*. Dit model is zeer geschikt voor het uitvoeren van snelle parameterstudies aan de stabiliteit van BWRs. Met behulp van het model kan man het fysisch inzicht in de rol van de relevante processen vergroten. De invloed van de verschillende type drukvallen op de stabiliteit van natuurlijke-circulatie tweefasenstromingen is bestudeerd. Het is bewezen dat de tweefasige frictiedrukval en de versnellingsdrukval van belang zijn voor de zogenaamde Type-II instabiliteit en dat de gravitatiedrukval in de riser de drijvende kracht voor de zogenaamde Type-I instabiliteit is. De polen van de natuurlijke-circulatie BWR zijn geassocieerd met neutron kinetische, splijtstofdynamische en thermohydraulische processen. Het is aangetoond dat de strekte van de void-reactiviteits terugkoppeling beïnvloedt welke pool paar van het systeem het minst stabiel is in de Type-I en in de Type-II regionen.

Het vereenvoudigd analytische model is uitgebreid met het modeleren van temperatuur variaties bij de inlaat van de rector kern. Het blijkt dat variaties in de inlaat temperatuur een sterke invloed op de stabiliteit van de natuurlijke-circulatie BWR hebben. Verplaatsen van het inlaatspruitstuk dicht bij de inlaat van de kern kan de stabiliteit van het systeem positief beïnvloeden. Vergelijkbare resultaat is gekregen met behulp van de MONA code voor relatief kleine afstanden tussen het inlaatspruitstuk en de kerninlaat.

De bruikbaarheid van de zogenaamde *decay ratio* als indicator voor BWR stabiliteitsbewaking is bestudeerd met behulp van het analytische model. Het is bewezen dat het systeem veel dichter bij de stabiliteitsgrens kan zijn in termen van operationele variabelen dan de waarde van de decay ratio dat indiceërt. Het gebruiken van de decay ratio kan misleidend zijn voor reactoroperators voor het beoordelen van de stabiliteitsmarge.

De invloed van de axiale vermogensverdeling op de *niet-lineaire dynamica* van BWRs is geanalyseerd met behulp van het analytische model. Berekeningen zijn uitgevoerd met een numerieke Hopf bifurcatieprogramma. De resultaten laten zien dat de bifurcatiekarakteritiek van het thermohydraulische systeem hangt van de axiale vermogensverdeling af. Sub- en superkritieke bifurcaties zijn aangetroffen. Over het algemeen, systemen met een maximum van de vermogensverdeling in de onderste helft van de kern onderhevig zijn aan

sub-kritieke bifurcaties vergezeld door divergerende oscillaties. De bifurcatiekarakteristiek van de reactor is uiterst afhankelijk van de sterkte van void-reactiviteits terugkoppeling, hetgeen onderdrukt de invloed van de vermogensverdeling aan de niet-lineaire dynamica.

Met behulp van de experimentele opstelling, de *DESIRE faciliteit*, het *thermohydraulische stabiliteit* natuurlijke-circulatie tweefasenstromingen is in kart gebracht. Uitgebreide experimentele data zijn verzameld dat richtlijnen kan geven ook voor de stabiliteit van nieuwe, innovatieve natuurlijke-circulatie BWR ontwerpen. De gemeten stabiliteitsindicatoren zijn goed te voorspelen met behulp van de MONA code. Het vereenvoudigd analytische model kan allen maar de stabiliteit trends voorspelen.

De niet-lineaire dynamica van natuurlijke- circulatie tweefasenstromingen is ook bestudeerd met behulp van de DESIRE opstelling. Voor de eerste maal is experimenteel aangetoond dat natuurlijke-circulatie twefasenstromingen onderhevig zijn aan de zogenaamde Feigenbaum scenario hetgeen *tot chaotisch gedrag via een opeenvolging van periodeverdubbeling bifurcaties* leidt.

De DESIRE opstelling is uitgerust met een *gesimuleerde void-reactiviteits terugkoppeling* om de experimentele potentieel uit te breiden. Dit hybride systeem is gebruikt om de stabiliteit van werkelijk natuurlijke-circulatie BWRs te bestuderen. Hoofdzaak is in de simulatie de correct real-time reconstructie van de axiale dampfractieverdeling. Nieuwe methodes zijn geïmplementeerd in de simulator voor het reconstrueren van de dampfractieverdeling om de prestatie van de simulator te verbeteren. Deze methodes zijn gebaseerd of op de meting van de totale drukval over de kern, of op een tweetal meting van de locale dampfractie of op een combinatie van deze twee. De verschillende methodes zijn vergeleken ten opzichte van het reconstructeren van de kerngemiddelde dampfractie. Over het algemeen, alle reconstructie methodes presteren redelijk goed wat de dynamica van de kerngemiddelde dampfractie betreft.

Metingen aan de dynamica van de gesimuleerde reactor tonen stabiliteit trends aan dat ook door het analytische model zijn voorspeld.

Dankwoord

Hierbij wil ik de gelegenheid nemen om mijn dankbaarheid te uiten voor iedereen die me geholpen heeft met het tot stand brengen van dit proefschrift.

Ten eerste wil ik mijn promotors prof. dr. ir. Hugo van Dam en prof. dr. ir. Tim van der Hagen bedanken voor de mogelijkheid om bij de afdeling Reactorfysica een promotie project te kunnen doen. Hun continue aandacht en waardevolle suggesties hebben veel bijgedragen aan de inhoud van dit proefschrift.

Ik bedank mijn dagelijkse begeleider dr. ir. Willy de Kruijf voor zijn inzet en zijn kritische houding ten opzichte van de kwaliteit van het onderzoek.

Ik wil prof. dr. Rob Mudde bedanken voor de waardevolle discussies tijdens de BWR vergaderingen.

Zonder de hulp van technici was dit proefschrift niet tot stand gekomen. Jelle 'de beste technicus ter wereld' Schut, Dick de Haas, Camiel Kaaijk en August Winkelman wil ik bedanken voor het door hen geleverde kwaliteitswerk. Zij waren er altijd voor me wanneer zich praktische problemen voordeden.

I would like to express my gratitude to prof. Rizwan-uddin of the University of Illinois at Urbana-Champaign for his interest in my work. I really appreciate his valuable comments and his willingness to perform bifurcation measurements after hours during his stay at IRI.

Ik bedank Annalisa Manera voor de samenwerking en voor de vele discussies.

Tenslotte wil ik alle medewerkers bij de afdeling Reactorfysica bedanken voor de gezellige sfeer.

Curriculum vitae

Róbert Zboray

Date of birth: 9th April 1974

Place of birth: Sátoraljaújhely (Hungary)

1988-1992:	High school "Gymnasium Lajos Kossuth" in Sátoraljaújhely
1992-1997:	M.Sc. in applied physics at the Technical University of Budapest, majored in Nuclear Engineering
	Graduation project:"Investigation of the influence of propagating perturbations in a training reactor"
1998-2002:	Ph.D. student at the Department of Reactor Physics of the Interfaculty Reactor Institute, Delft University of Technology, The Netherlands
	Ph.D topic: An experimental and modelling study of natural-circulation boiling water reactor dynamics
2002- :	Research engineer at the Laboratory for Thermalhydraulics at the Paul Scherrer Institute, Switzerland